Functional Inorganic Materials for Heterogeneous Electrocatalytic Water Splitting and Proton Conduction

A THESIS

Submitted in partial fulfillment of the
Requirements for the award of the degree
of
DOCTOR OF PHILOSOPHY

by
Athira Ravi

School of Chemistry
University of Hyderabad
Hyderabad - 500046, India.

November 2023

Dedicated to the forces that shaped my journey: my family, friends, teachers, and to the one who weathered it all— myself. Here's to us.

CONTENTS

Chapter 3. Hydroxylated Polyoxometalate with Cu(II)- and Cu(I)-Aqua Complexes: A Bifunctional Catalyst for Electrocatalytic Water Splitting at Neutral pH

DECLARATION

I, **Athira Ravi**, hereby declare that the matter embodied in the thesis '***Functional Inorganic Materials for Heterogeneous Electrocatalytic Water Splitting and Proton Conduction***' is the result of my investigation carried out in School of Chemistry, University of Hyderabad, Hyderabad, India, during the period of January 2019 to November 2023, under the supervision of **Prof. Samar K. Das**.

In keeping with the general practice of reporting scientific observation, due acknowledgements have been made wherever the work described is based on the findings of other investigations. Any omission, which might have occurred by oversight or error, is regretted. This research work is free from plagiarism. I hereby agree that my thesis can be deposited in Shodhganaga / NFLIBNET. A report on plagiarism statistics from the library, University of Hyderabad, is enclosed.

S.K. Das

Prof. Samar K. Das

(Thesis supervisor)

20.11.2023

Prof. Samar K. Das
School of Chemistry
University of Hyderabad
Hyderabad-500 046., INDIA.
skdas@uohyd.ac.in

A Athira

Athira Ravi

(18CHPH33)

हैदराबाद विश्वविद्यालय
University of Hyderabad

CERTIFICATE

INSTITUTION OF EMINENCE

This is to certify that the work described in this thesis entitled '***Functional Inorganic Materials for Heterogeneous Electrocatalytic Water Splitting and Proton Conduction***' submitted on 20.11.2023, has been carried out by **Athira Ravi**, bearing registration number **18CHPH33** (Date of joining: January 10, 2019), in partial fulfilment of the requirements for the award of Doctor of Philosophy in the School of Chemistry, University of Hyderabad, is a bonafide work carried out by her under my supervision and guidance. This thesis is free from plagiarism and has not been submitted previously in part or in full, to this or any other University or Institution for the award of any degree or diploma.

Parts of this thesis has been published in the following publications.

1. Mulkapuri, S.; Ravi, A.; Das, S. K. *Chem. Mater.* **2022**, *34*, 3624–3636. (**Chapter 2**)
2. Ravi, A.; Mulkapuri, S.; Das, S. K. *Inorg. Chem.* **2023**, *62*, 12650–12663. (**Chapter 3**)

The student has made presentation in the following conferences.

Oral presentation

1. Chemfest 2023 (Annual in-house symposium) at School of Chemistry. UoH.
2. Dr. K. V. Rao Scientific Society Research Award, 2022-23.

Poster presentation

1. Chemfest 2022 (Annual in-house symposium) at School of Chemistry. UoH.
2. International conference on Modern Trends in Inorganic Chemistry (MTIC-XIX).

The student has passed the following courses towards fulfilment of course work

S.No.	Course	Title	Credits	Pass/Fail
1.	CY-801	Research Proposal	4	Pass
2.	CY-802	Chemistry Pedagogy	4	Pass
3.	CY-806	Instrumental Methods - B	4	Pass

Dean
School of Chemistry
University of Hyderabad
Hyderabad – 500046, India.

Dean
School of Chemistry
University of Hyderabad
Hyderabad-500 046.

Prof. Samar K. Das
(Thesis supervisor)

20.11.2023

Prof. Samar K. Das
School of Chemistry
University of Hyderabad
Hyderabad-500 046., INDIA.
skdas@uohyd.ac.in

ACKNOWLEDGEMENTS

This thesis sums up the culmination of my research accomplishments, a vital component in attaining the coveted 'doctorate degree'. Nevertheless, I firmly assert that only few achievements in this world are accomplished in isolation. The Ph.D. journey, much like life itself, is incomplete without acknowledging the indispensable contributions of those who have played a pivotal role in shaping my life to this significant juncture.

To begin with, I would like to offer a heartfelt tribute to all the teachers who illuminated my path with wisdom and invaluable life lessons. I extend my deepest gratitude to my supervisor, Prof. Samar Kumar Das, whose guidance went beyond academia, emphasizing the integral connection between physical fitness and scholarly pursuits. His simple yet powerful advice, "Drink water and Do j(y)oga" may sound easy but it carries a insightful life lesson. In a world where many conceal their failures, he stands out as someone who openly shares his own setbacks, serving as a constant source of motivation for all of us. I take it as an honor to have been a part of his research group.

I would like to acknowledge the present and former Deans of School of Chemistry and my doctoral committee members Prof. V. Baskar and Prof. R. Nagarajan, who were kind and motivating whenever I had met them. My sincere thanks to all the non-teaching staff, especially Mahesh Bhayya and Sunil Sir, who always welcomed me with their warm smiles whenever I went with my samples. And, I would like to thank, University of Hyderabad, and IoE ,University of Hyderabad, for the much-needed financial assistance for the research works and for my fellowship.

The environment of our workspace holds paramount importance for a research scholar leading a strenuous journey of a Ph.D. The lab transforms into our home, and labmates become our extended family. I consider myself fortunate to have had a wonderful set of people as my workmates. I am truly speechless in conveying the extent of my gratitude to my senior, Sateesh Anna, who not only guided me but lifted me up in life. His incredible support, akin to that of a brother, is something I will be forever thankful for and more. I thank all my seniors, R.K. anna, Suresh anna, Tulasi akka, Subho bhayya, Tanmay bhayya, Chandani di, Joycy di, Vinod anna, Amit bhayya and Mousumi di for their support. I also wish to thank my colleague and friend, Debu, with whom I cherish a special bond of friendship or brotherhood. I also thank my juniors

Lakshmi, Florence, Rameswari, and Sarbani whom I wish would keep the lab spirit up. My UoH life would have become worthless without my 'Chai team' or my 'ready-to-adventure' team- Rajendar anna, Hema akka, Olivia di, Parvathy, Gopika and Karthik. I think they really have no idea how much each one of them had played a crucial role in the past five years of my life. My project fellows, Ratri, Suman and Akash, whom I had never regarded as my students since they generously, had shared their wealth of knowledge with me.

I feel fortunate to have got a lot of help and support from my friends, colleagues, and seniors in School of Chemistry. I fondly remember the moments which I had shared with Anil anna, Bala anna, Bilal, Mamina di, Pasha, Suman, Calvin, Smruthi, Seema, Vinay, Vinod, Hemanth, Anu, Reema, Anjali, Kumari, Sonali, Ritu, Jiji, Narmada, Anjali, Melchi, Ankur, Manoj, Avijit, Aradhana and so many. I am thankful to have a well-sorted batchmates, Somratan, Sarawani, Ritesh, Ithu, and Snehalatha.

My mornings were consistently rejuvenated thanks to my friends Monalisha, Vandana, and Amerinder, with whom I shared breakfast in the mess. Their company made it easier for me to savor the food served. Reflecting on the happy and challenging days of my Ph.D. journey, one name invariably rises to the top – my buddy, Gunjan. I can't imagine a life at UoH without her. Our resonance in ideas, lifestyle, maturity, and occasional playfulness is unparalleled. Words fall short in expressing my gratitude for her profound presence in my life. Also, I cannot overlook the significant role played by my friend Amesh, who served as a mentor and a partner and whose presence not only eased the challenges but also brought a sense of calmness and joy to my Ph.D. journey.

My college played a crucial role in helping me understand the intricacies of Chemistry, and my Professors, Radhika mam, Mallika mam, R.V. sir, Chandra mam, Rafia mam and Manonmani mam, planted the seeds of a Ph.D. dream in me. I am immensely grateful to them for their guidance and inspiration. My friends, Viba, Barani, Gokul, Kavya, Dhivya, and Adithya made my project days at Indira Gandhi Centre for Atomic Research, Kalpakkam, fun-filled. I appreciate my close buddies, Hari, Lissa, Rainu, Mubu, Jithu, and Vishnu, who had made my Coimbatore life the most memorable.

School was the crucible that molded me into the person I am today. My best friends from school Namita, Haritha, Vishnu, Sayed, Imadh and Neha played a pivotal role in shaping the trajectory of my life. I cannot forget to express my gratitude to all the school teachers who taught me to read and write, grooming me into the person I am today. They played a fundamental role in making me who I am.

I am overwhelmed with gratitude towards my Papa and Amma, whose boundless love and support have been the emotional pillars of my life. My dear brother, Arun Chettan, and his wife, Ambili Chechi, have consistently treated me and my wishes as their top priority over anything else. I proudly assert that they have raised me with high morals and compassion, fostering a unique bond of friendship among us five that surpasses mere parenthood. Equally, I take pride in the exceptional support system provided by my relatives and cousins. In a world full of judgmental individuals casting doubt on one's capabilities, my relatives have consistently elevated me and my aspirations, offering relentless support in my pursuit of goals. Their unwavering encouragement has been a cornerstone, and I am deeply grateful for the strength of this family network.

In closing, I extend heartfelt thanks and appreciation to myself for unshakably holding onto hope throughout both personal and professional challenges, keeping my head held high. I acknowledge the strength within me that never wavered. I humbly bow to my own confidence and discipline, the steadfast pillars supporting the small achievements I have accomplished.

I also express gratitude to those who, intentionally or not, withheld their helping hands and expressed lack of enthusiasm. Their actions have unwittingly fueled my realization of the inner strength I possess.

Finally, I take a deep bow to God for blessing me with a remarkable family, friends, and teachers. Their presence has simplified and enriched my life, making it a journey filled with simplicity and joy.

Athira Ravi

University of Hyderabad

November, 2023

SYNOPSIS

of the Thesis Entitled

"Functional Inorganic Materials for Heterogeneous Electrocatalytic Water Splitting and Proton Conduction"

To be submitted to the
University of Hyderabad

For the degree of
DOCTOR OF PHILOSOPHY

by

ATHIRA RAVI
(18CHPH33)

School of Chemistry
University of Hyderabad
Hyderabad - 500046, India.

November 2023

The doctoral thesis entitled as "**Functional Inorganic Materials for Heterogeneous Electrocatalytic Water Splitting and Proton Conduction**" contains five chapters: four working chapters and one chapter on general introduction on literature and motivation of the work. The chapters are as follow: (1) Introduction to Polyoxometalates Mediated Electrocatalytic Water Splitting and Proton Conduction and Motivation of the Thesis Work, (2) Fabricating a Functionalized Polyoxometalate with ZIF-8: A Composite Material for Water Oxidation in a Wide pH Range, (3) Hydroxylated Polyoxometalate with Cu(II)- and Cu(I)-Aqua Complexes: A Bifunctional Catalyst for Electrocatalytic Water Splitting at Neutral pH, (4) Tungsten–hydroxyl on Polyoxotungstate Surface for Green Energy: Electrochemical HER, (5) Superprotonic Conductivity Studies of W-OH Grafted Polyoxometalates.

The First Chapter which is the introduction chapter includes discussion about water splitting, which is basically two half cell reactions, viz. hydrogen evolution reaction (HER) and Oxygen evolution reaction (OER) catalysis. Then, a class of inorganic compounds, polyoxometalates, (POMs) and their structural versatility are discussed in details. It also explains how POMs are utilized or employed as electrocatalysts and proton conductors. The motivation of this thesis work is discussed in the end of this chapter. All other chapters are divided into the following parts: (a) Overview (brief overview of the work), (b) Introduction (literature survey relevant to the study), (c) Experimental section (including materials and methods employed for the study), (d) Results and discussion, (e) Conclusion and (f) References. The compounds in the thesis work are characterized by FT-IR spectral analysis, powder X-Ray diffraction (PXRD), Raman spectroscopy, thermogravimetric analysis (TGA), UV-Visible diffused reflectance spectroscopy (DRS), field emission scanning electron microscopy (FESEM), dynamic light scattering (DLS) analysis, high resolution transmittance electron microscopy (HRTEM), inductively coupled plasmon optical emission spectroscopy (ICP-OES), N_2 and water sorption analysis. Proton conductivity studies of concerned samples were performed using a two electrode setup.

Chapter 1

Introduction to Polyoxometalates Mediated Electrocatalytic Water Splitting and Proton Conduction and Motivation of the Thesis Work

This chapter aims to outline the current plight of ever-increasing energy demands in the world, the population's high dependency on depleting fossil fuels, and the severe urge to move towards feasible alternatives to quench energy needs. Progress towards these goals requires, in part, the development of advanced materials and their appropriate utilization for energy storage, conversion, and harnessing. In this respect, hydrogen (H_2) is rising as an excellent fuel that can either be burnt or recombined with oxygen to release the stored energy in a fuel cell. One of the carbon-free methods to produce hydrogen includes electrochemical water splitting, where the development of electrocatalysts plays a vital role. Here, the basics of electrochemical water splitting, the reaction mechanisms involved, and the electrocatalysts utilized, particularly polyoxometalates (POMs) and metal-organic frameworks (MOFs) are briefed. Finally, advancement in fuel-cell technology with sufficient emphasis on the design of proton-conducting materials has also been discussed in this chapter. The chapter ends with concluding remarks and the future scope of the thesis.

Chapter 2

Fabricating a Functionalized Polyoxometalate with ZIF-8: A Composite Material for Water Oxidation in a Wide pH Range

Designing an efficient oxygen evolution reaction (OER) electrocatalyst is a challenging task because molecular oxygen is essential to sustain life. Herein, we have synthesized and structurally characterized a $\{Bi(OH_2)_2\}^{3+}$–functionalized Keggin polyoxometalate (POM) compound, $K_5[Bi(H_2O)_2SiW_{11}O_{39}]\cdot 13H_2O$ (**$K_5$1·13H_2O**). Keeping in mind that $\{Bi(OH_2)_2\}^{3+}$ species on the surface of the POM has the potential to act as an active site for electrocatalytic water oxidation, we encapsulated the functionalized Keggin POM anion $[Bi(OH_2)_2SiW_{11}O_{39}]^{5-}$ inside the cavities of a well-known zeolite type framework material ZIF-8, a zinc-imidazole containing metal-organic framework (MOF), because compound **$K_5$1·13H_2O** *per se* is water soluble and unstable in the oxidation window of water oxidation. The resulting host-guest type composite material $H_5[Bi(H_2O)_2SiW_{11}O_{39}]$@ZIF8 (**$H_5$1@ZIF8**) functions as an efficient

electrocatalyst for water oxidation. The detailed electrochemical analyses have established that the title oxygen evolution reaction (OER) catalyst, **$H_5$1@ZIF8** works in a wide pH window, ranging from alkaline pH 13.0 to neutral pH 7.0 through an acidic pH 4.0. Diverse controlled experiments have been performed to infer that bismuth-aqua complex is the functional site responding to the OER, with a catalytic turnover frequency (TOF) of 1.24 s^{-1}, 5.90 s^{-1} and 0.93 s^{-1} of pH 13.0, pH 7.0 and pH 4.0 solutions, respectively at the respective overpotentials of 375.0 mV (vs RHE), 585.21 mV (vs RHE) and 830.10 mV (vs RHE).

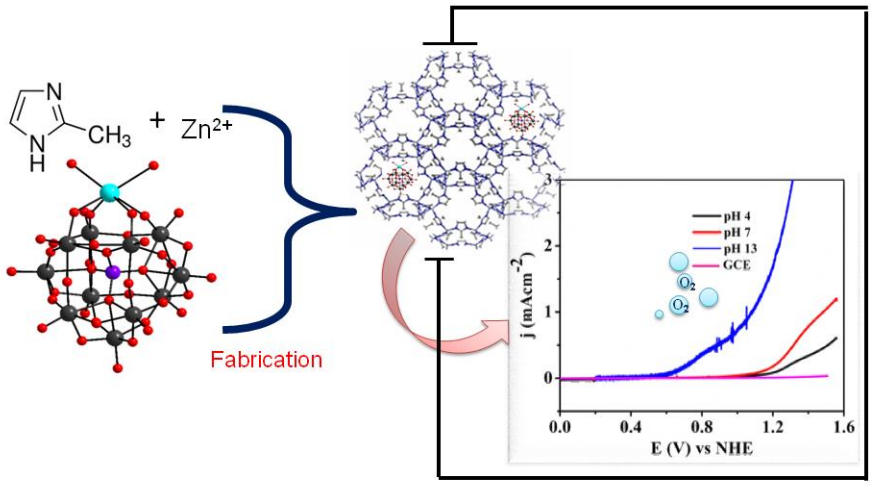

Figure 1. Schematic representation of fabrication of **$H_5$1@ZIF8** for electrocatalytic water oxidation in the wide pH spectrum.

Chapter 3

Hydroxylated Polyoxometalate with Cu(II)- and Cu(I)-Aqua Complexes: A Bifunctional Catalyst for Electrocatalytic Water Splitting

A sole inorganic framework material $[Li(H_2O)_4][\{Cu^{I}(H_2O)_{1.5}\}\{Cu^{II}(H_2O)_3\}_2\{W^{VI}_{12}O_{36}(OH)_6\}]\cdot N_2\cdot H_2S\cdot 3H_2O$ (**LiCu$_3$*para-D***), consisting of a hydroxylated polyoxometalate (POM) anion, $\{W^{VI}_{12}O_{36}(OH)_6\}^{6-}$, a mixed-valent Cu(II)– and Cu(I)–aqua cationic complex species, $[\{Cu^{I}(H_2O)_{1.5}\}\{Cu^{II}(H_2O)_3\}_2]^{5+}$, a Li(I)-aqua complex cation and three solvent molecules, has been synthesized and structurally characterized. During its synthesis, the POM cluster anion gets functionalized with six hydroxyl groups, i.e., six W^{VI}–OH groups per cluster unit. **LiCu$_3$*para-D*** functions as a bifunctional electrocatalyst exhibiting oxygen evolution reaction (OER) by water oxidation and hydrogen evolution reaction (HER) by water reduction at

the neutral pH. Diverse electrochemical controlled experiments have been performed to conclude that the title POM based material functions as a true bifunctional catalyst for electrocatalytic HER as well as OER at the neutral pH without catalyst reconstruction.

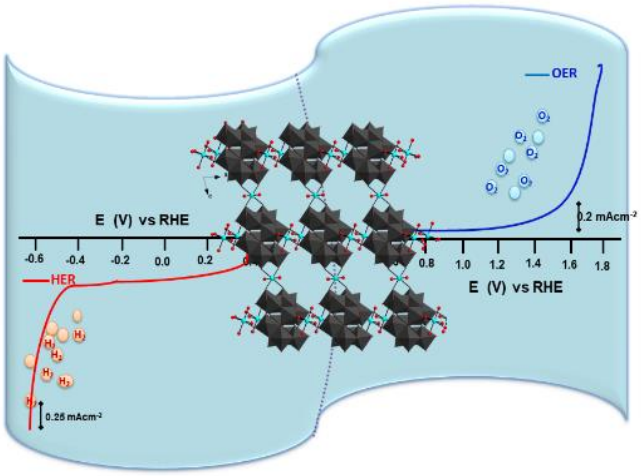

Figure 2. Schematic representation of **LiCu$_3$*para-D*** exhibiting the bifunctional behavior towards overall electrocatalytic water splitting in the neutral pH medium.

Chapter 4

Tungsten–hydroxyl on Polyoxotungstate Surface for Green Energy: Electrochemical HER

Transition metal-hydroxyls, M–OH, is recognized as one of the vital mass transport agents, including in the clean energy cycle. In this chapter, a tungsten-hydroxyl (W^{VI}–OH)-tethered polyoxotungstate complex, $Na_6[\{W^{VI}_{0.75}(OH)(ONa)\}_2\{Mn^{II}(H_2O)_2\}_2\{BiW^{VI}_9O_{33}\}_2]\cdot 18H_2O$ (**POM-MnW(OH)**), has been described, which is structurally characterized as a 2-D framework material. The presence of tungsten-hydroxyls drove us to investigate electrocatalytic hydrogen evolution. The title compound shows excellent hydrogen evolution reaction (HER) activity with a TOF value of 1.81 s^{-1} and stability in terms of 1000 cyclic voltammetric cycles besides 10 hours of chronoamperometry in acidic buffer environment of pH 4.

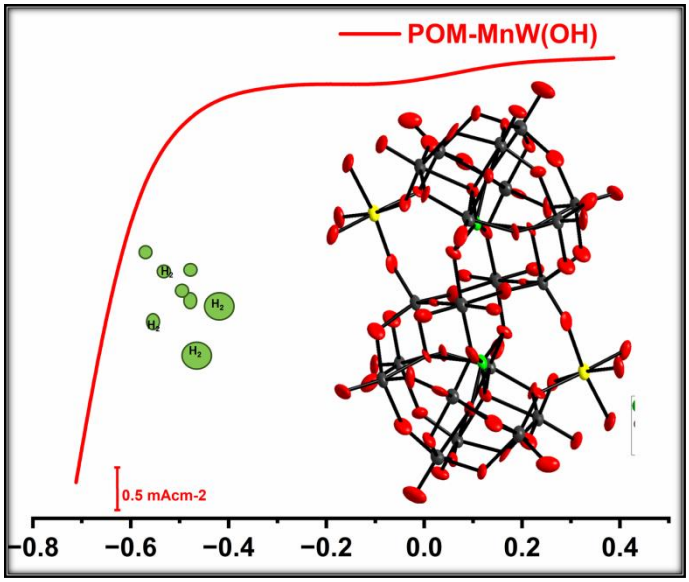

Figure 3. Schematic representation of **POM-MnW(OH)** exhibiting the electrocatalytic water reduction to produce hydrogen gas in the acidic pH medium.

Chapter 5

Superprotonic Conductivity Studies of W-OH Grafted Krebs-type Polyoxometalates

Achieving unique structural stability and exceptional proton conductivity in crystalline materials poses a formidable challenge within the realm of energy-material chemistry. Thus, two Krebs-type polyoxometalate clusters incorporated with cobalt- and manganese- aqua complexes caught our attention. These POM compounds possess unique structural distinctness with the presence of hydroxyl groups grafted onto the surface of tungsten centers which are present as the core of sandwiched between two $\{Bi^{III}W^{VI}_9O_{33}\}^{9-}$ units. The compounds formulated as $Na_6[\{Co^{II}(H_2O)_3\}_2\{W^{VI}(OH)_2\}_2\{(Bi^{III}W^{VI}_9O_{33})_2\}]\cdot 8H_2O$ (**1**) and $Na_8H_3[\{W^{VI}_{0.75}(OH)(O)\}_2\{Mn^{II}(H_2O)_2\}_2\{BiW^{VI}_9O_{33}\}_2]\cdot 18H_2O$ (**2**), possessing labile protons and lattice- and coordinated water molecules encouraged us to perform proton conductivity studies. The compounds have exhibited super protonic conductivity values of **0.978 ×10^{-1} Scm^{-1}** for **1** and **1.07 ×10^{-1} Scm^{-1}** for **2** at a temperature of 80 ℃ at 98% relative humidity (RH). The concerned Arrhenius plots constructed for compounds **1** and **2** have shown a good linearity throughout the temperature range of 40 to 80 ℃ revealing activation energy of 0.64 and 0.66 eV respectively.

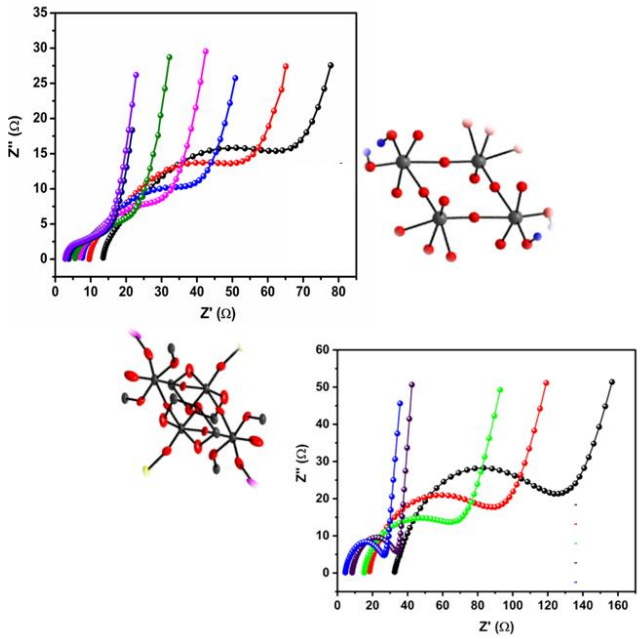

Figure 4. Schematic representation of compounds **1** and **2** which are hydroxyl grafted Krebs type POMs behaving as super-proton conductive materials.

Summary and Future Scope

The summary and future scopes of the work carried out in this thesis work are discussed at the end of the working chapters. The ranges of applications for polyoxometalates (POMs) based materials for energy harnessing are enormous and increasing on a daily basis, as the demand for the same are exponentially increasing. The works carried out in this thesis can be further taken ahead by utilizing POM compounds for photocatalytic water splitting, which is also regarded as a promising technique to produce green hydrogen. Similar to hydrogen evolution reaction (HER) and oxygen evolution reaction (OER), POMs or POM-based materials can be explored for oxygen reduction reaction (ORR) and CO_2- reduction reactions (CO_2-RR), which contribute extensively towards sustainable life. Finally, POMs or their composite materials can also be employed as nano-fillers in the proton exchange membranes (PEMs) which further can enhance the conductivity of PEM and could be used in the fuel cells.

List of Publications

1. Ravi**, A.**; Biswas, R.; Das, S.; Das, S. K. Exploring Proton Conductivity Studies of a Copper based Hydroxylated Polyoxometalate, *J. Chem. Sci.* **2023**, just accepted.
2. Mulkapuri, S.; † Siddikha, A.;† **Ravi, A.**;† Saha P.; Das. S. K. Electrocatalytic Hydrogen Evolution by a Uranium(VI) Polyoxometalate: an Environmental Toxin for Sustainable Energy Generation, ***Inorg. Chem.*** **2023**, just accepted. †(contributed equally)
3. Ravi, A.; Mulkapuri, S.; Das, S. K. Hydroxylated Polyoxometalate with Cu(II)- and Cu(I)-Aqua Complexes: A Bifunctional Catalyst for Electrocatalytic Water Splitting at Neutral pH. ***Inorg. Chem.*** **2023,** *62*, 32, 12650–12663.
4. Ravi, A.; Nasani, R.; Das, S. K. Cobalt Formate, a Functional MOF: Electrocatalytic Water Oxidation, ***Journal of Molecular and Engineering Materials***, **2022**, https://doi.org/10.1142/S2251237322400020
5. Mulkapuri, S.;† Ravi, A.;† Das, S. K. Fabricating a Functionalized Polyoxometalate with ZIF-8: A Composite Material for Water Oxidation in a Wide pH Range. ***Chem. Mater.*** **2022**, *34*, 3624–3636. †(contributed equally)
6. Mulkapuri, S.; Ravi, A.; Mukhopadhyay, S.; Kurapati, S. K.; Siby, V.; Das, S. K. W^{VI}–OH Functionality on Polyoxometalates for Water Reduction to Molecular Hydrogen. ***Inorg. Chem. Front.*** **2022**, *9*, 3566–3577.
7. Mulkapuri, S.; Ravi, A**.**; Nasani R.; Kurapati, S. K.; Das, S. K. Barrel-Shaped-Polyoxometalates Exhibiting Electrocatalytic Water Reduction at Neutral pH: A Synergy Effect. ***Inorg. Chem.*** **2022**, *61*, 13868 13882.

List of Scientific Presentations

1. Athira Ravi and Samar K. Das, delivered a talk on "Fabricating a Functionalized Polyoxometalate with ZIF-8: A Composite Material for Water Oxidation in a Wide pH Range" in *Dr. K. V. Rao Scientific Society Research Award*, 2022-23.

2. Athira Ravi and Samar K. Das, delivered an oral and a poster presentation on "Hydroxylated Polyoxometalate with Cu(II)- and Cu(I)-Aqua Complexes: A Bifunctional Catalyst for Electrocatalytic Water Splitting at Neutral pH" in ChemFest 2023 (*19th Annual In-House Symposium*, SoC, UoH)

3. Athira Ravi and Samar K. Das, presented a poster on “Fabricating a Functionalized Polyoxometalate with ZIF-8: A Composite Material for Water Oxidation in a Wide pH Range” in Modern Trends in Inorganic Chemistry- MTIC-2022 (MTIC-XIX, *International Conference*) organized by Banaras Hindu University (BHU), Varanasi, India.

4. Athira Ravi and Samar K. Das, presented a poster on “Fabricating a Functionalized Polyoxometalate with ZIF-8: A Composite Material for Water Oxidation in a Wide pH Range” in ChemFest 2022 (*18th Annual In-House Symposium*, SoC, UoH).

==========

Chapter 1

Introduction to Polyoxometalates Mediated Electrocatalytic Water Splitting and Proton Conduction

OVERVIEW

This chapter aims to outline the current plight of ever-increasing energy demands in the world, the population's high dependency on depleting fossil fuels, and the severe urge to move towards feasible alternatives to quench energy needs. Progress towards these goals requires, in part, the development of advanced materials and their appropriate utilization for energy storage, conversion, and harnessing. In this respect, hydrogen (H_2) is rising as an excellent fuel that can either be burnt or recombined with oxygen to release the stored energy in a fuel cell. One of the carbon-free methods to produce hydrogen includes electrochemical water splitting, where the development of electrocatalysts plays a vital role. Here, the basics of electrochemical water splitting, the reaction mechanisms involved, and the electrocatalysts utilized, particularly polyoxometalates (POMs) and metal-organic frameworks (MOFs) are briefed. Finally, advancement in fuel-cell technology with sufficient emphasis on the design of proton-conducting materials has also been discussed in this chapter. The chapter ends with concluding remarks and the future scope of the thesis.

1.1. INTRODUCTION

Can you believe that increased carbon emission is an indicative of higher economic growth? Yes, it is indeed. In other words, carbon emissions are an inevitable byproduct of a higher economic growth rate.[1-4]

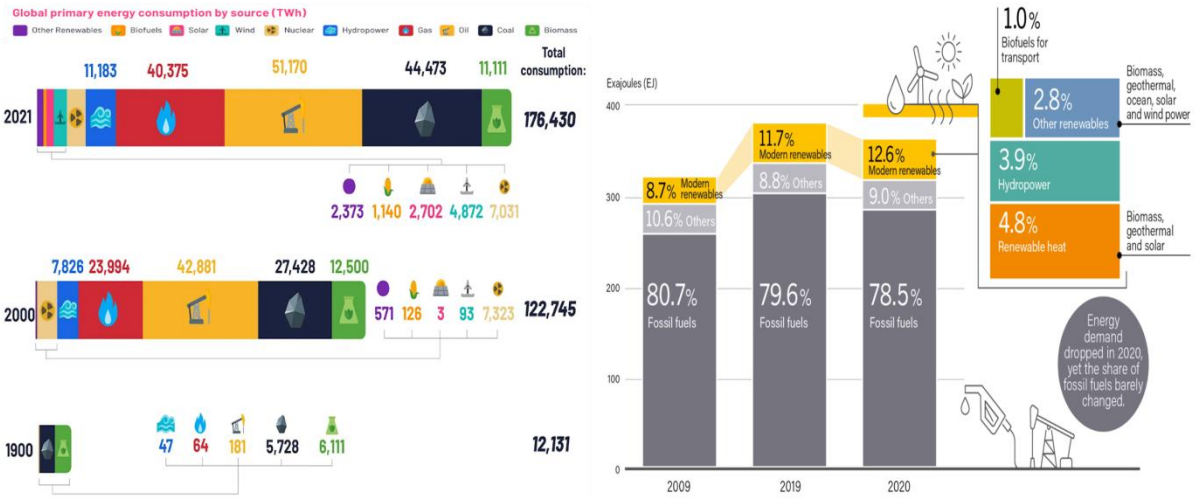

Figure 1.1. Global primary energy consumption by source measured in terawatt-hours (TWh) (left). Share of modern renewable energy of 2019 and 2020, compared with 2009.[4]

The current consumption of fossil fuels/non-renewable energy sources in various sectors for power generation keeps the world in an alarming state of global sustainability and stability.[5-8] The primary causes for this intimidating state of the globe could be attributed to the ever-increasing world population, rapid technological advancement, and resulting energy demands.[9,10] There was a time when fossil fuels could satisfy energy needs, but the way the present global scenario is leading, they could not offer a prolonged energy supply for the world (Figure 1.1, left). Unfortunately, burning fossil fuel-based energy sources, namely coal, petroleum, and natural gas, contribute the most greenhouse gases to the environment, leading to drastic climatic disruption and endangering life on Earth. Hence, we must switch to less-polluting energy sources leading to a carbon-neutral economy.[11,12] Despite the intense focus on various *green initiative* policies/programs over the last few decades, the contribution of renewable energy sources, like solar, wind, geothermal, and hydropower, account to be minimal. The data analytics for the year 2022 revealed that the global share of modern-renewable resources in final energy climbed marginally from 10.6% to 11.7 % from 2009 to 2019, indicating a prolonged rate of shift to renewable energy sources (Figure 1.1, right).[5,13]

Nevertheless, it has to be acknowledged that investments have risen in almost every sector of the market for energy storage, renewable energy, electrified transportation, nuclear, hydrogen, and, importantly, *sustainable materials*.[14-16] This hike in energy-transition investments is a sign of encouragement for investors, governments, and businesses globally to commit to a carbon-free economy.

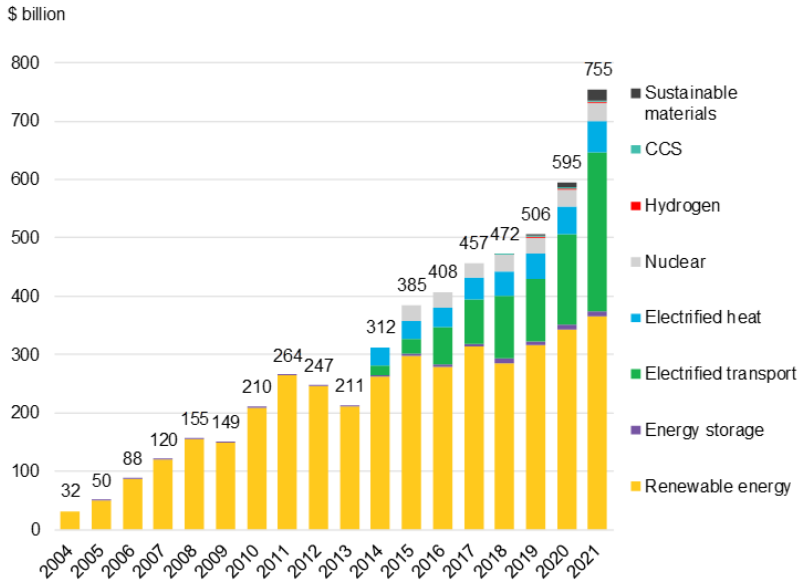

Figure 1.2. Global investment in energy transition by sector from the year 2004 to 2021.[16]

As seen from the above Figures, investments in hydrogen and sustainable materials are also rising remarkably, uplifting the field of *materials chemistry* and encouraging scientists worldwide to develop materials that could efficiently produce, store, and utilize hydrogen for energy requirements.[17-20] Here, one can ask, "What is so significant about the molecule *hydrogen* in the energy field?" Surprisingly, hydrogen gas offers fascinating properties and applications for sustainable energy as follows; (i) it offers a very high energy density of 146 kJ/g; (ii) hydrogen is a non-toxic green energy gas, which is high quality and environmentally benign energy carrier with zero carbon emission; (iii) on its application as a fuel, it showcases energetic performance, because its combustion reaction gives rise to a combination of two simple molecules to form water as the product.[21-24] Inspired by nature and utilizing the available resources, such as solar or wind-derived power and water-splitting technology, hydrogen is produced sustainably.[25]

The so-produced hydrogen fuel could further be utilized in fuel cells to produce electricity when required.[26] Also, extensive research is going on worldwide in fabricating efficient fuel cells for energy production, particularly in designing proton exchange membranes. Thus, hydrogen production via water splitting and fuel cell fabrication play a vital role in sustainable energy production.[27,28]

This chapter mainly streamlines the design and development of functional inorganic materials, i.e., polyoxometalates (POMs) and metal-organic framework (MOF) containing compounds, hereafter this will be termed as MOFs, for two major applications, namely (i) electrocatalytic water splitting; and (ii) proton conduction.

1.2. ELECTROCHEMICAL WATER SPLITTING

Electrochemical water splitting is regarded as one of the green paths to produce hydrogen apart from the other existing methods like, photochemical, photo-electrochemical, and thermo-chemical ways of water splitting. Water electrolysis was first reported in 1979,[29] Since then, studies and research on water electrolysis have seen massive growth in the scientific community. The method of electrochemical water splitting is highly flexible for producing hydrogen with high purity (100%). In the global market, hydrogen is mainly generated by steam methane reforming, which requires harsh conditions and is a highly energy-intensive method.[30,31] However, electrochemical water splitting (EWS) is a promising and clean approach for producing hydrogen fuel under mild operational conditions.

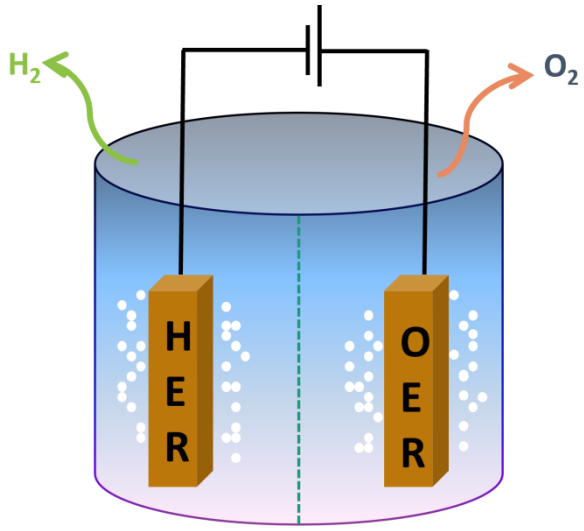

Figure 1.3. A schematic representation of an electrochemical cell showing electrochemical water splitting.

Water electrolysis takes place as two half-cell reactions: hydrogen evolution reaction (HER) at cathode and oxygen evolution reaction (OER) at anode (Figure 1.3). The reactions involved in both the half-cells in different aqueous pH media[32] are demonstrated in equations (1)-(4).

In acidic medium;

Cathode : $4H^+ + 4e^- \rightarrow 2H_2$; $E_o = 0.0\ V$ *vs.* NHE (1)

Anode : $2H_2O \rightarrow O_2 + 4H^+ + 4e^-$; $E_o = +\ 1.23V$ *vs.* NHE (2)

In alkaline medium;

Cathode : $4H_2O + 4e^- \rightarrow 2H_2 + 4OH^-$; $E_o = -0.828V$ *vs.* NHE (3)

Anode : $4OH^- \rightarrow O_2 + 2H_2O + 4e^-$; E_o = + 0.401V *vs.* NHE (4)

Thus, the overall reaction involved in electrochemical water splitting is given in equation (5);

$2H_2O \rightarrow 2H_2\,(g) + O_2$; ΔG_0 = + 237.2 kJ/mol; ΔE_0 = 1.23 V *vs.* RHE (5)

As seen from the above equations, oxidation of water (OER) is a kinetically demanding, 4-electron process, which makes overall water electrolysis sluggish in nature. Moreover, even though the thermodynamic potential required for water splitting is 1.23 V *vs* RHE, in practical operational conditions, a larger potential is always required to overcome the complex electron / ion transfer during the reactions.[33] Factors (that arise from diverse electrode materials) like, activation energy, gas or/and ion diffusion, and factors related to electrochemical cell like electrolyte concentration, wire and electrode resistances, bubble formation, heat release and so on contribute immensely for additional potential over the standard potential for water electrolysis.[34] This extra applied potential is technically called as overpotential (η). The lower the overpotential, the efficient the reaction turns out. Therefore, suitable electrocatalysts assist in decreasing the overpotential and thereby increasing the reaction rate and overall efficiency.

1.2.1 Hydrogen Evolution Reaction (HER)

Hydrogen evolution reaction (HER) could occur in acidic or alkaline medium through a combination of three possible mechanisms, either Volmer–Heyrovsky or Volmer–Tafel mechanisms.

In acidic medium, the possible mechanistic pathways are as described below.

i. Combination of a proton and an electron on the catalyst surface (A) resulting into an adsorbed hydrogen atom (Volmer Reaction):

$$A + H^+ + e^- \rightarrow AH_{ads} \quad (6).$$

ii. Adsorbed hydrogen atom again combines with a proton and an electron and results into a hydrogen molecule (Heyrovsky reaction):

$$AH_{ads} + H^+ + e^- \rightarrow H_2 + A \quad (7).$$

iii. Coupling of two adsorbed hydrogen atoms to produce H_2 molecule (Tafel reaction):

$$AH_{ads} + AH_{ads} \rightarrow H_2 + 2A \quad (8).$$

Whereas, in alkaline medium, the possible mechanistic pathways are as follows.

i. Molecular H_2O instead of H^+ couples with an electron resulting to adsorbed hydrogen atom on the catalyst surface (Volmer Reaction):

$$A + H_2O + e^- \rightarrow AH_{ads} + OH^- \quad (9).$$

ii. Adsorbed hydrogen atom again combines water molecule and an electron to form a hydrogen molecule (Heyrovsky reaction):

$$AH_{ads} + H_2O + e^- \rightarrow H_2 + OH^- + A \quad (10).$$

iii. Coupling of two adsorbed hydrogen atoms to produce H_2 molecule (Tafel reaction):

$$AH_{ads} + AH_{ads} \rightarrow H_2 + 2A \quad (11).$$

1.2.2 Oxygen Evolution Reaction (OER)

Oxygen evolution reaction (OER) takes place through various steps to produce oxygen, and the overpotential rises high due to the contribution of kinetic barriers from each step in the reaction mechanism.[35] The below equations, (11) to (14) describe the possible mechanistic pathway for OER exhibited by the catalyst in alkaline as well as in the acidic medium.

i. Active site of the catalyst surface (*) combines with water molecule (alkaline medium) resulting into an adsorbed oxygen atom:

$$2H_2O + * \rightarrow OH_{ads} + H_2O + e^- + H^+ \quad (12)$$

$$OH_{ads} + H_2O \rightarrow O_{ads} + H_2O + e^- + H^+ \quad (13).$$

ii. Intermediate OOH_{ads} is formed first by the reaction of O_{ads} with H_2O, which is subsequently combined to produce O_2:

$$O_{ads} + H_2O \rightarrow OOH_{ads} + e^- + H^+ \quad (14)$$

$$OOH_{ads} \rightarrow O_2 + e^- + H^+ \quad (15).$$

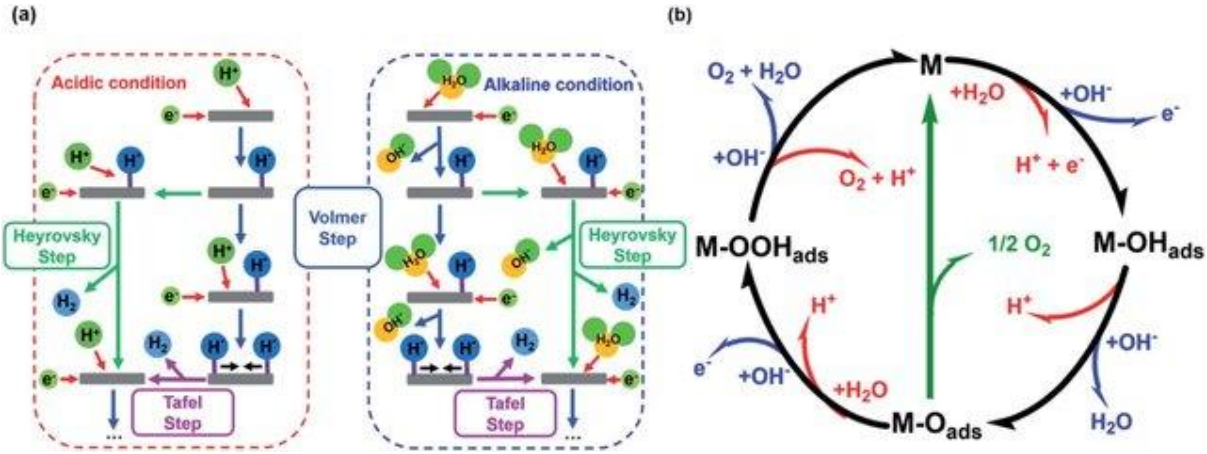

Figure 1.4. a) HER mechanistic pathways in acidic and alkaline media with the Volmer reaction (blue), Heyrovsky reaction (green), and Tafel reaction (purple); (b) OER mechanism for acidic (red) and alkaline (blue)

conditions. The black line shows the OER pathway via an active site with the M-OOH ads intermediate. The alternative pathway via two M-O ads intermediates is shown in green.[35]

Now that the fundamentals of HER and OER are discussed in the previous sections, it is imperative to comprehend the crucial role of electrocatalysts in the overall electrochemical water-splitting reaction. The current *state-of-the-art* electrolysis uses Pt- and Ru/Ir-based electrocatalysts for HER and the OER, respectively. However, the commercial-scale application of water electrolysis is highly restricted because of the scarce/low availability and high cost of those noble metal-based materials. Therefore, cost-efficient electrocatalysts are critical to be scrutinized and developed. In this regard, transition-based or post-transition metal-based materials are explored as water electrolysis catalysts due to their high electrocatalytic activities, earth abundance, and low cost. Recent research focus has been intensely shifted towards non-noble metal-based materials for electrocatalytic water splitting. In this regard, metal-oxide-based materials are booming, such as polyoxometalates (POMs), metal-organic frameworks (MOFs), and so on. All the chapters in this thesis revolve majorly around two of the systems mentioned above: POMs and MOFs.

1.3 SOLID-STATE PROTON CONDUCTION

Proton conduction has attracted immense attention in the field of ionic transport lately. Solid proton conductors play a key role in many technological innovations, like hydrogen permeation membranes, membranes for water electrolyzers, humidity, and hydrogen sensors, and significantly in fabricating electrochemical energy devices for fuel cells (polymer/proton exchange membrane fuel cells). Due to the exceptional mobility by protons in water[36] (36.2×10^{-8} m^2 s^{-1} V^{-1}), compared with other ionic species such as Li^+ and Na^+ ions, conduction by protons always has a higher demand. Also, these materials exhibit high conductivity due to the reduced net charge in electrostatic interactions and the partial covalent nature of hydrogen bonds (H-bond) in the solid material.[37] The first proton-conducting material used commercially was perfluorinated sulfonated polymer, named as Nafion in the 1960s. This discovery commenced the domain of solid proton conductors worldwide, followed by numerous discoveries in the same field. However, Nafion has shown limitations in its operational temperature, i.e., it is prone to degrade at higher temperatures (>100 °C) and humidity conditions and is highly expensive. Thus, the development of alternative and efficient materials is required. The prime demand for most solid-state proton conductors is the conducting medium to donate or carry the protons, which could relate strongly to the possible fuel cell operational conditions (temperature, humidity).

Thus, to satisfy the conduction medium for proton transport which includes transport of protons (H^+) and any assembly that carries protons (OH^-, H_2O, H_3O^+, NH_4^+, HS^-, etc.), two mechanisms are mainly followed. The transfer of protons (H^+) between relatively stationary host anions, in other words, hopping of proton from one host anionic site to another, is termed the Grotthuss or free-proton mechanism. In the other principle, the proton diffuses together with a vehicle (e.g., as H_3O^+, NH_4^+), or transport of protons happen by any of the other species, is termed a vehicle mechanism.

In the actual proton conduction processes, the vehicle and Grotthuss mechanisms show cooperative contributions during the conduction of protons and are not independent. However, the activation energy (E_a) of the proton conduction, can possibly speak much about which mechanism would dominantly contribute. If the vehicle mechanism is predominantly involved in proton conductivity, the activation energy, Ea will be >0.4 eV, consuming higher energy for proton migration. Whereas, the Grotthuss mechanism takes place with a lesser activation energy, Ea <0.4 eV, consuming relatively lower energy for transport.[38]

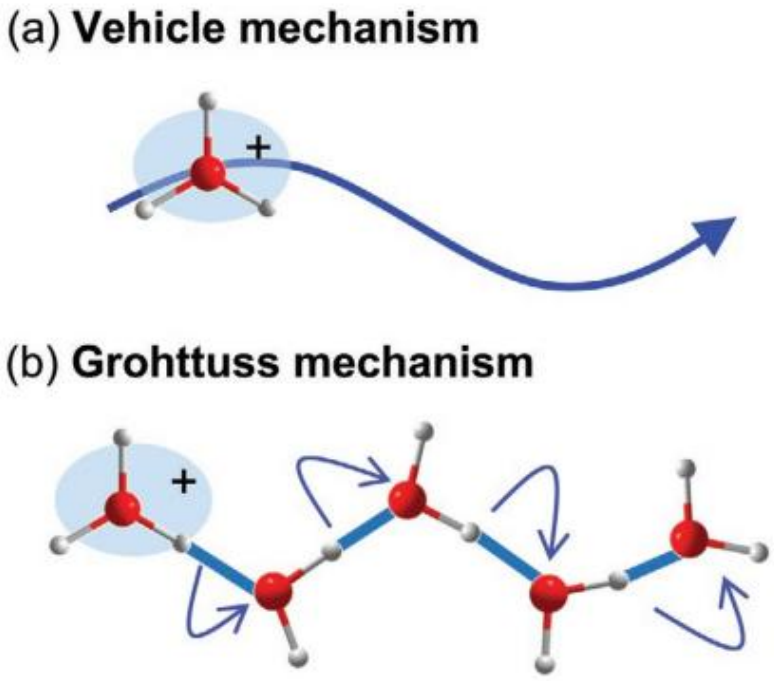

Figure 1.5. Schematic images of proton transport in the water medium. a) Vehicle mechanism. b) Grotthuss mechanism.[38]

1.3.1. Design Strategies for Solid Proton Conductors

Generally, conductivity, σ, can be expressed by the equation $\sigma = ne\mu$, in which, n is the mobile proton density; e is the elementary charge, and μ proton mobility. This indicates that a

perfect combination of high proton concentration and good conduction trail is essential to achieve high proton conductivity. Several strategies are employed to synthesize materials that can provide high proton conductivity, and some of them are described below:

(i) Introducing protonic counter-ions such as hydronium (H_3O^+), ammonium (NH_4^+, $MeNH_3^+$, $Me_2NH_2^+$), and so on, in the cluster ease the conduction of protons. These protonic counter-ions form hydrogen bonds network with the guest water or the cluster anions, forming a continuous hydrogen channel with well-organized proton conductivity.

(ii) Presence of intrinsic proton sources on the cluster framework, like hydroxyl (-OH^-) and/or aqua (-H_2O) groups, coordinated to the metal centers could also be regarded as the proton sources for easy conductions.

(iii) Inclusion of conducting materials into the matrix of metal-organic materials (MOMs) also is considered as a fine strategy to enhance the proton conductivity of the composite material as a whole.

As discussed in the earlier sections, in the fields of electrocatalytic water splitting as well as for proton conduction, judicious choices/development of materials are vital for their efficient functioning. Therefore, following sections are devoted for the discussion of some of those materials which are versatile electrocatalysts and solid proton conductors.

1.4. MATERIALS

1.4.1. Polyoxometalates (POMs)

Polyoxometalates (POMs) are a class of carbon-free, metal-oxide, polyanionic inorganic functional materials. They are the growing class of inorganic structures highly accessible, tunable, inexpensive, and stable to oxidative degradation. They are capable of accepting and donating multiple electrons for reduction and oxidation, respectively. They are cluster anions bridged by oxo-groups to the transition metal atoms (called addenda atoms) in their highest oxidation states (like Mo^{VI}, W^{VI}, V^V, Nb^V or Ta^V, and so on). These metal atoms present in the cluster are coordinated to six oxo ions giving rise to a $\{MO_6\}$ octahedral geometry, and the resultant $\{MO_6\}$ groups are further connected by corner- or edge- (rarely face-) sharing oxo ions to form the whole anionic cluster.[39] These polyanionic clusters can be further classified into several classical types: Keggin, Wells–Dawson, Lindqvist, Anderson–Evans, Weakley, Silverton, Strandberg, etc. (Figure 1.6).

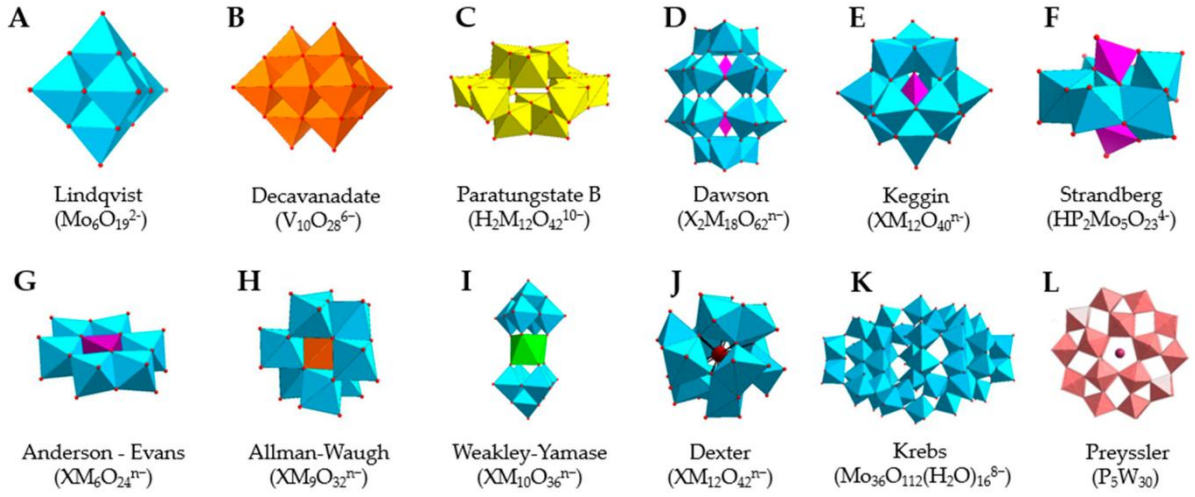

Figure 1.6. Examples of polyoxometalate (POM) clusters (A-L) reported so far in the literature.[39]

POM compounds are employed for many potential applications in various fields from catalysis[40] to medicine,[41] electroanalytical chemistry[42] and materials science.[43-45] Among the field of materials chemistry itself, they show interesting characteristic features such as photochromism and electrochromism,[46] luminescence[47] and magnetism.[48]

The fascinating electrochemical redox-behavior of POMs makes them unique in the area of catalysis. POMs stand out due to their excellent stability of the oxidation/reduction states, which aid them to take part in rapid reversible electron transfer reactions. Another fabulous feature of POM accounts for its structural integrity besides its fast redox transformations. POMs are excellent redox active compounds that involve multi-electron transfer during the redox activity. Remarkable outcomes have been achieved both in electrocatalytic reductions and oxidations when the most appropriate forms of the POM clusters are used.[49,50]

1.4.1.1. Polyoxometalates as Electrocatalysts for Water Splitting

Polyoxometalate clusters owing to their wondrous redox properties are extensively exploited in catalysis, especially in electrochemical water splitting. As discussed above, POMs act as reservoirs of electrons that are ever-ready for electronic transfer without structural alterations. However, these multi-electronic transfer processes result in high overpotentials, leading to lower conversion efficiencies.[51] Thus, as such, POMs (Figure 1.5a) are associated with various other moieties to form composite material like transition-metal (TM) inserted POMs (Figure 1.5b),[52,53] rare-earth ions (RE) substituted POMs (Figure 1.5c),[54] heterometallic POMs (Figure 1.5d),[55,56] and organic ligand modified POMs[57-60] (Figure 1.5e and f). These

combinations of POMs and other groups ultimately result in functionalizing the POM compounds for better stability, enhanced catalytic performances, and durability.[61]

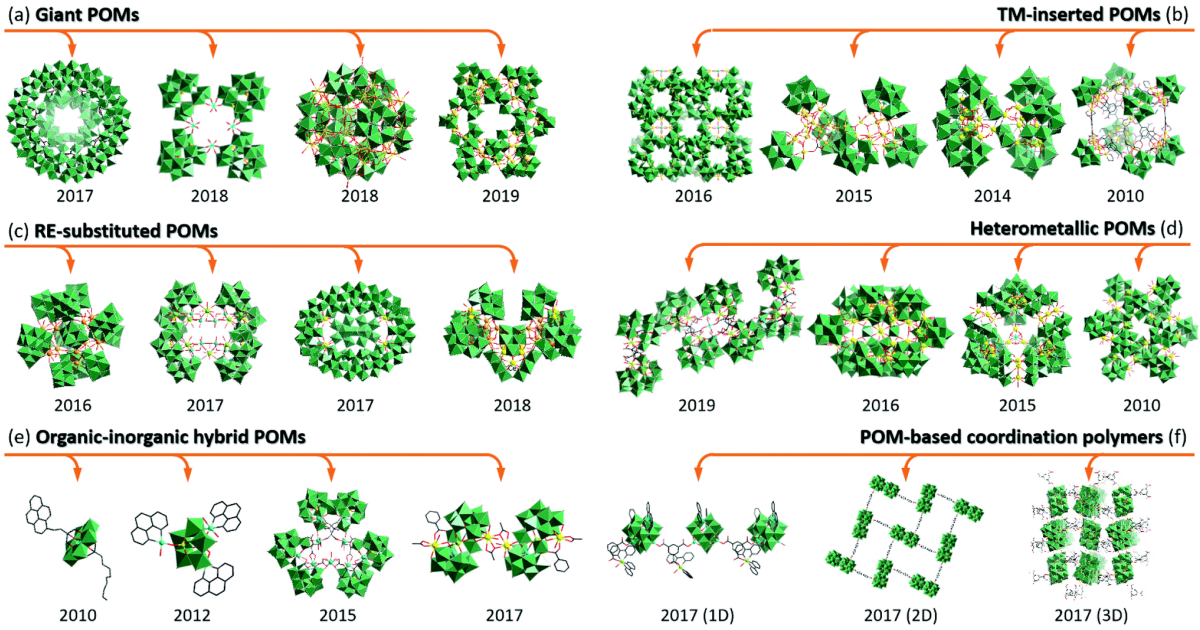

Figure 1.7 (a) Combined ball-and-stick and polyhedral views of some typical inorganic giant POMs. (b) Combined ball-and-stick and polyhedral views of some typical TM-inserted POMs. (c) Combined ball-and-stick and polyhedral views of some typical RE-substituted POMs. (d) Combined ball-andstick and polyhedral views of some typical TM-RE heterometallic POMs. (e) Views of some representative organic–inorganic hybrid POMs. (f) Views of some representative POM-based coordination polymers.[61]

In addition, combining POMs with catalytically active nanoparticles (NPs) adds up to the development of new catalysts with higher efficiency and larger specific surface area.[62] Similarly, POMs serve as the best guest molecules which can be immobilized into host porous materials such as self-assembly cages,[63] supramolecular networks,[64] metal–organic frameworks,[65] and zeolitic imidazolate frameworks [66] to build binary composite materials.

Zeolitic imidazolate framework-8 (ZIF-8)

Zeolitic imidazolate framework-8 (ZIF-8), a representative MOF with zeolite topology, is developed from Zn^{2+} (four-coordinated) ions and 2-methylimidazole (2-MeIm) ligands.[67,68] They have been widely exploited in chemical sensing, gas adsorption, catalysis, and so on.[69-73] Particularly, carbon-based materials resulting from ZIF-8 and ZIF-8 based MOFs have caught attention for their electrocatalytic application for HER, OER, ORR, and CO2RR. ZIF-8 acts as a promising host material to design various functional materials. There are reports where ZIF-8 functions as a protective host material for polyoxometalates and help achieve the encapsulated POM compound's efficient electrochemical activity, stability, and durability

even in harsh alkaline conditions. Thus, as discussed above, to functionalize POM compounds, ZIF-8 serves to be one of the best host materials.

1.4.1.2. Polyoxometalates as Solid Proton Conducting Electrolytes

The hydrophilic properties and plentiful terminal oxygen ions on the surface of the POM cluster give rise to proton conductivity in POM based materials. Hydrated POMs have been reported to be the highest solid proton conductors among other inorganic solid electrolytes at room temperature (such as, 27 $mScm^{-1}$ for $H_4SiW_{12}O_{40}{\cdot}28H_2O$),[74] which could be attributed to the abundant water moieties on the surface.[75,76] POMs tend to form stable hydrogen-bonded network with various hydrophilic compounds, thereby enabling the development and employment of POM-based solid-electrolytes as smart materials.[77-79] The structure–property relationship, tunable versatility and controllability bring up POM-based solid-state electrolytes in various functional devices for energy applications.

Solid-state POMs are prospective electrolytes for proton transport due to their strong Bronsted acidic nature. The constant delocalization of negative charges on the surface of cluster anions and the surplus existence of M=O double bonds on the POM structure gives rises to easy adsorption and dissociation of protons, enhancing the conductivity.[80] This rapid hydrogen bond formation and dissociation are reversible in nature, and adds up to the easy proton conduction throughout the material.[81,82]

Also, the arrangement of POMs in solids can be tuned by the choice of appropriate counter cations, which then controls the spatial distribution of protons around the POMs and the proton-hopping pathway, leading to an increase in η. Thus, it is possible to classify POM-based cluster into four categories by the type of counterpart: a) inorganic cations, b) organic cations, c) organic polymers, and 4) cationic complexes, and introduce the design strategies, the proton conductivity, and the proton conduction mechanism for selected examples.

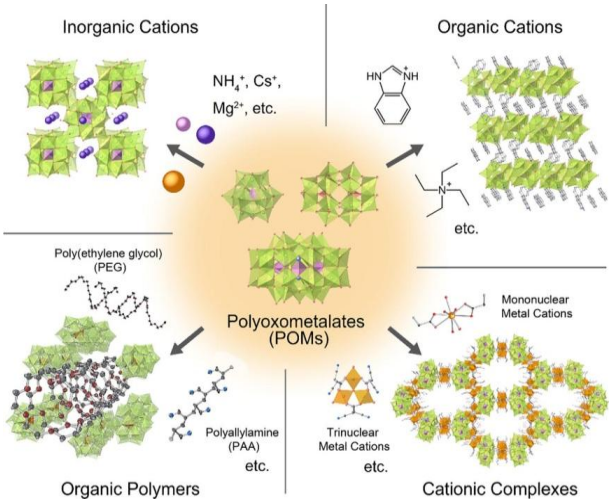

Figure 1.8. Design strategies, the proton conductivity, and the proton conduction mechanism for selected examples.[82]

How to employ POMs for the commercial application as soon as possible?

In the future, doping or fabricating POMs into organic polymeric materials and exploiting their interaction to manufacture durable and stable polymer composite membranes that can achieve high proton conductivity still needs a huge effort. In addition to applying these proton conductive POMs in fuel cells, their employment in other industrial areas should equally be boosted, like impedance sensors, molecular sieves and in, biological systems, etc. The design and development of POM-based proton conductive materials need new strategies to promote it to a broader range of fields and attain practical applications in fields such as fuel cells, impedance sensors, etc. Research in such areas will come up with vigorous development. The table below shows the solid proton conductivity data exhibited by several reported pristine POM compounds.

Compounds	Proton conductivity (Scm^{-1})	Relative humidity (RH), Temperature (°C)	Reference
$NaH_{15}\{[P_2W_{15}Nb_3O_{62}]_2(4PBA)_2((4PBA)_{2O})\}\cdot 53H_2O$	1.57×10^{-1}	98 RH %, 90 °C	83
$(NH_4)_{21}H^{+}_{59-2x}[Mo^{V}_{180}Mo^{VI}_{60}(OH)_{60}O_{620-x}(SO_3)_{20-x}(SO_4)_x]\cdot ca 337H_2O$	1.03×10^{-1}	98% RH, 80 °C	84
$(HIm)_{24}(NH_4)_{20}[Mo^{V}_{I72}Mo^{V}_{60}O_{372}(CH_3COO)_{30}(H_2O)_{72}]\cdot ca190H_2O$	4.98×10^{-2}	98% RH, 60 °C	84
$Na_{16}(NH_4)_{10}H_8\{[W_{14}CeIV_6O_{61}](W_3Bi_6CeIII_3(H_2O)_3O_{14}][\alpha\text{-}BiW9O_{33}]_3)_2\}\cdot ca38H_2O$	2.4×10^{-3}	90% RH, 25 °C	85
$Na_5[H_7\{N(CH_2PO_3)_3\}Mo_6O_{16}(OH)(H_2O)_4]_4\cdot 18H_2O$	2.55×10^{-2}	98% RH,100 °C	86
$[La_3(H_2O)_{22}][P_2W_{15}Ta_3O_{62}]\ nH_2O$	1.26×10^{-2}	98% RH, 95 °C	87

$K_8Na_3Li_5\{[Na(NO_3)(H_2O)]4[Al_{16}(OH)_{24}(H_2O)_8(P_8W_{48}O_{184})]\}\cdot 66H_2O$	4.5×10^{-2}	70% RH, 85 °C	88
[Zn12(trz)20][SiW12O40]·11H2O	1.2×10^{-4}	95% RH, 95 °C	89
$Na_{17}K_{14}(H_2pip)_{10}H_8[La_{27}Ge_{10}W_{106}O_{406}(OH)_4(H_2O)_{24}]\cdot nH_2O$	3.8×10^{-5}	98% RH, 30 °C	90
$(NH_4)_5[Mo_8(OH)_2O_{24}(\mu_8\text{-}PO_4)](H_2O)_2$	1.5×10^{-2}	98% RH, 85 °C	91
$Na_5[H_7\{N(CH_2PO_3)_3\}Mo_6O_{16}(OH)(H_2O)4]_4\cdot 18H_2O$	1.17×10^{-4}	95% RH, 80 °C	92
[H2en]4[Ni5(OH)3(trzS)3(en)(H2O)(B-α-PW9O34)]·6H2O	2.55×10^{-2}	98% RH, 100 °C	93
$[Co(bpz)(Hbpz)][Co(SO_4)_{0.5}(H_2O)_2(bpz)]_4$ $[PMo^{VI}_8Mo^{V}_4V^{IV}_4O_{42}]\cdot 13H_2O$	1.3×10^{-5}	98% RH, 85 °C	94
$[Cu_3(\mu_3\text{-}OH)(H_2O)3(atz)_3]_3[P_2W_{18}O_{62}]\cdot 14H_2O$	4.4×10^{-6}	97% RH, 25 °C	95
$[Mo_5P_2O_{23}]$ $[Cu(phen)(H_2O)]_3\cdot 5H_2O$	2.2×10^{-5}	98% RH, 25 °C	96
$[Sm(H_2O)_5(CO_2CH_2NH_3)_2][Al(OH)_6Mo_6O_{18}]\cdot 10H_2O$	4.53×10^{-3}	95% RH, 80 °C	97
$H[Ce(H_2O)_4]_2[MnV_{13}O_{38}]\cdot 9NMP\cdot 17H_2O$	4.68×10^{-3}	97% RH, 61 °C	98
$H_7Na_{19}(H_2O)_{26}\{Ni_{12}(OH)_9(PO_4)_4(A\text{-}\alpha\text{-}SiW9O34)$ $[W_4O_{10}(OH)(PO_2(OH)_2)_2(A\text{-}\alpha\text{-}SiW_9O_{34})_2]\}$ $\cdot 4C_2H_8N\cdot 27H_2O$	1.89×10^{-2}	98% RH, 50 °C	99
$Na_{70}K_4H_{12}[La_{10}Ni_{48}W_{140}Sb_{16}P_{12}O_{568}(OH)_{24}(H_2O)_{20}]\cdot 252\ H_2O$	2.05×10^{-2}	100% RH, 25 °C	100

1.5. MOTIVATION OF THE WORK

Exploration of new materials for efficient water splitting and proton conduction can significantly smooth the progress of the development of alternative energy technologies and environmental protection. Over the globe, intense research, laws, and policies have already been developed to protect and sustain all energy resources for future generations. Therefore, becoming a part of designing and developing such functional materials for the existing library of the *world of materials* is the only motivation for this thesis. The developed materials in this thesis might give a relatively easy competition to the existing ones. Still, the *idea or the strategies* involved in the development of materials could, some-a-day, motivate the research community to overcome the current shortcomings and succeed in designing better materials to satisfy the world's energy need. Throughout the thesis, we have focused on developing economic yet versatile functional materials for electrocatalytic water splitting and proton conduction.

The thesis begins with introducing (***Chapter 1***) the areas of electrochemical water splitting (HER and OER) and solid-state proton conduction for energy applications. Further, it moves on to an elaborate discussion of diverse materials like polyoxometalates (POMs), POM-based materials, and ZIF-8-derived compounds employed extensively for the

applications mentioned earlier. Then, ***Chapter 2*** focuses on fabricating a POM-encapsulated MOF composite material (**$H_5$1@ZIF8**) for electrochemical water oxidation (WO) in a wide pH range. This work deserves special attention due to its beauty of fabrication. The main challenge of POM-based electrocatalysts is to maintain them in alkaline conditions; thus, this work has shown an exemplary fabrication where this POM acts as the guest molecule and the ZIF-8 (metal-organic framework) functions as an excellent protective shield for the POM compound. This composite material works well for electrochemical WO in the wide pH spectrum, i.e., acidic to alkaline medium.

Chapter 3 deals with designing a bifunctional electrocatalyst for overall water splitting that works efficiently in the neutral aqueous medium. The compound has been functionalized with six tungsten-hydroxyl (W^{VI}-OH) groups, and the copper ions present in the compound exist in mixed-valency in the compound. The compound exhibits promising stability, durability and efficiency in the operational conditions. The very same compound has shown excellent solid-state proton conduction in the order of 10^{-2} Scm^{-1}, which is an exemplary conductivity data as far as the POM compounds are concerned.

Chapter 4 describes the synthesis and thorough characterization of a W^{VI}-OH functionalized Krebs-type polyoxometale, **POM-MnW^{VI}(OH)**. This 2-D POM cluster acts as a molecular catalyst for electrochemical water reduction to produce molecular hydrogen. The compound exhibits stable and commendable HER activity revealing highly promising results. Additionally, the same compound has demonstrated solid-state proton conduction. The proton conductivity studies have revealed that the compound acts as an excellent proton conducting material with one of the highest conductivity values, in the range of 10^{-1} Scm^{-1}. Thus, **POM-MnW^{VI}(OH)** acts as an excellent electrocatalyst as well as a solid proton conductor.

Finally, ***Chapter 5***, aims in discussing about the synthesis, characterizations and electrochemical studies of another copper incorporated paratungstate based compound, **Na_4Cu_2*para-B***. The compound shows hydrogen evolution reaction (HER) in acidic medium. The stability and kinetic studies on this electrocatalyst has proven it to be a highly robust and efficient compound for HER.

1.6. REFERENCES

1. Acheampong, A, O. Economic growth, CO_2 emissions and energy consumption: What causes what and where? *Energy Economics*, **2018**, *74*, 677-692.
2. Qazi, A.; Hussain, F.; Rahim, N. A.; Hardaker, G.; Alghazzawi, D.; Shaban, K.; Haruna, K. Towards Sustainable Energy: A Systematic Review of Renewable Energy Sources, Technologies, and Public Opinions. *IEEE Access*. **2019**, *7*, 63837-63851.
3. BP Statistical Review of World Energy, **2022**.

4. Stern, P.; Janda, K.; Brown, M.; Steg, L.; Vine, E. L.; Lutzenhisrer, L. Opportunities and insights for reducing fossil fuel consumption by households and organizations. *Nat Energy* **2016**, *1*, 16043.
5. Du, T. 'Global Energy Consumption by Source, and Carbon Emissions (1900-2021)', **2023**, "Energy". Published online at OurWorldInData.org. Retrieved from: 'https://ourworldindata.org/energy' [Online Resource].
6. Chu, S.; Majumdar, A. Opportunities and challenges for a sustainable energy future. *Nature*, **2012**, *488*, 294–303.
7. Chu, S., Cui, Y.; Liu, N. The path towards sustainable energy. *Nature Mater* **2017**, *16*, 16–22.
8. Kilner, J. A.; Skinner, S. J. Irvine, S. J. C.; Edwards, P. P. Functional Materials for Sustainable Energy Applications, *Woodword Publishing*, **2012**, *ISBN 978-0-85709-059-1*.
9. Nyambuu, U.; Semmler, W. Fossil Fuel Resource Depletion, Backstop Technology, and Renewable Energy. *Sustainable Macroeconomics, Climate Risks and Energy Transitions*, 2023, https://doi.org/10.1007/978-3-031-27982-9_6
10. Ritchie, H.; Roser, M.; Rosado, P. CO_2 and Greenhouse Gas Emissions", **2020**, https://ourworldindata.org/co2-and-greenhouse-gas-emissions
11. Siddik, M. A.; Islam, M. D.; Zaman, A. K. M. M.; Hasan, M. M. Current status and correlation of fossil fuels consumption and greenhouse gas emissions. *International Journal of Energy, Environment, and Economics*, **2021**, *28*, 103-119.
12. Crippa, M.; Guizzardi, D.; Muntean, M.; Schaaf, E.; Solazzo, E.; Monforti-Ferrario, F.; Olivier, J.G.J.; Vignati, E. *Fossil CO_2 emissions of all world countries - 2020 Report*; **2020**.
13. Global Energy Review 2021. Assessing the effects of economic recoveries on global energy demand and CO2 emissions in 2021. *International Energy Agency*, **2021**, 1-32.
14. Tahir, M. B.; Batool, A. Chapter 3 - Recent development in sustainable technologies for clean hydrogen evolution: Current scenario and future perspectives. *Sustainable Materials and Green Processing for Energy Conversion*. **2022**, 97-130.
15. Turner, J. A. A Realizable Renewable Energy Future. *Science*, **1999**, *285*, 687-689.
16. Global Investment in Low-Carbon Energy Transition Hit $755 Billion in 2021, Jan **2022**; https://about.bnef.com/blog/global-investment-in-low-carbon-energy-transition-hit-755-billion-in-2021
17. Dyatkin, B.; Presser, V.; Heon, M.; Lukatskaya, M. R.; Beidaghi, M.; Gogotsi, Y. Development of a Green Supercapacitor Composed Entirely of Environmentally Friendly Materials. *ChemSusChem*, **2013**, *6*, 2269-2280.
18. Wang, S.; Lu, A.; Zhong, C-J. Hydrogen production from water electrolysis: role of catalysts. *Nano Converg*. **2021**, *8*, 4.
19. Ma, T.; Yang, H.; Lu, L. Development of hybrid battery–supercapacitor energy storage for remote area renewable energy systems. *Applied Energy*, **2015**, *153*, 56-62.
20. Moller, K. T.; Jensen, T. R.; Akiba, E.; Li. H. W. Hydrogen - A sustainable energy carrier. *Progress in Natural Science: Materials International*. **2017**, *27*, 34-40.
21. Zhu, J.; Hu, L.; Zhao, P.; Lee, L. Y. S.; Wong, K-Y. Recent Advances in Electrocatalytic Hydrogen Evolution Using Nanoparticles. *Chem. Rev.* **2020**, *120*, 851–918.
22. Dubouis, N.; Grimaud, A. The hydrogen evolution reaction: from material to interfacial descriptors. *Chem. Sci*. **2019**, *10*, 9165-9181.
23. Vesborg, P. C. K.; Seger, B.; Chorkendorff, I. Recent Development in Hydrogen Evolution Reaction Catalysts and Their Practical Implementation. *J. Phys. Chem. Lett.* **2015**, *6*, 951–957.
24. Wang, S.; Lu, A.; Zhong, C-J. Hydrogen production from water electrolysis: role of catalysts. *Nano Converg*. **2021**, *8*, 4.
25. Akram, U.; Khalid, M.; Shafiq, S. An Innovative Hybrid Wind-Solar and Battery-Supercapacitor Microgrid System Development and Optimization. *IEEE Access*, **2017**, *5*, 2169-3536.
26. Moller, K. T.; Jensen, T. R.; Akiba, E.; Li. H. W. Hydrogen - A sustainable energy carrier. *Progress in Natural Science: Materials International*. **2017**, *27*, 34-40.
27. Carmo, M.; Fritz, D. L.; Mergel, J.; Stolten, D. A comprehensive review on PEM water electrolysis. International Journal of Hydrogen Energy. **2013**, *38*, 4901-4934.
28. Kumar, S. S.; Himabindu, V. Hydrogen production by PEM water electrolysis – A review. *Materials Science for Energy Technologies*. **2019**, *2*, 442–454.
29. Raveendran, A.; Chandran, M.; Dhanusuraman, R. A comprehensive review on the electrochemical parameters and recent material development of electrochemical water splitting electrocatalysts**.** *RSC Adv.* **2023**, *13*, 3843-3876.
30. Fabbri, E.; Habereder, A.; Waltar, K.; K¨otz R.; Schmidt, T. J. Developments and perspectives of oxide-based catalysts for the oxygen evolution reaction. *Catal. Sci. Technol.* **2014**, *4*, 3800–3821.

31. Zeng, M.; Li, Y. Recent advances in heterogeneous electrocatalysts for the hydrogen evolution reaction. *J. Mater. Chem. A*. **2015**, *3*, 14942–14962.
32. Zou, X.; Zhang, Y. Noble metal-free hydrogen evolution catalysts for water splitting. *Chem. Soc. Rev.* **2015**, *44*, 5148–5180.
33. Li, X.; Hao, X.; Abudula, A.; Guan, G. Nanostructured catalysts for electrochemical water splitting: current state and prospects. J. Mater. Chem. A, 2016, 4, 11973–12000
34. Walter, C.; Menezes, P. W.; Driess, M. Perspective on intermetallics towards efficient electrocatalytic water-splitting. *Chem. Sci.* **2021**, *12*, 8603-8631.
35. Philippe, K.; Vona, M. L. D. *Solid state proton conductors: properties and applications in fuel cells*. John Wiley & Sons, **2012**.
36. Atkins, P.; Paula, J. D. *Physical Chemistry*, W. H. Freeman and Company, New York, 2nd Edition, **2006**.
37. Lim, D. W.; Kitagawa, H. Rational strategies for proton-conductive metal–organic frameworks. *Chem. Soc. Rev*. **2021**, *50*, 6349.
38. Otake, K.-I.; Kitagawa, H. Control of Proton-Conductive Behavior with Nanoenvironment within Metal–Organic Materials**.** *Small* **2021**, 2006189.
39. Carvalho, F.; Aureliano, M. Polyoxometalates Impact as Anticancer Agents. *Int. J. Mol. Sci.* **2023**, *24*, 5043.
40. Hill, C. L.; Prossermccartha, C. M. Homogeneous catalysis by transition metal oxygen anion clusters. *Coord. Chem. Rev*. **1995**, *143*, 407-455.
41. Pope, M. T.; Müller, A. Polyoxometalate Chemistry: An Old Field with New Dimensions in Several Disciplines. *Angew. Chem. Int. Ed. Engl.* **1991**, *30*, 34–48.
42. Sadakane, M.; Steckhan, E. Electrochemical Properties of Polyoxometalates as Electrocatalysts. *Chem. Rev.* **1998**, *98*, 219–238.
43. Long, D.-L.; Burkholder, E.; Cronin, L. Polyoxometalate Clusters, Nanostructures and Materials: From Self Assembly to Designer Materials and Devices. *Chem. Soc. Rev.* **2007**, *36*, 105–121.
44. Miras, H. N.; Yan, J.; Long, D.-L.; Cronin, L. Engineering Polyoxometalates with Emergent Properties. *Chem. Soc. Rev.* **2012**, *41*, 7403.
45. Song, Y.-F.; Tsunashima, R. Recent Advances on Polyoxometalate-Based Molecular and Composite Materials. *Chem. Soc. Rev.* **2012**, *41*, 7384.
46. Yamase, T. Photo- and Electrochromism of Polyoxometalates and Related Materials. *Chem. Rev.* **1998**, *98*, 307–326.
47. Granadeiro, C. M.; De Castro, B.; Balula, S. S.; Cunha-Silva, L. Lanthanopolyoxometalates: From the Structure of Polyanions to the Design of Functional Materials. *Polyhedron* **2013**, *52*, 10–24.
48. Clemente-Juan, J. M.; Coronado, E.; Gaita-Ariño, A. Magnetic Polyoxometalates: From Molecular Magnetism to Molecular Spintronics and Quantum Computing. *Chem. Soc. Rev.* **2012**, *41*, 7464.
49. B. Keita and L. Nadjo, in Encyclopedia of Electrochemistry, eds. A. J. Bard and M. Stratmann, *Wiley-VCH*, **2006**, *10*, 706-728.
50. Freire, C.; Fernandes, D. M.; Nunes, M.; Abdelkader, V. K. POM & MOF-Based Electrocatalysts for Energy-Related Reactions. *ChemCatChem* **2018**, *10*, 1703–1730.
51. Zhao, J.-W.; Li, Y.-Z.; Chen, L.-J.; Yang, G.-Y. Research Progress on Polyoxometalate-Based Transition-Metal–Rare-Earth Heterometallic Derived Materials: Synthetic Strategies, Structural Overview and Functional Applications. *Chem. Commun.* **2016**, *52*, 4418–4445.
52. Li, D.; Ma, P.; Niu, J.; Wang, J. Recent Advances in Transition-Metal-Containing Keggin-Type Polyoxometalate-Based Coordination Polymers. *Coordination Chemistry Reviews* **2019**, *392*, 49–80.
53. Ma, X.; Li, H.; Chen, L.; Zhao, J. The Main Progress over the Past Decade and Future Outlook on High-Nuclear Transition-Metal Substituted Polyoxotungstates: From Synthetic Strategies, Structural Features to Functional Properties. *Dalton Trans.* **2016**, *45*, 4935–4960.
54. Boskovic, C. Rare Earth Polyoxometalates. *Acc. Chem. Res.* **2017**, *50*, 2205–2214.
55. Warzok, U.; Mahnke, L. K.; Bensch, W. Soluble Hetero-Polyoxovanadates and Their Solution Chemistry Analyzed by Electrospray Ionization Mass Spectrometry. *Chem. Eur. J.* **2019**, *25*, 1405–1419.
56. Liu, J.; Han, Q.; Chen, L.; Zhao, J. A Brief Review of the Crucial Progress on Heterometallic Polyoxotungstates in the Past Decade. *CrystEngComm* **2016**, *18*, 842–862.
57. Stuckart, M.; Monakhov, K. Yu. Polyoxometalates as Components of Supramolecular Assemblies. *Chem. Sci.* **2019**, *10*, 4364–4376.
58. Li, X.-X.; Zhao, D.; Zheng, S.-T. Recent Advances in POM-Organic Frameworks and POM-Organic Polyhedra. *Coordination Chemistry Reviews* **2019**, *397*, 220–240.

59. Vilà-Nadal, L.; Cronin, L. Design and Synthesis of Polyoxometalate-Framework Materials from Cluster Precursors. *Nat Rev Mater* **2017**, *2*, 17054.
60. Jiang, W.; Liu, X.-M.; Liu, J.; Shi, J.; Cao, J.-P.; Luo, X.-M.; You, W.-S.; Xu, Y. A Huge Novel Polyoxometalate-Based Cluster $Fe_{10}P_4W_{32}$ Exhibiting Prominent Electrocatalytic Activity for the Oxygen Evolution Reaction and Third-Order NLO Properties. *Chem. Commun.* **2019**, *55*, 9299–9302.
61. Wang, D.; Liu, L.; Jiang, J.; Chen, L.; Zhao, J. Polyoxometalate-Based Composite Materials in Electrochemistry: State-of-the-Art Progress and Future Outlook. *Nanoscale* **2020**, *12*, 5705–5718.
62. Wang, S.-S.; Yang, G.-Y. Recent Advances in Polyoxometalate-Catalyzed Reactions. *Chem. Rev.* **2015**, *115*, 4893–4962.
63. Taghiyar, H.; Yadollahi, B. Keggin Polyoxometalates Encapsulated in Molybdenum-Iron-Type Keplerate Nanoball as Efficient and Cost-Effective Catalysts in the Oxidative Desulfurization of Sulfides. *Science of The Total Environment* **2020**, *708*, 134860.
64. Feng, X.-J.; Yao, W.; Luo, M.-F.; Ma, R.-Y.; Xie, H.-W.; Yu, Y.; Li, Y.-G.; Wang, E.-B. New Polyoxometalate-Templated Supramolecular Networks Based on Transition Metal Ions and Pyridine-N-Oxide Ligands. *Inorganica Chimica Acta* **2011**, *368*, 29–36.
65. Fernandes, D. M.; Barbosa, A. D. S.; Pires, J.; Balula, S. S.; Cunha-Silva, L.; Freire, C. Novel Composite Material Polyoxovanadate@MIL-101(Cr): A Highly Efficient Electrocatalyst for Ascorbic Acid Oxidation. *ACS Appl. Mater. Interfaces* **2013**, *5*, 13382–13390.
66. Mukhopadhyay, S.; Debgupta, J.; Singh, C.; Kar, A.; Das, S. K. A Keggin Polyoxometalate Shows Water Oxidation Activity at Neutral PH: POM@ZIF-8, an Efficient and Robust Electrocatalyst. *Angew. Chem.* **2018**, *130*, 1936–1941.
67. Huang, X.-C.; Lin, Y.-Y.; Zhang, J.-P.; Chen, X.-M. Ligand-Directed Strategy for Zeolite-Type Metal–Organic Frameworks: Zinc(II) Imidazolates with Unusual Zeolitic Topologies. *Angew. Chem. Int. Ed.* **2006**, *45*, 1557–1559.
68. Park, K. S.; Ni, Z.; Côté, A. P.; Choi, J. Y.; Huang, R.; Uribe-Romo, F. J.; Chae, H. K.; O'Keeffe, M.; Yaghi, O. M. Exceptional Chemical and Thermal Stability of Zeolitic Imidazolate Frameworks. *Proc. Natl. Acad. Sci. U.S.A.* **2006**, *103*, 10186–10191.
69. Venna, S. R.; Jasinski, J. B.; Carreon, M. A. Structural Evolution of Zeolitic Imidazolate Framework-8. *J. Am. Chem. Soc.* **2010**, *132*, 18030–18033.
70. Kang, N.; Shen, R.; Li, B.; Fu, F.; Espuche, B.; Moya, S.; Salmon, L.; Pozzo, J.-L.; Astruc, D. Dramatic Acceleration by Visible Light and Mechanism of AuPd@ZIF-8-Catalyzed Ammonia Borane Methanolysis for Efficient Hydrogen Production. *J. Mater. Chem. A* **2023**, *11*, 5245–5256.
71. Gao, L.; Chen, Q.; Gong, T.; Liu, J.; Li, C. Recent Advancement of Imidazolate Framework (ZIF-8) Based Nanoformulations for Synergistic Tumor Therapy. *Nanoscale* **2019**, *11*, 21030–21045.
72. Kwon, H. T.; Jeong, H.-K. *In Situ* Synthesis of Thin Zeolitic–Imidazolate Framework ZIF-8 Membranes Exhibiting Exceptionally High Propylene/Propane Separation. *J. Am. Chem. Soc.* **2013**, *135*, 10763–10768.
73. Martínez-Pérez-Cejuela, H.; Gregucci, D.; Calabretta, M. M.; Simó-Alfonso, E. F.; Herrero-Martínez, J. M.; Michelini, E. Novel Nanozeolitic Imidazolate Framework (ZIF-8)–Luciferase Biocomposite for Nanosensing Applications. *Anal. Chem.* **2023**, *95*, 2540–2547.
74. Kreuer, K. D.; Hampele, M.; Dolde, K.; Rabenau, A. Proton Transport in Some Heteropolyacidhydrates a Single Crystal PFG-NMR and Conductivity Study. *Solid State Ionics* **1988**, *28–30*, 589–593.
75. Nakamura, O.; Ogino, I.; Kodama, T. The Water Content and Humidity Ranges of Dodecamolybdophosphoric Acid and Dodecatungstophosphoric Acid Crystals. *Materials Research Bulletin* **1980**, *15*, 1049–1054.
76. Nakamura, O.; Ogino, I.; Kodama, T. Temperature and Humidity Ranges of Some Hydrates of High-Proton-Conductive Dodecamolybdophosphoric Acid and Dodecatungstophosphoric Acid Crystals under an Atmosphere of Hydrogen or Either Oxygen or Air. *Solid State Ionics* **1981**, *3*, 347–351.
77. Karpakam, V.; Kamaraj, K.; Sathiyanarayanan, S.; Venkatachari, G.; Ramu, S. Electrosynthesis of Polyaniline–Molybdate Coating on Steel and Its Corrosion Protection Performance. *Electrochimica Acta* **2011**, *56*, 2165–2173.
78. Herrmann, S.; Kostrzewa, M.; Wierschem, A.; Streb, C. Polyoxometalate Ionic Liquids as Self-Repairing Acid-Resistant Corrosion Protection. *Angew. Chem. Int. Ed.* **2014**, *53*, 13596–13599.
79. Xu, J.; Li, X.; Li, J.; Li, X.; Li, B.; Wang, Y.; Wu, L.; Li, W. Wet and Functional Adhesives from One-Step Aqueous Self-Assembly of Natural Amino Acids and Polyoxometalates. *Angew. Chem.* **2017**, *129*, 8857–8861.
80. Yang, J.; Janik, M. J.; Ma, D.; Zheng, A.; Zhang, M.; Neurock, M.; Davis, R. J.; Ye, C.; Deng, F. Location, Acid Strength, and Mobility of the Acidic Protons in Keggin 12-$H_3PW_{12}O_{40}$: A Combined Solid-State NMR Spectroscopy and DFT Quantum Chemical Calculation Study. *J. Am. Chem. Soc.* **2005**, *127*, 18274–18280.

81. Li, C.; Yamaguchi, K.; Suzuki, K. Ligand-Directed Approach in Polyoxometalate Synthesis: Formation of a New Divacant Lacunary Polyoxomolybdate [Γ-$PMo_{10}O_{36}$]$^{7-}$. *Angew. Chem.* **2021**, *133*, 7036–7040.
82. Qian, X.; Tong, X.; Wu, Q.; He, Z.; Cao, F.; Yan, W. Synthesis and Electrochemical Properties of Substituted Heteropoly Acid with Dawson Structure $H_7[In(H_2O)P_2W_{17}O_{61}]\cdot 23H_2O$. *Dalton Trans.* **2012**, *41*, 9897.
83. Janik, M. J.; Campbell, K. A.; Bardin, B. B.; Davis, R. J.; Neurock, M. A Computational and Experimental Study of Anhydrous Phosphotungstic Acid and Its Interaction with Water Molecules. *Applied Catalysis A: General* **2003**, *256*, 51–68.
84. Li, S.; Zhao, Y.; Knoll, S.; Liu, R.; Li, G.; Peng, Q.; Qiu, P.; He, D.; Streb, C.; Chen, X. High Proton-Conductivity in Covalently Linked Polyoxometalate-Organoboronic Acid-Polymers. *Angew. Chem. Int. Ed.* **2021**, *60*, 16953–16957.
85. Liu, W.-J.; Dong, L.-Z.; Li, R.-H.; Chen, Y.-J.; Sun, S.-N.; Li, S.-L.; Lan, Y.-Q. Different Protonic Species Affecting Proton Conductivity in Hollow Spherelike Polyoxometalates. *ACS Appl. Mater. Interfaces* **2019**, *11*, 7030–7036.
86. Liu, J.; Han, Q.; Chen, L.; Zhao, J.; Streb, C.; Song, Y. Aggregation of Giant Cerium–Bismuth Tungstate Clusters into a 3D Porous Framework with High Proton Conductivity. *Angew. Chem. Int. Ed.* **2018**, *57*, 8416–8420.
87. Yang, L.; Ma, P.; Zhou, Z.; Wang, J.; Niu, J. A Crown-Shaped 24-Molybdate Cluster Constructed by Organotriphosphonate Ligand. *Inorg. Chem.* **2013**, *52*, 8285–8287.
88. Peng, Q.; Li, S.; Wang, R.; Liu, S.; Xie, L.; Zhai, J.; Zhang, J.; Zhao, Q.; Chen, X. Lanthanide Derivatives of Ta/W Mixed-Addendum POMs as Proton-Conducting Materials. *Dalton Trans.* **2017**, *46*, 4157–4160.
89. Yang, P.; Alsufyani, M.; Emwas, A.; Chen, C.; Khashab, N. M. Lewis Acid Guests in a $\{P_8W_{48}\}$ Archetypal Polyoxotungstate Host: Enhanced Proton Conductivity via Metal-Oxo Cluster within Cluster Assemblies. *Angewandte Chemie* **2018**, *130*, 13230–13235.
90. Zhou, E.-L.; Qin, C.; Wang, X.-L.; Shao, K.-Z.; Su, Z.-M. Steam-Assisted Synthesis of an Extra-Stable Polyoxometalate-Encapsulating Metal Azolate Framework: Applications in Reagent Purification and Proton Conduction. *Chem. Eur. J.* **2015**, *21*, 13058–13064.
91. Li, Z.; Li, X.-X.; Yang, T.; Cai, Z.-W.; Zheng, S.-T. Four-Shell Polyoxometalates Featuring High-Nuclearity Ln_{26} Clusters: Structural Transformations of Nanoclusters into Frameworks Triggered by Transition-Metal Ions. *Angew. Chem.* **2017**, *129*, 2708–2713.
92. Armakola, E.; Salcedo, I. R.; Bazaga-García, M.; Olivera-Pastor, P.; Mezei, G.; Cabeza, A.; Fernandes, T. A.; Kirillov, A. M.; Demadis, K. D. Phosphonate Decomposition-Induced Polyoxomolybdate Dumbbell-Type Cluster Formation: Structural Analysis, Proton Conduction, and Catalytic Sulfoxide Reduction. *Inorg. Chem.* **2019**, *58*, 11522–11533.
93. Cao, G.-J.; Liu, J.-D.; Zhuang, T.-T.; Cai, X.-H.; Zheng, S.-T. A Polyoxometalate–Organic Supramolecular Nanotube with High Chemical Stability and Proton-Conducting Properties. *Chem. Commun.* **2015**, *51*, 2048–2051.
94. Li, J.; Cao, X.-L.; Wang, Y.-Y.; Zhang, S.-R.; Du, D.-Y.; Qin, J.-S.; Li, S.-L.; Su, Z.-M.; Lan, Y.-Q. The Enhancement on Proton Conductivity of Stable Polyoxometalate-Based Coordination Polymers by the Synergistic Effect of MultiProton Units. *Chem. Eur. J.* **2016**, *22*, 9299–9304.
95. Jiao, Y.-Q.; Zang, H.-Y.; Wang, X.-L.; Zhou, E.-L.; Song, B.-Q.; Wang, C.-G.; Shao, K.-Z.; Su, Z.-M. Self-Assembled Arrays of Polyoxometalate-Based Metal–Organic Nanotubes for Proton Conduction and Magnetism. *Chem. Commun.* **2015**, *51*, 11313–11316.
96. Dey, C.; Kundu, T.; Banerjee, R. Reversible Phase Transformation in Proton Conducting Strandberg-Type POM Based Metal Organic Material. *Chem. Commun.* **2012**, *48*, 266–268.
97. Miao, J.; Liu, Y.; Tang, Q.; He, D.; Yang, G.; Shi, Z.; Liu, S.; Wu, Q. Proton Conductive Watery Channels Constructed by Anderson Polyanions and Lanthanide Coordination Cations. *Dalton Trans.* **2014**, *43*, 14749–14755.
98. Wang, J.-X.; Wang, Y.-D.; Wei, M.-J.; Tan, H.-Q.; Wang, Y.-H.; Zang, H.-Y.; Li, Y.-G. Inorganic Open Framework Based on Lanthanide Ions and Polyoxometalates with High Proton Conductivity. *Inorg. Chem. Front.* **2018**, *5*, 1213–1217.
99. Chen, Y.; Guo, Z.-W.; Chen, Y.-P.; Zhuang, Z.-Y.; Wang, G.-Q.; Li, X.-X.; Zheng, S.-T.; Yang, G.-Y. Two Novel Nickel Cluster Substituted Polyoxometalates: Syntheses, Structures and Their Photocatalytic Activities, Magnetic Behaviors, and Proton Conduction Properties. *Inorg. Chem. Front.* **2021**, *8*, 1303–1311.
100. Li, S.; Wang, H.; Su, H.; Chen, H.; Du, M.; Long, L.; Kong, X.; Zheng, L. A Giant 3d-4f Polyoxometalate Super-Tetrahedron with High Proton Conductivity. *Small Methods* **2021**, *5*, 2000777.

Chapter 2

Fabricating a Functionalized Polyoxometalate with ZIF-8: A Composite Material for Water Oxidation in a Wide pH Range

OVERVIEW

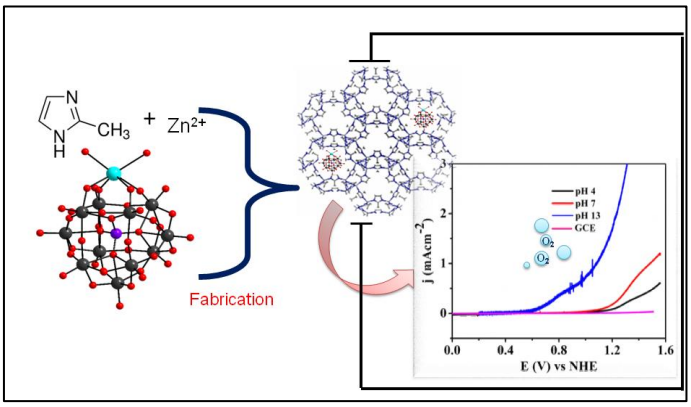

Designing an efficient oxygen evolution reaction (OER) electrocatalyst is a challenging task because molecular oxygen is essential to sustain life. Herein, we have synthesized and structurally characterized a $\{Bi(OH_2)_2\}^{3+}$–functionalized Keggin polyoxometalate (POM) compound, $K_5[Bi(H_2O)_2SiW_{11}O_{39}]\cdot 13H_2O$ (**$K_5$1·13H_2O**). Keeping in mind that $\{Bi(OH_2)_2\}^{3+}$ species on the surface of the POM has the potential to act as an active site for electrocatalytic water oxidation, we encapsulated the functionalized Keggin POM anion $[Bi(OH_2)_2SiW_{11}O_{39}]^{5-}$ inside the cavities of a well-known zeolite type framework material ZIF-8, a zinc-imidazole containing metal-organic framework (MOF), because compound **$K_5$1·13H_2O** *per se* is water soluble and unstable in the oxidation window of water oxidation. The resulting host-guest type composite material $H_5[Bi(H_2O)_2SiW_{11}O_{39}]$@ZIF8 (**$H_5$1@ZIF8**) functions as an efficient electrocatalyst for water oxidation. The detailed electrochemical analyses have established that the title oxygen evolution reaction (OER) catalyst, **$H_5$1@ZIF8** works in a wide pH window, ranging from alkaline pH 13.0 to neutral pH 7.0 through an acidic pH 4.0. Diverse controlled experiments have been performed to infer that bismuth-aqua complex is the functional site responding to the OER, with a catalytic turnover frequency (TOF) of 1.24 s^{-1}, 5.90 s^{-1} and 0.93 s^{-1} of pH 13.0, pH 7.0 and pH 4.0 solutions, respectively at the respective overpotentials of 375.0 mV (vs RHE), 585.21 mV (vs RHE) and 830.10 mV (vs RHE).

2.1. INTRODUCTION

Water splitting *via* electrocatalysis is a promising, sustainable and green practice to produce carbon free fuels,[1,2] which is basically a process consisting of two fundamental half-cell reactions, namely, hydrogen evolution reaction (HER) and oxygen evolution reaction (OER). Among these, OER is regarded as the crucial process of high energy demand with involvement of four electrons and four protons (OER: $2H_2O \rightarrow 4H^+ + O_2 + 4e^-$; $E^0 = 1.23$ V).[3,4] This leads to a challenge in the development of inexpensive and robust water oxidation catalysts (WOCs). Among metal-oxide based WOCs,[5-7] polyoxometalates (POMs) turn out to be one of the most intriguing classes of molecular metal oxide clusters exhibiting excellent water splitting (WS) properties.[8-12] It is noteworthy that, POMs show rapid and reversible multi-electron redox transformations without significant structural alteration, but in an acidic pH condition (in an alkaline pH condition, POMs decompose).[13-15] Numerous research groups worldwide have explored the process of water oxidation (WO), catalyzed by POMs and POM-based compounds including stabilization of POM water oxidation catalysts on hematite using atomic layer deposition by Hill and co-workers.[16] We have used POM in a confined space of the framework material[17] and POM supported transition metal coordination complex[18] as efficient electrocatalysts for water oxidation. In this regard, bismuth, a post-transition element, has drawn our special attention for the use of its aqua complex associated with a POM as an electrocatalyst for water oxidation because of two-fold reasons: (i) we have seen that a transition metal (e.g., Co^{2+} and Ni^{2+})-aqua complex, when it is encapsulated in the confined void space of a framework material or it is supported on a POM surface by coordinate covalent bonds, exhibits heterogeneous electrochemical water oxidation;[17,18] (ii) Bi^{3+}- based metal oxides, e.g., Bi_2WO_6, $BiVO_4$, and $Bi_4Ga_4O_{12}$ *etc.* are well-known catalysts for photoelectrocatalytic water splitting, [19-27] but electrocatalytic water splitting using Bi^{3+}-species as catalyst is hardly known.[28]

Thus, we intended to use Bi^{3+}−aqua species as an electrocatalyst for water oxidation, because $\{Bi^{III}(H_2O)\}^{3+}$ species can be oxidized to $\{Bi^{V}{=}O\}^{3+}$ electrochemically that can oxidize water chemically to produce molecular oxygen as shown in the following equations (1-5). In the present study, equations 1-4 would be electrochemically driven and equation 5 would be chemically driven.

$$\{-Bi^{III}(H_2O)\}^{3+} - e^- = \{-Bi^{IV}(H_2O)\}^{4+} \quad \text{---------- (eqn 1)}$$

$$\{-Bi^{IV}(H_2O)\}^{4+} - H^+ = \{-Bi^{IV}(HO)\}^{3+} \quad \text{---------- (eqn 2)}$$

$\{-Bi^{IV}(HO)\}^{3+} - e^{-} = \{-Bi^{V}(HO)\}^{4+}$ ---------- (eqn 3)

$\{-Bi^{V}(HO)\}^{4+} - H^{+} = \{-Bi^{V}=O)\}^{3+}$ ---------- (eqn 4)

$\{-Bi^{V}=O\}^{3+} + H_2O = \{-Bi^{III}\}^{3+} + O_2 + 2H^{+} + 2e^{-}$ (eqn 5)

However, in an aqueous homogeneous solution of a Bi^{3+} salt (e.g., bismuth nitrate), the formation of mono-nuclear oxidized $\{-Bi^{V}=O\}^{3+}$ species, an active form for water oxidation, is not easily possible because Bi^{3+} is hydrolysed in water forming binuclear and polynuclear compounds using Bi−O−Bi bond(s).[29]

An effective way to avoid this dimer/oligomer formation is to functionalize a POM cluster with $\{Bi^{III}(H_2O)\}^{3+}$ species by attaching this active species on the POM cluster surface using coordinate-covalent bonds (as if the POM cluster acts as the ligand through its terminal or bridging oxo donors) so that dimer formation of bismuth would be prevented by the bulky POM ligand, except the sandwich compounds, in which two or four Bi^{3+} are circularly arranged through bridged oxygen of the POM in the sandwiched position.[30] Most of the bismuth-containing reported POMs are bismuth-centered lacunary Keggin anions associated with other transition metal aqua cations (see Table S1, Supporting Information (SI)). On a par with equations 1-5 that a Bi^{3+}−aqua complex has the potential to be oxidized to $\{Bi^{V}=O\}$ species electrochemically that can oxidize water chemically to molecular O_2, we intended to synthesize a $\{(H_2O)Bi^{3+}\}$-functionalized POM. Even though, there are several Bi^{3+}−(H_2O)/(OH)-associated POM compounds, including lacunary Keggin POM compounds, known in the literature,[31-41] there are only a few reports on 2:1 and 1:1 complexes formed by mono-lacunary Keggin anion and Bi(III) cation. In most of these bismuth(III)-mono-lacunary Keggin compounds, the lacunary polyoxometalates act as tetradentate ligands, especially in the case of 2:1 mono-lacunary Keggin:Bi(III) compounds. Whereas, 2:1 mono-lacunary Keggin:Bi(III) compounds were designed, synthesized, and structurally characterized by Sadakane group, the 1:1 mono-lacunary Keggin:Bi(III) compound has not yet been isolated, although its formation in an aqueous solution was proved by the same group using ^{183}W NMR and ^{31}P NMR spectroscopy.[40] We were interested to isolate the 1:1 mono-lacunary Keggin:Bi(III) compound because in 1:1 system, Bi(III) center will have possible water coordination besides its four coordination with lacunary polyoxometalate. Water coordination to Bi(III) center is the prime factor for the Bi(III) center to act as the functional site for water oxidation (referring equations 1-5). After multiple efforts, we could functionalize a lacunary Keggin POM anion $[SiW_{11}O_{39}]^{8-}$ with a $\{Bi^{III}(H_2O)_2\}^{3+}$ species resulting in the isolation of a hitherto unknown compound $K_5[Bi(H_2O)_2SiW_{11}O_{39}]\cdot 13H_2O$ (**$K_5$1·13H_2O**), having 1:1 ratio

of mono-lacunary Keggin:Bi(III). We have characterized compound **$K_5$1·13H_2O** unambiguously by its single-crystal X-ray structure determination including its ICP elemental analyses. Compound **$K_5$1·13H_2O**, isolated as a potassium salt, is water soluble and as expected it exhibits electrochemical water oxidation but after few cycles it diminishes. Thus, compound **$K_5$1·13H_2O** is unstable in its homogeneous aqueous solution at its oxidation potential. When a catalytically active species, e.g., $[Bi(H_2O)_2SiW_{11}O_{39}]^{5-}$ (**1**) in the present study, cannot survive in its homogeneous solution during its catalytic cycles towards water oxidation, a meaningful fabrication may be needed so that the 'otherwise unstable catalyst' becomes stable enough to exhibit multiple cycles and better efficiency. In this regard, POM@MOFs, *i.e.*, POM molecule encapsulated into metal-organic frameworks' cavities / void spaces, is a useful fabrication because there are advantages of using a MOF (as a host matrix) to encapsulate a POM (guest). High surface areas of MOFs having well-defined internal cavities / channels enable a homogeneous distribution of the guest POM in the MOF host which suppresses the aggregation of POMs, thereby improves the stability of the encapsulated POM; a lower loading level helps in smooth diffusion of the substrate and product inside the host matrix (MOF).[42-44] R. Wang and co-workers reported an *in situ* self-assembly strategy to encapsulate a strong Brønsted acid, $H_3PMo_{12}O_{40}$, in the customized cavities of a Co-based MOF, ZIF-67 resulting in a series of $H_3PMo_{12}O_{40}$@ZIF-67 hybrids exhibiting OER catalytic activity.[45] Pang and his group demonstrated that 'Yolk/Shell' ZIF-67@POM hybrids (POM = $H_3PW_{12}O_{40}$) can act as efficient electrocatalysts for the OER with an overpotential of 287 mV at the current density of 10 mA cm^{-2} and Tafel slope of 58 mV/ decade.[46] The same group combined ZIF-8 with ZIF-67@POM to prepare the ZIF-8@ZIF-67@POM hybrids and used as heterogeneous OER catalysts.[47] We have shown that a Co(II)-centered Keggin cluster anion, $[CoW_{12}O_{40}]^{6-}$, which is unstable in its homogeneous aqueous solution at a moderate oxidation potential, shows efficient heterogeneous electrocatalytic water oxidation up to 1000 cycles when it is confined/encapsulated in the void spaces of a zeolite-like framework material ZIF-8 in a "ship in a bottle" manner.[17] Voort, Song and their co-workers have covered POM@MOF research nicely in their review articles[48,49] including the review article by Liu, Dong, and Lan.[50]

In the present work, we have fabricated a POM@MOF composite material by encapsulating the active species, $[Bi(H_2O)_2SiW_{11}O_{39}]^{5-}$ in the well-defined cavities of ZIF-8 resulting in a host-guest type heterogeneous catalyst, $H_5[Bi(H_2O)_2SiW_{11}O_{39}]$@ZIF8 (**$H_5$1@ZIF8**). The beauty of this fabrication lies in the fact that the resulting composite material **$H_5$1@ZIF8** offers protection to its encapsulated polyoxometalate (POM) guest

species not only in neutral aqueous medium but surprisingly also in a harsh alkaline aqueous solution. It is surprising because a POM cluster anion, which is generally formed in an acidic aqueous solution, does not survive in an alkaline aqueous medium. We have demonstrated that the title host-guest type composite material **$H_5$1@ZIF8** exhibits heterogeneous electrocatalytic water oxidation in a wide pH window, ranging from acidic solution of pH 4.0 to the neutral solution (pH 7.0) through harsh alkaline aqueous solution of pH 13.0.[51-53] An account of this electrocatalytic oxygen evolution reaction (OER) including detailed kinetic studies and related controlled experiments has been described in this article.

2.2. EXPERIMENTAL SECTION

2.2.1. Materials

All the experiments were conducted with deionized water at ambient atmospheric conditions. All the chemicals taken for synthesis are utilized without any purification. Bismuth nitrate pentahydrate, potassium nitrate, zinc nitrate hexahydrate are purchased from Finar Chemicals, India. Solvents like methanol and DMF are purchased from SRL Chemicals, India.

2.2.2. Synthesis

2.2.2.1. Synthesis of $K_5[Bi(H_2O)_2SiW_{11}O_{39}]\cdot 13H_2O$ ($K_5$1·$13H_2O$)

An aqueous solution of $K_8[SiW_{11}O_{39}]\cdot 13H_2O$ (0.5 mmol in 20 mL water) was heated to 55 °C for 5 minutes, under constant stirring, to form a clear solution. A solution of $Bi(NO_3)_3\cdot 5H_2O$ (0.5 mmol dissolved in 13 ml of 50% glacial acetic acid) was then added to the above solution drop-wise in such a way that the local precipitation was completely dissolved before the addition of the next drop, by maintaining the reaction condition. The reaction was continued for another 15 minutes. Further, a solution of KNO_3 (20 mmol in 13 mL water) was added drop-wise to the above solution and stirred for ten more minutes maintaining the same reaction conditions. The resulting white opalescent solution was filtered through a celite bed. Subsequently, it was cooled down to room temperature and found that the resultant filtrate had a pH 2.01. The colourless needle-type crystals were grown from this transparent-colourless solution in four days.

2.2.2.2. Synthesis of Zeolitic Imidazolate Framework-8 (ZIF-8)[60]

A solution of $Zn(NO_3)_2\cdot 6H_2O$ (5 mmol) in methanol (MeOH; 25 mL) was added slowly to a 25 mL of methanolic solution of 2-methylimidazole (24.4 mmol) under stirring. The reaction mixture was then kept undisturbed for 24 hours at an ambient condition. The resulting white

color material was centrifuged and washed with DMF, water, and MeOH repeatedly to get rid of unreacted material and dried at 70 ℃ for 24 hours.

2.2.2.3. Synthesis of $H_5$1@ZIF8

A 25 mL of methanolic solution of $Zn(NO_3)_2 \cdot 6H_2O$ (5 mmol) and 5 mL of an aqueous methanolic solution of **$K_5$1·13H_2O** (0.2 % w/v, 40 mg in 2.5: 2.5 mL of H_2O: MeOH) were added simultaneously drop-wise to the 25 mL of methanolic solution of 2-methylimidazole (24.4 mmol) with vigorous stirring at room temperature. The mixture was then kept undisturbed for 24 hours at room temperature, and **$H_5$1@ZIF8** composite was obtained as a white color crystalline material. It was centrifuged and washed with DMF, MeOH, and water repeatedly to eliminate unreacted material (each for 5 times). The obtained final product was dried at 70 ℃ for 24 hours. Further, the composite material was stirred in an aqueous solution of 0.01M NaCl for 48 hours to get rid of surface adsorbed POM units if any. Finally, it was again dried at 70 ℃ for 24 hours.

2.2.2.4 Synthesis of SiW_{11}@ZIF8

The same synthesis procedure was maintained as used for **$H_5$1@ZIF8**, except the use of $K_8[SiW_{11}O_{39}] \cdot 13H_2O$ mono-lacunary cluster instead of **$K_5$1·13H_2O**.

2.2.3. Methods

2.2.3.1. Physical Characterizations

The functionalized Keggin POM compound **$K_5$1·13H_2O** has unambiguously been characterized by single-crystal X-ray diffraction (SCXRD). Further, the **$K_5$1·13H_2O**, the title composite **$H_5$1@ZIF8** and ZIF-8 have been characterized by ATR-FTIR, Raman, PXRD, electronic spectra, TGA, ICP-OES, XPS, BET analyses. The electrochemical measurements are performed to prove the catalytic nature of the characterized composite, **$H_5$1@ZIF8**.

2.2.3.2. X-ray Crystallography

A suitable nascent single-crystal of **$K_5$1·13H_2O** compound was selected from the mother liquor and mounted on a fibre-loop using Araldite resin mask for X-ray diffraction data collection (at 100 K). The Rigaku Oxford XtalLAB Synergy diffractometer is having a Mo–Kα (λ = 0.71073 Å) graphite monochromatic X-ray beam source used for structure determination, and 40 mm of the crystal-to-detector distance was maintained. The collected data reduction was performed with AutoLab software. Empirical absorption corrections were accomplished with the SADABS program. Structure solutions and full-matrix least-squares refinement were done by standard crystallographic software Olex2-1.3-ac4 embedded with SHELX 2018/1 package for the title compound. The single crystals of **$K_5$1·13H_2O** are very

sensitive to the room temperature and the crystals could lose their quality very quickly. Except some lattice water and few framework oxygen atoms, all the non-hydrogen atoms were refined anisotropically. Hence, the atomic displacement parameter (ADP) alerts containing oxygen atoms were modelled with crystallographically allowed EADP command. The crystallographic details and structure refinement parameters for **$K_5$1·13H_2O** compound are listed in Table 2.1. CSD 2110621 contains the supplementary crystallographic data for **$K_5$1·13H_2O**.

Table 2.1. Crystal data and structure refinement parameters for **$K_5$1·13H_2O**

Parameter	**$K_5$1·13H_2O**
Empirical formula	$BiK_5O_{54}SiW_{11}$
Formula weight	3318.92
T(K)/ λ (Å)	100(2)/ 0.71073
Crystal system	Triclinic
Space group	*P-1*
Unit cell dimensions	a = 11.6029(2) Å b = 11.9120(2) Å c = 19.8162(4) Å α = 96.202(2)° β = 97.574(2)° γ= 118.594(2)°
Volume	2337.31(7) $Å^3$
Z	2
Density (calculated)	4.716 Mg/m^3
Absorption coefficient (M)	31.294 mm^{-1}
***F*(000)**	2876
Independent reflections	8228 [$R_{(int)}$ = 0.0814]
Goodness-of-fit on F^2	1.024
R1/ wR2 [I > 2σ (I)]	0.0486/0.1133
R1/ wR2 (all data)	0.0614/0.1190
Absolute structure parameter	0.027(19)
Largest diff. peak and hole	3.334 and -3.257 e $Å^{-3}$

2.2.3.3. Electrochemical Measurements

All the electrochemical experiments were performed heterogeneously using conventional three-electrode electrochemical cell employing the **$H_5$1@ZIF8** modified glassy carbon

electrode (GCE) as working, a home-made Ag/AgCl (3M) as a reference, and Pt mesh as counter electrodes at acidic pH 4 and neutral pH 7.0. Whereas in the case of alkaline 0.1 M KOH (pH 13) eleoctrolyte, **$H_5$1@ZIF8** modified glassy carbon was used as working-, Hg/HgO (MMO) as a reference-, and graphite rod as counter-electrodes. A homogeneous suspension of **$H_5$1@ZIF8** for electrochemical analysis was made by following our recent literature.[17] In pH 4.0 and neutral pH 7.0, 25 µL of this homogeneous sample-suspension was coated on the glassy carbon electrode (GCE) having a 3 mm diameter (0.0706 cm^2 geometrical area), resulting in the ~100 µg of the sample on the GCE. Whereas in the case of alkaline pH 13.0, 20 µL of sample suspension was loaded corresponding to ~80 µg of the sample on the GCE. A diluted Nafion solution was prepared by mixing 40 µL (5 wt %) Nafion solution into a 60 µL of ethanol (in the ratio of 2:3 Nafion-ethanol mixture), and a drop of it was coated over the sample loaded electrode. The same amount of sample loading was maintained for all electrochemical experiments unless otherwise mentioned. The drop-casted sample ink was dried under IR-lamp (temp ~70 °C) and the coated electrode left at room temperature for 5 min to obtain an ambient condition, before using it. All the electrochemical experiments were carried out under the nitrogen atmosphere at room temperature. The experimentally observed potentials were converted to the RHE scale following the relation of $E_{(RHE)} = E_{(Ag/AgCl)} + 0.204\ V + 0.059\ pH$ where the Ag/AgCl (3M KCl) electrode was used as the standard reference electrode. In the case MMO (pH 13.0, 0.1M KOH), the potential of the MMO would be $E_{(RHE)} = E_{(MMO)} + 0.916\ V$ (see below the section of calibration of MMO with respect to RHE). The cyclic voltammogram scans were initiated at the open circuit potential (OCP) and first scanned to the anodic side. Before every electrochemical experiment, at least five cyclic voltammogram (CV) scans were recorded continuously to understand the quality of prepared homogeneous **$H_5$1@ZIF8** ink, and in most of the electrochemical experiments 100 mV/s scan rate was used to collect the CV cycles unless otherwise stated. All the electrochemical studies were performed at pH 13 of 0.1 M KOH and neutral pH (0.1 M) potassium phosphate buffer as well as in acidic pH 4 solution of 0.1 M potassium phosphate. The chronoamperometry experiments were done with a GCE /stainless steel mesh/FTO as working, and a large surface Pt mesh/graphite rod as counter electrodes. The stainless steel mesh working electrode preparation for bulk electrolysis was carried out as 1 mg/cm^2 area catalyst loading. Controlled experiments of electrochemically fabricated FTO electrodes were conducted to establish the true electrocatalytic oxygen evolution reaction activity of encapsulated **$K_5$1·13H_2O** inside the ZIF-8 cage. The Tafel data were collected in a galvanostatic mode under steady-state mass

flow, the electrolyte solution was stirred at 480 rpm throughout the experiments. The internal cell resistance was manually calibrated. Differential pulsed voltammogram (DPV) was performed using the 50 mV pulse for 100 ms time and 5 mV step height for 80 ms step width and the integration time was 5 ms.

Calibration of MMO with respect to RHE

The calibration of Hg/HgO (0.1 M KOH) electrode was performed by running a linear sweep voltammogram (LSV) using Pt-disk (2 mm diameter) in H_2 saturated 0.1 M KOH at a scan rate of 1 mV/s using MMO as reference electrode. The electrolyte was purged with H_2 gas for 30 minutes prior to the experiments and the same condition was maintained throughout the analysis. The potential was scanned from 0 to -1.3 V *vs* MMO. The potential at which the LSV curve crosses the zero current was considered the potential of the MMO *vs* RHE. Here, the corresponding potential is - 0.916 V.

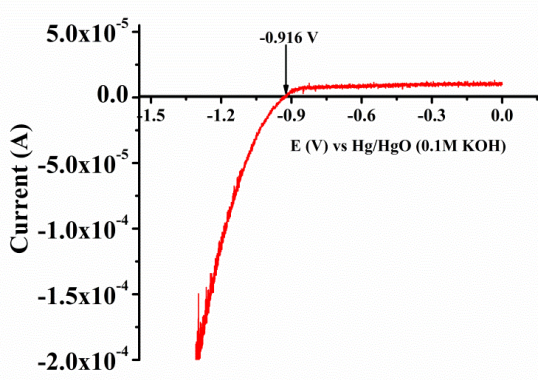

Figure 2.1. LSV plot for MMO calibration using Pt-disk as WE, Pt mesh and MMO as counter and reference electrodes respectively in H_2-saturated 0.1 M KOH solution; scan rate was 1 mV/s.

2.3. RESULTS AND DISCUSSION

2.3.1. Physical Characterizations of $K_5$1·13H_2O

2.3.1.1. Single Crystal X-ray Diffraction description of $K_5$1·13H_2O

The bismuth-aqua complex attached Keggin-type polyoxometalate (POM) compound has been isolated in an aqueous synthesis. The aqueous solution of mono-lacunary Keggin compound $K_8[SiW_{11}O_{39}]\cdot 13H_2O$ was reacted with bismuth nitrate solution at 55 ℃ and obtained as colorless needle-type crystals. The molecular formula of these needle crystals is determined as $K_5[Bi(H_2O)_2SiW_{11}O_{39}]\cdot 13H_2O$ (**$K_5$1·13H_2O**) from single-crystal X-ray structure analysis and ICP-OES analyses. The synthesized compound $K_5$1·13H_2O is freely soluble in an aqueous solution (0.28 g/mL). Furthermore, the presence of bismuth in the

synthesized POM compound K_5**1**·$13H_2O$ is analyzed by its qualitative test, XPS (*vide infra*) and EDX elemental mapping and TGA has also been performed on K_5**1**·$13H_2O$.

Compound **$K_5$1·$13H_2O$** is crystallized in the triclinic *P-1* space group. The crystal structure includes a mononuclear bis(aqua)Bi(III) complex, $\{Bi(H_2O)_2\}^{3+}$ attached to the peripheral position of the mono-lacunary Keggin $\{SiW_{11}O_{39}\}^{8-}$, resulting in a Bi(III)-aqua complex functionalized polyoxometalate (POM), $[Bi(H_2O)_2SiW_{11}O_{39}]^{5-}$ (Figure 2.1a). In the crystal structure, the mono-lacunary Keggin POM anion $\{SiW_{11}O_{39}\}^{8-}$ acts as a tetra dentate ligand towards the coordination around Bi(III) center of $\{Bi(H_2O)_2\}^{3+}$, thus bismuth ion in the crystal structure has distorted octahedral geometry (Figure 1a,b), consistent with the reported literature.[54-58]

The bismuth(III) ion has compatibility to exist in the wide coordination numbers from 3, 4, 5, 6 (*octahedral, distorted octahedral* and *pentagonal pyramidal* geometry of the BiO_6) to 7, 8 (square-antiprismatic geometry of the BiO_8) through 10 (*pentagonal prismatic* geometry of BiO_{10} unit). In 2011, our group has shown the presence of Bi^{3+} ion in octahedral geometry[54] and very recently in 2021, C. Lichtenberg group has also claimed that the existence of distorted octahedral[55] and other geometries for the same Bi^{3+} ion. The higher coordination numbers for the Bi^{3+} ion are common in polyoxometalate chemistry. T. Yamase and his group reported the formation of pentagonal pyramidal geometry with the coordination number of six for Bi^{3+} ion and they have observed the bond lengths of 2.15-2.52 Å and 2.41-2.55 Å range

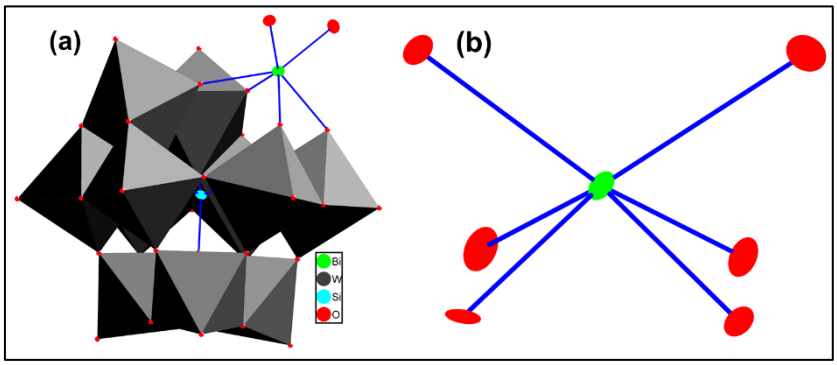

Figure 2.2. (a) Polyhedral representation of $[Bi(H_2O)_2SiW_{11}O_{39}]^{5-}$ (**1**) in the single-crystal X-ray structure of $K_5[Bi(H_2O)_2SiW_{11}O_{39}]\cdot 13H_2O$ (**$K_5$1·$13H_2O$**); coordination around Bi(III) is shown in thermal-ellipsoidal representation. (b) Thermal ellipsoidal diagram of $\{BiO_6\}$ entity in the crystal structure of compound **$K_5$1·$13H_2O$** (colour code: O, red; Si, cyan; W, dark-grey; Bi, green).

for Bi–O(W) and Bi–OH_2 groups respectively.[56] Furthermore, in 2018, M. Sadakane and U. Kortz groups have isolated bismuth(III) containing polyoxometalates with the square-antiprismatic (BiO_8) and pentagonal prismatic (BiO_{10}) geometries having the Bi–O(W) bond

lengths in the range of 2.31-2.66 Å.[57,58] In the present system, the bond lengths 2.30, 2.30, 2.33 and 2.38 Å for Bi–O(W) and 2.50, 2.68 for Bi–OH_2 groups are found that are consistent with the reported literature.[54-58] There are five potassium cations to counterbalance the five negative charges (–5) of the functionalized POM cluster anion $[Bi(H_2O)_2SiW_{11}O_{39}]^{5-}$ (**1**) and 13 solvent water molecules per formula unit of compound **$K_5$1·13H_2O**.

2.3.1.2. PXRD spectrum

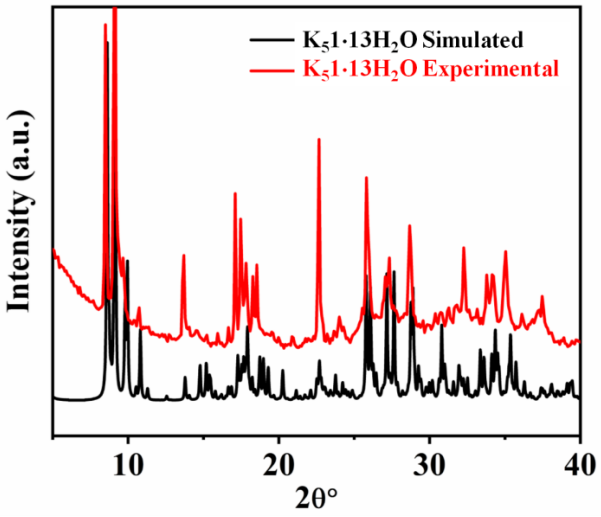

Figure 2.3. Powder X-ray diffraction patterns of **$K_5$1·13H_2O**.

The phase purity and homogeneity of the synthesized compound **$K_5$1·13H_2O** have been verified by PXRD analysis by comparing simulated and observed PXRD patterns. It is clearly visible from the Figure 2.3 that there is a close match of the PXRD pattern of **$K_5$1·13H_2O** to that of its simulated pattern, indicating same phase compound has been formed in the whole bulk.

The compound **$K_5$1·13H_2O** characterized further with UV-DRS, XPS ICP-OES, FESEM-EDX analyses and the complete data have been provided in Appendix 2.2 to 2.4.

Why fabrication in this Work?

The prime objective of this work is to perform electrocatalytic WO using the synthesized POM compound. However, the POM compounds are sensitive in an alkaline aqueous solution, sometimes even in a neutral aqueous medium. As already mentioned in the introduction, the water-soluble compound **$K_5$1·13H_2O** collapses in its neutral aqueous solution within few cyclic voltammetry (CV) cycles in the oxidation window. This prompted us to fabricate this synthesized compound **$K_5$1·13H_2O** with a framework material so that we can use this as a heterogeneous electrocatalyst in an aqueous solution covering a wide pH

range. We have fabricated the composite material **$H_5$1@ZIF8** following our well-established procedure[17] (see the Experimental Section for detailed synthesis). The fabrication includes the encapsulation of the functionalized POM anion, $[Bi(H_2O)_2SiW_{11}O_{39}]^{5-}$, inside the cavities of the zeolite-type framework material ZIF-8.

A proper "ship-in-a-bottle"-type inclusion of a guest species into a framework host material needs some primary criteria to be followed:[59] (i) cavity size of the host framework material (ZIF-8) matches with the guest (Keggin POM) size, (ii) the window aperture of ZIF-8 is smaller than the Keggin size (to avoid leaching), and (iii) presynthesized Keggin encapsulation occurs by the in situ synthesis of ZIF-8, as shown in the following Figure 2. The present fabrication (Figure 2.3.) not only fulfills these three norms for the successful encapsulation of the functionalized Keggin anion into the cavity of the ZIF-8 but also provides protection for the encapsulated Keggin POM anion, which per se is not stable in a neutral and in an alkaline aqueous solution in the anodic window of WO. But the resulting composite $H_5[Bi(H_2O)_2SiW_{11}O_{39}]$@ZIF8 (**$H_5$1@ZIF8**) works as a heterogeneous electrocatalyst in a wide pH range of pH 4 to pH 7 through pH 13. In the formula, we have used five protons as cations, because ZIF-8 is a neutral framework, the charge of the functionalized Keggin anion is –5 and we could not find the presence of any potassium ion in the composite by ICP and EDX analyses. However, the possibility of the coordination to the Zn^{2+} ions (of host framework material) by the oxo groups of the guest POM anion $[Bi(H_2O)_2SiW_{11}O_{39}]^{5-}$cannot not be ruled out.

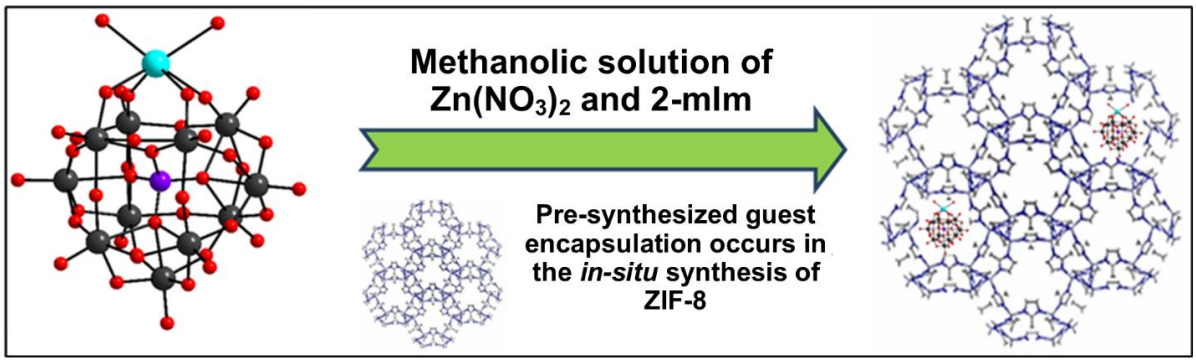

Figure 2.4. Synthetic strategy of the composite material $H_5[Bi(H_2O)_2SiW_{11}O_{39}]$@ZIF8 ($H_5$1@ZIF8) representing the inclusion of one functionalized Keggin POM per three cages of ZIF-8.

2.3.2. Physical Characterizations of $H_5$1@ZIF8

The synthesized composite material $H_5[Bi(H_2O)_2SiW_{11}O_{39}]$@ZIF8 (**$H_5$1@ZIF8**) is thoroughly analyzed by various physical techniques, such as, PXRD and XPS studies, HRTEM-EDS and FESEM-EDX microscopy (see Appendix Axx.), BET, FTIR, electronic

absorption and ICP-OES and thermogravimetric analysis (TGA) (see Appendix Section Axx). The functionalized Keggin POM compound $K_5[Bi(H_2O)_2SiW_{11}O_{39}]\cdot 13H_2O$ (**$K_5$1·13H_2O**) and ZIF-8 separately are also considered for comprehensive characterization of the composite **$H_5$1@ZIF8**.

2.3.2.1. PXRD analysis

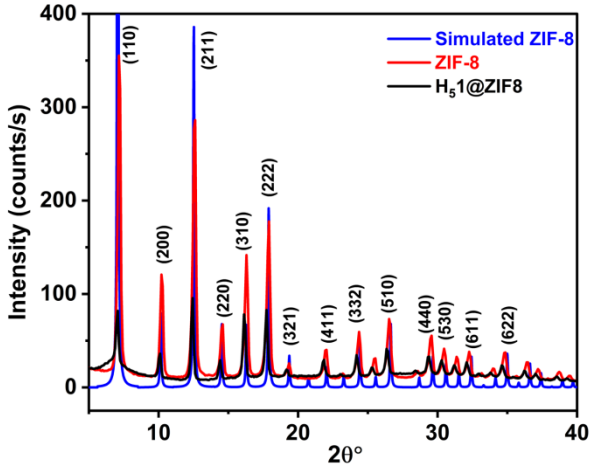

Figure 2.5. (a) Powder X-ray diffraction profiles of ZIF-8 and $H_5[Bi(H_2O)_2SiW_{11}O_{39}]$@ZIF8 (**$H_5$1@ZIF8**).

The PXRD profile of the composite **$H_5$1@ZIF8** is found to be matching very well with that of ZIF-8 itself (Figure 2.5). Thus, the crystal planes of ZIF-8 of the composite **$H_5$1@ZIF8** are not affected due to the in situ encapsulation of **$K_5$1·13H_2O**, $H_5[Bi(H_2O)_2SiW_{11}O_{39}]$ (guest) inside ZIF-8 (host) cavities. From the PXRD profiles, the average crystallite sizes of ZIF-8 and **$H_5$1@ZIF8** have been calculated using Scherrer's equation and the concerned calculated values are 28.436 nm and 26.995 nm respectively (see Appendix, section A2.6 for details).

2.3.2.2. FTIR analysis

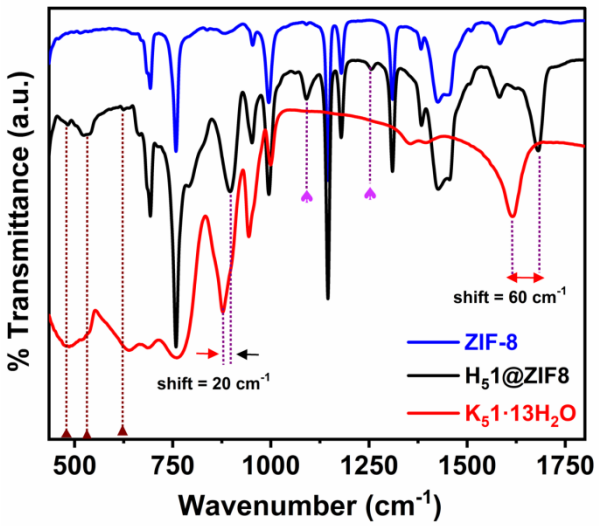

Figure 2.6. ATR-FTIR spectra of $K_5[Bi(H_2O)_2SiW_{11}O_{39}]\cdot 13H_2O$ (**$K_5$1·13H_2O)**, ZIF-8 and **$H_5$1@ZIF8.**

The ATR-FTIR spectra of functionalized POM **$K_5$1·13H_2O**, ZIF-8 and **$H_5$1@ZIF8** are shown in Figure 2.6. The FTIR spectrum of **$K_5$1·13H_2O** has characteristic peaks in the region of 500 to 1000 cm^{-1} for Si-O-W, Bi-O-W, W-O-W, and W=O stretching and bending vibrations.[63] The indicative FTIR peaks ranging from 695 to 1584 cm^{-1} for Zn-N(imidazole) imply a smooth formation of ZIF-8.[17] From Figure 2.6, the presence of combined FTIR features of **$K_5$1·13H_2O** and ZIF-8 in the IR spectrum of the resulting composite **$H_5$1@ZIF8** at 690, 760, 890, 953, 994, and 1386 cm^{-1} supports the successful fabrication of the title host-guest composite. A careful observation on the FTIR spectra indicates that the IR bands at 876 and 1620 cm^{-1} of the pristine POM compound **$K_5$1·13H_2O** are shifted by 20 and 60 cm^{-1} (marked with purple color dotted lines, Figure 2.6) to 896 and 1680 cm^{-1} respectively, when the POM is encapsulated in ZIF-8, i.e., the formation of the composite **$H_5$1@ZIF8**; particularly the distinctive shift of 60 cm^{-1} of the bismuth coordinated water O–H bending mode towards a higher wavenumber is notable in going from pristine POM (**$K_5$1·13H_2O**) to composite POM (**$H_5$1@ZIF8**). This shift towards higher wavenumber is a direct consequence to gaining more stability by strengthening of Bi–O–W, W–O–W, W=O bonds and bismuth coordinated water O–H bonds of the encapsulated POM, due to the interactions with ZIF-8 inner surface. The IR bands at 477, 530 and 623 cm^{-1} (highlighted with brown color dotted lines, Figure 5b) which are present in IR spectra of **$K_5$1·13H_2O** and **$H_5$1@ZIF8**, are not visible in the case of as such ZIF-8 framework material, indicates the existence of POM clusters within the ZIF-8 framework voids. Two new IR bands at 1090 and 1256 cm^{-1} (marked with ♠ symbol), that have arisen in the IR spectrum of the resulting composite (**$H_5$1@ZIF8**) but are absent in the IR spectra of **$K_5$1·13H_2O** and ZIF-8, could be attributed to

the consequence of interactions between encapsulated POM surface and ZIF-8 framework interior of **$H_5$1@ZIF8**.

2.3.2.3. Raman analysis

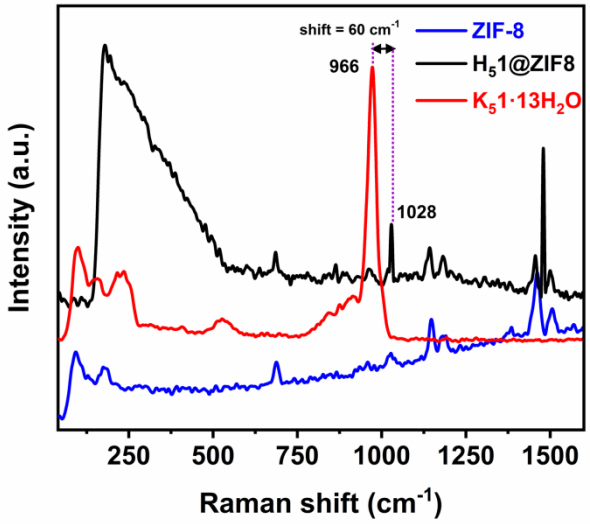

Figure 2.7. Raman spectra of **$K_5$1·13H_2O**, ZIF-8 and the composite $H_5[Bi(H_2O)_2SiW_{11}O_{39}]$@ZIF8 (**$H_5$1@ZIF8**).

The Raman spectra of the pristine Keggin POM compound **$K_5$1·13H_2O**, ZIF-8 and the host-guest composite material **$H_5$1@ZIF8** are compared in Figure 5c, which clearly show that the characteristic Raman peaks of the functionalized Keggin POM anion are present in the Raman spectrum of the composite **$H_5$1@ZIF8** but with shifted positions toward higher wavenumbers. As shown in Figure 2.7, the Raman spectrum of the functionalized Keggin compound **$K_5$1·13H_2O** is dominated by a strong feature at 966 cm^{-1} which gets shifted to 1028 cm^{-1} in the Raman spectrum of the resulting composite **$H_5$1@ZIF8**. Additionally, the Raman active features of ZIF-8 *per se* are clearly visible in the Raman spectrum of the title composite **$H_5$1@ZIF8**, which is consistent with relevant literatures[64,65] and confirms the fine construction of the composite **$H_5$1@ZIF8**. Thus, the Raman spectral studies are on par with IR results supporting host-guest interactions and successful fabrication of the title composite.

2.3.2.4. Electronic spectral analysis

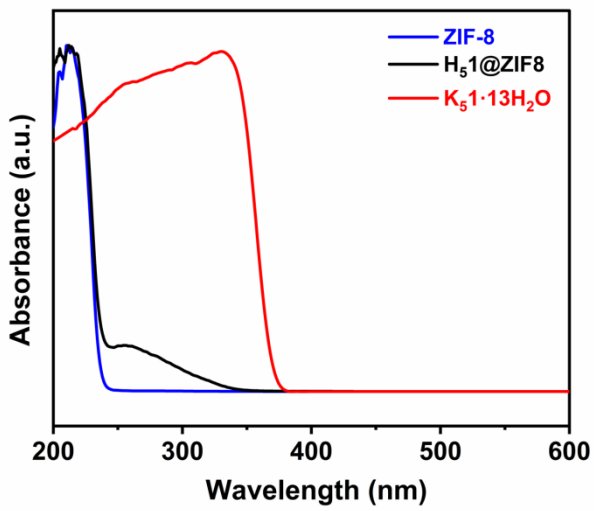

Figure 2.8. Electronic absorption spectra of **$K_5$1·13H_2O**, ZIF-8 and the composite **$H_5$1@ZIF8.**

From the electronic spectra (Figure 2.8), it is clearly evident that ZIF-8 does not have any prominent absorption except imidazole π–π* transitions, whereas **$K_5$1·13H_2O** and **$H_5$1@ZIF8** have absorption maxima at 276 and 330 nm, respectively which can be attributed to O→W LMCT transitions. The shift of this O→W charge transfer band from 330 nm to 276 nm, in going from pristine Keggin POM to encapsulated Keggin POM (**$K_5$1·13H_2O** to **$H_5$1@ZIF8**), is again due to the host-guest interactions in the composite.

2.3.2.5. HR-TEM analysis

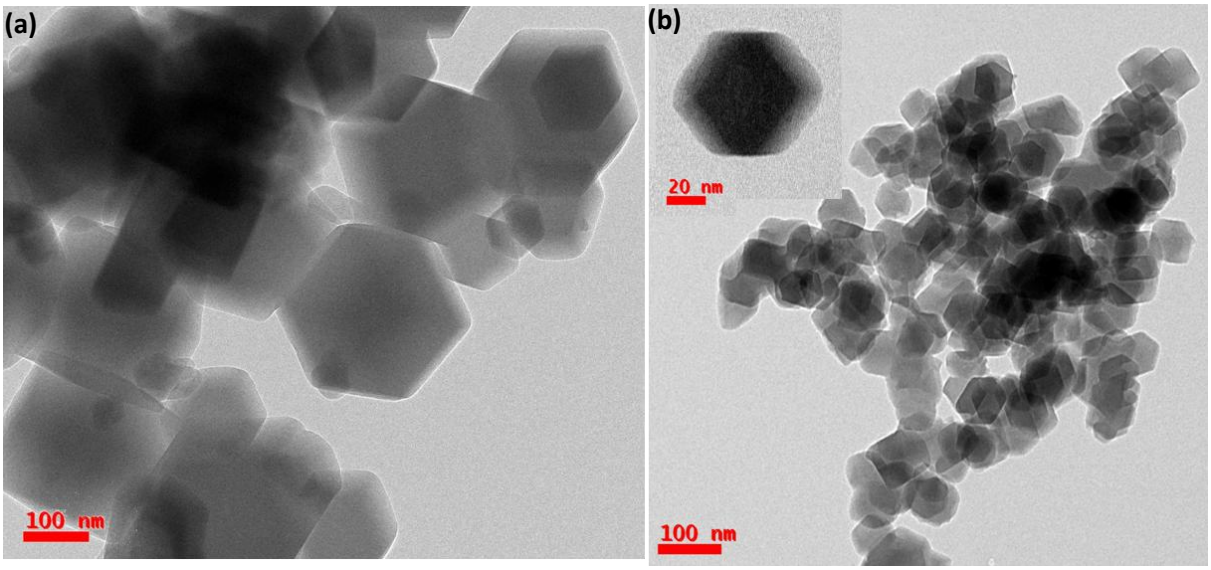

Figure 2.9. High resolution transmission electron microscopy (HRTEM) morphologies of (a) ZIF-8 and (b) **$H_5$1@ZIF8**, respectively

The fabrication does not affect the overall crystal structure of ZIF-8 is also supported by the fact that the common hexagonal morphology of ZIF-8 crystals remained the same

before and after the encapsulation of molecular $H_5[Bi(H_2O)_2SiW_{11}O_{39}]$ (**$H_5$1**) into the cages of ZIF-8 as shown in HRTEM images (Figure 2.9) along with HRTEM-EDS and FESEM-EDX (see Appendix Axx). It is observed from figure 3 that the size of the hexagonal particles of **$H_5$1@ZIF8** has a smaller compared to that of ZIF-8 itself, which is in line with the average crystallite size obtained from Scherrer's equation.

2.3.2.6. N_2 sorption isotherm, BET surface area and pore size distribution analysis

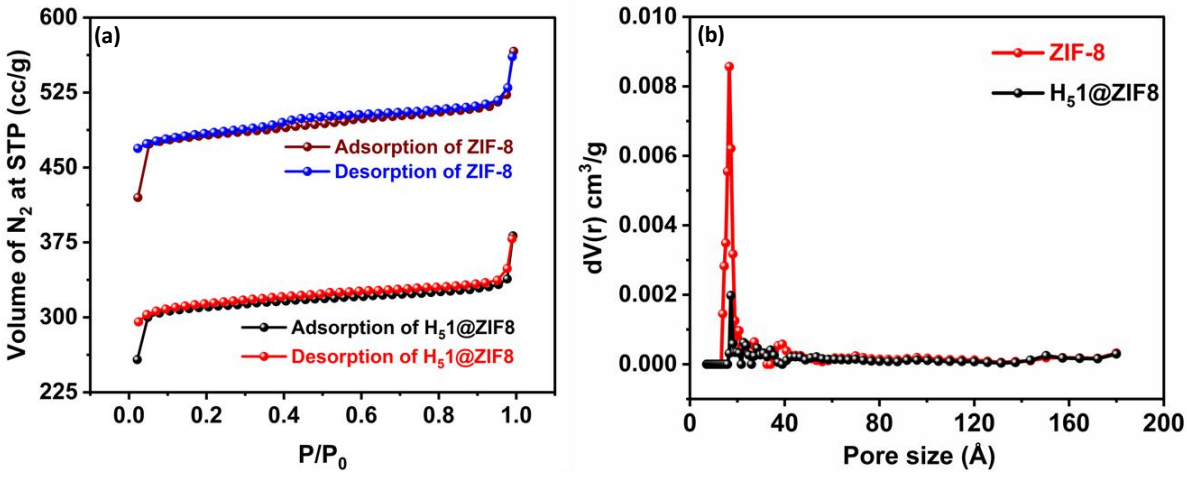

Figure 2.10. N_2 gas adsorption-desorption isotherms for ZIF-8 and composite material **$H_5$1@ZIF8**; (e) pore size distribution of ZIF-8 and **$H_5$1@ZIF8.**

The Brunauer-Emmett-Teller (BET) isotherm profiles for ZIF-8 and **$H_5$1@ZIF8** have also been collected and the obtained BET surface area values 1441.481 and 933.074 m^2g^{-1} for ZIF-8 and **$H_5$1@ZIF8** respectively have confirmed the smooth in-situ encapsulation of $[Bi(H_2O)_2SiW_{11}O_{39}]^{5-}$ cluster molecules into the ZIF-8 cavities (Figure 2.9a). The average pore radius (half pore width) values for ZIF-8 and **$H_5$1@ZIF8** have been obtained from the pore size distribution data and are found to be 16.576 Å and 7.049 Å respectively which further supports the encapsulation strategy (Figure 2.9b). X-ray photoelectron spectroscopy (XPS) has been performed on functionalized Keggin POM compound, **$K_5$1·13H_2O** and the resulting composite material, **$H_5$1@ZIF8** to study the insertion of the guest unit **$H_5$1** inside the well-defined host ZIF-8 cavities.

2.3.2.7. XPS Analyses

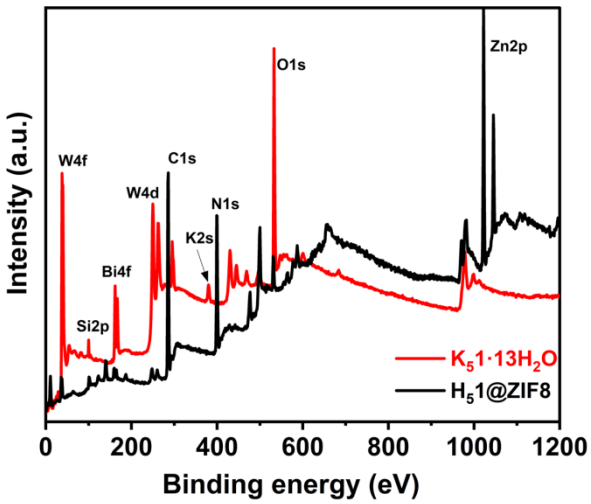

Figure 2.11. X-ray photoelectron spectra (XPS) survey scans of $K_5[Bi(H_2O)_2SiW_{11}O_{39}]\cdot 13H_2O$ (**$K_5$1·13H_2O**) and **$H_5$1@ZIF8.**

The presence of O1s, Si^{4+}2p, W^{6+}4f, and Bi^{3+}4f responses from the functionalized POM **1** along with C1s, N1s and Zn^{2+}2p responses from the host ZIF-8 in the XPS survey scan (Figure 3f) of the resulting composite **$H_5$1@ZIF8** have added further support in establishing successful fabrication resulting in the formation of host-guest composite material.

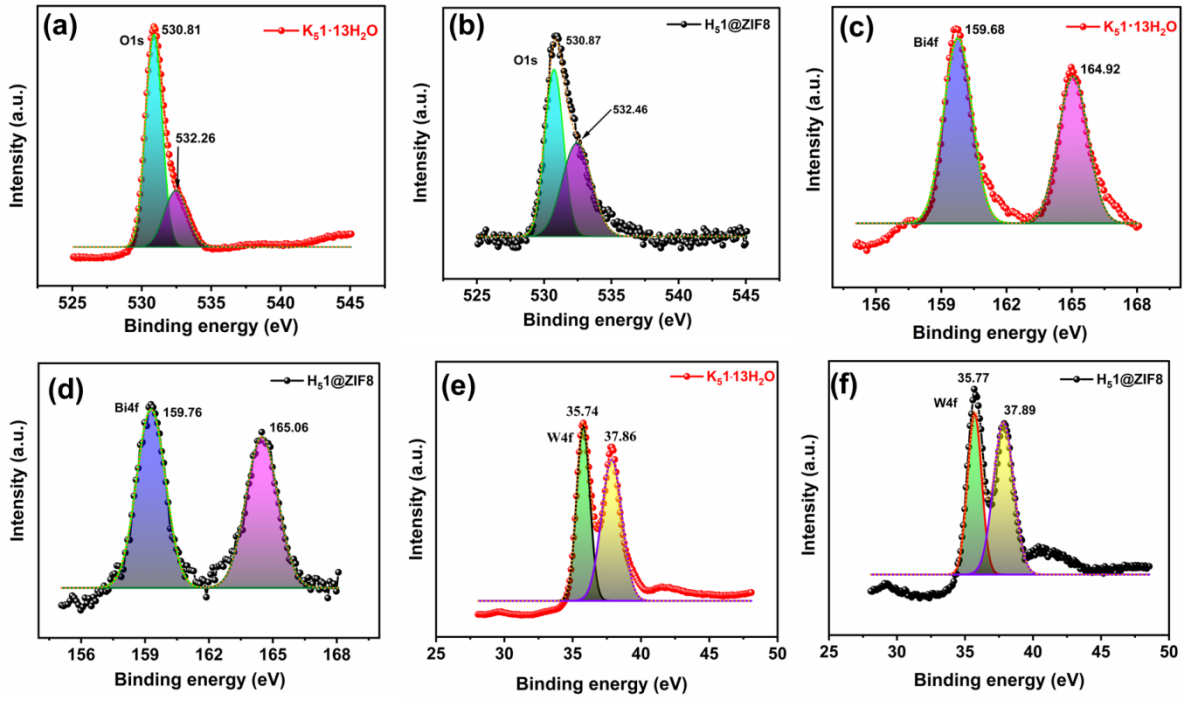

Figure 2.12. Core level XPS spectra: (a-b) O1s, (c-d) Bi4f and (e-f) W4f of $K_5[Bi(H_2O)_2SiW_{11}O_{39}]\cdot 13H_2O$ (**$K_5$1·13H_2O**) and **$H_5$1@ZIF8**.

The XPS analysis of both the compounds are studied with respect to the C1s response at 284.8 eV.[61] The core level XPS profiles of O1s have shown the presence of 2 types of oxygens (Figure 4a,b), attributed for M-O-M (530.81 eV for **$K_5$1·13H_2O** and 530.87 eV for **$H_5$1@ZIF8**) and M-O-H (532.26 eV for **$K_5$1·13H_2O** and 532.46 eV for **$H_5$1@ZIF8**).[62] As shown in Figure 4a,b, the peak area ratio of 532.46 eV : 530.87 eV has been increased after the immobilization / encapsulation. This can tentatively be understood by the logic that the host ZIF-8 is a microporous material and in the present work, the host (ZIF-8) accommodates one POM guest per three cages (vide supra); thus, there could be chances of adsorption of atmospheric water molecules into the vacant cages of ZIF-8 (host) and this adsorbed H_2O, which could be weakly coordinated to the host metal Zn^{2+}, *i.e,* $(H_2O)_{adsorb}$–$(Zn^{2+})_{host}$ could cause this increase in the peak area ratio.[43] Similarly, Figures 4c and 4d show the core level XPS plots of Bi4f for **$K_5$1·13H_2O** and composite, **$H_5$1@ZIF8** respectively; Figures 4e and 4f show the core level XPS plots of W4f for **$K_5$1·13H_2O** and composite, **$H_5$1@ZIF8** respectively and Figures A2.7a and A2.7b (Appendix 2.9) show the core level XPS plots of Si2p for **$K_5$1·13H_2O** and composite, **$H_5$1@ZIF8** respectively. All these confirm the presence of POM cluster inside the ZIF-8 cavities. There is no XPS response of potassium ion (Figure 3f) for the composite **$H_5$1@ZIF8**, which is indicative of the presence of H^+ ions instead of K^+ satisfying the negative charge of the encapsulated POM cluster anion (ZIF-8 is a neutral framework!).

From all these characterizations (discussed above) of functionalized POM compound (**$K_5$1·13H_2O**) and fabricated composite material (**$H_5$1@ZIF8**), it is clearly evident that we have followed an approach of "*molecule to material*". The functionalized Keggin compound **$K_5$1·13H_2O** is the molecule and the resulting composite **$H_5$1@ZIF8** is the material here. The rationale of naming **$H_5$1@ZIF8** a composite is that the spectral features of the host-guest compound **$H_5$1@ZIF8** are quite different from those of the individual host (ZIF-8) and individual guest (**1)** separately.

2.3.3. Electrocatalytic Water Oxidation

2.3.3.1. Electrochemical oxygen evolution reaction by $H_5$1@ZIF8

Oxygen evolution reaction (OER) by water oxidation using **$H_5$1@ZIF8** as an electrocatalyst is assessed in a wide pH window, from acidic pH 4.0 to neutral pH 7.0 through an alkaline pH 13.0. The OER studies have been conducted in a conventional three electrode cell under nitrogen atmosphere and the measured potentials are reported against RHE scale. The cyclic voltammograms (CVs) of aqua-Bi(III) functionalized Keggin **$K_5$1·13H_2O** and the parent

lacunary Keggin $K_8[SiW_{11}O_{39}]\cdot 13H_2O$ (hereafter referred to as SiW_{11}) were recorded homogeneously, whereas CVs of title composite **$H_5$1@ZIF8**, SiW_{11}@ZIF8 and ZIF-8 have been performed in a heterogeneous manner. The glassy carbon electrode (GCE) (blank), coated with conductive acetylene carbon-Nafion mixture, does not have any catalytic response in the operational potential window (Figure 6).

As shown in Figure 6a, the parent lacunary Keggin compound SiW_{11} (without bismuth) does not have any redox response in the anodic potential window. However, bis(aqua)Bi(III)-functionalized Keggin compound **$K_5$1·13H_2O** shows two irreversible hump-like redox responses centered at 1.09 and 1.33V vs RHE (Figure 2.11a), that can be assigned to the two single electron electrochemical oxidation of bismuth, as shown in equations 1-4 (vide supra). This is followed by a prominent anodic current surge at 1.43V vs RHE, indicating the electrocatalytic water oxidation. However, **$K_5$1·13H_2O** undergoes an oxidative degradation within few CV cycles as shown in third CV cycle (Figure 6a) signifying the lack of stable catalytic behavior by the functionalized Keggin itself. At this stage, the significance of fabrication (encapsulation of the same functionalized Keggin anion inside the confined space of a framework material ZIF-8 resulting in the functional composite) begins. Can the composite **$H_5$1@ZIF8** [protected Bi(III)-functionalized Keggin] be able to perform stable electrocatalytic water oxidation at a varied pH range?! The fabricated composite, **$H_5$1@ZIF8** was immersed in the three different operational electrolytes, i.e., aqueous electrolytes with pH 4.0, pH 7.0, and pH 13.0, and respective dried samples were subjected to powder X-ray diffraction analyses. The PXRD patterns of these three solids, obtained by dipping **$H_5$1@ZIF8** in these electrolytes of three different pH values followed by their filtration and drying at room temperature, are essentially identical (see Appendix A2.x, Figure A14), indicating stability of the composite in a widespread pH window. The electrochemical water oxidation studies of the fabricated composite, **$H_5$1@ZIF8** show its promising oxygen evolution reaction (OER) in a widespread pH window. Figures 2.11(b-d) show CV profiles of GCE blank, ZIF-8, and the composite **$H_5$1@ZIF8** at pH 4.0, pH 7.0, and pH 13.0, respectively.

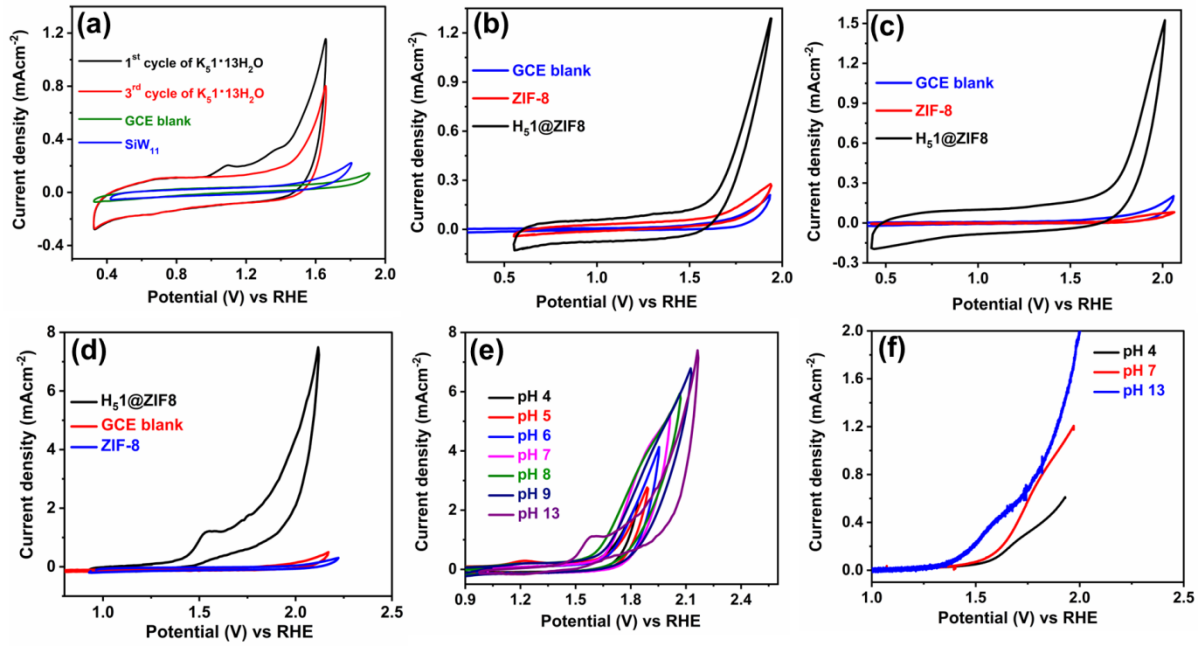

Figure 2.11. Cyclic– and linear–sweep voltammograms recorded in an acidic pH 4.0, neutral pH 7.0 and in an alkaline pH 13.0: (a) CVs of blank GCE, SiW_{11} and **$K_5$1·13H_2O** recorded homogeneously using 1 mmol compounds in neutral pH, 0.1 M potassium phosphate buffer solution; (b-d) CVs of $H_5$1@ZIF8, ZIF-8 and GCE recorded heterogenously at pH 4.0, neutral pH 7.0 and pH 13.0, respectively; (e) CVs of **$H_5$1@ZIF8** recorded in variable pH electrolytes from pH 4 to pH 13.0; (f) linear sweep voltammogram (LSV) of **$H_5$1@ZIF8**, performed heterogenously at pH 4.0, neutral pH 7.0 and pH 13.0. The CVs and LSVs were performed with a scan rate of 100 mVs^{-1} and 5 mVs^{-1}, respectively.

As shown in Figures 2.11(b-d), the GCE blank and ZIF-8, as expected, do not show any redox responses in all three pH values (4.0, 7.0 and 13.0). But in the case of composite, **$H_5$1@ZIF8** a substantial increase in the anodic current is observed after 1.50 V vs RHE for all the pH values (4.0, 7.0 and 13.0). As shown in Figure 2.11(b-d), the CV profile of composite **$H_5$1@ZIF8** at pH 13.0 is quite different from those of the composite at pH 4.0 and pH 7.0. More specifically, at pH 13.0, the CV of the composite displays an oxidative response centered at 1.54 V vs RHE followed by a tiny hump (not properly visible), and then there is a sudden current surge. Thus, at pH 13.0, a differential pulse voltammogram (DPV) analysis was performed on composite **$H_5$1@ZIF8.** This reveals two oxidative responses (see SI, Figure S15), indicating Bi(III) → Bi(IV) and Bi(IV) → Bi(V) electrochemical oxidation, which is consistent with equations 1-4. These two oxidative responses (at pH 13.0) are also seen in the CV plot of a homogeneous solution of aqua-Bi(III) functionalized POM Keggin, **$K_5$1·13H_2O** at neutral pH 7.0 (Figure 2.11a, first cycle), but these diminish in the third cycle. Thus, the heterogeneous CV of the composite **$H_5$1@ZIF8** at pH 13.0 and homogeneous first cycle CV of functionalized Keggin compound **$K_5$1·13H_2O** at pH 7.0 clearly indicate that the functional site of both of these compounds is the bis(aqua)Bi(III) species, which undergoes proton-coupled two-electron transfer electrochemical reactions forming the $\{-Bi^{V}=O\}^{3+}$

species as shown in equations 1-4 (vide supra). The electrochemically generated $\{-Bi^{V}=O\}^{3+}$ species then oxidizes water chemically to molecular oxygen as shown in equation 5. The oxidation of water (eqn 5) by $\{-Bi^{V}=O\}^{3+}$ species may occur *via* equations 6 and 7 in acidic aqueous medium and *via* equations 8 and 9 in alkaline aqueous medium.

$$\{-Bi^{V}=O\}^{3+} + H_2O = \{-Bi^{III}\}^{3+} + O_2 + 2H^{+} + 2e^{-} \quad \text{(eqn 5)}$$

(i) In acidic medium,

$$\{-Bi^{V}=O\}^{3+} + H_2O \rightarrow \{-Bi^{IV}-O-OH\}^{3+} + H^{+} + e^{-} \quad \text{(eqn 6)}$$

$$\{-Bi^{IV}-O-OH\}^{3+} \rightarrow \{Bi^{III}\}^{3+} + O_2 + H^{+} + e^{-} \quad \text{(eqn 7)}$$

(ii) In alkaline medium,

$$\{-Bi^{V}=O\}^{3+} + OH^{-} \rightarrow \{-Bi^{IV}-O-OH\}^{3+} + e^{-} \quad \text{(eqn 8)}$$

$$\{-Bi^{IV}-O-OH\}^{3+} + OH^{-} \rightarrow \{Bi^{III}\}^{3+} + O_2 + H_2O + e^{-} \quad \text{(eqn 9)}$$

Equations 1-4 explains that the present electrocatalytic water oxidation would be favored in an alkaline aqueous solution through the participation of the hydroxyl group in equations 2 and 4 *via* deprotonation. This is reflected in Figure 2.11e that represents the electrocatalytic OER of the composite material **$H_5$1@ZIF8** at different pH values starting from pH 4.0 to pH 9.0 and at pH 13.0. At pH 13.0, we get maximum current surge. Similarly, the linear sweep voltammograms (LSVs) for **$H_5$1@ZIF8** have been recorded at the pH values of 4.0, 7.0 and 13.0 with a sweep rate of 5 mVs^{-1} (Figure 2.11f) and the LSV plots show the same trend as CVs at different pH values, i.e., electrocatalytic water oxidation activity with respect to current density increases from pH 4.0 to pH 7.0 through pH 13.0. In order to prove that the "bis(aqua)Bi(III)-functionality" of the lacunary Keggin cluster is the functional site in the present OER activity, a series of controlled electrochemical experiments have carefully been performed (Figure 7) at three different pH values (pH 4.0, 7.0 and 13.0) using the title composite **$H_5$1@ZIF8**, ZIF-8 (MOF only), GCE blank, ZIF-8 encapsulated lacunary Keggin POM (SiW_{11}@ZIF8; a bismuth free composite).

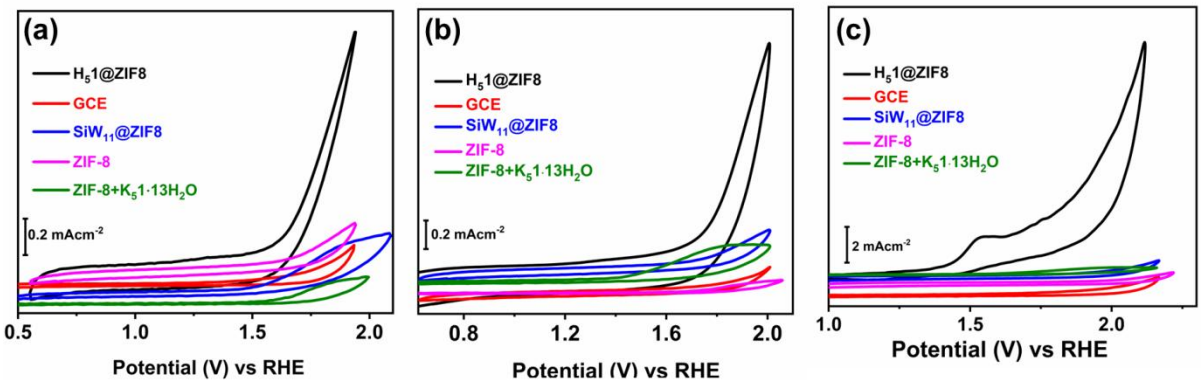

Figure 2.12. Cyclic voltammograms of composite **$H_5$1@ZIF8**, SiW_{11}@ZIF8 (bismuth free composite), ZIF-8, GCE blank and ZIF-8+$K_5$1.13H_2O (physical mixture) at a scan rate of 100 mVs^{-1}: (a) at pH 4.0, (b) at pH 7.0 and (c) at pH 13.0.

We have also prepared a physical mixture of ZIF-8 and **$K_5$1.13H2O** (ZIF-8+$K_5$1·13H_2O) and then it was subjected to perform OER under identical operational conditions to comprehend the true catalytic nature of our composite material and the detailed procedure of preparation of physical mixture is available in the supporting information (see Appendix, section A16). None of the above systems show current surge/OER activity and the CV patterns of all these blank systems are not at all comparable to that of the composite **$H_5$1@ZIF8**, measured at pH 4.0, pH 7.0 and pH 13.0 as shown in Figure 2.12(a-c), respectively. All these blank systems do not contain any bismuth content except the title composite. All these controlled experiments have collectively provided concrete evidence that the bismuth-aqua complex on POM surface in composite **$H_5$1@ZIF8**, not only works as a true molecular electrocatalytic water oxidation catalyst but also functions in a wide pH window (Figure 2.12a-c). The importance of the fabrication/encapsulation of the functionalized POM is evidenced by the fact that the physical mixture does not show any electrocatalytic water oxidation but the fabricated composite does.

2.3.3.2. Electrochemical Stability Check on $H_5$1@ZIF8

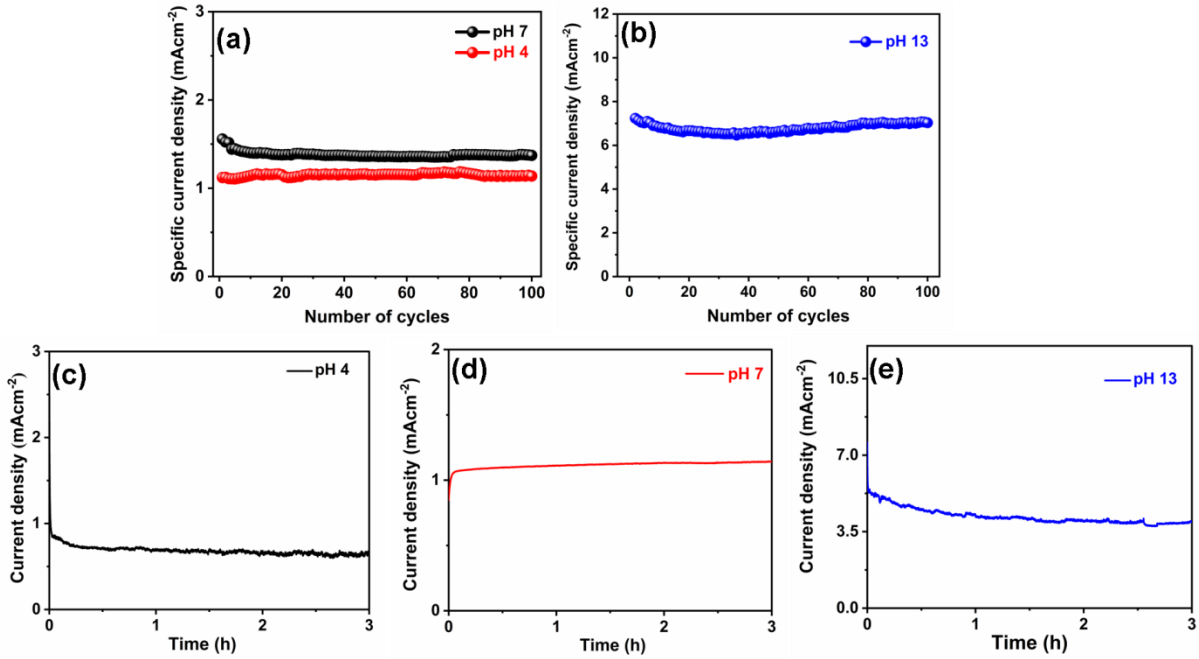

Figure 2.13. (a,b) Derived plots of specific current density *vs* number of CV cycles for **$H_5$1@ZIF8** composite as a heterogeneous catalyst: (a) in an acidic pH 4.0 and in the neutral pH 7.0; (b) in an alkaline pH 13.0. (c,d,e) Chronoamperometric (CA) electrolysis at 1.75 V vs RHE, mediated by **$H_5$1@ZIF8** catalyst-loaded GC electrode: (c) in pH 4.0 (d) pH 7.0 and (e) in an alkaline pH 13.0; (f) CVs of **$H_5$1@ZIF8**, performed in non-aqueous solution on sequential addition of a controlled amount of water, using 0.1 M tetrabutylammonium perchlorate as supporting electrolyte in dry acetonitrile at a scan rate of 100 mVs^{-1}

Stability is an important factor for determining the durability of any catalyst. The sustainability of present OER catalyst (composite) is investigated by (i) continuous CV scans and (ii) chronoamperometric measurements for a long time. The composite, **$H_5$1@ZIF8** has been subjected for multiple CV cycles and has been found to be stable for 100 CV cycles at an acidic pH 4.0, the neutral pH 7.0 as well as in an alkaline pH 13.0 (see Appendix, Figure Axx). This 100-cycles CV-stability in three different pH values (pH 4.0, pH 7.0 and pH 13.0) is shown by the plots of specific current density *vs* number of CV cycles, where the specific current density data points have been collected at the end of the catalytic OER current (Figures 2.13a and 2.3b). The relevant observations emphasize the stability of the present OER catalyst for 100 CV cycles in a wide pH range as shown in Figures 2.13a,b. Furthermore, the chronoamperometric measurements on **$H_5$1@ZIF8** at 1.75 V vs RHE show the stable and steady-state current flow for a period of 3 hours at pH 4.0, neutral pH 7.0 and at pH 13.0 (Figures 2.13c-e). These two experiments have clearly verified that the present composite catalyst **$H_5$1@ZIF8** performs stable OER by electrocatalytic water oxidation under operational conditions.

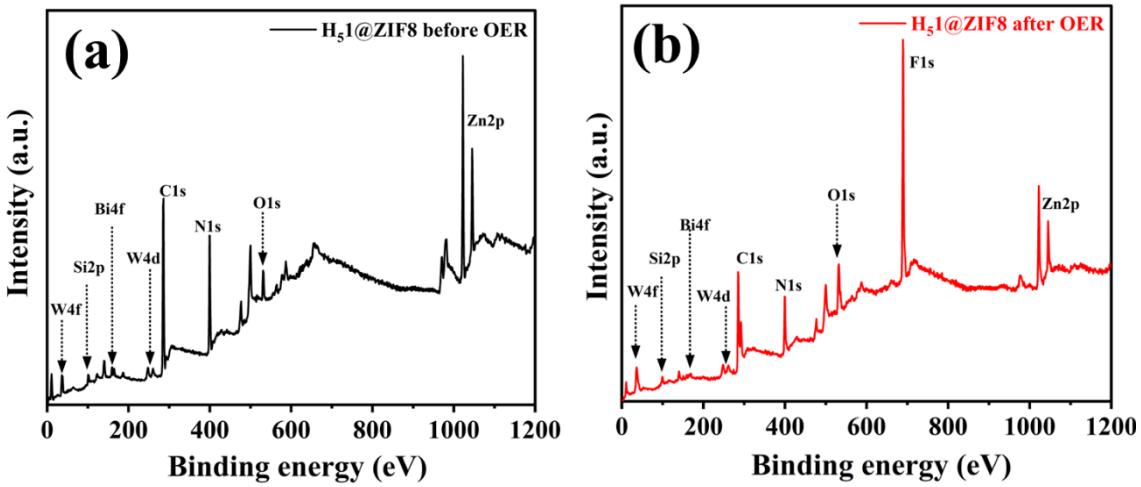

Figure 2.14. XPS survey scans of composite **$H_5$1@ZIF8**: (a) before electrolysis (b) after electrolysis at pH 13. F1s peak is from FTO plate.

It is important to check the structural integrity of the catalyst, before and after the OER activity. To do this, we have performed the following experiments after 100 CV cycles: (i) inductively coupled plasma (ICP) optical emission spectroscopy analysis for a residual electrolyte after electrolysis (see Appendix, Figure A2.11); (ii) electronic spectral analysis of the residual electrolytes (see Appendix, Figure A2.12). We have also examined the chronoamperometric (CA) electrode material of **$H_5$1@ZIF8** (after electrolysis at pH 13) by X-ray photoelectron spectroscopic (XPS) study (see Appendix, Figure A2.13 and 14). We performed FTIR analyses (see Appendix, Figure A2.15) and Raman spectral studies (see Appendix, Figure A2.16) on the CA films of **$H_5$1@ZIF8** after electrolysis at three different pH values (4.0, 7.0 and 13.0). The Field emission scanning electron microscopy energy dispersive X-ray (FESEM-EDX) elemental mappings (see Appendix, Figure A2.19-A2.22) of the surfaces of the working electrodes after CPE at three different pH values (4.0, 7.0 and 13.0) were performed. All these controlled experiments before and after electrolysis convincingly establish the structural integrity of the title catalyst **$H_5$1@ZIF8** during electrolysis and that no leaching of the catalyst has been taken place from the electrode surface during the electrocatalysis.

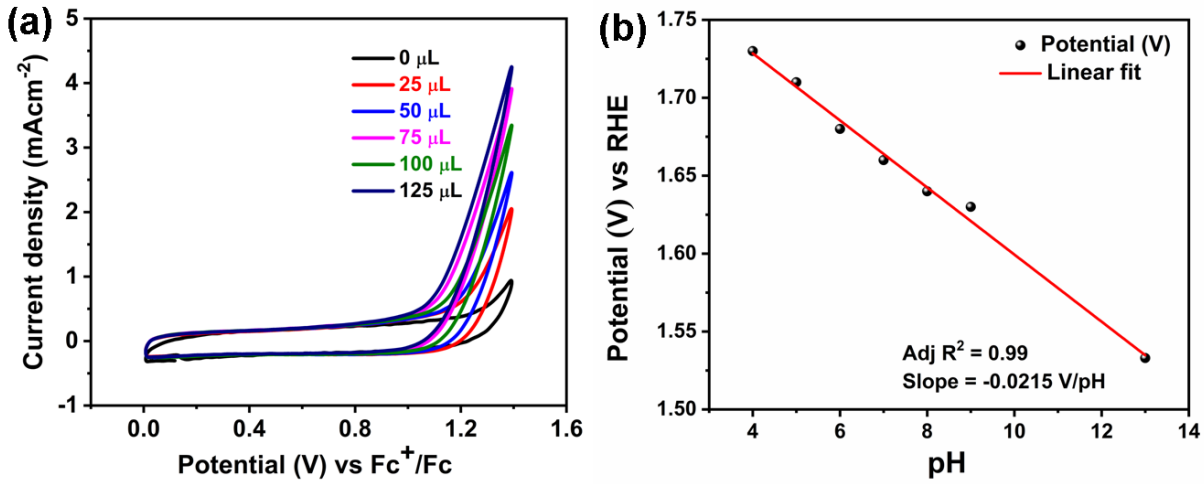

Figure 2.15. (a) CVs of **$H_5$1@ZIF8**, performed in non-aqueous solution on sequential addition of a controlled amount of water, using 0.1 M tetrabutylammonium perchlorate as supporting electrolyte in dry acetonitrile at a scan rate of 100 mVs^{-1}. (b) Derived plot of potential values (required to reach a specific current density of 0.5 $mAcm^{-2}$) *versus* operative pH values, obtained from variable pH CV profiles of the title catalyst **$H_5$1@ZIF8**.

In order to prove that this oxygen evolution reaction (OER) is the result of electrocatalytic water oxidation, catalyzed by **$H_5$1@ZIF8**, the CV features of OER electrode has been checked in a non-aqueous medium while adding a controlled amount of water sequentially. The sequential addition of water results in a chronological enhancement in the anodic catalytic current (Figure 2.15a) suggesting the OER by water oxidation (not by proton reduction). To understand the insights about oxygen evolution reaction mechanism, a plot has been constructed between the potential required to reach a specific current density of 0.5 $mAcm^{-2}$ and the operative pH values (Figure 2.15b). A linear dependence with the slope value of -21.5 mV/pH is observed from the derived plot. The concerned slope value has shown the involvement of ($1H^+$–$2e^-$) proton coupled-electron transfer (PCET) step in the electrocatalytic molecular oxygen evolution reaction, catalyzed by the **$H_5$1@ZIF8** composite.

2.3.3.3. Kinetic study of $H_5$1@ZIF8 on a wide pH range

2.3.3.3.1. Tafel analysis for determining overpotential of $H_5$1@ZIF8

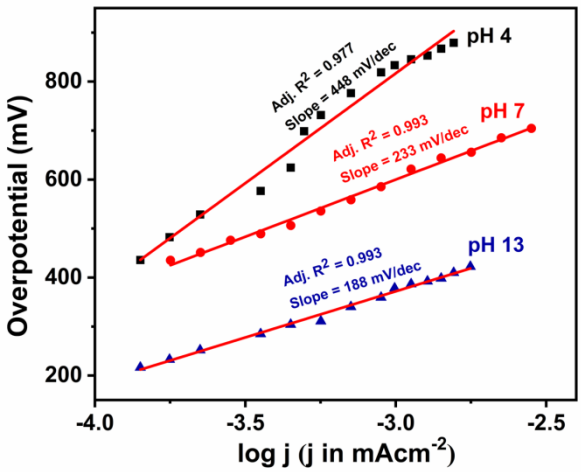

Figure 2.16. Linear iR-corrected Tafel plots for **$H_5$1@ZIF8**, recorded at the catalytic OER region in acidic pH 4.0, neutral pH 7.0 and in an alkaline pH 13.0.

The reaction kinetics has been investigated in terms of slopes and overpotential values of Tafel plots. Linear Tafel plots in the catalytic OER region are constructed for **$H_5$1@ZIF8** in respective pH media under study-state mass flow (Figure 2.16, detailed procedure has been given in the section see Appendix, Section A2.15). The Tafel slope values 448 mV/dec, 233 mV/dec and 188 mV/dec have been obtained at pH 4.0, pH 7.0 and pH 13.0 respectively for **$H_5$1@ZIF8** which show that better OER activity occurs when we move from acidic pH to neutral pH through alkaline pH. The catalyst **$H_5$1@ZIF8** consumes overpotentials (η) of 830.1 mV, 585.21 mV and 375 mV to reach current density (j) of 1 $mAcm^{-2}$ at acidic pH 4.0, neutral pH 7.0 and in alkaline pH 13, respectively. The trend of decreasing overpotential values with increase in pH values clearly indicate that the present composite is an efficient electrocatalyst at an alkaline pH, justifying equations 1-5. The obtained overpotential values have been compared with those of some of the relevant reported ZIF-8 based composite OER catalysts (see Appendix, Table A2.1). This comparison clearly shows an excellent oxygen evolution reaction (OER) activity by **$H_5$1@ZIF8** (present work) at an alkaline pH 13.0.

2.3.3.3.2. Electrochemical impedance spectroscopy of $H_5$1@ZIF8

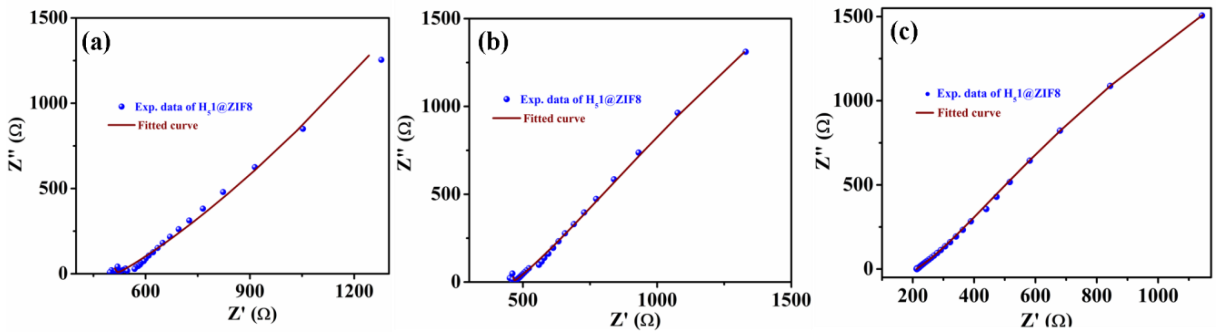

Figure 2.17. Nyquist plots of impedence spectra for the compound **$H_5$1@ZIF8** modified glassy carbon electrode (GCE) at (a) pH 4.0, (b) pH 7.0 and (c) pH 13.0.

We have also performed electrochemical impedance spectroscopy (EIS) for **$H_5$1@ZIF8** modified GCE in the catalytic OER region for all the three pH values (acidic pH 4.0, neutral pH 7.0 and at alkaline pH 13.0); the relevant procedure has been given in Section Axx, in see Appendix. For an electrocatalyst, the more is the resistance value the less is the overall catalytic activity. The charge-transfer resistance R_1 (R_{ct}) values of 515, 463.9 and 210 ohms, obtained from Nyquist plots of the EIS data at acidic pH 4, neutral pH and alkaline pH 13, respectively are thus consistent with the observed trend, *i.e.*, the performance of the catalyst follows the order: pH 13 > pH 7 > pH 4. The fitting of the equivalent circuit in the present EIS study is in accordance with our earlier relevant proton conductivity work.[66]

2.3.3.3.3. Faradaic efficiency of $H_5$1@ZIF8

The Faradaic efficiency can be calculated by bulk electrolysis where a constant current was applied for a period of time using a two-electrode cell.

The Faradaic efficiency of **$H_5$1@ZIF8**, in the studied pH window, has been verified in a chronopotentiometric electrolysis mode using our reported procedure.[17] The Faradaic efficiency of **$H_5$1@ZIF8** has been found to be 95.7%, 87.6% and 79.8% at acidic pH 4.0, pH 7.0 and alkaline pH 13.0, respectively (see Appendix, Section A2.16). The Faradaic efficiency values decrease with increase in the pH values of electrochemical reaction mixtures. The evolved gas in the bulk electrolysis of **$H_5$1@ZIF8** has been identified as oxygen by gas chromatography (see Appendix, Section A2.18). Overall, the acquired kinetic parameters have demonstrated a consistent and predominant oxygen evolution activity of the title composite **$H_5$1@ZIF8** in a wide pH spectrum.

2.3.3.3.4. Turnover frequency calculation of $H_5$1@ZIF8

The turnover frequency (TOF) values of 0.93 s^{-1}, 5.90 s^{-1} and 1.24 s^{-1} for composite **$H_5$1@ZIF8** have been obtained for pH 4.0, pH 7.0 and pH 13.0, respectively (see Appendix, Section A2.17). A comparison table for thus obtained TOF values to those of a series of OER catalysts has been provided in the Appendix, Table A2.2. The trend of increasing TOF values (from 0.93 s^{-1} to 5.90 s^{-1}) with increase in pH values (from pH 4.0 to pH 7.0) is consistent with the trend of decreasing over potential values (830 mV to 585 mV) with increase in pH values from pH 4.0 to pH 7.0. But at pH 13.0, TOF value unexpectedly decreases. This may be due to the partial hydrolysis of labile $\{\text{-Bi}(H_2O)_2\}^{3+}$ moiety (active site for OER in the present study) at harsh alkaline condition of pH 13.0.

2.4. CONCLUSIONS

The present contribution has potential to open a gateway in the employment of the post-transition metal ion in a confined system for sustainable electrochemical water oxidation. More particularly, this report brings up a fascinating way of utilizing functionalized polyoxometalate cluster containing compound $\mathbf{K_5 1 \cdot 13 H_2 O}$ to fabricate with ZIF-8 resulting in a host-guest composite material $\mathbf{H_5 1@ZIF8}$ in an economical way. The title composite performs excellent electrocatalytic water oxidation in a broader range of pH. The novelty of this work in the perspective of 'materials chemistry' lies in the fact that a polyoxometalate compound, which cannot be imagined to function in an alkaline aqueous pH medium, can be made possible to electro-catalyze water oxidation in a harsh alkaline aqueous solution of pH 13.0, when it is enclosed in the well-defined cages of a framework material. The tile composite exhibits the OER turnover frequency (TOF) of 5.90 s^{-1} at the neutral pH 7.0 with 88% Faradaic efficiency; this will have an immense impact on the contemporary materials chemistry as far as functional materials are concerned.

2.5. REFERENCES

(1) Formal, F. L.; Bourée, W. S.; Prévot, M. S.; Sivula, K. Challenges towards economic fuel generation from renewable electricity: the need for efficient electro-catalysis. *Chimia.* **2015**, *69*, 789–798.

(2) Roger, I.; Shipman, M. A.; Symes, M. D. Earth-abundant catalysts for electrochemical and photoelectrochemical water splitting. *Nat. Rev. Chem.* **2017**, *3*, 1-11.

(3) Matheu, R, Garrido-Barros, P.; Gil-Sepulcre, M.; Ertem, M. Z.; Sala, X.; Gimbert-Suriñach, C.; Llobet, A. The development of molecular water oxidation catalysts, *Nat. Rev. Chem.* **2019**, *3*, 331–341.

(4) Doyle, R. L.; Lyons, M. E. G. The oxygen evolution reaction: mechanistic concepts and catalyst design. *Photoelectrochemical Solar Fuel Production*, **2016**, 41-104.

(5) Shi, Q.; Zhu, C.; Dan, D.; Lin, Y. Robust noble metal-based electrocatalysts for oxygen evolution reaction. *Chem. Soc. Rev.* **2019**, *48*, 3181-3192.

(6) Du, J.; Li, F.; Sun, L. Metal–organic frameworks and their derivatives as electrocatalysts for the oxygen evolution reaction. *Chem. Soc. Rev.* **2021**, *50*, 2663-2695.

(7) Wang, Z.; Lu, Y.; Yan, Y.; Larissa, T. Y. P.; Zhang, X.; Wuu, D.; Zhang, H.; Yang, Y.; Wang, X. Core-shell carbon materials derived from metal-organic frameworks as an efficient oxygen bifunctional electrocatalyst. *Nano Energy* **2016**, *30*, 368−378.

(8) Gao, D.; Trentin, I.; Schwiedrzik, L.; González, L.; Streb, C. The reactivity and stability of polyoxometalate water oxidation electrocatalysts. *Molecules* **2020**, *25*, 157.

(9) Lauinger, S. M.; Sumliner, J. M.; Yin, Q.; Xu, Z.; Liang, G.; Glass, E. N.; Lian, T.; Hill, C. L. High stability of immobilized polyoxometalates on TiO_2 nanoparticles and nanoporous films for robust, light-induced water oxidation. *Chem. Mater.* **2015**, *27*, 5886−5891.

(10) Soriano-López, J.; Musaev, D. G.; Hill, C. L.; Galán-Mascarós, J. R.; Carbó, J. J.; Poblet, J. M. Tetracobalt-polyoxometalate catalysts for water oxidation: key mechanistic details. *J. Catal.* **2017**, *350*, 56–63.

(11) Luo, W.; Hu, J.; Diao, H.; Schwarz, B.; Streb, C.; Song, Y.-F. Robust polyoxometalate/nickel foam composite electrodes for sustained electrochemical oxygen evolution at high pH. *Angew. Chem. Int. Ed.* **2017**, *56*, 4941–4944.

(12) Li, N.; Liu, J.; Dong, B-X.; Lan, Y-Q. Polyoxometalate-based compounds for photo- and electrocatalytic applications. *Angew. Chem. Int. Ed.* **2020**, *59*, 20779 – 20793.
(13) Yin, Q.; Hill, C. L. Passing the acid test. *Nat. Chem.* **2018**, *10*, 6–7.
(14) Reier, T.; Nong, H. N.; Teschner, D.; Schlögl, R.; Strasser, P. Electrocatalytic oxygen evolution reaction in acidic environments – reaction mechanisms and catalysts. *Adv. Energy Mater.* **2016**, 1601275.
(15) Blasco-Ahicart, M.; Soriano-López, J.; Carbó, J. J.; Poblet, M. J.; Galan-Mascaros J. R. Polyoxometalate electrocatalysts based on earth-abundant metals for efficient water oxidation in acidic media. *Nat. Chem.* **2018**, *10*, 24–30.
(16) Lauinger, S. M., Piercy, B. D.; Li, W.; Yin, Q.; Collins-Wildman, D. L.; Glass, E. N.; Losego, M. D.; Wang, D.; Geletii, Y. V.; Hill, C. L. Stabilization of polyoxometalate water oxidation catalysts on hematite by atomic layer deposition. *ACS Appl. Mater. Interfaces* **2017**, *9*, 35048−35056.
(17) Mukhopadhyay, S.; Debgupta, J.; Singh, C.; Kar, A.; Das, S. K. A Keggin polyoxometalate shows water oxidation activity at neutral pH: POM@ZIF-8, an efficient and robust electrocatalyst. *Angew. Chem. Int. Ed.* **2018**, *57*, 1918–1923.
(18) Singh, C.; Mukhopadhyay, S.; Das, S. K. Polyoxometalate-supported Bis(2,2′-bipyridine)mono(aqua)nickel(II) coordination complex: an efficient electrocatalyst for water oxidation. *Inorg. Chem.* **2018**, *57*, 6479-6490.
(19) Bhat, S. S. M.; Jang, H. W.; Recent advances in bismuth based nanomaterials for photoelectrochemical water splitting. *ChemSusChem* **2017**, *10*, 3001-3018.
(20) Bae, S.; Kim, H.; Jeon, D.; Ryu, J. Catalytic multilayers for efficient solar water oxidation through catalyst loading and surface-state passivation of $BiVO_4$ photoanodes. *ACS Appl. Mater. Interfaces*, **2019**, *11*, 7990−7999.
(21) Govindaraju, G. V.; Morbec, J. M.; Galli, G. A.; Choi, K.-S. Experimental and computational investigation of lanthanide ion doping on $BiVO_4$ photoanodes for solar water splitting, *J. Phys. Chem. C.* **2018**, *122*, 19416-19424.
(22) Lee, D.; Kvit, A.; Choi, K.-S. Enabling solar water oxidation by $BiVO_4$ photoanodes in basic media, *Chem. Mater.* **2018**, *30*, 4704-4712.
(23) Lee, D. K.; Choi, K.-S. Enhancing long-term photostability of $BiVO_4$ photoanodes for solar water splitting by tuning electrolyte composition, *Nat. Energy* **2018**, *3*, 53-60.
(24) Kim, T. W.; Ping, Y.; Galli, G. A.; Choi, K.-S. Simultaneous enhancements in photon absorption and charge transport of bismuth vanadate photoanodes for solar water splitting, *Nat. Commun.* **2015**, *6*, 8769.
(25) Yang, J.; Jiang, P.; Yue, M.; Yang, D.; Cong, R.; Gao, W. $Bi_2Ga_4O_9$: an undoped single-phase photocatalyst for overall water splitting under visible light, *J. Catal.* **2017**, *345*, 236-244.
(26) Sardar, K.; Ball, S. C.; Sharman, J. D. B.; Thompsett, D.; Fisher, J. M.; Smith, R. A. P.; Biswas, P. K.; Lees, M. R.; Kashtiban, R. J.; Sloan, J.; Walton, R. I. Bismuth iridium oxide oxygen evolution catalyst from hydrothermal synthesis. *Chem. Mater.* **2012**, *24*, 4192–4200.
(27) Bae, S.; Jang, J.-E.; Lee, H.-W.; Ryu, J. Tailored assembly of molecular water oxidation catalysts on photoelectrodes for artificial photosynthesis. *Eur. J. Inorg. Chem.* **2019**, 2040-2057.
(28) Gao, M. R.; Yu, S. H.; Yuan, J.; Zhang, W.; Antonietti, M. Poly (ionic liquid)-mediated morphogenesis of bismuth sulfide with a tunable band gap and enhanced electrocatalytic properties. *Angew. Chem., Int. Ed.* **2016**, *55*, 12812–12816.
(29) Graner, F.; Sillen, L. G. Hydrolysis of Bi^{3+}. Oxygen bridging—a new type of ionic equilibrium. *Nature* **1947**, *160*, 715-716.
(30) Hanaya, T.; Suzuki, K.; Sato, R.; Yamaguchi, K.; Mizuno, N. Creation of bismuth–tungsten oxide nanoclusters using lacunary polyoxometalates. *Dalton Trans.* **2017**, *46*, 7384-7387.
(31) Bösing, M.; Nöh, A.; Loose, I.; Krebs, B. Highly efficient catalysts in directed oxygen-transfer processes: synthesis, structures of novel manganese-containing heteropolyanions, and applications in regioselective epoxidation of dienes with hydrogen peroxide. *J. Am. Chem. Soc.* **1998**, *120*, 7252–7259.
(32) Loose, I.; Droste, E.; Bösing, M.; Pohlmann, H.; Dickman, M. H.; Rosu, C.; Pope, M. T.; Krebs, B. Heteropolymetalate clusters of the subvalent main group elements Bi(III) and Sb(III). *Inorg. Chem.* **1999**, *38*, 2688–2694.

(33) Von Allmen, K. D.; Grundmann, H.; Linden, A.; Patzke, G. R. Synthesis and characterization of 0D−3D copper-containing tungstobismuthates obtained from the lacunary precursor $Na_9[B\text{-}\alpha BiW_9O_{33}]$. *Inorg. Chem.* **2017**, *56*, 327–335.

(34) Rosu, C.; Rasu, D.; Weakley, T. J. R. X-ray structure of dodecasodium tricopper(II)bis[nonatungstabismuthate(III)] hydrate, a polyoxometalate salt containing α-B-BiW_9O_{33} units. *J. Chem. Crystallogr.* **2003**, *33*, 751–755.

(35) McGlone, T.; Streb, C.; Busquets-Fité, M.; Yan, J.; Gabb, D.; Long, D. L.; Cronin, L. Silver linked polyoxometalate open frameworks (Ag-POMOFs) for the directed fabrication of silver nanomaterials. *Cryst. Growth Des.* **2011**, *11*, 2471–2478.

(36) Bi, L. H.; Hou, G. F.; Bao, Y. Y.; Li, B.; Wu, L. X.; Gao, Z. M.; McCormac, T.; Mal, S. S.; Dickman, M. H.; Kortz, U. Syntheses and crystal structures of dmso-coordinated tungstoantimonates(III) and -bismuthates(III). *Eur. J. Inorg. Chem.* **2009**, *70*, 5259–5266.

(37) Evangelisti, F.; Car, P.-E.; Blacque, O.; Patzke, G. R. Photocatalytic water oxidation with cobalt-containing tungstobismutates: tuning the metal core. *Catal. Sci. Technol.* **2013**, *3*, 3117-3129.

(38) Tucher, J.; Nye, L. C.; Ivanovic-Burmazovic, I.; Notarnicola, A.; Streb, C. Chemical and photochemical functionality of the first molecular bismuth vanadium oxide. *Chem. - A Eur. J.* **2012**, *18*, 10949–10953.

(39) Mukhacheva, A. A.; Adonin, S. A.; Abramov, P. A.; Sokolov, M. N. Different behavior of Bi^{3+} to $[XW_{12}O_{40}]^{n-}$ (X = P, Si; *n* = 3, 4). *Polyhedron* **2018**, *141*, 393-397.

(40) Wihadi, M. N. K.; Hayashi, A.; Ichihashi, K.; Ota, H.; Nishihara, S.; Inoue, K.; Tsunoji, N.; Sano T.; Sadakane, M. A sandwich complex of bismuth cation and mono-lacunary α-Keggin-type phosphotungstate: preparation and structural characterization. *Eur. J. Inorg. Chem.* **2019**, *2019, 4*, 357-362.

(41) Amanchi, S. R.; Khenkin, A. M.; Diskin-Posner, Y.; Neumann, R. Bismuth-substituted "sandwich" type polyoxometalate catalyst for activation of peroxide: umpolung of the peroxo intermediate and change of chemoselectivity. *ACS Catal.* **2015**, *5*, 3336–3341.

(42) Abdelkader-Fernández, V. K.; Fernandes, D. M.; Balula, S. S.; Cunha-Silva, L.; Freire, C. Advanced framework-modified POM@ZIF-67 nanocomposites as enhanced oxygen evolution reaction electrocatalysts. *J. Mater. Chem. A*, **2020**, *8*, 13509– 13521.

(43) Abdelkader-Fernandez, V. K.; Fernandes, D. M.; Balula, S. S.; Cunha-Silva, L.; Freire, C. Oxygen evolution reaction electrocatalytic improvement in POM@ZIF nanocomposites: A bidirectional synergistic effect. *ACS Appl. Energy Mater.* **2020**, *3*, 2925-2934.

(44) Glomb, S.; Woschko, D.; Makhloufi. G.; Janiak, C. Metal–organic frameworks with internal urea-functionalized dicarboxylate linkers for SO_2 and NH_3 adsorption. *ACS Appl. Mater. Interfaces* **2017**, *9*, 37419–37434.

(45) Zhang. L.; Mi, T.; Ziaee, M.A.; Liang, L.; Wang, R. Hollow POM@MOF hybrid-derived porous $Co_3O_4/CoMoO_4$ nanocages for enhanced electrocatalytic water oxidation. *J. Mater. Chem. A*, **2018**, *6*, 1639–1647.

(46) Li, Q.Y.; Zhang,; Xu, Y.X.; Li, Q.; Xue, H.; Pang, H. Smart yolk/shell ZIF-67@POM hybrids as efficient electrocatalysts for the oxygen evolution reaction. *ACS Sustain. Chem. Eng*. **2019**, *7*, 5027−5033.

(47) Wang, Y.; Wang, Y.; Zhang, L.; Liu, C-S.; Pang, H. Core–shell-type ZIF-8@ZIF-67@POM hybrids as efficient electrocatalysts for the oxygen evolution reaction**.** *Inorg. Chem. Front*., **2019**, *6*, 2514–2520.

(48) Sun, J.; Abednatanzi, S.; Voort, P. V.; Liu, Y-Y.; Leus, K. POM@MOF hybrids: synthesis and applications. *Catalysts* **2020**, *10*, 578.

(49) Wang, Z.-H.; Wang, X.-F.; Tan, Z.; Song, X.-Z. Polyoxometalate/metal–organic framework hybrids and their derivatives for hydrogen and oxygen evolution electrocatalysis. *Mater. Today Energy* 19, **2021**, *19*, 100618.

(50) Li, N.; Liu, J.; Dong, B-X.; Lan, Y-Q. Polyoxometalate-based compounds for photo- and electrocatalytic applications**.** *Angew. Chem. Int. Ed*. **2020**, *59*, 20779 – 20793.

(51) Li, Y.; Zhou, L.; Guo, S. Noble metal-free electrocatalytic materials for water splitting in alkaline electrolyte. *EnergyChem.* **2021**, *3*, 100053.

(52) Hou, J.; Yang, M.; Ke, C.; Wei, G.; Priest, C.; Qiao, Z.; Wu, G.; Zhang, J. Platinum-group-metal catalysts for proton exchange membrane fuel cells: From catalyst design to electrode structure optimization. *Energy Chem.*, **2020**, *2*, 100023.

(53) Zheng, S.; Li, Q.; Xue, H.; Pang, H.; Xu, Q. A highly alkaline-stable metal oxide@metal–organic framework composite for high-performance electrochemical energy storage. *Natl. Sci. Rev.*, **2020**, *7*, 305–314.

(54) Rao, A. S.; Baruah, U.; Das, S. K. Stabilization of $[BiCl_6]^{3-}$ and $[Bi_2Cl_{10}]^{4-}$ with various organic precursors as cations leading to inorganic–organic supramolecular adducts: syntheses, crystal structures and properties of $[C_5H_7N_2]_3[BiCl_6]$, $[C_5H_7N_2][C_5H_8N_2][BiCl_6]$ and $[C_{10}H_{10}N_2]_2[Bi_2Cl_{10}]$. *Inorg. Chimica Acta.* **2011**, *372*, 206–212.

(55) Hanft, A.; Radacki, K.; Lichtenberg, P-D. C. Cationic bismuth aminotroponiminates: charge controls redox properties. *Chem. Eur. J.* **2021**, *27*, 6230–6239

(56) Botar, B.; Yamase, T.; Ishikawa, E. A highly nuclear vanadium-containing tungstobismutate: synthesis and crystal structure of $K_{11}H[(BiW_9O_{33)3}Bi_6(OH)_3(H_2O)_3V_4O_{10}]\cdot 25H_2O$. *Inorg. Chem. Commun.*, **2000**, *3*, 579–584.

(57) Zhang, Z.; Sadakane, M.; Murayama, T.; Izumi, S.; Yasuda, N.; Sakaguchi, N.; Ueda, W. Tetrahedral connection of ε-Keggin-type polyoxometalates to form an all-inorganic octahedral molecular sieve with an intrinsic 3D pore system. *Inorg. Chem.* **2014**, *53*, 903–911.

(58) Manna, P.; Szücs, D.; Csupász, T.; Fekete, A.; Szikra, D.; Lin, Z.; Gáspár, A.; Bhattacharya, S.; Zulaica, A.; Tóth, I.; Kortz, U. Shape and size tuning of Bi^{III}-centered polyoxopalladates: High resolution ^{209}Bi NMR and $^{205/206}Bi$ radiolabelling for potential pharmaceutical applications. *Inorg. Chem.* **2020**, 59, 16769– 16782.

(59) O'Keeffe, M.; Brese, N. E. Atom sizes and bond lengths in molecules and crystals. *J. Am. Chem. Soc.* **1991**, *113*, 3226-3229.

(60) Park, K.S.; Ni, Z.; Côté, A. P.; Choi, J. Y.; Haung, R.; Uribe-Romo, F. J. Chae, H. K.; ÓKeeffe, M.; Yaghi, O. M. Exceptional chemical and thermal stability of zeolitic imidazolate frameworks. *PNAS*, **2006**, *103*, 10186–10191.

(61) Fang, D.; He, F.; Xie, J.; Xue, L. Calibration of binding energy positions with C1s for XPS results. *J. Wuhan Univ. Technol.-Mat. Sci. Edit.* **2020**, *35*, 711–718.

(62) Barr, T. L. An ESCA study of the termination of the passivation of elemental metals. *J. Phys. Chem.* **1978**, *82*, 1801-1810.

(63) He, F.; He, Z.; Xie, J.; Li, Y. IR and Raman spectra properties of Bi_2O_3-ZnO-B_2O_3-BaO quaternary glass system. *Am. J. Analyt. Chem.* **2014**, *5*, 1142-1150.

(64) Tanaka, S.; Fujita, K.; Miyake, Y.; Miyamoto, M.; Hasegawa, Y.; Makino, T.; Perre, S. V.; Remi, J. C. S.; Assche, T. V.; Baron, G. V.; Denayer, J. F. M. Adsorption and diffusion phenomena in crystal size engineered ZIF-8 MOF. *J. Phys. Chem. C* **2015**, *119*, 28430-28439.

(65) Basu, O.; Mukhopadhyay, S.; De, A.; Das, A.; Das, S. K. Tuning the electrochemical and catalytic ORR performance of C_{60} by its encapsulation in ZIF-8: a solid-state analogue of dilute fullerene solution. *Mater. Chem. Front.*, **2021**, *5*, 7654–7665.

(66) Mulkapuri, S.; Kurapati, S. K.; Mukhopadhyay, S.; Das, S. K. A fully reduced $\{V^{IV}_{18}O_{42}\}$ host and VO_4^{3-}, Cl^- as guest anions: synthesis, characterization and proton conductivity. *New J. Chem.*, **2019**, *43*, 17670-17679.

(67) Ginsberg, A. P. Inorganic syntheses. *John Wiley & Sons, Inc*. **1990**, *Vol. 27*, Pg. No. 89-90. *ISBN 0-471-50976-0*.

Chapter 3

Hydroxylated Polyoxometalate with Cu(II)- and Cu(I)-Aqua Complexes: A Bifunctional Catalyst for Electrocatalytic Water Splitting

OVERVIEW

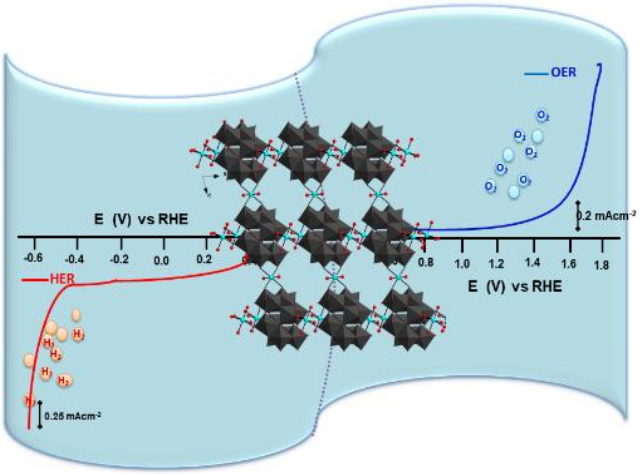

A sole inorganic framework material $[Li(H_2O)_4][\{Cu^{I}(H_2O)_{1.5}\}\ \{Cu^{II}(H_2O)_3\}_2\ \{W^{VI}_{12}O_{36}(OH)_6\}]\cdot N_2\cdot H_2S\cdot 3H_2O$ (**$LiCu_3$*para-D***), consisting of a hydroxylated polyoxometalate (POM) anion, $\{W^{VI}_{12}O_{36}(OH)_6\}^{6-}$, a mixed-valent Cu(II)– and Cu(I)–aqua cationic complex species, $[\{Cu^{I}(H_2O)_{1.5}\}\{Cu^{II}(H_2O)_3\}_2]^{5+}$, a Li(I)-aqua complex cation and three solvent molecules, has been synthesized and structurally characterized. During its synthesis, the POM cluster anion gets functionalized with six hydroxyl groups, i.e., six W^{VI}–OH groups per cluster unit. **$LiCu_3$*para-D*** functions as a bifunctional electrocatalyst exhibiting oxygen evolution reaction (OER) by water oxidation and hydrogen evolution reaction (HER) by water reduction at the neutral pH. Diverse electrochemical controlled experiments have been performed to conclude that the title POM based material functions as a true bifunctional catalyst for electrocatalytic HER as well as OER at the neutral pH without catalyst reconstruction.

3.1. INTRODUCTION

In the last few decades, the exponential increase in the use of fossil fuels has put forth a high demand for researchers across the globe for alternative sustainable energy sources that serve the very same purposes as those of non-renewable resources. Electrochemical water splitting (ECWS) to produce molecular H_2 and O_2 is one of the sustainable ways to mitigate the

growing energy demands.[1-3] The half-cell reactions, namely oxygen evolution reaction (OER) by water oxidation, $2H_2O = O_2 + 4H^+ + 4e^-$ and hydrogen evolution reaction (HER) by water reduction, $2H_2O + 2e^- = H_2 + 2OH^-$ are important in the context of renewable energy but these are kinetically sluggish processes. Devising a sustainable electrocatalyst that exhibits both OER and HER is the most challenging task in the area of clean energy research. Contemporary researchers are looking for promising OER and HER catalysts that can minimize the net overpotential (η) of the electrochemical cell, making the OER and HER half-cell reactions efficient.

The *state-of-the-art* catalysts, for example, Pt for HER, RuO_2, and/or IrO_2 for OER, are widely employed for ECWS.[4-6] Due to their limited resources and high-cost production, these are considered as less economical water-splitting (WS) catalysts for practical applications. Thus, it is important to develop non-precious and versatile electrocatalysts that can perform economical water splitting (WS).[7-12] Most of the reported non-precious WS photo/electrocatalysts including polyoxometalates (POMs) can show high OER or/and HER activity in the selective electrolytes (function either in alkaline or in an acidic medium),[13-18] but the earth-abundant bifunctional WS electrocatalysts that work at neutral pH are under-explored.

Generally, POMs exhibit rapid multi-electron redox transformations (including reversible electron transfer) maintaining structural integrity and thereby, many POMs can exhibit excellent electrocatalytic activity.[16-25] Numerous POM-based systems including redox active POM cluster containing compounds, metal organic framework (MOF) encapsulated POM compounds (POM@MOFs), POMOF (POM based metal organic framework) containing compounds, POM@Substrates (POM compounds deposited onto conductive substrates) and POM supported transition metal-aqua coordination complexes, have been explored extensively as heterogeneous catalysts exhibiting photo- and electrocatalytic-water splitting and -CO_2 reduction reactions, as documented in recent review articles.[22-24] In 2016, Hill and co-workers reported photocatalytic H_2 evolution using copper-containing POM catalyst,[25] and on the same line in 2017, the Patzke group claimed the photocatalytic H_2 and O_2 evolution using Cu-POM system as a catalyst.[26] In this regard, copper-based catalysts have drawn our special attention because copper is an abundant element but less explored as an electrocatalyst for water oxidation (WO).[27-29] In 2018, Ding and co-workers reported homogeneous electrocatalytic water oxidation by copper–containing POM, $[(\alpha\text{-}SbW_9O_{33})_2Cu_3(H_2O)_3]^{12-}$.[30] However, copper-containing POMs have rarely been employed as heterogeneous electrocatalysts for catalytic water oxidation. Last several years, we have been

exploring functional POMs as homogeneous–[31] as well as heterogeneous–electrocatalysts[32-37] for water splitting. A POM–based bifunctional catalyst that shows electrocatalytic water oxidation, as well as water reduction in the neutral aqueous medium, is hardly known. In our very recent report, we have shown the catalytic HER activity by a tungsten POM cluster, which is synergistically activated by a redox-active copper–wheel.[38] We have also demonstrated that if a transition metal aqua species is confined in a constrained space or put on the POM cluster surface by a coordinate covalent bond, it drives electrocatalytic water oxidation.[34,35] And, our other report has shown that, if $–W(OH)_2$ moiety is grafted on a POM cluster surface, this moiety acts as a functional group for electrocatalytic water reduction to molecular hydrogen.[39] These two important facts inspired us to explore a POM–based compound that has W–OH moiety (referring to water reduction) and $–M(H_2O)_n$ group (referring to electrocatalytic water oxidation) so that it would act as a bifunctional catalyst for HER as well as for OER.

Thus, in the present work, we have reported the synthesis and crystal structure of a three-dimensional-framework-containing polyoxometalate (POM) compound $[Li(H_2O)_4][\{Cu^{I}(H_2O)_{1.5}\}\ \{Cu^{II}(H_2O)_3\}_2\{W^{VI}_{12}O_{36}(OH)_6\}]\cdot N_2\cdot H_2S\cdot 3H_2O$ (**LiCu$_3$*para-D***), which is characterized with $6\{W^{VI}–OH\}$ groups on the cluster surface and a mixed-valent copper-aqua species, $[\{Cu^{I}(H_2O)_{1.5}\}\{Cu^{II}(H_2O)_3\}_2]^{5+}$ per formula unit of **LiCu$_3$*para-D***. As expected, **LiCu$_3$*para-D*** exhibits electrocatalytic OER by water oxidation and HER by water reduction, importantly both in the neutral pH aqueous medium. We have understood that the POM cluster $\{W_{12}O_{34}(OH)_6\}^{6–}$ (anionic part) and the copper-aqua complexes $[\{Cu^{I}(H_2O)_{1.5}\}\{Cu^{II}(H_2O)_3\}_2]^{5+}$ (cationic part) of **LiCu$_3$*para-D*** individually respond to the electrocatalytic water reduction and water oxidation, respectively. To the best of our knowledge, **LiCu$_3$*para-D*** is a rare paradigm of polyoxometalate (POM) system, which functions as a bifunctional electrocatalyst showing HER and OER at the neutral pH.

3.2. EXPERIMENTAL SECTION

3.2.1. Materials

The chemicals used for the synthesis were of analytical grade which are commercially available and used without any further purification. Lithium tungstate (Li_2WO_4, 98%) was purchased from Sigma Aldrich India. Bismuth nitrate pentahydrate ($Bi(NO_3)_3\cdot 5H_2O$, 98%) was purchased from Alfa Aesar, India. Copper(II) sulphate pentahydrate pure ($CuSO_4\cdot 5H_2O$) was purchased from Merck, India. Nitric acid extra-pure and ammonia solution extra pure were purchased from Finar chemicals. Double distilled water was utilized to carry out all the

syntheses and Milli-Q water for electrochemical experiments. **$LiCu_3$*para-D*** was synthesized in a one-pot wet synthesis procedure, as discussed below.

3.2.2. Synthesis

3.2.2.1. Synthesis of $[Li(H_2O)_4][\{Cu^I(H_2O)_{1.5}\}\{Cu^{II}(H_2O)_3\}_2\{W^{VI}_{12}O_{36}(OH)_6\}]\cdot N_2\cdot H_2S\cdot 3H_2O$ ($LiCu_3$*para-D*).

Typically, Li_2WO_4 (2.3 mmol, 0.6 g) was dissolved in 30 mL of distilled water and was heated to 90 ℃ on a hot plate. Then, a solution of bismuth nitrate (0.3 mmol, 0.12 g $Bi(NO_3)_3\cdot 5H_2O$ dissolved in 1 mL of 6 M HNO_3) was added to the solution at 90 ℃. After 15 min of stirring, a solution of copper sulfate (0.5 mmol, 0.125 g of $CuSO_4\cdot 5H_2O$ in 2 mL of water) was added dropwise to the above-mentioned reaction mixture. The reaction mixture was then treated with 125 µL of 6 M HNO_3 and stirred for another 15 minutes. Next, the pH of the reaction mixture was adjusted to 8.25 using a 15% aqueous ammonia solution. And the reaction was carried out under the same reaction conditions for another one hour. The resultant reaction mixture was filtered twice to obtain a clear filtrate. It was left for crystallization at room temperature to obtain blue color block–type crystals after 10 days. The obtained crystals of **1** were separated by filtration and washed with ice–cold water and dried under ambient conditions. Yield: 26.6% based on tungsten. Anal. calc.% (Found from ICP-OES) for Cu 5.61 (5.80), W 64.94 (64.05), Li 0.20 (0.11), S 0.94 (0.62).

3.2.3. Methods

3.2.3.1. Physical Characterizations

Powder X-ray diffraction (PXRD) patterns of **$LiCu_3$*para-D*** were recorded on a Bruker D8–Advance diffractometer using graphite monochromated Cu Kα1 (1.5406 Å) and Kα2 (1.54439 Å) radiation. FT-IR spectra of **$LiCu_3$*para-D*** were recorded by an iD7 ATR Thermo Fisher Scientific-Nicolet iS5 instrument equipped with Platinum ATR (Attenuated Total Reflectance) accessory. Thermogravimetric analyses were carried out on a PerkinElmer–STA 6000, and Raman spectra were recorded on a Wi-Tec alpha 300AR laser confocal optical microscope (T-LCM) facility equipped with a Peltier–cooled CCD detector using a 683 nm Argon ion laser. Electronic absorption spectra were performed on a UV–2600 Shimadzu UV−visible spectrometer at room temperature (in the diffuse reflection mode). Field emission scanning electron microscopy (FESEM) images and Electron dispersive X-ray spectroscopy (EDX) mapping were obtained from a Carl Zeiss model Ultra-55 microscope equipped with Oxford Instruments X–MaxN SDD (50 mm^2) system functioning with INCA analysis

software. The electrochemical studies were performed on Zahner Zanium electrochemical workstation operated with Thales software.

3.2.3.2. Single-crystal X-ray Diffraction (SC-XRD) Analysis. A nascent single-crystal of **LiCu$_3$*para-D*** was selected from the mother liquor and mounted on a glass fiber tip using grease for its single-crystal X-ray diffraction. The SCXRD data were collected under liquid N_2 flow at 100 K using the Bruker APEX-II CCD diffractometer, equipped with a Mo–Kα (λ = 0.71073 Å) graphite monochromatic X-ray beam source and 40 mm of the crystal-to-detector distance was maintained. The data reduction was achieved with Bruker SAINT software and Empirical absorption corrections were performed with the SADABS program.[40] Structure solutions and full-matrix least-squares refinement for **LiCu$_3$*para-D*** were done by standard crystallographic software's WinGX v2021.3 and Olex2-1.3-ac4 embedded with SHELX 2018/1 package.[41-43] All the non-hydrogen atoms were refined anisotropically. The lithium-ion (Li_1) is located in a special position; hence, it was refined with the crystallographic EADP command. The sulfur atom (as H_2S) is also present in a special position in the crystal structure of **LiCu$_3$*para-D***; due to this, we were unsuccessful to assign hydrogen atoms for the sulfur atom by the Fourier electron density refinement. Therefore it has shown Alert level-A with short inter D···A contact of S1···O16 which is addressed in detail in the supporting information (SI), Section S1. The crystallographic details along with structure refinement parameters for **LiCu$_3$*para-D*** are listed in Table 1. The CSD 2240626 contains the supplementary crystallographic data for **LiCu$_3$*para-D***.

Table 1. **LiCu$_3$*para-D*** single-crystal data and its structure refinement parameters

Compound name	**LiCu$_3$*para-D***
Empirical formula	$Cu_3W_{12}H_{37}Li_1N_2S_1O_{56.50}$
Formula weight	3397
T(K)/ λ (Å)	100(2) K/0.71073
Crystal system	Triclinic
Space group	*P–1*
Unit cell dimensions	a = 10.7152(14) Å □= 70.072(4)° b = 11.8339(16) Å □= 69.291(4)° c = 13.3753(18) Å □ = 64.533(4)°
Volume	1396.0(3) Å^3
Z	1

ρ(caled)	4.006 Mg/m^3
Absorption coefficient (M)	25.827 mm^{-1}
***F*(000)**	1464
Theta range for data collection	2.270 to 24.999°
Independent reflections	4779 [$R_{(int)}$ = 0.0550]
Completeness to theta = 24.999°	97.0 %
Refinement method	Full-matrix least-squares on F2
Goodness-of-fit on F^2	1.236
R1/wR2 [I > 2σ (I)]	0.0363/0.0950
R1/wR2 (all data)	0.0367/0.0953
Largest diff. peak and hole	3.252 and -2.347 $e.Å^{-3}$
Note: the required numbers of hydrogens for sulfur and lattice water molecules are added to the molecular formula to satisfy their coordination.	

3.2.3.3. Electrochemical Measurements. All the electrochemical experiments were performed heterogeneously using a conventional three-electrode electrochemical cell employing **$LiCu_3$*para-D*** modified glassy carbon electrode as working–, a home-made Ag/AgCl (3M) as a reference–, and Pt mesh as the counter–electrode. The method for coating **$LiCu_3$*para-D*** on glassy carbon electrode (GCE) involves an ink preparation using 10 µL of 5% Nafion solution, 4 mg of the well-grinded **$LiCu_3$*para-D***, and 1 mg of carbon black in 1 mL of a mixture of ethanol-water (3:2, v/v). The obtained ink was sonicated for 30 minutes and was used for electrochemical experiments. 25 µL of this homogeneous ink was coated on the GCE working electrode having a 3 mm diameter (0.0706 cm^2 geometrical area), resulting in the ~100 µg of the sample on the GCE. The same amount of sample loading was maintained for all electrochemical experiments unless otherwise mentioned. The drop–cast sample ink was dried under IR–lamp (temp ~70 °C) and the coated electrode was left at room temperature for 5 min to obtain an ambient condition, before using it. All the electrochemical experiments were carried out under the nitrogen atmosphere at room temperature. The experimentally observed potentials were converted to the RHE (reversible hydrogen electrode) scale following the relation of $E_{(RHE)} = E_{(Ag/AgCl)} + 0.204\ V + 0.059pH$ where the Ag/AgCl electrode was used as the standard reference electrode. All the electrochemical studies were performed at a neutral pH of 7.0 of 0.1 M KCl electrolyte. The chronoamperometry experiments were done on 1 cm^2 carbon paper with large surface as a

working electrode using Pt wire as a counter electrode. 250 µL of the above-mentioned homogeneous ink suspension was coated on carbon paper of 1 cm^2 geometrical area. This provides 1 mg of the catalyst sample (**$LiCu_3$*para-D***) in 1 cm^2 carbon paper working electrode for the CPE experiments. The Tafel data was collected in a galvanostatic mode under steady-state mass flow, where the electrolyte solution was stirred at 480 rpm throughout the experiment. The internal cell resistance was manually calibrated.

3.3. RESULTS AND DISCUSSION

3.3.1. Structural Analysis

In a typical synthesis, the title compound $[Li(H_2O)_4][\{Cu^{I}(H_2O)_{1.5}\}\{Cu^{II}(H_2O)_3\}_2\{W^{VI}_{12}O_{36}(OH)_6\}]\cdot N_2\cdot H_2S\cdot 3H_2O$ (**$LiCu_3$*para-D***) has been formed at 100 °C and pH 8.25 involving the reaction mixture of lithium tungstate, bismuth nitrate, copper sulfate and an aqueous ammonia solution. Even though, bismuth nitrate has been used in this synthesis, bismuth does not get included in **$LiCu_3$*para-D***. However, it is necessary to add bismuth nitrate to achieve the isolation of **$LiCu_3$*para-D***. Interesting redox reactions occur during the synthesis of **$LiCu_3$*para-D***, which is obvious if we look carefully at the formula of **$LiCu_3$*para-D***, formulated from diverse characterization techniques including XPS studies, ICP elemental analysis and single crystal X-ray crystallography. A closer look on the formula of **$LiCu_3$*para-D*** gives the following important information: (i) generation of H_2S in the reaction, (ii) formation of N_2 molecule in the reaction and (iii) formation of Cu(I)-aqua species. The formations of H_2S and N_2 molecules in the synthesis of title compound can be accounted from the following redox reaction:

$$8NH_4^+ + 3SO_4^{2-} \rightarrow 3H_2S + 4N_2 + 12H_2O + 2H^+ \quad (1)$$

The above reaction (eqn 1) is ammonium ion assisted reduction of sulfate anion in which ammonium ion itself gets oxidized to N_2 molecule. This is a thermodynamically feasible metabolic reaction, commonly known as 'sulfate-reducing ammonium oxidation (SRAO)', that happened in subseafloor sediment.[44] This reaction justifies the presence of H_2S and N_2 in **$LiCu_3$*para-D*** as lattice molecules. In the above reaction (eqn 1), the sources of ammonium cation and sulfate anion are the ammonia solution and copper sulfate, respectively used in the synthesis of **$LiCu_3$*para-D***. The formation of Cu(I) species in **$LiCu_3$*para-D*** can be understood this way that a partial amount of H_2S, formed in eqn 1, reduces Cu(II) species (source, copper sulfate used in the synthesis of **$LiCu_3$*para-D***) to Cu(I) species, that forms Cu(I)-aqua complex species in **$LiCu_3$*para-D*** as shown in eqn 2. This

reaction is thermodynamically feasible as far as standard reduction potential values of S^{2-}/S^0- and Cu^{2+}/Cu^+-couples are concerned.[45]

$$H_2S + 2Cu^{2+} \rightarrow S + 2Cu^+ + 2H^+ \quad (2)$$

In the present synthesis, the formation of hydroxylated paratungstate type POM cluster, $[W^{VI}_{12}O_{36}(OH)_6]^{6-}$ can be described in two steps: first the formation of $[W_{12}O_{42}]^{12-}$ in an acidic pH (eqn 3) and then its hydrolysis in an alkaline pH to form the hydroxylated paratungstate, $[W^{VI}_{12}O_{36}(OH)_6]^{6-}$ (eqn 4), the POM anion of the title compound, **$LiCu_3$*para-D***.

$$12[WO_4]^{2-} + 12H^+ \rightarrow [W^{VI}_{12}O_{42}]^{12-} + 6H_2O \quad (3)$$

$$[W^{VI}_{12}O_{42}]^{12-} + 6H_2O \rightarrow [W^{VI}_{12}O_{36}(OH)_6]^{6-} + 6OH^- \quad (4)$$

It is already established that the paratungstate $[W_{12}O_{42}]^{12-}$ is formed in an acidic pH (below pH 4). In the present synthesis, the initial reaction mixture of sodium tungstate, bismuth nitrate and copper sulfate were treated with (6 M) HNO_3 and in this acidic pH, the paratungstate $[W_{12}O_{42}]^{12-}$ is formed, justifying the eqn (3). Then the reaction mixture was treated with 15% aqueous ammonia solution to achieve the pH of 8.25 of the resulting reaction mixture. And in this unusual alkaline pH, we could achieve the hydroxylated paratungstate **$LiCu_3$*para-D***.

Notably, the title paratungstate is characterized with six hydroxyl groups, which is, to our knowledge, the first example of this kind. The dihydroxy paratungstate, $[W^{VI}_{12}O_{40}(OH)_2]^{10-}$, known as 'paratungstate B', is well known and known to be formed in the pH range of 5-6.5.8[46-56] In this context, it can be noted that, 'paratungstate A' ion has the formula, $[W^{VI}_{12}O_{42}]^{12-}$. According to this naming convention, $[W^{VI}_{12}O_{38}(OH)_4]^{8-}$ (hypothetical one) should be named as 'paratungstate C' and therefore, the title paratungstate anion (in the present work), $[W^{VI}_{12}O_{36}(OH)_6]^{6-}$ can be named as 'paratungstate D'. The POM anion, 'paratungstate D', which we have achieved in the present work is unique in the sense that it is synthesized in an alkaline pH and it has six hydroxyl groups that are attached with six different tungsten(VI) centers out of the twelve tungsten(VI) centers in paratungstate. Expectedly, these six tungsten(VI) centers (attached with hydroxyl groups) would behave differently than other six tungsten(VI) centers (that are not attached with hydroxyl groups) as far as the electrochemistry of this 'paratungstate D' is concerned. A tungsten(VI) center which is connected to –OH group (W^{VI}–OH) would be reduced easily compared with a tungsten(VI) center with a terminal oxo group (W^{VI}=O). The serendipitous isolation of

LiCu$_3$*para-D* having ‘paratungstate D’ type POM anion has enabled us to perform hydrogen evolution reaction (HER) using **LiCu$_3$*para-D*** as an electrocatalyst (vide infra).

In the synthesis of **LiCu$_3$*para-D***, Li_2WO_4 was used as tungsten source and $CuSO_4{\cdot}5H_2O$ was used to functionalize the present POM system to have Cu(II)-aqua species. But in the title LiCu3para-D, the cationic part is turned out to be mixed valent copper-aqua species $[\{Cu^{I}(H_2O)_{1.5}\}\{Cu^{II}(H_2O)_3\}_2]^{5+}$ and lithium-aqua coordination complex. We have exploited this mixed valent copper-aqua species as catalytic site for oxygen evolution reaction (OER) so that the overall system (**LiCu$_3$*para-D***) can be used as a bifunctional electrocatalyst for HER as well as OER (vide infra).

3.3.2. Single-crystal X-ray Crystallography

The single-crystal X-ray diffraction (SCXRD) analysis reveals that **LiCu$_3$*para-D*** crystallizes in the triclinic *P*–1 space group. The relevant asymmetric unit (Figure 3.1a) consists of six tungsten atoms with full occupancies, two copper atoms (Cu1 having half occupancy and Cu2 having full occupancy), one Li^+-ion with half occupancy, 21 POM-oxygens with full occupancies, 3.75 units of copper ions-coordinated water molecules, two lithium ion coordinated water molecules, 1.5 units of oxygen atoms as lattice water molecules, one-half unit of H_2S and one-half unit of N_2. Accordingly, **LiCu$_3$*para-D*** has been formulated as $[Li(H_2O)_4][\{Cu^{I}(H_2O)_{1.5}\}\{Cu^{II}(H_2O)_3\}_2\ \{W^{VI}_{12}O_{36}(OH)_6\}]\cdot N_2\cdot H_2S\cdot 3H_2O$ (**LiCu$_3$*para-D***). In the crystal structure of **LiCu$_3$*para-D***, as already mentioned, there are two types of copper ions: Cu1 in +1 oxidation state and Cu2 in +2 oxidation state.

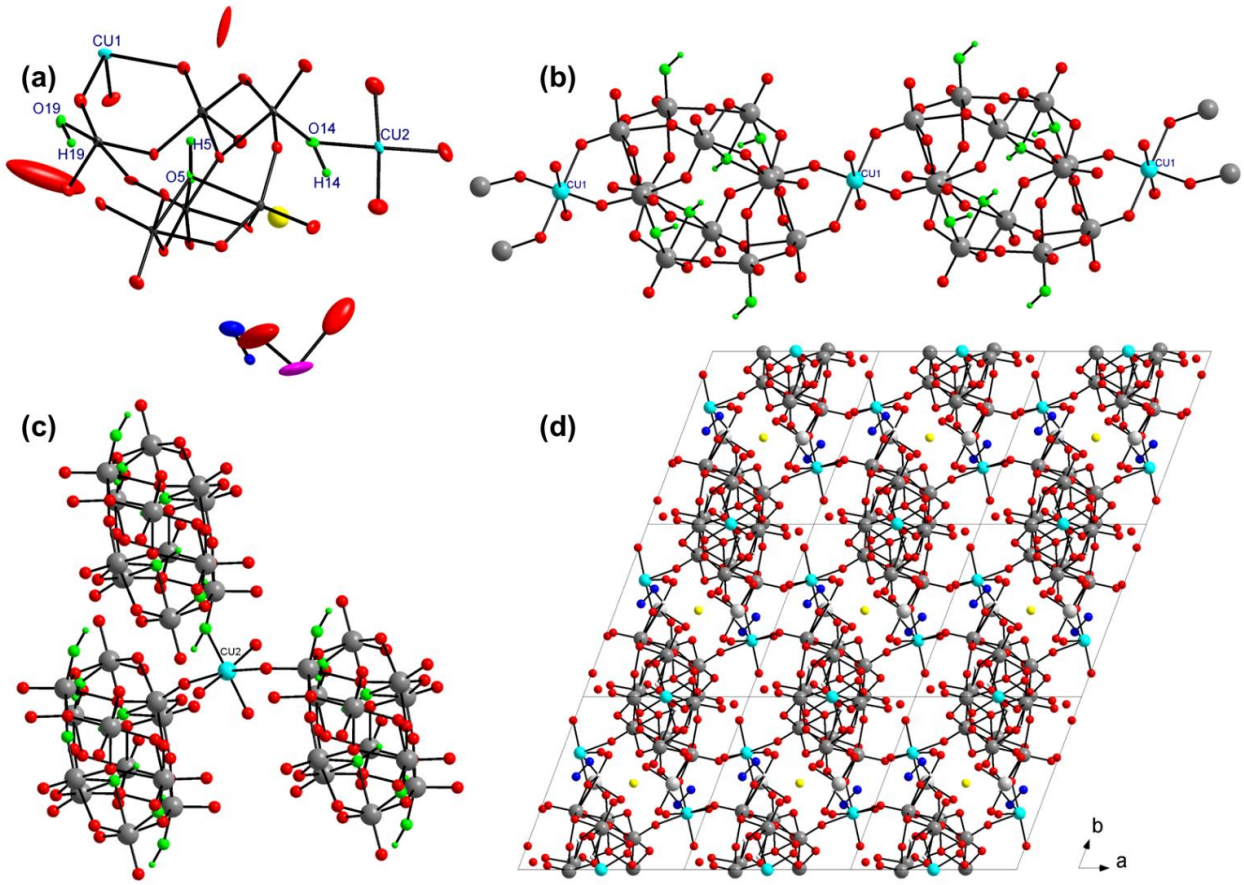

Figure 3.1. Single-crystal structure analysis of **LiCu$_3$*para-D***: (a) asymmetric unit represented in 50% thermal-ellipsoidal probability; (b) ball-and-stick representation of distorted octahedral geometry around Cu1 center and its interaction with two POM clusters; (c) ball-and-stick representation of distorted octahedral geometry around Cu2 center and its complexation with three POM clusters and three aqua-ligands; (d) 3×3×3 super cell packing of **LiCu$_3$*para-D*** in ball-and-stick mode. Color code: tungsten, grey; copper, cyan; lithium, pink; nitrogen, blue; sulphur, yellow; oxygen, red; hydroxylated oxygen atoms and hydrogen atoms are shown in green color.

Both types of copper centers have distorted octahedral geometry: four equatorial positions of Cu1 are coordinated by four terminal oxo-groups (W=O→Cu) of two different $[W^{VI}_{12}O_{34}(OH)_6\}]^{6-}$ clusters from opposite sides, and the remaining two axial positions are occupied by two aqua-ligands (Figure 3.1b) resulting in a chainlike arrangement; the Cu2 center has been locked by three different POM clusters and three aqua–ligands (Figure 3.1c). As shown in Figure 3.1d, the POM cluster $\{W^{VI}_{12}O_{34}(OH)_6\}^{6-}$ anion is interconnected through the both types of copper–aqua–complex cations, which in turn results in a sole inorganic three–dimensional (3D) framework type architecture having well-defined void spaces. The most fascinating aspect in the crystal structure of **LiCu$_3$*para-D*** is the hydroxylation of the POM cluster. There are three W^{VI}–OH groups in the asymmetric unit; two of them are bridging oxo groups (one μ_3–OH, named as O5 and one μ_2–OH, named as O14) and other one a terminal W=O group (named as O19), which got protonated during the isolation / synthesis of the title compound (see eqn. 4 in the synthesis discussion).

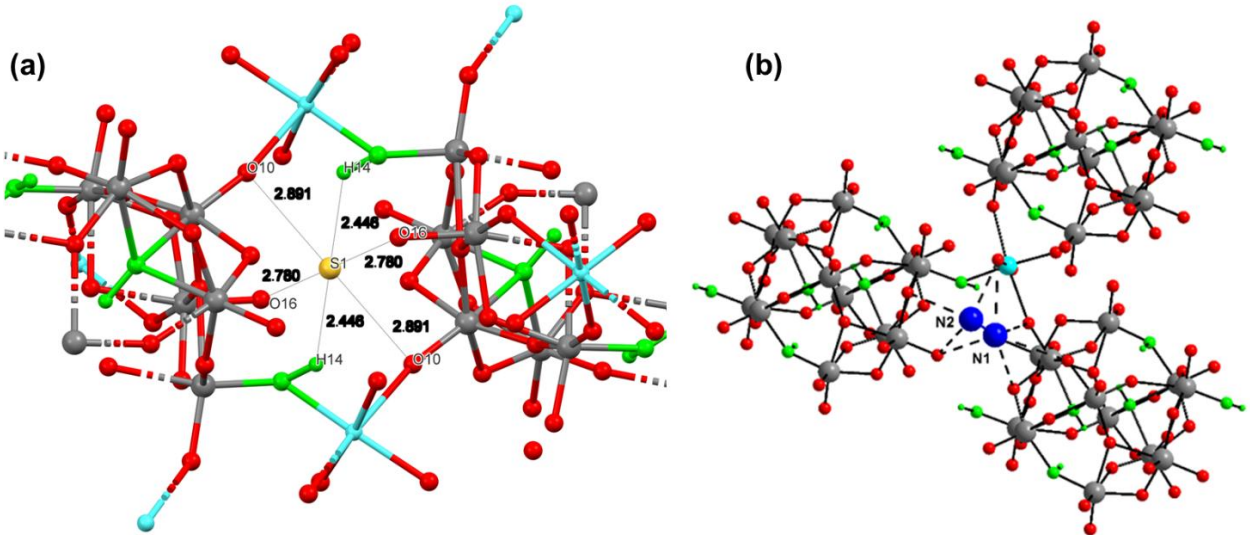

Figure 3.2. (a) The presence of sulfur in the 3D void of **LiCu$_3$*para-D*** and its interaction with cluster framework oxygens through the strong H-bonding. (b) Supramolecular interactions between N_2 molecule and terminal and bridging oxygen atoms of the surrounding paratungstate cluster anions. Color code: tungsten, grey; copper, cyan; nitrogen, blue; oxygen, red; hydroxylated oxygen atoms and hydrogen atoms are shown in green color. The interactions are shown by dashed-lines.

Figures 1b and 1c show these hydroxyl groups in green color. This protonated terminal {W=OH} group undergoes coordination to Cu(II) ion making this hydroxyl group as a μ_2−OH entity, bridging a W(VI) center and a Cu(II) center as shown in Figure 3.1c. The hexa-hydroxylation on a paratungstate type POM cluster anion makes this system a new member (we have named this as a paratungstate-D) of the paratungstate family of paratungstate-A, paratungstate-B and paratungstate-D. The structurally characterized paratungstate B (i.e., having two W−OH groups) is known in many reported compounds.[46-56] The presence of these hydroxyl groups in **LiCu$_3$*para-D*** is validated by bond valence sum (BVS) calculations[57] using its crystal data (for details, see Appendix, Section A3.2) and XPS analysis of **LiCu$_3$*para-D*** (vide infra). The void spaces of 3D-network in the crystal structure of **LiCu$_3$*para-D*** have trapped H_2S, N_2, distorted tetrahedral lithium–aqua–complex cations, and lattice water molecules as shown in Figure 1d. Figure 3.2a shows the presence of H_2S in the form of sulphur in the crystal structure of **LiCu$_3$*para-D*** (the hydrogens of H_2S could not be located in the crystal structure; the presence of sulphur is confirmed from ICP and XPS analyses). As shown in Figure 3.2a, the encapsulated H_2S is strongly interacted with cluster framework oxygens through the H-bonding, with hydrogen bond distances in the range of 2.7 to 2.9 Å. The presence of un-interacted N_2 molecule in a crystal lattice is surprising, because it may get escaped easily from the crystal. We have thus investigated the supramolecular interactions of the N_2 molecule with its surrounding atoms carefully in the crystal structure of **LiCu$_3$*para-D***. We found interesting N···O interactions between N_2 molecule and surrounding

POM clusters as shown in Figure 3.2b. The terminal oxygen atoms associated with these N···O interactions offer the N···O separation in the range of 2.870 Å-2.995 Å, whereas the bridging oxygen atoms of the surrounding POM clusters give the N···O separation in the range of 3.115 Å-3.290 Å. This justifies the presence of N_2 molecule (formed in the concerned synthesis reaction) in the crystal lattice of **LiCu$_3$*para-D***. The single crystal X-ray diffraction (SCXRD) parameters are given in Table 3.1, and other relevant details, such as, bond angles and bond distances, observed in the crystal structure of **LiCu$_3$*para-D***, are given in section A1 in Appendix 3, which are in good agreement with the relevant literature. The overall composition (formulation) of **LiCu$_3$*para-D*** has been verified by ICP-OES analyses (see Appendix, Section A3.3) including diverse spectral studies as discussed in the succeeding section.

The bond valence sum (BVS) calculations, as already mentioned, have been performed on the crystal data of **LiCu$_3$*para-D*** and it indicates that Cu1, Cu2, and all W centers are in +1, +2, and +6 oxidation states, respectively. The bond valence sum (BVS) calculations, as already mentioned, have been performed on the crystal data of **LiCu$_3$*para-D*** and it indicates that Cu1, Cu2, and all W centers are in +1, +2, and +6 oxidation states, respectively.

3.3.3. Spectroscopic Analysis

3.3.3.1. FTIR Analysis

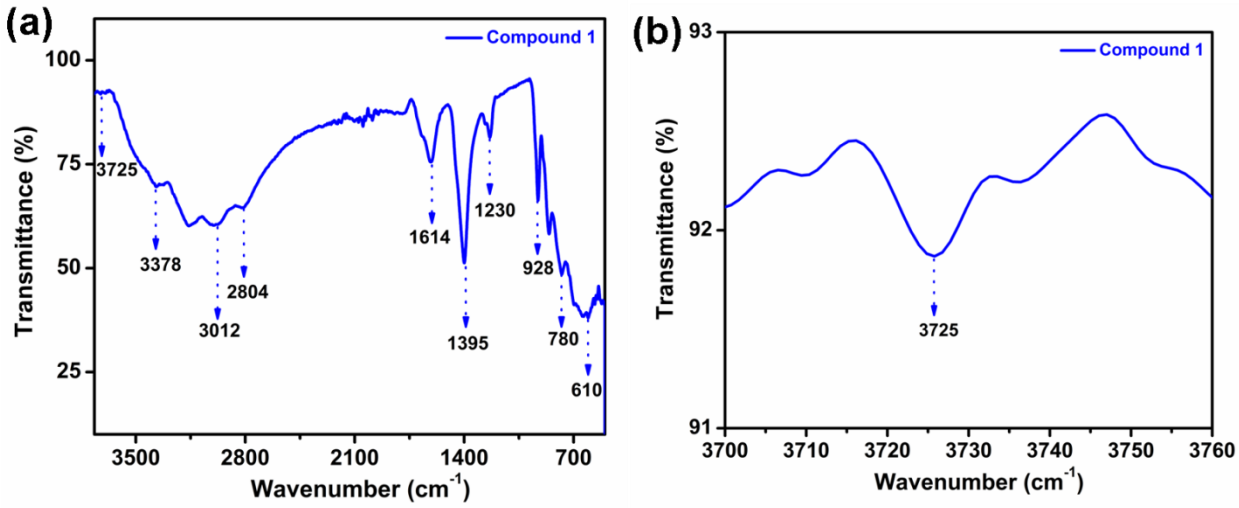

Figure 3.3. (a) FT-IR spectrum of **LiCu$_3$*para-D***, (b) Magnified view of the FTIR profile to show the presence of W–OH group in **LiCu$_3$*para-D***.

Figure 3.3a shows the FTIR spectral analysis for title **LiCu$_3$*para-D***. The FTIR spectrum has displayed the major peaks belonging to the POM cluster in the range of 950–

500 cm^{-1} showing the W=O, W–O–W, and Cu–O stretching and bending vibrations. A peak at 2804 cm^{-1} in the IR spectrum can be attributed to the S–H stretching, hence signifying the presence of H_2S in **LiCu$_3$*para-D***.[37,58] The broad bands at 1614 and 3378 cm^{-1} are ascribed to the O–H bending and stretching modes of the water molecules respectively. A magnified view of the FTIR spectrum in the region of 3700–3760 cm^{-1} has been displayed in Figure 3.3b, which shows a distinct IR band at 3725 cm^{-1} which can be assigned to the O–H stretching mode of a metal-hydroxyl group. This strongly supports the presence of tungsten-hydroxyl (W–OH) groups in **LiCu$_3$*para-D***, as found from X-ray crystallography studies along with BVS calculations (vide supra).[38]

3.3.3.2. PXRD Analysis

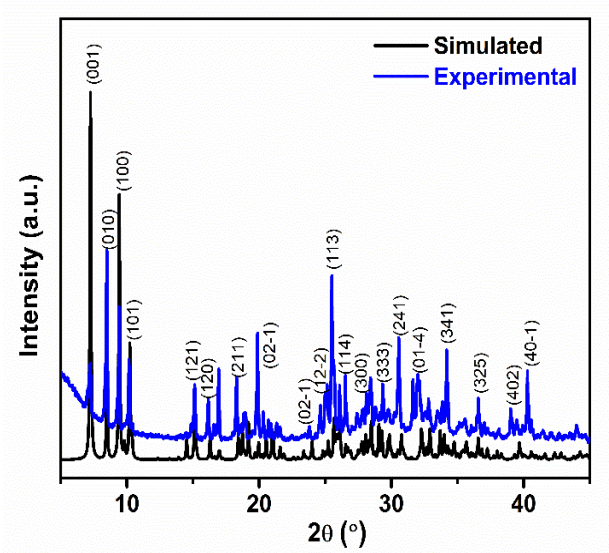

Figure 3.4. PXRD profile of experimentally obtained **LiCu$_3$*para-D*** compared with that of simulated one from SCXRD data.

The observed powder X-ray diffraction (PXRD) pattern of **LiCu$_3$*para-D*** is consistent to the simulated pattern, obtained from single crystal data of **LiCu$_3$*para-D***, suggesting the bulk purity of the synthesis of the title compound (Figure 3.4).

3.3.3.2. Raman Analysis

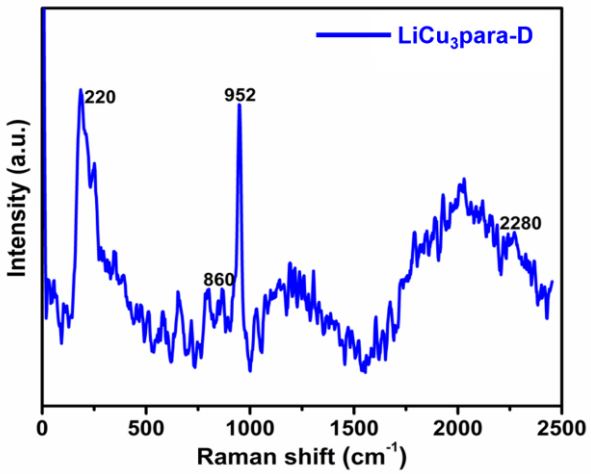

Figure 3.5. Raman spectrum of **LiCu$_3$*para-D***.

The Raman spectrum of **LiCu$_3$*para-D*** features prominent peaks in the region of 200–2500 cm^{-1} corresponding to the W=O bonds and W–O–W bonds (Figure 3.5). It is noteworthy to mention that, the Raman active mode for N_2 can be seen at 2280 cm^{-1}, supporting the single crystal structure of **LiCu$_3$*para-D***.[59]

3.3.3.2. Electronic Absorbance Spectral Analysis

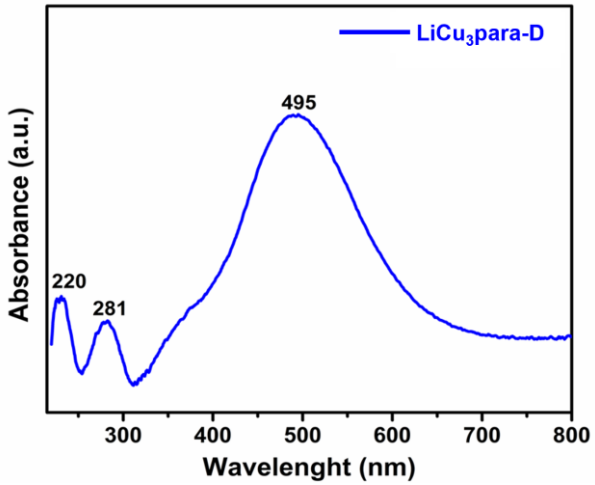

Figure 3.6. UV-DRS electronic spectrum of **LiCu$_3$*para-D***.

The absorbance peak at 495 nm in the solid state electronic spectrum of **LiCu$_3$*para-D*** can be attributed to the *d-d* electronic transitions of copper, present in **LiCu$_3$*para-D***, and the peaks present below the region of 300 nm in the electronic spectrum (Figure 3.6) may be due to ligand to metal charge transfer (LMCT) transition.

3.3.3.3. Thermogravimetric Analysis

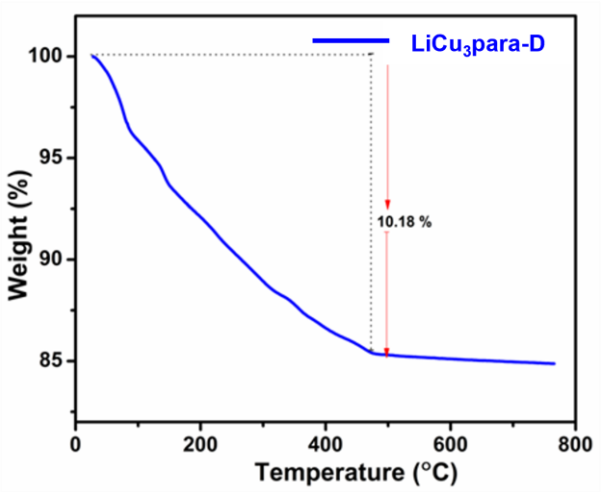

Figure 3.7. UV-DRS electronic spectrum of **LiCu$_3$*para-D*.**

The thermal stability of as-synthesized **LiCu$_3$*para-D*** has been investigated under the He gas atmosphere (Figure 3.7). From the obtained TGA curve, a continuous weight loss (10.16%) till 5000 °C was observed, which could be attributed to the loss of lattice water-, N_2- and coordinated water molecules. The stagnated weight loss after 500 °C can be considered as the complete degradation of the 3D POM framework structure and formation of respective metal-oxides.

3.3.3.4. FESEM-EDX Analysis

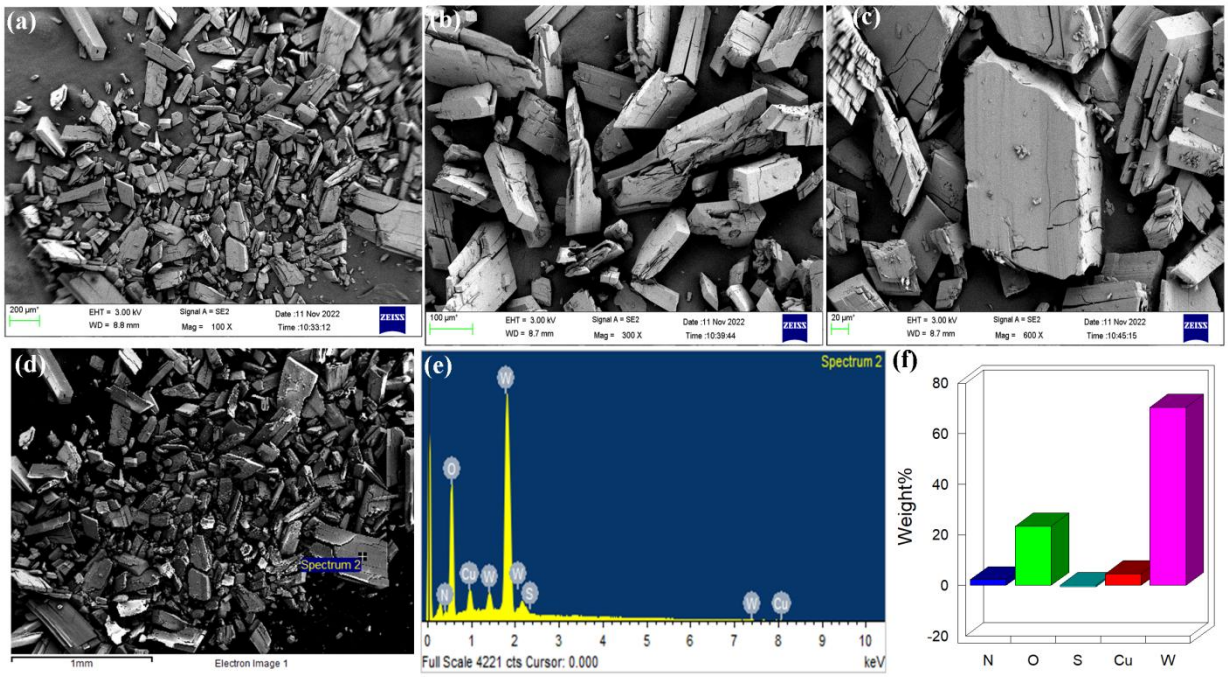

Figure 3.8. (a-c) FESEM images under different magnification **LiCu$_3$*para-D*** (d-f) EDX elemental analysis of **LiCu$_3$*para-D***.

Additionally, field emission scanning electron microscopy energy dispersive X-ray (FESEM-EDX) was performed to analyze the morphology and the surface elements present in **LiCu$_3$*para-D*** (Figure 3.8).

3.3.3.5. X-ray Photoelectron Spectrocsopic Analysis

In order to identify constituent elements and comprehend their oxidation states, we performed the X-ray photoelectron spectroscopy (XPS) analysis on **LiCu$_3$*para-D*** (Figure 3.9 a-c). For the de-convolution of the obtained XPS data, Lorentzian-Gauguin (LG) fitting was used with permitted error (in terms of Adj. R^2). The survey scan XPS plot reveals the presence of O, Cu, W, S, N, and Li elements in **LiCu$_3$*para-D*** as shown in Figure 3.9a. Figure 3.9b shows the high-resolution XPS plot of O 1s in **LiCu$_3$*para-D***; the de-convolution of the O 1s peak resulted in two peaks centered at 530.69 eV and 533.78 eV. The respective peaks correspond to the existence of different oxygen bonding interactions for O^{2-}, namely, W–O–W / W=O (bridging oxygen / terminal oxygen) and hydroxyl oxygen (that is, W–OH group in the present work).[38,60] To be more precise, the latter O 1s XPS shoulder peak at 533.78 eV validates the presence of metal-hydroxyl groups in **LiCu$_3$*para-D***, consistent with SCXRD studies (vide supra).

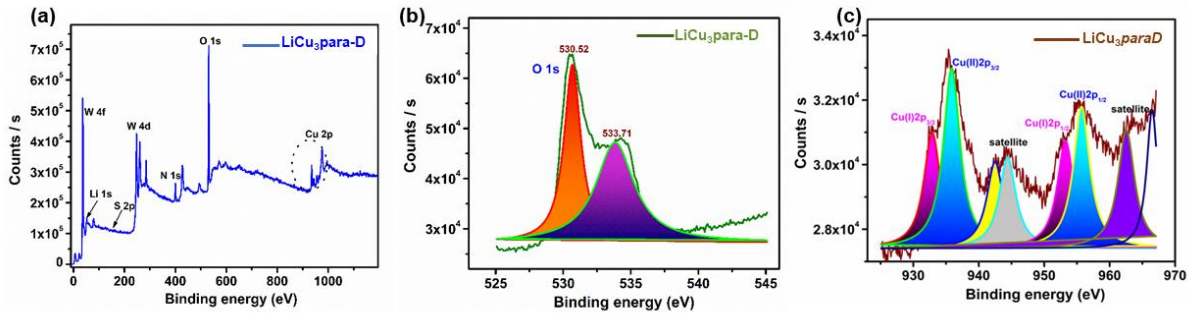

Figure 3.9. (a) Survey scan XPS plot of **LiCu$_3$*para-D***; (b) high-resolution XPS plots of O 1s of **LiCu$_3$*para-D***; (c) high-resolution XPS plots of Cu 2p **LiCu$_3$*para-D***.

Figure 3.9c displays the high-resolution XPS plots of copper for **LiCu$_3$*para-D***: the Cu $2p_{3/2}$ signal positioned at 932.84 eV has been assigned to the monovalent copper (Cu^I) and its pertinent Cu $2p_{1/2}$ peak appears at 953.30 eV. Another Cu $2p_{3/2}$ peak, that appeared at 935.84 eV, can be assigned to the divalent copper (Cu^{II}) — its related Cu $2p_{1/2}$ signal is found at 955.67 eV. As shown in Figure 3c, two additional unidentified peaks, positioned at the higher energy side of the Cu 2p signals (around 943 eV and 962 eV), may be due to the multi-electronic transitions in the different energy levels of the copper ions in the POM cluster.[30,61] The LG fitting of the copper 2p XPS spectra evidently shows the higher intensity for Cu^{II}

peak compared to its Cu^{I} peak. This is consistent with single crystal X-ray crystallography results combined with BVS calculations (vide supra) that showed the ratio of Cu^{II} : Cu^{I} centers as 2:1, which is in accordance with the formula of compound $[Li(H_2O)_4][\{Cu^{I}(H_2O)_{1.5}\}\ \{Cu^{II}(H_2O)_3\}_2\{W^{VI}{}_{12}O_{36}(OH)_6\}]\cdot N_2\cdot H_2S\cdot 3H_2O$ (**1**). The presence of tungsten (W 4f) is well observed in the XPS survey spectrum of **LiCu$_3$*para-D***, which has been de-convoluted to show two peaks at 35.69 and 37.89 eV (see Appendix, Section A3.4). The XPS plot of **LiCu$_3$*para-D*** has shown a peak at 54.87 eV for Li 1s (see Appendix, Section A3.4). XPS analyses also show the presence of sulfur in **LiCu$_3$*para-D*** which was already observed in the single crystal structure of **LiCu$_3$*para-D*** (vide supra). In particular, a small response for S 2p has been detected at 159.5 eV in the XPS plot which indicates the existence of sulphur in **LiCu$_3$*para-D*** in the form of H_2S (see Appendix, Section A3.4).[62,63] Likewise, a distinct response at 400.38 eV for N 1s is observed in the XPS profile of **LiCu$_3$*para-D***, (see Appendix, Section A3.4) which is the proof of the presence of nitrogen as N_2 in **LiCu$_3$*para-D***,[65] which is again in accordance with crystallographic results (vide supra) supporting the crystal structure of **LiCu$_3$*para-D***, thereby supporting the formula of **LiCu$_3$*para-D***.

3.3.4. Bifunctional Electrocatalytic Water Splitting

3.3.4.1. Hydrogen Evolution Reaction (HER) by Water Reduction

We have seen in our earlier report that POM surface grafted *cis*-$\{W^{VI}(OH)_2\}_2$ can act as the active site for electrocatalytic water reduction (WR) to molecular hydrogen.[38] This prompted us to explore the title compound $[Li(H_2O)_4][\{Cu^{I}(H_2O)_{1.5}\}\{Cu^{II}(H_2O)_3\}_2\{W^{VI}{}_{12}O_{36}(OH)_6\}]\cdot N_2\cdot H_2S\cdot 3H_2O$ (**LiCu$_3$*para-D***) as an electrocatalyst for water reduction since **LiCu$_3$*para-D*** is characterized with an enriched number of tungsten-hydroxyl (W^{VI}–OH) groups. In order to understand the importance of the {W^{VI}–OH} functional group in **LiCu$_3$*para-D*** toward HER activity, we synthesized a known compound $[NH_4]_{10}[W_{12}O_{40}(OH)_2]\cdot 4H_2O$ (***para-B***) having 'paratungstate B' POM anion,[66] which have two {W^{VI}–OH} groups, and compared its electrocatalytic HER activity with that of title **LiCu$_3$*para-D***.

All the electrochemical experiments have been performed in 0.1 M potassium chloride solution at neutral pH; a 3 mm diameter glassy carbon (GC), Ag/AgCl (3 M), and Pt wire were used as working, reference, and auxiliary electrodes, respectively, unless otherwise stated. The potential values in the present study are reported against reversible hydrogen electrode (RHE) using the relation: $E_{(RHE)} = E_{(Ag/AgCl)} + 0.204\ V + 0.059pH$ where the

Ag/AgCl (3 M) electrode was used as the standard reference electrode. Figure 3.10a shows the cyclic voltammograms of blank-GCE, **LiCu$_3$*para-D*** and ***para-B***. The CV of blank-GCE does not show any redox activity. ***para-B*** (paratungstate B) having two hydroxyl groups shows a little HER activity with a very small current surge (–0.53 mA/cm^2 at -0.58 V vs RHE). On the other hand, **LiCu$_3$*para-D*** (present work) shows a broad reductive response at –0.025 V vs RHE followed by a sudden cathodic current surge at –0.150 V vs RHE due to the electrocatalytic water reduction leading to HER at neutral pH. The broad reductive response at –0.025 V vs RHE can be assigned to the W^{VI}/W^{V} reduction because the relevant ***para-B*** shows a similar reductive response at –0.12 V vs RHE which is known to be the reduction of W^{VI} to W^{V} of the POM cluster anion, $[W_{12}O_{40}(OH)_2]^{10-}$.[38] Since the current surge appears (at –0.150 V vs RHE) right after the broad and irreversible reductive response (–0.025 V vs RHE), we believe that the electrochemically reduced W(V) centers of the hydroxylated POM cluster anion reduce water chemically to molecular hydrogen. Even though, we have assigned the concerned reductive response at –0.025 V vs RHE in **LiCu$_3$*para-D*** to W^{VI}/W^{V} reduction, which is responsible for observed HER in the present study, we cannot rule out the role of the copper centers (present in **LiCu$_3$*para-D***) in the present HER action.[38] In the title compound, there are 12 tungsten(VI) centers, out of which six tungsten(VI) centers got hydroxylated during synthesis (vide supra, synthesis discussion). Since it would be easy to reduce a $\{W^{VI}–OH\}$ moiety compared to reducing a $\{W^{VI}=O\}$ moiety,[38,58] the broad reductive response at –0.025 V vs RHE in **LiCu$_3$*para-D*** can be thought to be due the reduction of $\{W^{VI}–OH\}$ centers [not {W=O} centers]. Thus, it can be accepted that the W^{VI}–OH functional groups, present in **LiCu$_3$*para-D***, respond to the electrocatalytic HER. Figure 3.10b shows the linear sweep voltammogram (LSV) curves for compounds $[Li(H_2O)_4][\{Cu^{I}(H_2O)_{1.5}\}\{Cu^{II}(H_2O)_3\}_2\{W^{VI}_{12}O_{36}(OH)_6\}]\cdot N_2\cdot H_2S\cdot 3H_2O$ (**LiCu$_3$*para-D***) and $[NH_4]_{10}[W_{12}O_{40}(OH)_2]\cdot 4H_2O$ (***para-B***), that are in line with their respective CV profiles (Figure 3.10a).

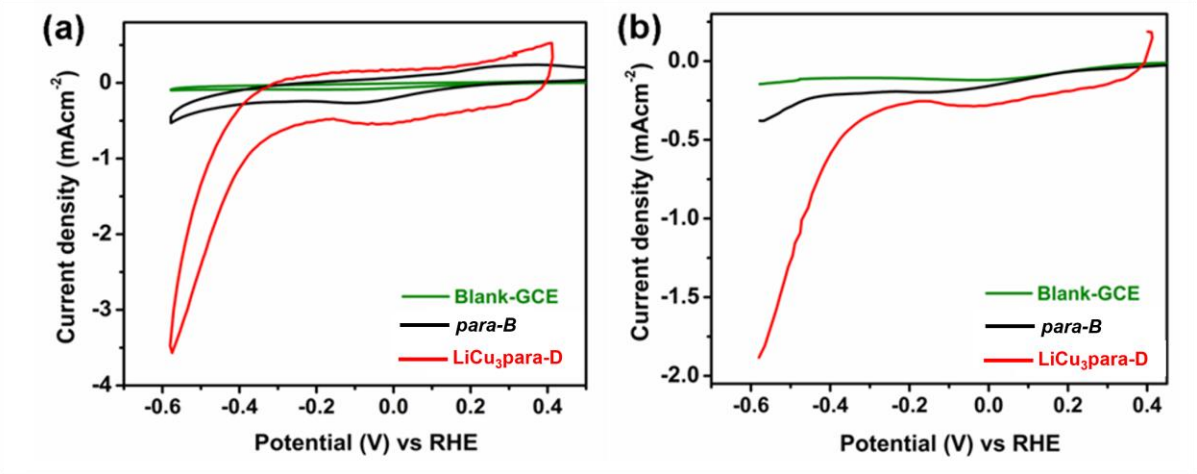

Figure 3.10. (a) Cyclic– and (b) linear–sweep voltammograms for **LiCu$_3$*para-D***, ***para-B***, and blank-GCE (scan rate 100 and 10 mV/s, respectively).

It is well known that POMs exhibit multi-electron redox responses in a single step and it is important to find out the number of electrons involved in the redox reactions of the present system, especially in the redox event at –0.025 V vs RHE in the electrochemistry of **LiCu$_3$*para-D***. The DPV plot (see Appendix, Section A3.5) indicates five electrons participation in the overall electrocatalytic water reduction as shown in equations (5) and (6).

$$2[\{Cu^{I}(H_2O)_{1.5}\}\{Cu^{II}(H_2O)_3\}_2\{W^{VI}{}_{12}O_{36}(OH)_6\}]^{1-} + 10e^- \rightarrow 2[\{Cu^{I}(H_2O)_{1.5}\}\{Cu^{II}(H_2O)_3\}_2\{W^{VI}{}_{7}W^{V}{}_{5}O_{36}(OH)_6\}]^{6-} \quad (5)$$

$$2[\{Cu^{I}(H_2O)_{1.5}\}\{Cu^{II}(H_2O)_3\}_2\{W^{VI}{}_{7}W^{V}{}_{5}O_{36}(OH)_6\}]^{6-} + 10H_2O \rightarrow 2[\{Cu^{I}(H_2O)_{1.5}\}\{Cu^{II}(H_2O)_3\}_2\{W^{VI}{}_{12}O_{36}(OH)_6\}]^{1-} + 5H_2 + 10OH^- \quad (6)$$

We believe that six tungsten(VI) centers, that are attached to bridging hydroxyl groups (two μ_3–OH groups, named as O5, two μ_2–OH groups, named as O14, and terminal hydroxyl groups (two W=OH groups, named as O19), include these five tungsten centers that got reduced during electrochemical reduction.

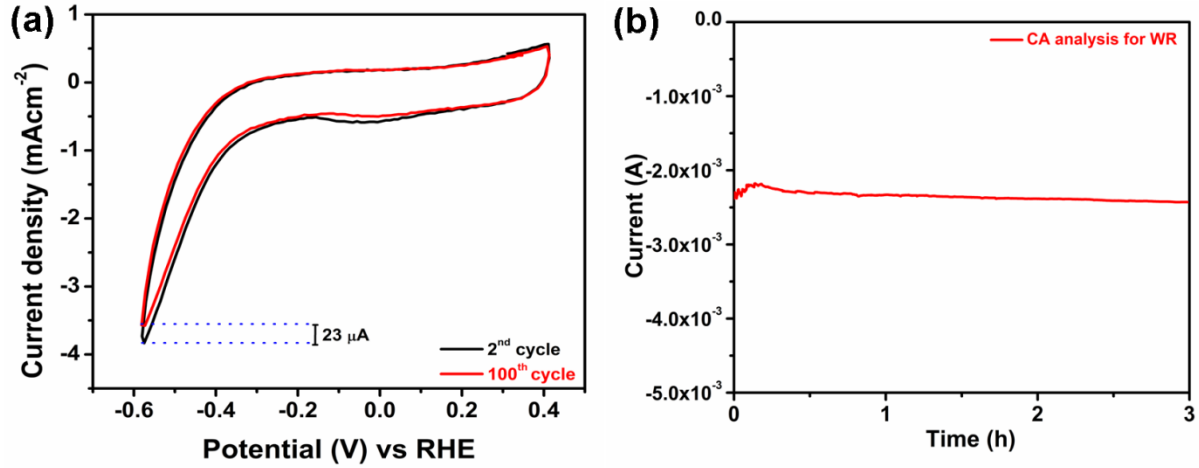

Figure 3.11. (a) Cycling stability analysis of **LiCu$_3$*para-D*** for hydrogen evolution reaction by 100 CV cycles with a scan rate of 100 mVs^{-1} in 0.1 M KCl at pH 7.0; (b) Chronoamperometry (CA) electrolysis of **LiCu$_3$*para-D*** performed at -0.7 V vs RHE for 3 hours.

The stability of **LiCu$_3$*para-D*** as a water reduction (WR) catalyst is primarily examined by two basic electrochemical techniques: (i) we performed 100 CV cycles in the catalytic potential window (from 0.4 to –0.6 V vs RHE) for WR (Figure 3.11a) and (ii) the catalyst **LiCu$_3$*para-D*** modified carbon paper (CP) was used as an electrode for 3 hours of chronoamperometry (CA) electrolysis at –0.7 V vs RHE (Figure 3.11b). No significant fluctuations have been observed in these two experiments, suggesting its stability under operational conditions. Post-electrolysis analyses of CA electrolysis electrode material by FTIR (see Appendix, Figure A3.5), X-ray photoelectron spectroscopy (XPS) (see Appendix, Figure A3.6,7), and FESEM-EDX (see Appendix, Figure A3.8,9) have confirmed the molecular catalytic behaviour of **LiCu$_3$*para-D*** as a water reduction true catalyst at neutral pH.

The insights of water reduction kinetics of **LiCu$_3$*para-D*** have been assessed by performing scan rate variation, analyzing the turnover frequency (TOF), Tafel slope-, overpotential (η)-, and Faradaic efficiency-values. Figure 3.12a shows the linear dependence of peak current with the square root of scan rates indicating the diffusion-controlled electrochemical hydrogen evolution by **LiCu$_3$*para-D***. Double-layer capacitance measurements are performed by running a cyclic voltammogram in a non-Faradaic region of the CV profiles of **LiCu$_3$*para-D*** (see Appendix, Section A3.7). With the increase in the scan rate in the non-Faradaic region, the capacitive current also increases, and the concerned C_{dl} value for the title **LiCu$_3$*para-D*** is found to be 7.732×10^{-4} Fcm^{-2} (Figure 3.12b).[31,37,38]

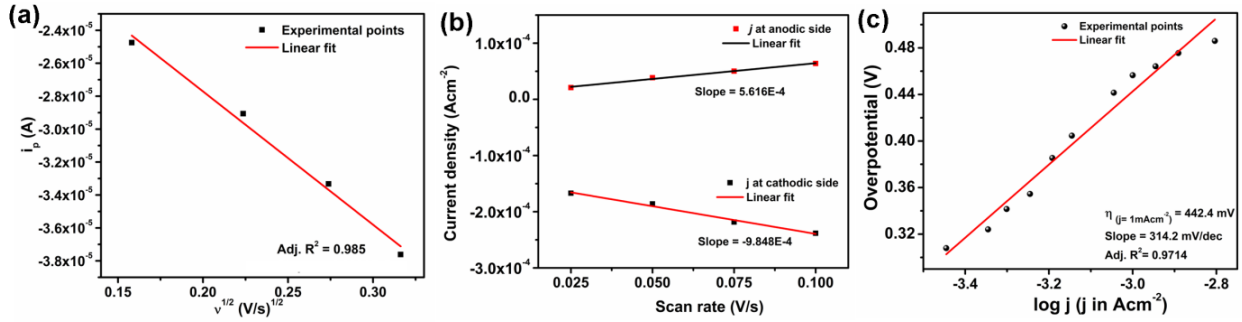

Figure 3.12. (a) Derived plot constructed from the peak current (i_p) as a function of the square root of scan rate (-0.025 to -0.1 Vs^{-1}) for **LiCu$_3$*para-D***; (b) The plot of slopes of current density against scan rates at a potential of -0.35 V vs RHE for **LiCu$_3$*para-D*** illustrating the double layer capacitance of **LiCu$_3$*para-D***; (c) iR corrected Tafel plot for **LiCu$_3$*para-D*** in the catalytic WR region.

We have calculated the TOF value for **LiCu$_3$*para-D*** by following a reported procedure (see Appendix, Section A3.8 for detailed calculations), and is found to be 4.66 s^{-1} for electrochemical hydrogen evolution reaction (HER) by water reduction. In the catalytic HER region, the obtained Tafel slope value of 314.2 mV/dec and the overpotential value of 442.75 mV (at 1 mA/cm^2) for **LiCu$_3$*para-D*** (Figure 3.12c) are considerably lower compared to those of related tungsten-mediated HER catalysts.[33,35,37] A decent Faradaic efficiency value of 84% in the present HER study has confirmed the efficient electrical energy to chemical energy conversion (see Appendix, Section A3.9). All these above-described electrochemical parameters approve that the title **LiCu$_3$*para-D*** having {W^{VI}–OH} functionality is an efficient electrocatalyst for HER by water reduction.

3.3.3.2. Oxygen Evolution Reaction (OER) by Water Oxidation.

We have been working on electrocatalysis toward OER by water oxidation last several years and we found that transition metal-aqua coordination complexes, that are in a constrained confined space or supported on a POM cluster by coordination covalent bonds, can act as electrochemical OER catalysts.[67,68] However, there are not many reports with copper–aqua systems functioning as OER catalysts. The single-crystal X-ray crystallography of our title compound shows the presence of copper–aqua complexes $[\{Cu^{I}(H_2O)_{1.5}\}\{Cu^{II}(H_2O)_3\}_2]^{5+}$ as the linkers joining the POM clusters into the sole inorganic 3D architecture (*vide-supra*). Although, most of the known copper–aqua (Cu–OH_2) POM systems exhibit electrocatalytic HER,[69-71] in the present system, the Cu–OH_2 functionality of title **LiCu$_3$*para-D*** responds to electrocatalytic OER, even at the neutral pH. Figure 3.13a,b show the CV and LSV profiles of $[Li(H_2O)_4][\{Cu^{I}(H_2O)_{1.5}\}\{Cu^{II}(H_2O)_3\}_2\{W^{VI}{}_{12}O_{36}(OH)_6\}]\cdot N_2\cdot H_2S\cdot 3H_2O$ (**LiCu$_3$*para-D***), $[NH_4]_{10}[W_{12}O_{40}(OH)_2]\cdot 4H_2O$ (***para-B***) and CuO_x–GCE (CuO_x was electrochemically

deposited on GCE from a 1 mmol aqueous solution of copper sulfate, and this deposited CuO_x is termed as CuO_x–GCE in this work), and blank-GCE. As expected, ***para-D*** (devoid of the copper center), CuO_x–GCE, and blank–GCE are inactive in the anodic potential window as shown in Figure 7a,b. On the other hand, **$LiCu_3$*para-D*** (having Cu–OH_2 moieties) shows a prominent current surge at +1.52 V vs RHE, indicating the electrocatalytic water oxidation, mediated by the copper-aqua-complexes, present in **$LiCu_3$*para-D***. We could not find any other oxidative response for the Cu–OH_2 centers, other than the OER current surge (Figures 3.13a,b). We, therefore, performed the DPV experiment on the catalyst–modified GCE.

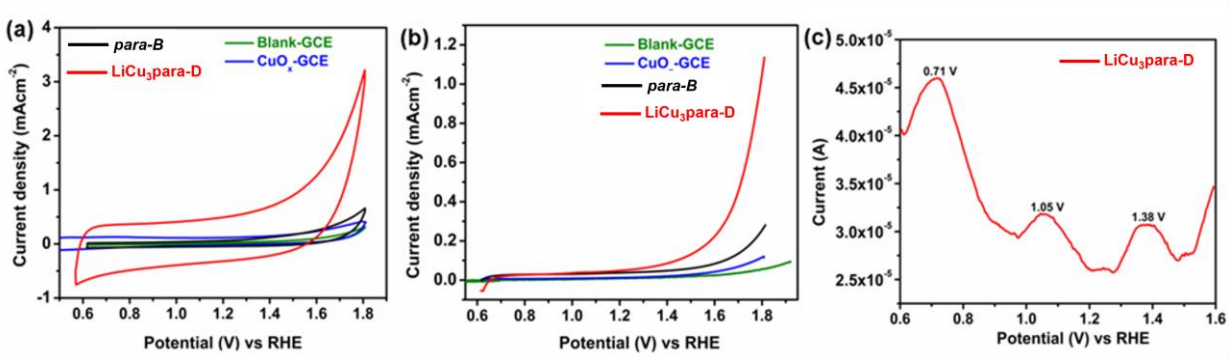

Figure 3.13. (a) Cyclic- and (b) linear-sweep voltammograms for compounds **$LiCu_3$*para-D*** and PARA-B, blank-GCE, and CuO_x-GCE (scan rate: 100 mV/s for CV and 10 mV/s for LSV); (c) DPV recorded for **$LiCu_3$*para-D*** in the anodic potential window prior to the onset potential, DPV was performed using the 50 mV pulse for 100 ms time and 5 mV step height for 80 ms step width and the integration time was 5 ms.

The DPV profile of **$LiCu_3$*para-D*** (Figure 3.13c) displays three distinct oxidative peaks centered at +0.71 V, +1.05 V, and +1.38 V vs RHE in the anodic potential window. The first oxidative response at +0.71 V can be assigned to the oxidation of $\{Cu^{I}(H_2O)_{1.5}\}^{+}$ species to $\{Cu^{II}(H_2O)_{1.5}\}^{2+}$ species; in other words, the oxidative response at 0.71 V vs RHE can be attributed to the couple, $\{Cu^{II}(H_2O)_{1.5}\}^{2+}$ / $\{Cu^{I}(H_2O)_{1.5}\}^{+}$. The response at +1.05 V can be assigned to $\{Cu^{III}(HO)\}$ / $\{Cu^{II}(H_2O)\}$ for both the species, $\{Cu^{II}(H_2O)_{1.5}\}^{2+}$ (formed electrochemically at +0.71V) and $\{Cu^{II}(H_2O)_3\}^{2+}$. Finally, the oxidative response at +1.38 V vs RHE on the DPV plot (Figure 7c) is attributed to $\{Cu^{IV}=O\}$ / $\{Cu^{III}(HO)\}$ couple. Right after this, the current surge at +1.52 V vs RHE is observed with the formation of visible oxygen bubbles suggesting electrocatalytic water oxidation to molecular oxygen, mediated by the copper-aqua complexes, as shown in equations 7-13. The existence of Cu(I) and Cu(II) centers in **$LiCu_3$*para-D*** has already been validated from SCXRD, BVS, and XPS analyses (*vide-supra*).

Equations 7-11 demonstrate proton-coupled electrochemical reactions leading to the formation of $[Cu^{IV}=O]^{2+}$group that can oxidize water chemically to form oxygen with the

regeneration of Cu(II) species (equations 12-13). This electrocatalytic water oxidation description (equations 7-13) is also supported by various literatures.[72-78]

$$[Cu^{I}(H_2O)]^{+} - e^{-} \rightarrow [Cu^{II}(H_2O)]^{2+} \quad (7)$$

$$[Cu^{II}(H_2O)]^{2+} - e^{-} \rightarrow [Cu^{III}(H_2O)]^{3+} \quad (8)$$

$$[Cu^{III}(H_2O)]^{3+} - H^{+} \rightarrow [Cu^{III}(OH)]^{2+} \quad (9)$$

$$[Cu^{III}(OH)]^{2+} - e^{-} \rightarrow [Cu^{IV}(OH)]^{3+} \quad (10)$$

$$[Cu^{IV}(OH)]^{3+} - H^{+} \rightarrow [Cu^{IV}{=}O]^{2+} \quad (11)$$

$$[Cu^{IV}{=}O]^{2+}/[Cu^{III}{-}O^{\bullet}]^{2+} + H_2O \rightarrow [Cu^{III}{-}O{-}O{-}H]^{2+} + e^{-} + H^{+} \quad (12)$$

$$[Cu^{III}{-}O{-}O{-}H]^{2+} \rightarrow [Cu^{II}]^{2+} + O_2 + e^{-} + H^{+} \quad (13)$$

In order to confirm the non-involvement of *in-situ* generated metal-oxide (CuO_x) nanoparticles in catalytic water oxidation (WO) activity, the CV and LSV of electrochemically prepared CuO_x–GCE were scanned in an identical condition and compared with that of title **$LiCu_3$*para-D***; the CuO_x–GCE has shown no similar features with that of **$LiCu_3$*para-D*** in the water oxidation (WO) window, confirming that the obtained WO activity, in the present work, is originated by the copper-aqua-complex of **$LiCu_3$*para-D*** (Figures 3.13a,b).

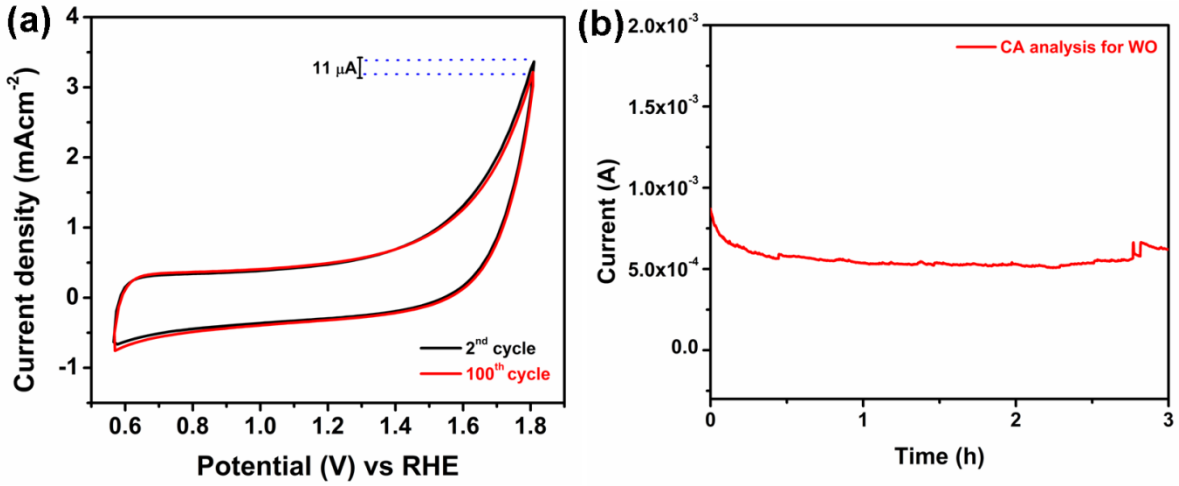

Figure 3.14. (a) Cycling stability analysis of **$LiCu_3$*para-D*** for oxygen evolution reaction for 100 CV cycles with a scan rate of 100 mVs^{-1}, in the neural pH of 0.1 M KCl electrolyte; (b) Chronoamperometry (CA) electrolysis of **$LiCu_3$*para-D*** conducted at 1.53 V vs RHE.

The stability of **$LiCu_3$*para-D*** as an oxygen evolution reaction (OER) catalyst is again investigated using similar techniques as used for hydrogen evolution reaction (HER) catalyst in the present work (*vide-supra*), *i.e.*, (i) by performing 100 CV cycles in the catalytic water oxidation potential window (from 0.55 to 1.8 V vs RHE; Figure 3.14a) and (ii) by using the **$LiCu_3$*para-D*** modified carbon paper as a working electrode for chronoamperometry (CA)

electrolysis for 3 hours at 1.53 V vs RHE (Figure 3.14b). No significant variations have been observed in the CV– and CA–plots in these respective two experiments, suggesting the stability of **LiCu$_3$*para-D*** under WO operational conditions (at neutral pH). Routine post–electrolysis studies of post–CA electrolysis electrode material by FTIR spectral studies (see Appendix, Figure A12), XPS analysis (see Appendix, Figures A3.13,14), and FESEM-EDX microscopy (see Appendix, Figures A3.15,16) have confirmed the molecular catalytic nature of **LiCu$_3$*para-D*** as a WO catalyst towards OER at neutral pH. Furthermore, the efficiency of **LiCu$_3$*para-D*** as an OER catalyst was assessed by determining routine kinetic parameters as described below.

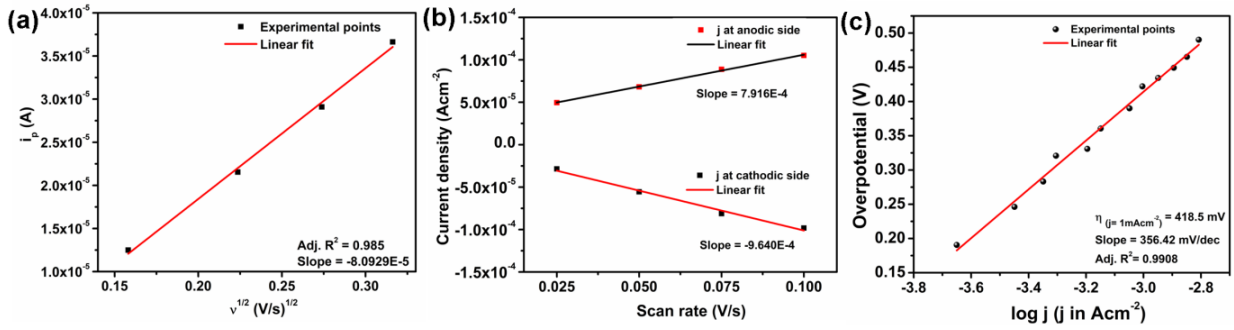

Figure 3.15. (a) Derived plots constructed with peak current (i_p) as a function of square root of scan rate (0.025 to 0.1 Vs^{-1}); (b) Plots of slopes of current density against scan rates at a potential of 0.35 V vs RHE illustrating the double layer capacitance for **LiCu$_3$*para-D***; (c) iR-corrected Tafel plot for **LiCu$_3$*para-D*** in the catalytic WO region.

A linear plot has been obtained when peak current is plotted against the square root of scan rates, indicating that the electrochemical OER reaction is diffusion controlled (Figure 3.15a). Similarly, an enhancement in capacitive current in the non-Faradaic region with an increase in scan rates of the concerned CV cycles for **LiCu$_3$*para-D*** has been observed (see Appendix, A3.11, for details) and the related C_{dl} value is found to be 8.578×10^{-4} Fcm^{-2} (Figure 3.15b). Tafel data collection was carried out for **LiCu$_3$*para-D*** at neutral pH in galvanostatic mode. A linear plot has been obtained with a Tafel slope value of 356.42 mV/dec for the OER catalytic region of **LiCu$_3$*para-D*** (Figure 3.15c). An overpotential of 418.5 mV was required to attain a current density of 1 mA/cm^2 at the neutral pH. Also, the TOF value, which gives insights into the electrocatalytic activities, has been obtained for **LiCu$_3$*para-D***, which is found to be 2.81 s^{-1} for the present electrocatalytic water oxidation (for details, see Appendix, A3.12).

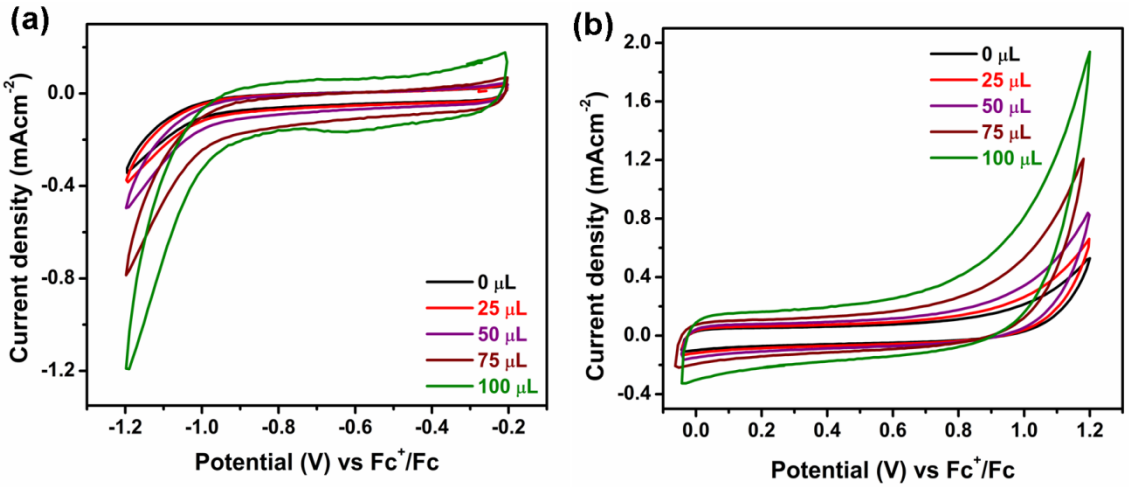

Figure 3.16. Non-aqueous medium cyclic voltammograms (CVs), performed under an inert atmosphere for LiCu3para-D, (a) showing the water reduction profiles in the cathodic region; (b) showing the water oxidation profiles in the anodic region. The CVs were collected during the sequential addition of water to the electrochemical cell (before adding water it was a dry acetonitrile solution having 0.1 M tetrabutylammonium perchlorate (TBA-ClO_4) as a supporting electrolyte and the CV data were collected with 100 mVs^{-1} scan rate).

From the quantitative measurements of evolved oxygen gas, the Faradaic efficiency of **$LiCu_3$*para-D*** was calculated to be 80% at neutral pH assuring that a good amount of electrical energy is converted to chemical energy in this electrocatalytic OER (for details see Appendix, A3.13). The electrochemical performance of **$LiCu_3$*para-D*** in terms of its overpotential value has been compared with the overpotential values of other well-established water splitting catalysts in Table S3.2 (Appendix), and we found that the present bifunctional **$LiCu_3$*para-D*** is a considerably efficient electrocatalyst for HER as well as for OER.

In order to comprehend, whether the HER and OER in the present work are the results of water reduction and water oxidation respectively, **$LiCu_3$*para-D*** modified GC-electrode was employed as a working electrode separately in the cathodic and anodic potential windows and the CV profiles were collected in a non-aqueous medium while adding a controlled and sequential amount of water. The sequential addition of water in both experiments results in linear growth in the cathodic as well as in the anodic catalytic currents (Figure 3.16a and 3.16b), suggesting the electrocatalytic water reduction and water oxidation behavior, respectively of **$LiCu_3$*para-D***. Further, to have insights into the present electrocatalytic HER and OER mechanism, CVs of **$LiCu_3$*para-D*** modified GC-electrode have been recorded in variable pH electrolytes from neutral pH to pH 4.0, separately in the cathodic and anodic potential windows, and the respective derived plots of potential (V against RHE; at a fixed 0.5 mA/cm^2 current) vs operative pH values have been constructed. In the case of HER, the slope value of –33.5 mV/pH (from the concerned derived plot) suggests the involvement of $2H^{+}$–$1e^{-}$, proton-coupled electron transfer (PCET) process in

electrocatalytic water reduction (Figure 3.17a). On the other hand, in the case of OER, the slope value of –20.38 mV/pH from the pertinent derived plot (Figure 3.17b), indicates the involvement of $1H^{+}$–$2e^{-}$ PCET path in electrocatalytic water oxidation.

In order to analyze the electrochemically generated gases, two individual bulk electrolysis experiments were performed: (i) with the catalyst-modified carbon paper (CP)–electrode as cathode for H_2 production (water reduction), and (ii) with catalyst-coated CP–electrode as an anode for O_2 generation (water oxidation). And, the electrochemically generated gases have been identified as H_2 and O_2 respectively by gas chromatography (Figures A3.19,20 in Appendix).

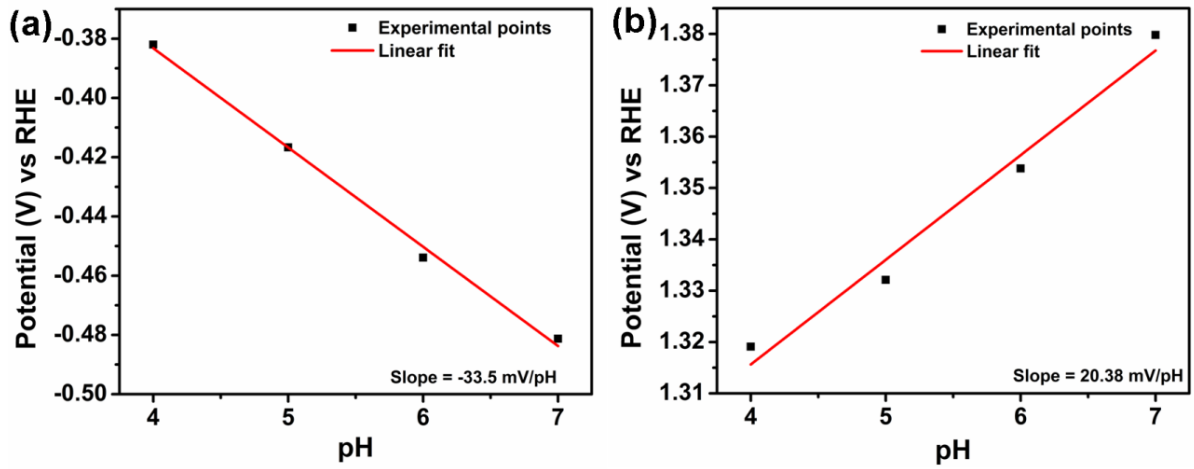

Figure 3.17. A plot of potential (V) *vs.* pH, where for every pH at a fixed current density of (a) -0.5 $mAcm^{-2}$ for HER; (b) 0.5 $mAcm^{-2}$ for OER, potential (E) was noted.

In the present work, in order to detect, whether any copper gets leached out during electrocatalytic HER and OER experiments, we performed ICP-OES analyses of the residual electrolyte solutions before and after CPE experiments for OER as well as HER. As shown in Figure A3.21 (Appendix), copper is not detectable from the residual electrolyte solutions for both HER and OER experiments after CPE.

3.4. CONCLUSIONS

The dual active sites for electrochemical water reduction (WR) and water oxidation (WO) are embedded in a single polyoxometalate (POM)-based compound $[Li(H_2O)_4][\{Cu^{I}(H_2O)_{1.5}\}\{Cu^{II}(H_2O)_3\}_2\{W^{VI}{}_{12}O_{36}(OH)_6\}]\cdot N_2\cdot H_2S\cdot 3H_2O$ (**$LiCu_3$*para-D***) and devised as a bifunctional electrocatalyst for hydrogen evolution reaction (HER) as well as oxygen evolution reaction (OER) by water reduction and water oxidation, respectively. The title compound represents a new paratungstate POM having six hydroxyl groups (paratungstate D). These $\{W^{VI}$-OH$\}$ groups of ‘paratungstate D’ act as the functional sites for water reduction and Cu(II)-aqua

species acts as the active site for water oxidation. The detailed electrochemical investigations including control experiments prove that the bifunctional catalyst is stable and efficient electrocatalyst toward water splitting (WS) at neutral pH. An overpotential of 443 mV is required to achieve a current density of 1 mA/cm^2 in the case of HER (water reduction) with a Faradaic efficiency of 92% and a turnover frequency of 4.66 s^{-1}. In the case of OER (by water oxidation), the overpotential of 418 mV is needed to achieve a current density of 1 mA/cm^2 with a Faradaic efficiency of 88% and turnover frequency of 2.81 s^{-1}. **$LiCu_3$*para-D*** claims to be the first polyoxometalate (POM) compound acting as a dual functional molecular electrocatalyst at the neutral pH. This work has provided new insights into the development of noble-metal-free efficient multi-functional electrocatalysts for clean energy generation from water.

3.5. REFERENCES

1. Roger, I.; Shipman M. A.; Symes, M. D. Earth-abundant catalysts for electrochemical and photoelectrochemical water splitting. *Nat. Rev. Chem.* **2017**, *1*, 3.
2. Formal, F. L.; Bourée, W. S.; Prévot M. S.; Sivula, K.; Challenges towards economic fuel generation from renewable electricity: the need for efficient electro-catalysis. *Chimia*, **2015**, *69*, 789-798.
3. Li, X.; Zhao, L.; Yu, J.; Liu, X.; Zhang, X.; Liu H.; Zhou, W. Water splitting: From electrode to green energy system. *Nano-Micro. Lett.* **2020**, *12*, 131.
4. Tian, L.; Li, Z.; Song M.; Li, J. Recent progress in water-splitting electrocatalysis mediated by 2D noble metal materials. *Nanoscale*, **2021**, *13*, 12088-12101.
5. Li, Y.; Sun, Y.; Qin, Y.; Zhang, W.; Wang, L.; Luo, M.; Yang, H.; Guo, S. Recent advances on water-splitting electrocatalysis mediated by noble-metal-based nanostructured materials. *Adv. Energy Mater.* **2020**, *10*, 1903120.
6. Tian, L.; Li, Z.; Xu X.; Zhang, C. Advances in noble metal (Ru, Rh, and Ir) doping for boosting water splitting electrocatalysis. *J. Mater. Chem. A.* **2021**, *9*, 13459-13470.
7. Ao, K.; Wei, Q.; Daoud, W. A. MOF-Derived sulfide-based electrocatalyst and scaffold for boosted hydrogen production. *ACS Appl. Mater. Interfaces*, **2020**, *12*, 33595–33602.
8. Guo, Y.; Zhou, X.; Tang, J.; Tanaka, S.; Kaneti, Y. V.; Na, J.; Jiang, B.; Yamauchi, Y.; Bando, Y.; Sugahara, Y. Multiscale structural optimization: Highly efficient hollow iron-doped metal sulfide heterostructures as bifunctional electrocatalysts for water splitting. Nano Energy, **2020**, *75*, 104913.
9. Guo, Y.; Zhang, C.; Zhang, J.; Dastafkan, K.; Wang, K.; Zhao, C.; Shi, Z. Metal−organic framework-derived bimetallic NiFe selenide electrocatalysts with multiple phases for efficient oxygen evolution reaction. *ACS Sustainable Chem. Eng.* **2021**, *9*, 2047–2056.
10. Septiani, N. L. W.; Kaneti, Y. V.; Guo, Y.; Yuliarto, B.; Jiang, X.; Ide, Y.; Nugraha, N.; Dipojono, H. K.; Yu, A.; Sugahara, Y.; Golberg, D.; Yamauchi, Y. Holey assembly of two-dimensional iron-doped nickel-cobalt layered double hydroxide nanosheets for energy conversion application. *ChemSusChem*, **2020**, *13*, 1645 –1655.
11. Hu, S.; Wang, S.; Feng, C.; Wu, H.; Zhang, J.; Mei, H. Novel MOF-derived nickel nitride as high-performance bifunctional electrocatalysts for hydrogen evolution and urea oxidation. *ACS Sustainable Chem. Eng.* **2020**, *8*, 7414–7422.
12. Septiani, N. L. W.; Kaneti, Y. V.; Fathoni, K. B.; Guo, Y.; Ide, Y.; Yuliarto, B.; Jiang, X.; Nugraha, N.; Dipojono, H. K.; Golberg, D.; Yamauchi, Y. Tailorable nanoarchitecturing of bimetallic nickel–cobalt hydrogen phosphate via the self-weaving of nanotubes for efficient oxygen evolution. *J. Mater. Chem. A.* 2020, **8**, 3035-3047.

13. Wang, H.; Lee, H-W.; Deng, Y.; Lu, Z.; Hsu, P.-C.; Liu, Y.; Lin D. Cui, Y. Bifunctional non-noble metal oxide nanoparticle electrocatalysts through lithium-induced conversion for overall water splitting. *Nat. Commun*. **2015**, *6*, 7261.
14. Khan, R.; Mehran, M. T.; Naqvi, S. R.; Khoja, A. H.; Mahmood, K.; Shahzad, F.; Hussain, S. Role of perovskites as a bi-functional catalyst for electrochemical water splitting: A review. *Int. J. Energy Res.* **2020**, *44*, 9714–9747.
15. Das, J. K.; Samantara, A. K.; Nayak, A. K.; Pradhan, D.; Behera, J. N. VS 2: An efficient catalyst for an electrochemical hydrogen evolution reaction in an acidic medium. *Dalton Trans.* **2018**, *47*, 13792–13799.
16. Natali, M.; Bazzan, I.; Goberna-Ferrón, S.; Al-Oweini, R.; Ibrahim, M.; Bassil, B. S.; Dau, H.; Scandola, F.; Galán-Mascarós, J. R.; Kortz, U.; Sartorel, A.; Zaharieva, I.; Bonchio, M. Photo-assisted water oxidation by high-nuclearity cobalt-oxo cores: tracing the catalyst fate during oxygen evolution turnover. *Green Chem*., **2017**, *19*, 2416-2426.
17. Al-Oweini, R.; Sartorel, A.; Bassil, B. S.; Natali, M.; Berardi, S.; Scandola, F.; Kortz, U.; Bonchio, M. Photocatalytic water oxidation by a mixed-valent $Mn^{III}{}_3Mn^{IV}O_3$ manganese oxo core that mimics the natural oxygen-evolving center. *Angew. Chem. Int. Ed*. **2014**, *53*, 11182 –11185.
18. Fried, J.; Al-Oweini, R.; Herpich, M.; Keita, B.; Kortz, U.; Stimming, U. Electrochemical studies of tri-manganese substituted Keggin polyoxoanions. *Electrochimica Acta*, **2014**, *141*, 357–366.
19. Li, J-S.; Tang, Y-J.; Liu, C.-H.; Li, S.-L.; Li, R.-H.; Dong, L.-Z.; Dai, Z.-H.; Bao J.-C.; Lan, Y.-Q. Polyoxometalate-based metal–organic framework-derived hybrid electrocatalysts for highly efficient hydrogen evolution reaction. *J. Mater. Chem. A*. **2016**, *4*, 1202–1207.
20. Gao, D.; Trentin, I.; Schwiedrzik, L.; González, L.; Streb, C.; The reactivity and stability of polyoxometalate water oxidation electrocatalysts. *Molecules*, **2020**, *25*, 157.
21. Luo, W.; Hu, J.; Diao, H.; Schwarz, B.; Streb, C.; Song, Y.-F. Robust polyoxometalate/nickel foam composite electrodes for sustained electrochemical oxygen evolution at high pH. *Angew. Chem. Int. Ed.*, **2017**, *56***,** 4941–4944.
22. Zhang, Q.; Li, F.; Xu, L. Application of polyoxometalates in third-generation solar cells. *Polyoxometalates*, **2023**, *2*, 9140018.
23. Sumliner, J. M.; Lv, H.; Fielden, J.; Geletii, Y. V.; Hill, C. L. Polyoxometalate multi-electron-transfer catalytic systems for water splitting. *Eur. J. Inorg. Chem.* **2014**, *2014*, 635-644.
24. Li, N.; Liu, J.; Dong, B.-X.; Lan, Y.-Q. Polyoxometalate-based compounds for photo- and electrocatalytic applications. *Angew. Chem. Int. Ed.* **2020**, *59*, 20779-20793.
25. Lv, H.; Gao, Y.; Guo, W.; Lauinger, S. M.; Chi, Y.; Bacsa, J.; Sullivan, K. P.; Wieliczko, M.; Musaev D. G.; Hill, C. L. Cu-based polyoxometalate catalyst for efficient catalytic hydrogen evolution. *Inorg. Chem.* **2016**, *55*, 6750–6758.
26. von Allmen, K. D.; Grundmann, H.; Linden A.; Patzke, G. R. Synthesis and characterization of 0D–3D copper-containing tungstobismuthates obtained from the lacunary precursor $Na_9[B\text{-}\alpha\text{-}BiW_9O_{33}]$. *Inorg. Chem.* **2017**, *56*, 327−335.
27. Chen Z.; Meyer, T. J. Copper (II) catalysis of water oxidation. *Angew. Chem. Int. Ed.* **2013**, *52*, 700 – 703.
28. Lee, H.; Wu, X.; Sun, L. Copper-based homogeneous and heterogeneous catalysts for electrochemical water oxidation. *Nanoscale*, **2020**, *12*, 4187.
29. Barnett, S. M.; Goldberg K. I.; Mayer, J. M. A soluble copper–bipyridine water-oxidation electrocatalyst. *Nat. Chem.* **2012**, *4***,** 498–502.
30. Yu, L.; Lin, J.; Zheng, M.; Chen M.; Ding, Y. Homogeneous electrocatalytic water oxidation at neutral pH by a robust trinuclear copper (II)-substituted polyoxometalate. *Chem. Commun.* **2018**, *54*, 354-357.
31. Jana, D.; Kolli, H. K.; Sabnam S.; Das, S. K. Efficient homogeneous electrocatalytic hydrogen evolution using a Ni-containing polyoxometalate catalyst. *Chem. Commun.* **2021**, *57*, 9910.
32. Mulkapuri, S.; Ravi, A.; Das, S. K. Fabricating a functionalized polyoxometalate with ZIF-8: A composite material for water oxidation in a wide pH range. *Chem. Mater.* **2022**, *34*, 3624−3636.

33. Mukhopadhyay, S.; Debgupta, J.; Singh, C.; Kar A.; Das, S. K. A Keggin polyoxometalate shows water oxidation activity at neutral pH: POM@ZIF-8, an efficient and robust electrocatalyst. *Angew. Chem. Int. Ed.* **2018**, *57*, 1918–1923.
34. Singh, C.; Mukhopadhyay, S.; Das, S. K. Polyoxometalate-supported bis (2, 2′-bipyridine) mono (aqua) nickel (ii) coordination complex: an efficient electrocatalyst for water oxidation. *Inorg. Chem.* **2018**, *57*, 6479-6490.
35. Manna, P.; Debgupta, J.; Bose, S.; Das, S. K. A mononuclear Co^{II} coordination complex locked in a confined space and acting as an electrochemical water-oxidation catalyst: A "Ship-in-a-Bottle" Approach. *Angew. Chem. Int. Ed.* **2016**, *55*, 2425-2430.
36. Kolli, H. K.; Jana D.; Das, S. K. Nanoblackberries of $\{W_{72}Fe_{33}\}$ and $\{Mo_{72}Fe_{30}\}$: electrocatalytic water reduction. *Inorg. Chem.* **2021**, *60*, 15569−15582.
37. Jana, D.; Kolli, H. K.; Das, S. K. Single crystals of α-MoO_3-intercalated $\{Ni(H_2O)_6\}^{2+}$ and electrocatalytic water reduction: toward a class of molybdenum bronzes. *Inorg. Chem.* **2022**, *61*, 3816-3820.
38. Mulkapuri, S.; Ravi, A.; Nasani, R.; Kurapati, S. K.; Das, S. K. Barrel-shaped-polyoxometalates exhibiting electrocatalytic water reduction at neutral pH: A synergy effect. *Inorg. Chem.* **2022**, *35*, 13868–13882.
39. Mulkapuri, S.; Ravi, A.; Mukhopadhyay, S.; Kurapati, S. K.; Siby V.; Das, S. K. W^{VI}–OH functionality on polyoxometalates for water reduction to molecular hydrogen. *Inorg. Chem. Front.* **2022**, *9*, 3566-3577.
40. Sheldrick, G. M., SADABS, Program for absorption correction. University of Gottingen, Gottingen, Germany, **1997**.
41. Dolomanov, O.V.; Bourhis, L.J.; Gildea, R.J.; Howard, J.A.K.; Puschmann, H., Olex2: A complete structure solution, refinement and analysis program. *J. Appl. Cryst.* **2009**, *42*, 339-341.
42. Sheldrick, G.M. *Acta Cryst.* **2015**, *C71*, 3-8. The SHELX-97 Manual. http://linux.uniac.gwdg.de/SHELX/
43. Bourhis, L. J.; Dolomanov, O. V.; Gildea, R. J.; Howard, J. A. K.; Puschmann, H. The anatomy of a comprehensive constrained, restrained refinement program for the modern computing environment - *Olex2* dissected. *Acta Cryst.* **2015**, *A71*, 59-75.
44. Fdz-Polanco, F.; Fdz-Polanco, M.; Fernandez, N.; Urueña, M. A.; Garcia, P. A.; Villaverde, S. New process for simultaneous removal of nitrogen and sulphur under anaerobic conditions. *Water Res.* **2001**, *35*, 1111-1114.
45. Vanysek, P. Electrochemical series. *CRC handbook of chemistry and physics*, **2000**, *8*, 8-33.
46. Gao, S.; Zhao, J.; Zhou, B.; Yu, K.; Su, Z.; Wang, L.; Yin, Y.; Zhao, Z.; Yu, Y.; Chen. Y. Four novel polytungstate compounds built up of paradodecatungstate clusters and transition-metal complexes/transition metal: Synthesis, structure, and electrochemical properties. *Inorg. Chim. Acta*, **2011**, *379*,151-157.
47. Radio, S. V.; Melnik, N. A.; Ivantsova, E. S.; Baumer, V. N. Crystal structure of double sodium-copper(II) paratungstate B: $Na_2Cu_3(CuOH)_2[W_{12}O_{40}(OH)_2]\cdot 32H_2O$. *J. Struct. Chem.* **2014**, *55*, 879-886.
48. Li, B.; Bi, L.; Li. W. Synthesis, crystal structure, and property of one- and two-dimensional complexes based on paradodecatungstate-B cluster. *J. Solid State Chem.* **2008**, *181*, 3337-3343.
49. Gumerova, N. I.; Dobrov, A.; Rollerb A.; Rompel, A. Iron (II) and copper (II) paratungstates B: A single-crystal X-ray diffraction study. *Acta Cryst.* **2018**, *74*, 1252–1259.
50. Qu, X.; Yang, Y.; Zhang, F.; Yu. X. Synthesis and characterization of a three-dimensional framework built up of paradodecatungstate-B clusters and transition metals as linkers. *J. Struct. Chem.* **2012**, *23*, 1867-1872.
51. Qu, X.; Yang, Y.; Yu, X.; Lv, Z.; Ji, M.; Feng. S. Y. A novel paradodecatungstate-B compound decorated by transition metal copper, $Na_2Cu_5(H_2O)_{24}(OH)_2[H_2W_{12}O_{42}]\cdot 10H_2O$: Synthesis, structure and antitumor activities. *Inorg. Chem. Commun*. **2015**, *60*, 126-130.
52. Li, Y. W.; Wang, Y.-H.; Li. Y.-G. A new (8,3)-connected anionic 3-D open-framework based on paradodecatungstate and Cu^{II} linkers. *Inorg. Chim. Acta*, **2009**, *362*, 1078-1082.

53. Kong, Q.-J.; Zhang, C.-J.; Chen. Y.-G. Synthesis, structure and characterization of three highly-connected 3D inorganic compounds based on paradodecatungstate-B**.** *J. Mol. Struct*. **2010**, 964, 82-87.
54. Chen, Y.; Zhang, C.; Zhang, J.; Ye, Z.; Zheng, K.; Fang. Q.; Cu-Induced $[H_6W_{12}O_{42}]^{6-}$ polyoxometalate-based bimetallic cluster formation for renewable biomass inulin hydrolysis toward fructose production**.** *Inorg. Chem. Front*. **2017**, *4*, 1917-1922.
55. Zhang, C.-J.; Chen, Y.-G.; Shi, D.-M.; Pang. H.-J. *Z.* Synthesis and characterization of a three-dimensional porous compound: $[Cu(H_2O)_6][\{Cu(H_2O)_2\}_2\{Cu(H_2O)_4H_4W_{12}O_{42}\}]\cdot 12H_2O$. *Naturforsch. B.* **2008**, *63*, 187-192.
56. Zhang, Z. Two novel purely inorganic coordination polymers constructed from bivalent transition metal ions and paratungstate clusters. *Chem. Crystallogr.* **2012**, *42*, 333–337.
57. O'Keefe, M.; Brese, N. E., Atom sizes and bond lengths in molecules and crystals. *J. Am. Chem. Soc.* **1991**, *113*, 3226-3229.
58. Xua, W.-Q.; Hea, S.; Liua, S.-J.; Liua, X.-H.; Qiua, Y.-X.; Liua, W.-T.; Liua, X.-J.; Jianga, L.-C.; Jiang, J.-J., Post-synthetic modification of a metal-organic framework based on 5-aminoisophthalic acid for mercury sorption. *Inorg. Chem. Commun*. **2019**, *108*, 107515.
59. Ray, P.; Xu, E.; Crespi, V. H.; Badding, J. V.; Lueking, A. D. *In situ* vibrational spectroscopy of adsorbed nitrogen in porous carbon materials. *Phys. Chem. Chem. Phys.* **2018**, *20*, 15411-15418.
60. Barr, T. L. An ESCA study of the termination of the passivation of elemental metals. *J. Phys. Chem.* **1978**, *82*, 1801-1810.
61. Swadźba-Kwaśny, M.; Chancelier, L.; Ng, S.; Manyar, H. G.; Hardacre, C.; Nockemann, P. Facile *in-situ* synthesis of nanofluids based on ionic liquids and copper oxide clusters and nanoparticles. *Dalton Trans.* **2012**, *41*, 219-227.
62. Rauf, A.; Sher Shah, M. S. A.; Choi, G. H.; Humayoun, U. B.; Yoon, D. H.; Bae, J. W.; Park, J.; Kim, W.-J.; Yoo, P. J., Facile synthesis of hierarchically structured Bi_2S_3/Bi_2WO_6 photocatalysts for highly efficient reduction of Cr(VI). *ACS Sustain. Chem. Eng.* **2015**, *3*, 2847-2855.
63. Shi, Y.; Chen, Y.; Tian, G.; Fu, H.; Pan, K.; Zhou, J.; Yan, H., One-pot controlled synthesis of sea-urchin shaped Bi_2S_3/CdS hierarchical heterostructures with excellent visible-light photocatalytic activity. *Dalton Trans.* **2014**, *43*, 12396-12404.
64. Shah, D.; Bahr, S.; Dietrich, P.; Meyer, M.; Thißen, A.; Linford, M. R. Nitrogen gas (N_2), by near-ambient pressure XPS. *Surf. Sci. Spectra*, **2019**, *26*, 014023.
65. Hsu, J.-C.; Lin, Y.-H.; Wang, P. W. X-ray photoelectron spectroscopy analysis of nitrogen-doped TiO_2 films prepared by reactive-ion-beam sputtering with various NH_3/O_2 gas mixture ratio. *Coatings*, **2020**, *10*, 47.
66. Morajkar, S. M.; Srinivasan, B. R. Synthesis, spectral and structural characterization of organic ammonium paratungstates. *Indian J. Chem.* **2021**, *60*, 185-195.
67. Mukhopadhyay, S.; Basu, O.; Kar, A.; Das, S. K. Efficient Electrocatalytic Water Oxidation by Fe(salen)−MOF Composite: Effect of Modified Microenvironment. *Inorg. Chem*. **2020**, *59*, 472−483.
68. Mukhopadhyay, S.; Basu, O.; Nasani, R.; Das, S. K. Evolution of metal organic frameworks as electrocatalysts for water oxidation. *Chem. Commun.* **2020**, *56*, 11735-11748.
69. Singh, C.; Haldar, A.; Basu, O.; Das, S. K. Devising a polyoxometalate-based functional material as an efficient electrocatalyst for the hydrogen evolution reaction. *Inorg. Chem.* **2021**, *60*, 10302–10314.
70. Singh, C.; Das, S. K. Anderson polyoxometalate supported $Cu(H_2O)$(phen) complex as an electrocatalyst for hydrogen evolution reaction in neutral medium. *Polyhedron*, **2019**, *172*, 80-86.
71. Kim, Y.; Shanmugam, S. Polyoxometalate–reduced graphene oxide hybrid catalyst: synthesis, structure, and electrochemical properties. *ACS Appl. Mater. Interfaces*. **2013**, *5*, 12197-12204.
72. Ding, Y.-X.; Zheng, Q.-H.; Peng, M.-T.; Chen, C.; Zou, K.-F.; Dong, B.-X.; Liu, W.-L.; Teng, Y.-L. A new ε-Keggin polyoxometalate-based metal-organic framework: From design and synthesis to electrochemical hydrogen evolution. *Catal. Commun.* **2021**, *161*, 106367.
73. Geer, A. M.; Musgrave III, C.; Webber, C.; Nielsen, R. J. McKeown, B. A.; Liu, C.; Schleker, P. P. M.; Jakes, P.; Jia, X.; Dickie, D. A.; Granwehr, J.; Zhang, S.; Machan, C. W.; Goddard III, W. A.; Gunnoe, T. B. Electrocatalytic water oxidation by a trinuclear copper (II) complex. *ACS Catal.* **2021**, *11*, 7223−7240.

74. Shen, J.; Wang, M.; Zhang, P.; Jianga J.; Sun, L. Electrocatalytic water oxidation by copper (II) complexes containing a tetra-or pentadentate amine-pyridine ligand. *Chem. Commun.* **2017**, *53*, 4374–4377.
75. Kumar, N. T.; Bhoi, U.; Naulakha P.; Das, S. K. A polyoxometalate supported copper dimeric complex: Synthesis, structure and electrocatalysis. *Inorganica Chim. Acta*. **2020**, *506*, 119554.
76. Su, X.-F.; Guan, W.; Yan L.-K.; Su, Z.-M. Tricopper-polyoxometalate catalysts for water oxidation: Redox-inertness of copper center. *J. Catal.* **2020**, *381*, 402–407.
77. Lin, J.; Wang, Chen, X.; Wang, N.; Liu, S.; Chen, Y.; Tian, Z.; Ruan, Z. Octanuclear Cu(II) cluster–tungstosilicate composite as efficient electrocatalyst for oxygen evolution reaction at near-neutral pH. *Sustain. Energy Fuels*, **2022**, *6*, 223–230.
78. Zhang, M.-T.; Chen, Z.; Kang, P.; Meyer, T. J. Electrocatalytic water oxidation with a copper(II) polypeptide complex. *J. Am. Chem. Soc.* **2013**, *135*, 2048−2051.

Chapter 4

Tungsten–hydroxyl on Polyoxotungstate Surface: Persistent Electrocatalyst for HER

OVERVIEW

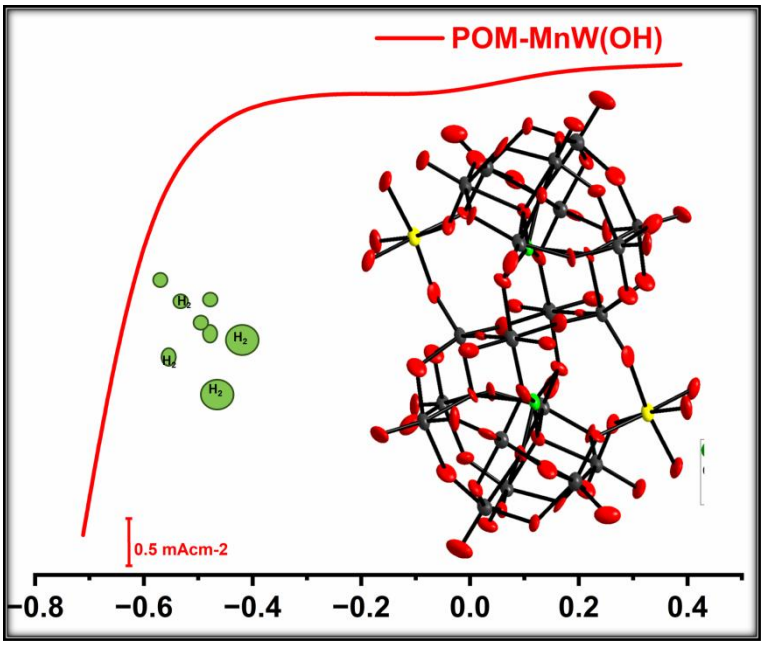

Transition metal-hydroxyl, M–OH is recognized as one of the vital mass transport agents, including in the clean energy cycle. In this work, a tungsten-hydroxyl, W^{VI}–OH, tethered polyoxometalate (POM) complex, $Na_6[\{W^{VI}_{0.75}(OH)(ONa)\}_2\{Mn^{II}(H_2O)_2\}_2\{BiW^{VI}_9O_{33}\}_2]\cdot 18H_2O$ (**1**), has been synthesized in an aqueous synthesis and structurally characterized as a 2-D framework material. The presence of tungsten-hydroxyl groups on the surface of the POM of compound **1** has driven us to investigate electrocatalytic hydrogen evolution reaction (HER). Compound **1** shows excellent hydrogen evolution reaction (HER) activity with a TOF value of 1.81 s^{-1} and long-term stability of 1000 cyclic voltammetric cycles besides its stability of 10 hours of chronoamperometry in an acidic buffer environment of pH 4.0.

4.1. INTRODUCTION

With the advancement in science and technology, the growing demand for innovative materials, particularly in energy-related fields, has always motivated the world scientific community. Thus, it is the *need of the hour* to devise such new materials with outstanding electrochemical properties to meet the demands of the growing population.[1]

Polyoxometalates (POMs) stand for a unique class of polynuclear metal-oxygen cluster complexes constructed by bridging oxygen atoms with two or more metals.[2,3] POMs possess various definite structures and exhibit unique physical and chemical properties. The ability to tailor or configure the redox properties, features to be one of the fascinating highlights of POMs, which has paved a potential path in the development of diverse functional systems.[4] Owing to various properties like inherent resistance to oxidative decomposition, high thermal stability, and impressive sensitivity to light and electricity, POMs are utilized as excellent molecular catalysts.[5] Also, POMs are activated by incorporating various conductive materials. The chemical modifications of POM structures have put forth a wider chance of exploiting the synergistic effects of POM-based materials, which in turn open a new class of materials in energy and conductivity applications.[6]

On the other hand, the scarcity and harsh consequences arising from the extensive utilization of fossil fuels for energy consumption in the world have urged researchers to develop new materials and/or techniques to switch away from the fossil fuel-dependent economy. An alternative yet one of the best techniques to tackle the above-mentioned challenges is to utilize hydrogen gas, which is considered to be the potential future fuel, with a high energy density of 146 kJ/g.[7] The global agencies and scientific world have already commenced to develop novel materials that help in generating green H_2 as well as utilize them in fuel cells for clean energy harnessing.

In this regard, electrochemical splitting of water is practiced as one of the cleaner ways to produce H_2 gas, wherein non-noble transition metal-based electrocatalysts have shown its tremendous demand. The era of utilizing noble metal based electrocatalysts is slowly vanishing due to their less availability and exorbitant cost, with the replacement of earth-abundant transition metal based electrocatalysts for water splitting.[8] Owing to this fact, Lv *et al*. have shown an exciting approach of tailoring -$Ni(OH)_2$ on the tungsten nitride nanowire surfaces to offer an enhanced alkaline hydrogen evolution reaction for electrochemical water splitting.[9] Liu et al. reviewed metal alkoxide-based catalysts, and their derivatives (hydroxides, oxides, phosphides, and selenides) for electrochemical water splitting.[10] Building on these seminal studies, the strategy of grafting/incorporating hydroxyl moieties onto metal surfaces has received immense scientific attraction due to their proactive nature toward catalytic water splitting.[11-13] It is noteworthy that there are various reports where these metal-hydroxyl tethered catalysts have been employed for electrical conductivity due to their higher accessibility for reaction and electron/mass transport paths.[14-16]

Herein, we have synthesized and structurally characterized a Krebs-type POM-based compound where a $[\{W^{VI}_{0.75}(OH)(ONa)\}_2\{Mn^{II}(H_2O)_2\}_2]$ core is sandwiched by two $\{Bi^{III}W^{VI}_9O_{33})\}^{9-}$ units. The compound has been formulated as $Na_6[\{W^{VI}_{0.75}(OH)(ONa)\}_2\{Mn^{II}(H_2O)_2\}_2\{BiW^{VI}_9O_{33}\}_2]\cdot 18H_2O$ (**POM-MnW(OH)**). In 1999, Krebs and co-workers developed a unique set of sandwiched-type POMs,[17] which were further taken forward for anti-cancer activities by Wang et al.[18-20] Our group recently started exploring the energy applications of similar types of POMs that incorporate the W–OH groups into them.

The W^{VI}–OH structure-functional relationship for hydrogen evolution reaction (HER) has been proven extensively in our previous works.[21,22] The present work reveals an addition to the library of Krebs-type POMs, wherein here, the tungsten present on the surface of the POM cluster is grafted with a tungsten-hydroxyl, W^{VI}–OH group (along with W–ONa or W–O^- moiety; the complex moiety, $[\{W^{VI}_{0.75}(OH)(ONa)\}_2\{Mn^{II}(H_2O)_2\}_2]$, present in the sandwich zone of the compound, **POM-MnW(OH)**, has been experimentally shown to be the active site for water reduction at acidic pH and the title compound acts as a solid-state proton conductor too (see next chapter). The HER action and the solid-state proton conduction could be a useful contribution to the clean energy cycle that is energy storage in the form of molecular H_2 from water and as the proton transfer medium for the formation of water.

Thus, we have designed and developed a POM-based solid-oxide-based material, $Na_6[\{W^{VI}_{0.75}(OH)(ONa)\}_2\{Mn^{II}(H_2O)_2\}_2\{BiW^{VI}_9O_{33}\}_2]\cdot 18H_2O$ (**POM-MnW(OH)**) that acts as an excellent HER electrocatalyst with a stability of 1000 multiple CV cycles and a promising super proton conductor with a conductivity value of 1.07×10^{-1} S cm^{-1} (at 80 °C and 98% RH). The detailed heterogeneous catalytic hydrogen evolution reaction (HER) mediated by **POM-MnW(OH)** is discussed in this chapter including its kinetic details.

4.2. EXPERIMENTAL SECTION

4.2.1. Materials

The chemicals used for the synthesis were of analytical grade which are commercially available and used without any further purification. Lithium tungstate (Li_2WO_4, 98%) was purchased from Sigma Aldrich, India. Bismuth nitrate pentahydrate ($Bi(NO_3)_3\cdot 5H_2O$, 98%) was purchased from Alfa Aesar, India. Manganese acetate was purchased from India. Nitric acid extra-pure and ammonia solution extra pure were purchased from Finar chemicals.

Double distilled water was utilized to carry out all the syntheses and Milli-Q water for electrochemical experiments.

4.2.2. Synthesis

4.2.2.1. Synthesis of $Na_6[\{W^{VI}_{0.75}(OH)(ONa)\}_2\{Mn^{II}(H_2O)_2\}_2\{BiW^{VI}_9O_{33}\}_2]\cdot 18H_2O$ (POM-MnW(OH)).

In a typical sythesis, 3g (10.22 mmol) of $Na_2WO_4.2H_2O$ was dissolved in 50 mL of distilled water and subsequently 0.5 mL of 6 M $HNO_3$was added. The reaction mixture was heated to 90 ℃ on a hot plate under stirring for 15 minutes. An aqueous solution of $Mn(CH_3COO)_2\cdot 4H2O$ (0.5 g in 2 mL of water) was added dropwise to the above reaction mixture with continuous stirring upon which the colour of the reaction mixture turned bright yellow from colourless. Subsequently, an acidic solution of bismuth nitrate (1.03 mmol, 0.49 g of $Bi(NO_3)_3\cdot 5H_2O$ dissolved in 1 mL of 6 M HNO_3) was added to the solution at 90 °C. The reaction mixture was then treated with and stirred for another 15 minutes. Next, the pH of the reaction mixture was adjusted to 8.25 using a 15% aqueous ammonia solution. And the reaction was carried out under the same reaction conditions for another one hour. The resultant reaction mixture was filtered twice to obtain a clear filtrate. It was left for crystallization at room temperature to obtain yellow color block–type crystals after 2 weeks. The obtained crystals of **POM-MnW(OH)** were separated by filtration and washed with ice–cold water and dried under ambient conditions. Yield: 21.7% based on manganese.

4.2.3. Methods

4.2.3.1. Physical Characterizations

The characterization techniques used includes PXRD, FTIR, TGA, Raman analysis, FESEM-EDX, ICP-OES, XPS analysis, UV-DRS analysis and so on. The details of the instruments used for carrying out these characterization analyses have already been discussed in the previous chapter under the Section 3.2.3.1.

4.2.3.2. Single-crystal X-ray Diffraction (SC-XRD) Analysis. A nascent single-crystal of compound $Na_6[\{W^{VI}_{0.75}(OH)(ONa)\}_2\{Mn^{II}(H_2O)_2\}_2\{BiW^{VI}_9O_{33}\}_2]\cdot 18H_2O$ (**POM-MnW(OH)**) was mounted on a glass-fiber tip for X-ray diffraction data collection at 100 K. The single crystals of compound **POM-MnW(OH)** are found to be sensitive at room temperature, which could quickly lose their quality. The disorder in the crystal structure mainly occurred due to the presence of heavy elements like bismuth and tungsten in the structure. Additionally, the crystal structure has shown the highest difference peak of 4.881

with the deepest hole -3.771, which falls below 1 Å distance from heavy elements. The framework oxygen atoms (O_3, O_5, O_{12}, O_{15} and O_{29}) and oxygen atoms of lattice water (O_{35} and O_{42}) have shown atomic displacement parameter (ADP) disorder; and the respective ADP alerts possessing oxygen atoms were refined with crystallographically allowed SHELXTL (EADP) command. Similarly, tungsten centers (W_9 with 0.73298 and W_6 with 0.98765 occupancies) displaying electron-occupancy disorder were treated using occupancy factor free-refinement and their occupancies were constrained. the crystallographic details and structure refinement parameters for **POM-MnW(OH)** are listed in Table 4.1.

Table 4.1. Crystal data and structure refinement for **POM-MnW(OH)**

Parameter	**POM-MnW(OH)**
Empirical formula	$Bi_2Mn_2Na_6O_{88}W_{19.47}$
Formula weight	5652.42
T(K)/ λ (Å)	293(2) K/0.71073
Crystal system	Monoclinic
Space group	P 21/n
Unit cell dimensions	a = 13.1922(3) Å b = 18.1891(5) Å c = 19.7810(7) Å α = 90° β = 97.226(3)° γ= 90°
Volume	4708.8(2) $Å^3$
Z	2
Density (calculated)	3.987 Mg/m^3
Absorption coefficient (M)	27.773 mm^{-1}
F(000)	4853
Independent reflections	8294 [R(int) = 0.2099]
Goodness-of-fit on F^2	1.044
R1/ wR2 [I > 2σ (I)]	0.0846/0.2152
R1/ wR2 (all data)	0.1183/0.2388
Theta range for data collection	1.917 to 24.999°
Data completeness	100 %
Largest diff. peak and hole	4.881 and -3.778 e $Å^{-3}$

4.2.3.3. Electrochemical Measurements. 20 µL of this homogeneous ink was coated on the GCE working electrode resulting in 80 µg of the sample. The same amount was maintained for all experiments unless otherwise stated. The experimentally obtained potentials were converted to RHE scale following the relation $E_{(RHE)} = E_{(Ag/AgCl)} + 0.204\ V + 0.059pH$ where the Ag/AgCl electrode was used as the reference electrode. All the electrochemical studies were performed in 0.1 M sodium acetate buffer of pH 4.8. The chronoamperometry experiments were done on 1 cm^2 carbon paper as the working electrode and Pt wire as the counter electrode.

4.3. RESULTS AND DISCUSSION

4.3.1. Structural Analysis

The typical one-pot wet synthesis of the title compound $Na_6[\{W^{VI}_{0.75}(OH)(ONa)\}_2\{Mn^{II}(H_2O)_2\}_2\{BiW^{VI}_9O_{33}\}_2]\cdot 18H_2O$ (**POM-MnW(OH)**) has resulted in the formation of a Krebs-type POM, incorporated with W^{VI}–OH functionality in its structure. The synthesis procedure was adapted from the reported literature with slight variations.[22] In brief, sodium tungsten dihydrate, bismuth nitrate pentahydrate, and manganese acetate were reacted in an aqueous medium at 80 °C, at a slightly alkaline pH value of 8.25. The single crystal X-ray diffraction (SCXRD) analyses of the resulting yellow colored crystals have revealed the molecular formula of the titled compound as $Na_6[\{W^{VI}_{0.75}(OH)(ONa)\}_2\{Mn^{II}(H_2O)_2\}_2\{BiW^{VI}_9O_{33}\}_2]\cdot 18H_2O$ (**POM-MnW(OH)**), and also has been found persistent with inductive coupled plasma optical emission spectroscopy (ICP-OES) elemental analysis (see Appendix, section 4.1.1.). The composition of **POM-MnW(OH)** has been verified by diverse spectroscopic characterization techniques such as X-ray photoelectron spectroscopy (XPS), FTIR, electronic spectra, powder X-ray diffraction (PXRD) including SCXRD and bond valence sum (BVS) calculation (see Appendix, section 4.1.2.) discussed in the following sections.

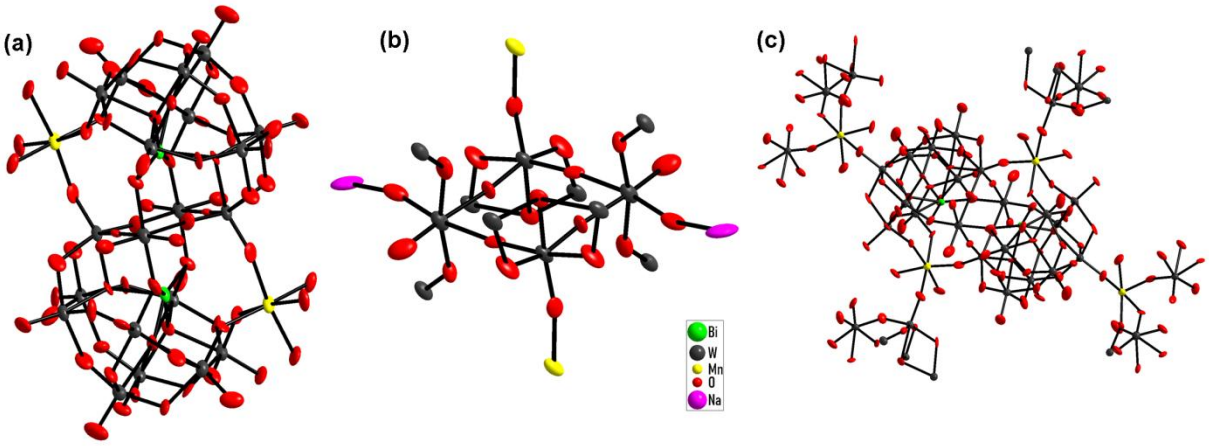

Figure. 4.1. (a) Ball-stick representation of molecular structure of **POM-MnW(OH)**, (b) magnified view of -{$W^{VI}_{0.75}$(OH)(ONa)}, core of **POM-MnW(OH)**, (c) Formation of 2D architecture in **POM-MnW(OH)**.

The analysis using single-crystal X-ray diffraction (SCXRD) has revealed that **POM-MnW(OH)** crystallizes in the monoclinic P 21/n space group, with a molecular formula of $Na_6[\{W^{VI}_{0.75}(OH)(ONa)\}_2\{Mn^{II}(H_2O)_2\}_2\{BiW^{VI}_9O_{33}\}_2]\cdot 18H_2O$ (**POM-MnW(OH)**). The SCXRD analysis of **POM-MnW(OH)** has illustrated a two-dimensional framework structure characterized by Mn–O=W connections, further interconnected through sodium-aqua-complexes (as depicted in Figure.4.1(a,b)). Notably, within the compound, one and a half units of tungsten with mono-hydroxyl groups, represented as cis-{$W^{VI}_{0.75}$(OH)(ONa)}, occupy individual environments compared to the rest of the framework tungsten centers (as illustrated in Figure.4.1c.) The bond distances obtained for Bi–O and O–W in the Bi–O–W and W–O–W in the cluster fragments are consistent with previously reported ones.[17-20,28,29] Consequently, there are two W^{VI}–OH groups with identical W–OH bond distances measured as 1.831 Å. The BVS value of the hydroxyl oxygen (O_{31}) atom in **POM-MnW(OH)** is found to be 0.9208 (see Appendix, section 4.2.).

4.3.3. Spectroscopic Analysis

4.3.3.1. FTIR Analysis

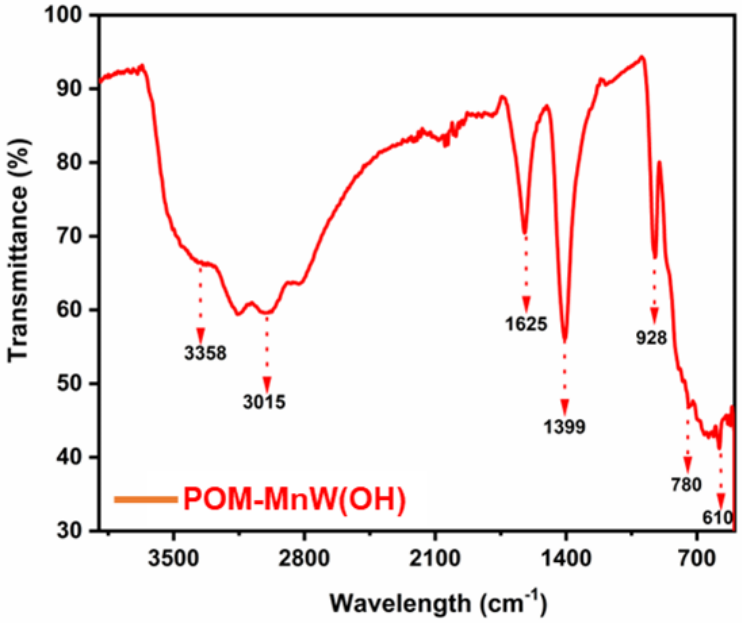

Figure 4.2. (a) FT-IR spectrum of **POM-MnW(OH)**.

The FT-IR spectral pattern of **POM-MnW(OH)** has displayed significant peaks in the range of 950 to 550 cm^{-1} for W=O, W–O–W, and Bi–O–W belonging to the stretching and bending vibrations of the POM cluster (Figure 4.2).[30] A broad feature at 3358 cm^{-1} and 1625 cm^{-1} correspond to O–H stretching and bending modes of lattice water molelcules, respectively. This is in par with the BVS analyses, which have shown the presence of W-OH group in **POM-MnW(OH)**.

4.3.3.2. PXRD Analysis

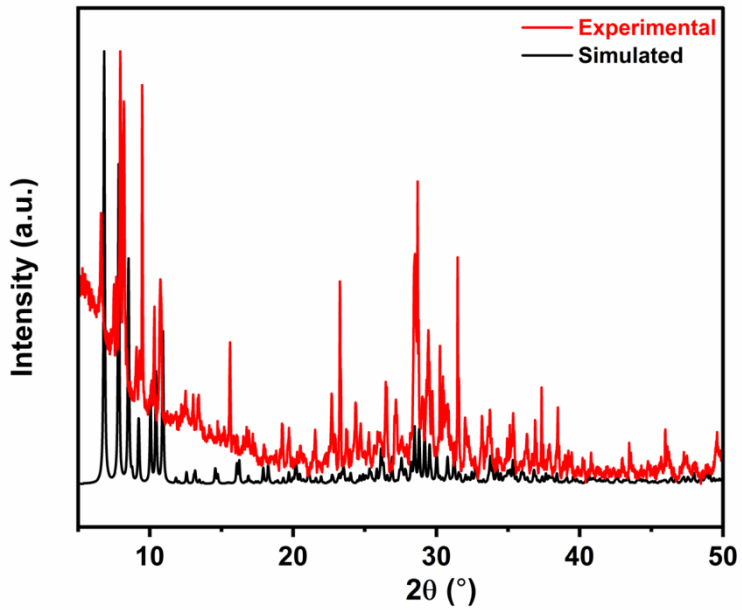

Figure 4.3. PXRD profile of experimentally obtained **POM-MnW(OH)** compared with that of simulated one from SCXRD data.

The powder X-ray diffraction pattern (PXRD) of **POM-MnW(OH)** has exhibited a matching pattern to the simulated one, indicating the compound's bulk purity and uniformity with the synthesized material (Figure 4.3).

4.3.3.3. Raman Analysis

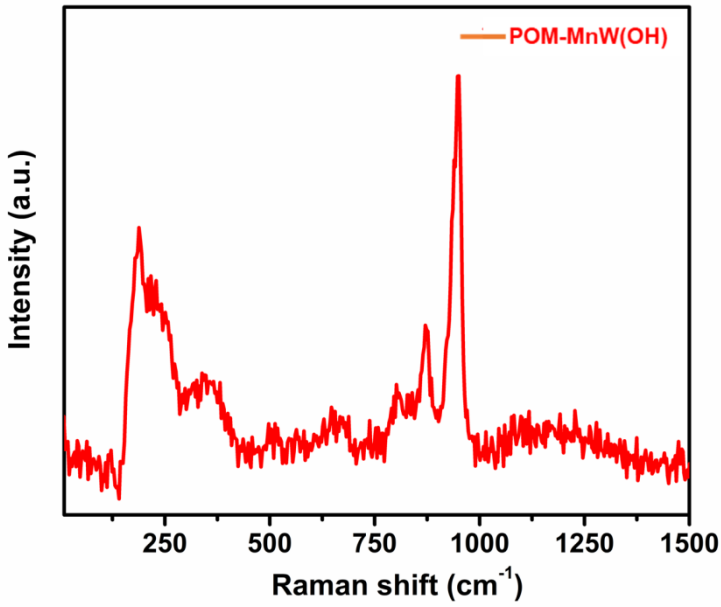

Figure 4.4. Raman spectrum of **POM-MnW(OH)**.

The Raman spectrum of **POM-MnW(OH)** has displayed in Figure 4.4 strong peaks in the 870-930 cm^{-1} region, featuring the terminal W=O Raman active bands of the POM cluster anion.

4.3.3.4. Electronic Absorbance Spectral Analysis

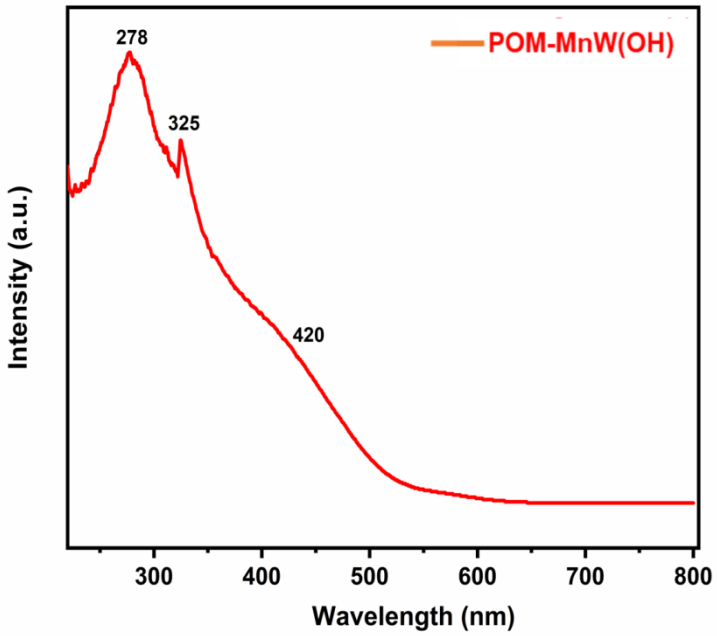

Figure 4.5. UV-DRS electronic spectrum of **POM-MnW(OH)**.

The weak d-d transition in the 800-520 nm region in the electronic spectrum (Figure 4.5) corresponds to the d-d transition of Mn^{2+} ion, present in the title **POM-MnW(OH)**.[21] The bands present below the range of 300 nm could be considered as the ligand to metal charge transfer (LMCT) bands.

4.3.3.5. FESEM-EDX Analysis

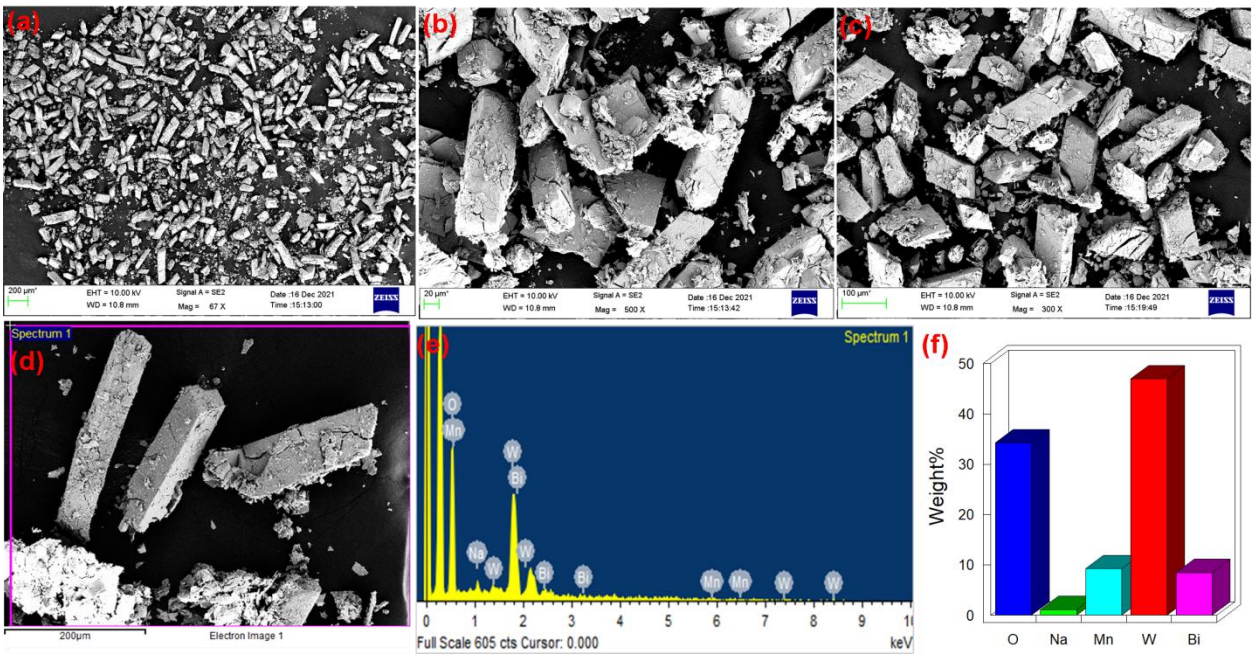

Figure 4.6. (a-c) FESEM images under different magnification **POM-MnW(OH)** (d-f) EDX elemental analysis of **POM-MnW(OH)**.

The microscopic analysis of crystals of **POM-MnW(OH)** was also thoroughly examined using a field emission scanning electron microscope (FESEM) and the surface elemental mapping by energy dispersive X-ray (EDX) spectroscopy as shown in Figure 4.6. The rectangular block-type crystals of **POM-MnW(OH)** are clearly shown by FESEM, and the presence of respective elements in **POM-MnW(OH)** through EDX mapping

4.3.3.6. X-ray Photoelectron Spectrocsopic Analysis

POM-MnW(OH) was further analyzed with XPS to further comprehend the presence of tungsten-hydroxyl moieties along with the other metals present in **POM-MnW(OH)**. As expected, the XPS provides a deeper understanding of the constituent elements and their respective oxidation states present in the title compound. The survey scan shown in Figure 4.7a reveals the presence of bismuth, tungsten, manganese, sodium, and oxygen elements in **POM-MnW(OH)**. The core-level XPS of carbon at 284.4 eV is considered as the reference to interpret the obtained data.[31] The Lorentzian-Gaussian (LG) fitting has been used to deconvolute the concerned XPS data with permitted error (in terms of Adj. R^2). The O 1s XPS spectrum interpretation has given rise to two peaks centered at 530.75 and 532.80 eV (Figure 4.7a). The resultant two peaks for the O 1s band disclose the presence of oxygen ions in different bonding interactions, particularly bridging / terminal oxygen (W-O-W / W=O) and the hydroxyl oxygen (W–OH group) in the present work, and is consistent with the reported literature.[21,22] The O 1s response with a shoulder peak at 532.80 eV has conveniently confirmed the presence of metal-hydroxyl groups, i.e., W–OH functionality in compound 1.[32] Similarly, the core-XPS of Mn 2p confirms the presence of manganese at an oxidation state of +2 (Figure 4.7c). Further, the HR-XPS spectra of W 4f, Bi 4f, and Na 1s display the oxidation states of +6, +3, and +1 respectively in **POM-MnW(OH)** (see Appendix, section 4.1.3), which are also supported by the relevant literature.[33] Thus, XPS studies affirms a good agreement with the SCXRD and BVS results (vide supra) obtained for **POM-MnW(OH)**.

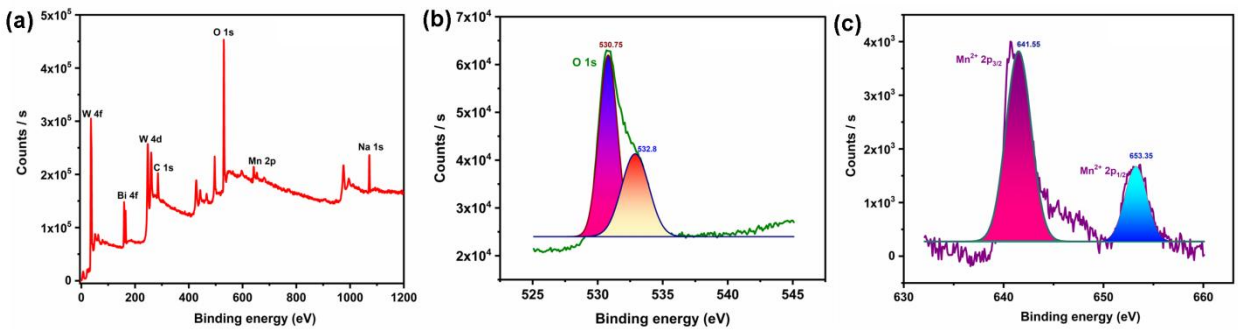

Figure 4.7. (a) Survey scan XPS plot of **POM-MnW(OH)**; (b) high-resolution XPS plots of O 1s of **POM-MnW(OH)**; (c) high-resolution XPS plots of Mn 2p **POM-MnW(OH)**.

4.3.4. Electrochemical analyses

4.3.4.1. Hydrogen Evolution Reaction (HER) by Water Reduction

In our prior reports, we established the significance of W^{VI}–OH functionalities on the POM surface in catalyzing the reduction of water into molecular hydrogen.[21,22] It is crucial to recognize that the stability of these W^{VI}–OH functionalities on the POM surface varies significantly under different pH conditions during catalytic hydrogen evolution. While these moieties are effective for HER under neutral pH conditions, they have exhibited limited catalytic stability, lasting up to just 100 cyclic voltammetric cycles.[22] However, when subjected to the same conditions at an acidic pH of 3, they remained stable even after 1000 cyclic voltammetric cycles.[21] This experimental evidence underscores the importance of fine-tuning the electrolyte pH in relation to the W^{VI}–OH functionality for enhanced and sustainable green hydrogen production. Building upon this premise, the compound described in the title, features two W^{VI}–OH functional groups on the surface of POM cluster, prompting us to explore their potential in electrochemical water splitting and adjust the hydrogen evolution reaction environment through electrolyte pH. The entire electrochemical studies were conducted in 0.1 M sodium acetate buffer with a pH of 4.6, deemed to be an appropriate pH condition for HER.

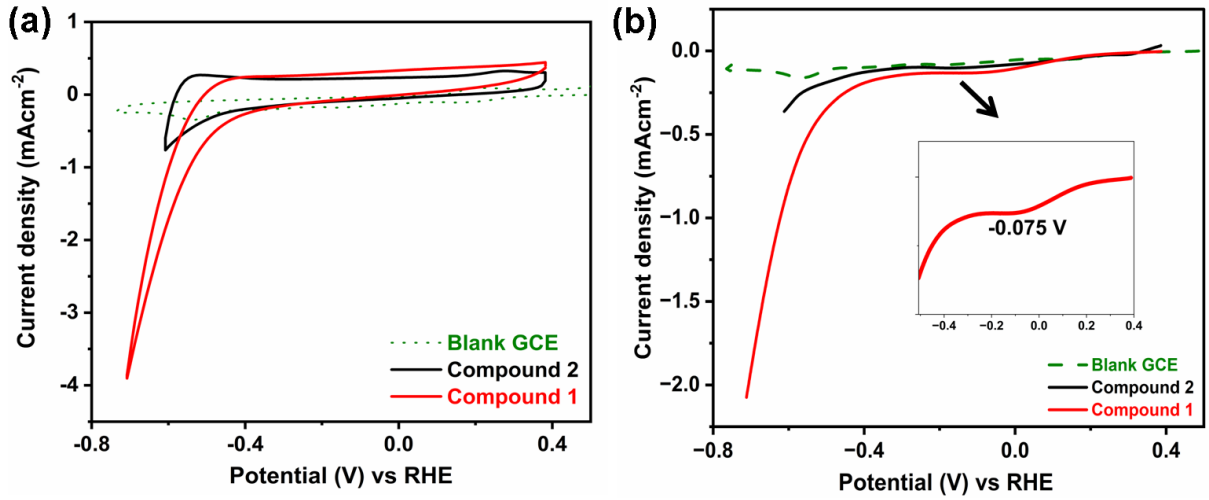

Figure 4.8. (a) Cyclic– and (b) linear–sweep voltammograms for **POM-MnW(OH)**, **POM-MnW(O_t)**, and blank-GCE (scan rate 100 and 10 mV/s, respectively).

We recorded cyclic voltammetry (CV) and linear sweep voltammetry (LSV) profiles for three distinct electrodes: the bare glassy-carbon electrode (blank GCE), **POM-MnW(OH)**, and $Na_{12}[Mn_3(H_2O)_3(BiW_9O_{33})_2]\cdot 43H_2O$ (**POM-MnW(O_t)**), synthesized as per established literature methods.[34] Markedly, the latter compound lacks W^{VI}–OH functionality but contains a manganese complex. This experimental approach was aimed to elucidate the

respective contributions of W^{VI}–OH functionality and the manganese centres towards the hydrogen evolution reaction (HER) under identical operational conditions. The CV profile of the blank GCE has shown no notable catalytic current, which was coated with the acetylene carbon-Nafion mixture without a catalyst (Figure 4.8a).

The CV profile of **POM-MnW(O_t)** has not shown any prominent reductive responses in the operational (cathodic) window but has displayed a small current surge at a potential of -0.52 V vs RHE. However, the CV profile of **POM-MnW(OH)** has shown a significant catalytic current surge, marking an onset potential of -0.38 V vs. RHE for hydrogen evolution reaction. Similarly, a closer look at the LSV profiles of **POM-MnW(OH)** and **POM-MnW(O_t)**, in Figure 4.8b, has clearly depicted a broad redox peak centered at -0.075 V vs RHE for **POM-MnW(OH)** (inset Figure 4.8b), which is absent in the case of **POM-MnW(O_t)**. The reductive response at -0.075 V vs. RHE could be ascribed to the reduction of W^{VI}/W^{V}, which closely matches the reductive responses for tungsten centers exhibited by relevant compounds of the literature.[21,22]

It is already proven that the tungsten of the W^{VI}–OH moiety would easily be electrochemically reduced over the corresponding W^{VI}=O groups, which in turn could reduce the water molecules chemically to generate hydrogen in catalytic HER action. Thus, the broad reductive response at –0.075 V vs RHE in **POM-MnW(OH)** could have arisen due to the reduction of W^{VI}–OH centers [not W^{VI}=O centers]. Thus, from the electrochemical perspective, the W^{VI}–OH functional groups present in **POM-MnW(OH)** could be the potential active sites for electrocatalytic HER and are supported by the earlier observations. In a close view, a thorough analysis of the CV and LSV profiles of **POM-MnW(OH)** and **POM-MnW(O_t)** discloses that the former offers a significantly lower onset potential compared to the latter. In other words, this considerable shift in the onset potential among the compounds has directly strengthened the role of hydroxyl groups present on the surface of POM for efficient electrochemical reduction of water. The W^{VI}–OH groups on the POM surface have undoubtedly enhanced the catalytic activity of **POM-MnW(OH)** and strengthened the role of W^{VI}–OH functionality on HER. To unveil the number of electrons involved in the catalytic HER action by the electrochemically reduced W^{VI}–OH centers, the differential pulse voltammogram (DPV) of **POM-MnW(OH)** was recorded prior to the HER onset potential (see Appendix, Section A4.4), where reductive response is present as shown in the LSV. The DPV measurement showed the involvement of two electrons, which supports the W^{VI}/W^{V} redox reaction of the tungsten-hydroxyls. Thus, equation (1) below could be

considered the potential redox reaction, and equation (2) could be the consequent HER action exhibited by the hydroxylated POM cluster, compound **1**.

$$2W^{VI} + 2e^{-} \rightarrow 2W^{V} \qquad \text{(eqn. 1)}$$

$$2W^{V} + 2H_2O \rightarrow 2W^{VI} + H_2 + OH^{-} \qquad \text{(eqn. 2)}$$

To gain insights into the stability and degradation behavior of catalyst (**POM-MnW(OH)**) during HER, a series of multiple cyclic voltammetric experiments were conducted within the catalytic potential window (ranging from 0.38 to -0.71 V vs. RHE) on the GC electrode coated with catalyst **POM-MnW(OH)**. As depicted in Figure 4.9a, these experiments demonstrated that the catalyst exhibited remarkable stability, maintaining its performance over 1000 cycles without significant degradation. This remarkable endurance stands out as a compelling feature of the polyoxometalate-based catalyst described in this study, showcasing its exceptional electrochemical stability within the acidic buffer medium (Figure 4.9a).

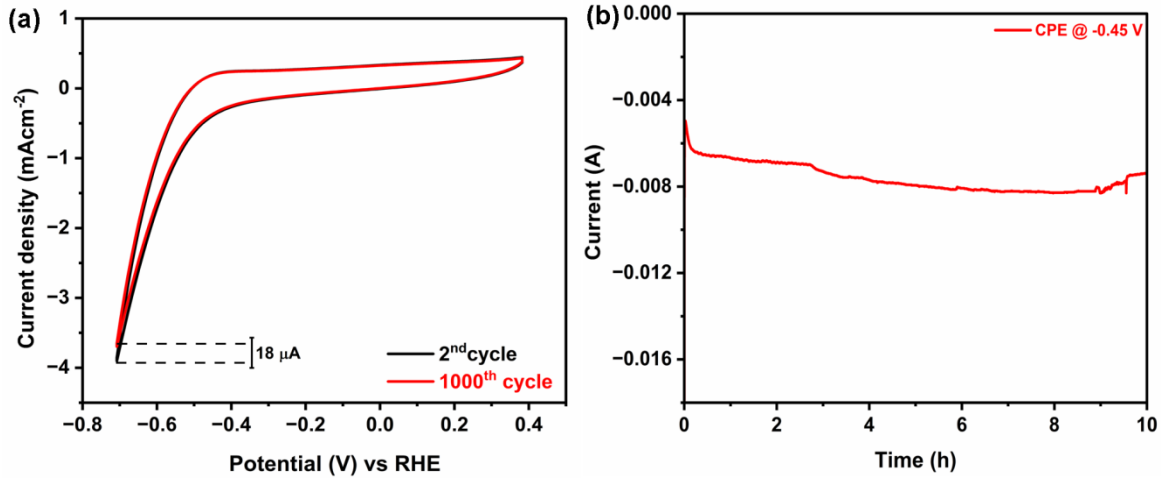

Figure 4.9. (a) Cycling stability analysis of **POM-MnW(OH)** for hydrogen evolution reaction by 1000 CV cycles with a scan rate of 100 mVs^{-1} in 0.1 M sodium acetate buffer of pH 4.6; (b) Chronoamperometry (CA) electrolysis of **POM-MnW(OH)** performed at -0.45 V vs RHE for 10 hours.

Additionally, we utilized a **POM-MnW(OH)**-modified carbon paper electrode to conduct a chronoamperometric (CA) experiment over a period of 10-hour at -0.45 V vs. RHE. Figure 4.9b illustrates a consistent current production by the catalyst-coated electrode at the applied potential of -0.45 V vs. RHE, affirming the exceptional HER activity of **POM-MnW(OH)**. The stability experiments mentioned above provide strong evidence of the promising HER catalytic performance exhibited by **POM-MnW(OH)**. However, it is equally essential to understand the structural and compositional aspects of the catalyst after the

extensive long-term stability experiments. The post–chronoamperometry (p-CA) electrolysis electrode material was subjected to various spectroscopic studies like FTIR (see Appendix Figure A4.4.) and FESEM-EDX microscopy (see Appendix Figure A4.5,6).

These extensive analyses unequivocally establish that there was no discernible catalyst reconstruction or degradation observed in the case of **POM-MnW(OH)**. This reaffirms the authentic catalytic essence of **POM-MnW(OH)** as an efficient HER catalyst for electrochemical water reduction. A key highlight of this research lies in the rarity of pristine polyoxometalate-based compounds demonstrating both excellent stability and durability under electrochemical operational conditions. Such characteristics are often unique or exceptionally challenging to achieve. Fortunately, our functional POM-based catalyst, as described in this study, stands out by driving a dominant hydrogen evolution reaction through the fine-tuning of reaction conditions.

Kinetic insights play a major role in evaluating the efficiency of catalysts. Therefore, various critical kinetic experiments were carried out to assess the water reduction activity of the electrocatalyst. By varying the scan rates of cyclic voltammograms, we observed an increment in peak current with an increase in the scan rates (see Appendix Figure A4.7.). Thus, a derived plot was constructed with current *vs* square root of scan rates, resulting into a linear plot, as displayed in Figure 4.10a. This observation indicates that a diffusion-controlled electrochemical hydrogen evolution is demonstrated by **POM-MnW(OH)**.

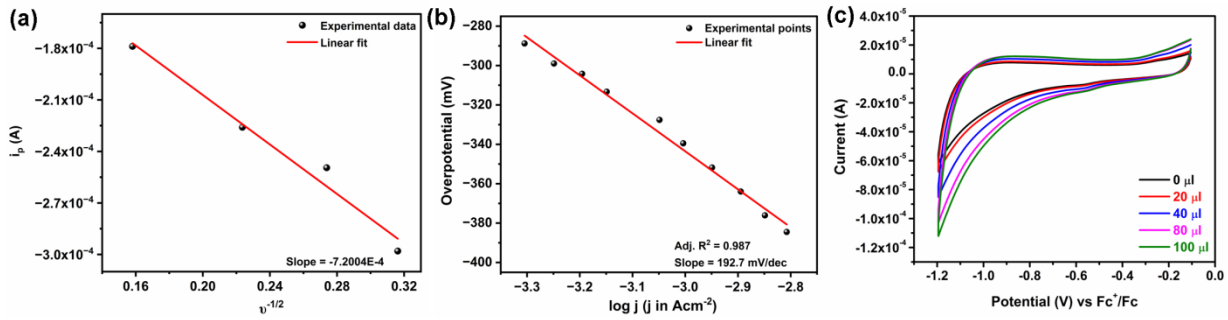

Figure 4.10. (a) Derived plot constructed from the peak current (i_p) as a function of the square root of scan rate (-0.025 to -0.1 Vs^{-1}) for **POM-MnW(OH)**; (b) iR corrected Tafel plot for **POM-MnW(OH)** in the catalytic WR region; (c)) CV profiles of compound **1** in non-aqueous medium with controlled addition of water. CVs were collected during the sequential addition of water to the electrochemical cell (before adding water it was a dry acetonitrile solution having 0.1 M tetrabutylammonium perchlorate (TBA-ClO_4) as a supporting electrolyte and the CV data were collected with 100 mVs^{-1} scan rate).

Further kinetic investigations involve the determination of the double-layer capacitance (C_{dl}) value for **POM-MnW(OH)**, which discloses insights regarding the non-Faradaic processes happening at the electrode-electrolyte interfaces during the reaction.[35] The C_{dl} value were obtain by running cyclic voltammograms of the catalyst coated GC electrodes

in the non-Faradaic region (0.09 V to 0.19 V *vs* RHE) varying the scan rates. The slope value obtained from the graph of capacitative current density *vs* scan rates, reveals the C_{dl} value and was found to be -6.9 $mFcm^{-2}$ for **POM-MnW(OH)**. The C_{dl} value of a blank GCE has also been obtained in the same way and was found to be -1.97 $mFcm^{-2}$. This suggests that the electrochemically active surface area (directly proportional to the C_{dl} value) of the catalyst-coated electrode is evidently higher than that of the blank GCE (see Appendix Figure A4.8).

Furthermore, we conducted a Tafel plot analysis for compound **1**, as illustrated in Figure 4.10b. **POM-MnW(OH)** exhibited an overpotential of 340 mV at a current density of 1 $mAcm^{-2}$, with a notably low Tafel slope value of 197 mV dec^{-1}. It is worth emphasizing that such a low overpotential and minimal Tafel slope value, as observed in a POM-based compound engaged in water reduction, is quite remarkable.[36,37] We also calculated the Turnover Frequency (TOF) value for **POM-MnW(OH)** using established procedures,[38,39] and it was determined to be 1.81 moles of H_2 produced per second (see Appendix Figure A4.2.5). This underlines the promising reaction rate achieved by this molecular catalyst in the context of HER activity. In addition, we assessed the Faradaic efficiency of **POM-MnW(OH)** through a bulk-electrolysis experiment, revealing an impressive value of 84% (see Appendix Figure A4.2.6). Therefore, as previously mentioned, comprehensive examinations of diverse electrochemical experiments suggest that **POM-MnW(OH)** serves as a highly efficient, versatile, and durable electrocatalyst for hydrogen evolution reactions.

Additionally, to comprehend whether the HER exhibited by **POM-MnW(OH)** is the result of reduction of water or acidic proton, the CV profiles of **POM-MnW(OH)** modified GC-electrode were collected in a non-aqueous medium while adding a controlled amount of water. The sequential addition of water has resulted in a linear increment in the cathodic catalytic current) (Figure 4.10c), signifying the electrocatalytic water reduction behavior, not of proton reduction, of **POM-MnW(OH)**.

4.4. CONCLUSIONS

The present work aspires to provide a distinct approach of employing an electrocatalyst as a solid electrolyte for the conduction of protons. Also, it establishes the role and activity of a small moeity (-OH) on the surface of POM for enhancing the catalytic as well as conductivity behaviour. A manganese-based Krebs-type polyoxometalate functionalized with –OH moeity has been synthesized and unambiguously characterized with SCXRD and various other characterizations, confirming its chemical composition and structural integrity. This compound holds significant promise for advancing the fields of electrochemical water

reduction and solid-state proton conduction. The utilization of the synthesized polyoxometalate in electrochemical water reduction demonstrated its remarkable catalytic activity with more than 1000 cycles of multiple cycling stability, and promising values for kinetic parameters, which is absolutely rare for POM catalysts, showcasing its potential as a key player in green energy technologies.

4.5. REFERENCES

1. Wang, D.; Liu, L.; Jiang, J.; Chen, L.; Zhao, J. 1. Polyoxometalate-Based Composite Materials in Electrochemistry: State-of-the-Art Progress and Future Outlook. *Nanoscale* **2020**, *12* (10), 5705–5718.
2. O'Keefe, M.; Brese, N. E. 2. Atom Sizes and Bond Lengths in Molecules and Crystals. *J. Am. Chem. Soc.* **1991**, *113* (9), 3226–3229.
3. Wei, Y. Polyoxometalates: An interdisciplinary journal focused on all aspects of polyoxometalates *Polyoxometalates* **2022**, *1*, 9140014.
4. Long, D.-L.; Tsunashima, R.; Cronin, L. Polyoxometalates: Building Blocks for Functional Nanoscale Systems**,** *Angew. Chem. Int. Ed*. **2010**, *49*, 1736–1758.
5. Wang, S.-S.; Yang, G.-Y. *Chem. Rev.* **2015**, *115*, 4893–4962.
6. Li, Q.; Zhang, L.; Dai, J.; Tang, H.; Li, Q.; Xue, H.; Pang, H. *Chemical Engineering Journal*, 2018, 351, 441–461.
7. Hassan, Q.; Sameen, A. Z.; Salman, H. M.; Jaszczur, M.; Al-Jiboory, A. K. *Journal of Energy Storage* **2023**, *72*, 108404.
8. Zouc, X.; Zhang, Y. *Chem. Soc. Rev.* **2015**, *44*, 5148-5180.
9. Lv, C.; Wang, X.; Gao, L.; Wang, A.; Wang, S.; Wang, R.; Ning, X.; Li, Y.; Boukhvalov, D. W.; Huang, Z.; Zhang, C. *ACS Catal.* **2020**, *10*, 13323–13333.
10. Liu, X.; Gong, M.; Deng, S.; Zhao, T.; Zhang, J.; Wang, D. *J. Mater. Chem. A*, **2020**, *8*, 10130-10149.
11. Danilovic, N.; Subbaraman, R.; Strmcnik, D.; Chang, K.-C.; Paulikas, A. P.; Stamenkovic, V. R.; Markovic, N. M. *Angew. Chem. Int. Ed*. **2012**,*124*, 12663 – 12666.
12. Zhang, L.; Chen, Z. *Int J Energy Res.* **2020**, *44*, 3316–3346.
13. S. Sriram, S. Mathi, Bakthavachalam Vishnu, J. Jayabharathi, *Energy & Fuels*, **2022**, *36*, 7006-7016.

14. Zhang, L.; Wang, J. Liu, P.; Liang, J.; Luo, Y.; Cui, G.; Tang, B.; Liu, Q.; Yan, X.; Hao, H.; Liu, M.; Gao, R.; Sun, X. *Nano Res.,* **2022**, *15*, 6084–6090.
15. Zou, X.; Liu, Y.; Li, G.-D.; Wu, Y.; Liu, D.-P.; Li, W.; Li, H.-W.; Wang, D.; Zhang, Y.; Zou, X. *Adv.Mater.* **2017**, *29*, 1700404.
16. Liu, S.; Jiang, Y.; Yang, M.; Zhang, M.; Guo, Q.; Shen, W.; He, R.; Li, M. *Nanoscale*, **2019**, *11*, 7959–7966.
17. Loose, I.; Droste, E.; Bösing, M.; Pohlmann, H.; Dickman, M. H.; Rosu, C.; Pope, M. T.; Krebs, B. *Inorg. Chem.* **1999**, *38*, 2688–2694.
18. Wang, L. B.-B. Zhou, K. Yu, Z.-H. Su, S. Gao, L.-L. Chu, J.-R. Liu, G.-Y. Yang, *Inorg. Chem.*, **2013**, *52*, 5119−5127.
19. Wang, L.; Yu, K.; Zhou, B.-B.; Su, Z.-H.; Gao, S.; Chu, L.-L.; Liu, J.-R. *Dalton Trans.* **2014**, *43*, 6070.
20. Wang, L.; Yu, K.; Zhu, J.; Zhou, B. B.; Liu, J. R.; Yang, G. Y. *Dalton Trans.* **2017**, *46*, 2874–2883.
21. Mulkapuri, S.; Ravi, A.; Mukhopadhyay, S.; Kurapati, S. K.; Siby, V.; Das, S. K. *Inorg. Chem. Front.* **2022**, *9*, 3566–3577.
22. Ravi, A.; Mulkapuri, S.; Das, S. K. *Inorg. Chem.* **2023**, *62*, 12650–12663.
23. Sheldrick, G. M., SADABS, Program for absorption correction. University of Gottingen, Gottingen, Germany, **1997**.
24. Dolomanov, O.V.; Bourhis, L.J.; Gildea, R.J.; Howard, J.A.K.; Puschmann, H., Olex2: A complete structure solution, refinement and analysis program. J. Appl. Cryst. 2009, 42, 339-341.
25. Sheldrick, G.M. Acta Cryst. 2015, C71, 3-8. The SHELX-97 Manual. http://linux.uniac.gwdg.de/SHELX/
26. Bourhis, L. J.; Dolomanov, O. V.; Gildea, R. J.; Howard, J. A. K.; Puschmann, H. The anatomy of a comprehensive constrained, restrained refinement program for the modern computing environment - Olex2 dissected. Acta Cryst. 2015, A71,59-75.
27. Han, G.-Q.; Liu, Y.-R.; Hu, W.-H.; Dong, B.; Li, X.; Shang, X.; Chai, Y.-M.; Liu, Y.-Q.; Liu, C.-G.; *J. Electrochem. Soc.* **2016**, *163*, H67–H73.
28. Topsoe, N. Y.; Dumesic, J. A.; Topsoe, H. *J. Catal.* **1995**, *151*, 241-252.
29. Topsoe, N. Y.;. Topsoe, H; Dumesic, J. A. *J. Catal.* **1995**, *151*, 226-240.
30. Fang, D.; He, F.; Xie J.; Xue, L. *J. Wuhan Univ. Technol.-Mat. Sci. Edit.*, **2020**, *35*, 711–718.
31. Barr, T. L. *J. Phys. Chem.* **1978**, *82*, 1801–1810.

32. Bösing, M.; Loose, I.; Pohlmann, H. Krebs, B. *Chem. Eur.*, **1997**, *3*, 1232-1237.
33. Bösing, M.; Nöh, A.; Loose, I.; Krebs, B. *J. Am. Chem. Soc.*, **1998**, *120*, 7252-7259.
34. Balici, S.; Niculae, M.; Pall, E.; Rusu, M.; Rusu, D.; Matei, H. *Rev. Chim*, **2016**, *67*, 485-490.
35. Bard, A. J.; Faulkner, L. R. *Electrochemical Methods: Fundamentals and Applications*, Wiley, New York, **2001**.
36. Shinagawa, T.; Takanabe, K. *ChemSusChem* **2017**, *10*, 1318-1336.
37. Anantharaj, S.; Noda, S.; Jothi, V. R.; Yi, S. C.; Driess, M.; Menezes, P. W. *Angew. Chem. Int. Ed*. **2021**, *60*, 2–28.
38. Mulkapuri, S.; Ravi, A.; Das, S. K. *Chem. Mater.* **2022**, *34*, 3624–3636.
39. Singh, C.; Haldar, A.; Basu, O.; Das, S. K. *Inorg. Chem.* **2021**, *60*, 10302–10314.
40. Hausmann, N.; Mebs, S.; Laun, K.; Zebger, I.; Dau, H.; Menezes, P. W.; Driess, M. *Energy Environ. Sci.*, **2020**, *13*, 3607-3619.

Chapter 5

Superprotonic Conductivity Studies of W-OH Grafted Polyoxometalates

OVERVIEW

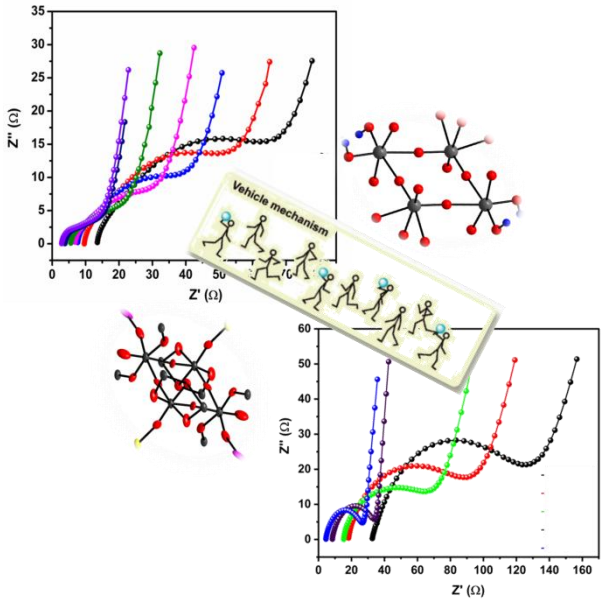

Achieving unique structural stability and exceptional proton conductivity in crystalline materials poses a formidable challenge within the realm of energy-material chemistry. Thus, two Krebs-type polyoxometalate clusters incorporated with cobalt- and manganese- aqua complexes caught our attention. The respective POM compounds possess unique structural distinctness with the presence of hydroxyl groups grafted onto the surface of tungsten centers which are present as the core of sandwiched between two $\{Bi^{III}W^{VI}_{9}O_{33}\}^{9-}$ units. The compounds formulated as $Na_6[\{Co^{II}(H_2O)_3\}_2\{W^{VI}(OH)_2\}_2\{(Bi^{III}W^{VI}_{9}O_{33})_2\}]\cdot 8H_2O$ (**1**) and $Na_8H_3[\{W^{VI}_{0.75}(OH)(O)\}_2\{Mn^{II}(H_2O)_2\}_2\{BiW^{VI}_{9}O_{33}\}_2]\cdot 18H_2O$ (**2**), possessing labile protons and lattice- and coordinated water molecules encouraged us to perform proton conductivity studies. The compounds have exhibited super protonic conductivity values of 0.978 $\times 10^{-1}$ Scm^{-1} for **1** and 1.07 $\times 10^{-1}$ Scm^{-1} for **2** at a temperature of 80 °C at 98% relative humidity (R.H.). The concerned Arrhenius plots constructed for compounds **1** and **2** have shown a good linearity throughout the temperature range of 40 to 80 °C revealing activation energy of 0.64 and 0.66 eV respectively.

5.1. INTRODUCTION

Unprecedented climate change and worldwide energy crisis have led to large-scale efforts towards the development of sustainable energy conversion and storage technologies.[1] Renewable energy solutions to move away from the burning of fossil fuels is receiving considerable attention in today's world.[2] To address these challenging energy and environmental issues, particular emphasis has been given to the design and engineering of electrochemical energy systems and new functional materials. Fuel cells are electrochemical energy conversion devices that produce electrical energy from chemical energy of fuels such as hydrogen, oxygen, methanol, natural gas, etc. through redox reactions providing extraordinary superiorities in power density, energy conversion efficiency and environmental compatibility.[3-6] Among various types of fuel cells, proton exchange membrane fuel cells (PEMFCs) have received considerable attention in the past decades as they might be the best potential solution to high consumption of fossil fuel and environmental pollution. The efficiency of PEMFCs is determined by the proton conducting proficiency of the proton exchange membrane which serves as not only a conductor for protons but also barrier for reactants *e.g.*, oxygen and hydrogen. So far, commercially available perfluorosulfonic acid (PFSA) ionomer membranes or Nafion has been well established as supreme proton conductor due to its chemical stability and high proton conductivity (10^{-1} S cm^{-1}) under wet conditions.[7,8] However, its practical usage is limited due to its high cost, high methanol permeability, low operating temperature and low proton conductivity at low humidity.

In this regard, polyoxometalates (POMs), a class of metal oxide cluster containing materials with their unique ability to control redox reactions, have recently proven themselves as the breakthrough materials for proton conduction. When a POM cluster unit gets linked to an extended network-like structure, in many cases, it results in a POM-based framework material having well-defined voids / cavities. Because of the open framework with independent structural units and large number of redox active sites, these POMs have become appropriate materials to advance unconventional energy-related technologies. Polyoxometalates are anionic metal-oxo clusters based on early, high-valent transition metals (e.g. Mo, W, and V) with oxygen enriched surfaces, strong acidity and strong electron accepting capability.[9,10] The negative charge distributed on the external surface oxygen atoms can provide abundant proton transfer sites to construct hydrogen bond networks for efficient proton transport, a crucial criteria for designing fuel cells.[11]

In the present work, two Krebs type POM compounds are studied for their solid-state proton conductivity. The compounds which are formulated as $Na_6[\{Co^{II}(H_2O)_3\}_2\{W^{VI}(OH)_2\}_2\{(Bi^{III}W^{VI}_9O_{33})_2\}]\cdot 8H_2O$ (**1**) and $Na_8H_3[\{W^{VI}_{0.75}(OH)(O)\}_2\{Mn^{II}(H_2O)_2\}_2\{BiW^{VI}_9O_{33}\}_2]\cdot 18H_2O$ (**2**) have similar skeleton of sandwiched type structure, but possess distinct core species connecting the two $\{Bi^{III}W^{VI}_9O_{33}\}^{9-}$ units. Compound **1** has been incorporated with *cis*-$\{W^{VI}(OH)_2\}$ and $-Co(H_2O)_3$ as the core sandwiched between two $\{Bi^{III}W^{VI}_9O_{33}\}^{9-}$ units, whereas, in compound **2**, the core has been found to possessing two *cis*-$\{W^{VI}(OH)(ONa)\}$ groups along with $-Mn(H_2O)_2$ complexes between the two tri-lacunary $\{Bi^{III}W^{VI}_9O_{33}\}^{9-}$ units. These two structural aspects make these compounds distict and unique form each other even though they fall into the same category of Krebs type POMs. The labile protons from the free hydroxyl groups on the surface of the POM cluster make the compound act as a proton pool. In this work, we have described its detailed proton conductivity studies including kinetics and thermodynamics of this proton conduction.

5.2. EXPERIMENTAL SECTION

5.2.1. Materials

The chemicals used for the synthesis were of analytical grade which are commercially available and used without any further purification. Sodium tungstate (Na_2WO_4, 98%) was purchased from Sigma Aldrich India. Bismuth nitrate pentahydrate ($Bi(NO_3)_3\cdot 5H_2O$, 98%) was purchased from Alfa Aesar, India. Cobalt(II) nitrate hexahydrate pure ($Co(NO_3)_2\cdot 6H_2O$) was purchased from SRL Chemicals, India. Nitric acid extra-pure and ammonia solution extra pure were purchased from Finar chemicals. Double distilled water was utilized to carry out all the syntheses and Milli-Q water for electrochemical experiments. Compound $Na_6[\{Co^{II}(H_2O)_3\}_2\{W^{VI}(OH)_2\}_2\{(Bi^{III}W^{VI}_9O_{33})_2\}]\cdot 8H_2O$ (**1**) was prepared according to the literature procedure[12] whereas $Na_8H_3[\{W^{VI}_{0.75}(OH)(O)\}_2\{Mn^{II}(H_2O)_2\}_2\{BiW^{VI}_9O_{33}\}_2]\cdot 18H_2O$ (**2**) was isolated in a one-pot wet synthesis (as discussed in the previous chapter).

5.2.2. Synthesis

5.2.2.1. Synthesis of $Na_6[\{Co^{II}(H_2O)_3\}_2\{W^{VI}(OH)_2\}_2\{(Bi^{III}W^{VI}_9O_{33})_2\}]\cdot 8H_2O$ (1)

To an aqueous solution of $Na_2WO_4\cdot 2H_2O$ (9 mmol in 25 mL of water), 0.5 mL of 6 M nitric acid (HNO_3) was added drop wise and heated at 90 ℃ for 15 min under stirring. An aqueous solution of cobalt nitrate solution (2 mmol of $Co(NO_3)_2\cdot 6H_2O$ dissolved in 2 mL of water)

was added drop wise to the above reaction mixture at room temperature with constant stirring. Subsequently to this purple color solution, an acidic solution of bismuth nitrate (1 mmol of $Bi(NO_3)_3 \cdot 5H_2O$ in 1 mL of 6 M nitric acid) was added slowly with vigorous stirring and the pH of the reaction mixture was adjusted to 6.82, using 15% aqueous ammonia solution. The reaction was continued for one hour. The dilution turned blue with production of purple color slurry which was filtered in hot condition. The clear filtrate was left for crystallization at ambient condition. The block pink color crystals were isolated in ten days. Yield: 1.2 g (5.13% based on tungsten).

5.2.2.2. Synthesis of $Na_8H_3[\{W^{VI}_{0.75}(OH)(O)\}_2\{Mn^{II}(H_2O)_2\}_2\{BiW^{VI}_9O_{33}\}_2]\cdot 18H_2O$ (2)

Followed the same synthetic procedures as discussed in the previous chapter under the Section, Section 4.3.3.

5.2.3. Methods

5.2.3.1. Physical Characterizations

All the compounds synthesized were characterized by PXRD analyses, FTIR analysis and UV-visible diffused reflectance spectral (DRS) studies. The characterization analyses of the reported compound **1** were found to be matching well with their reported analytical studies.

5.2.3.2. Proton Conductivity Measurements

Proton conductivity studies of the compounds **1** and **2** were measured by alternating current (AC) impedance spectroscopy with a two-electrode setup (parallel-plate mode). Micro-crystals of the compounds were powdered finely and were pelletized and sandwiched between two carbon wafers (to lower the contact resistance between the electrodes and the sample) before placing inside a homemade cell of two-electrode setup. The powdered sample was pelletized under a pressure of 3 $toncm^{-2}$ for 2 min using a hydraulic press. Impedance spectra were recorded in the temperature range of 40 to 80 °C at a constant relative humidity (RH) of 98%. A home-made setup was used to maintain the different temperature range and a constant relative humidity of 98%. Long-term stability of the conductors was checked by proton conductivity measurements in a constant time interval, while the sample was kept in the humidified elevated temperature throughout the whole period.[13-15] Conductivity calculations were done from the Nyquist plots of impedance spectra by fitting with the most suitable equivalent circuit.[16] Appendix A5.1. includes the details of the proton conductivity cell and the EIS measurement. The details of equivalent circuit and their fitting are provided

in Appendix A5.2. The calculations involving the activation energy from Arrhenius plots are supplied in Appendix A5.3.

5.3. RESULTS AND DISCUSSION

5.3.1. Description of Crystal Structures

5.3.1.1. $Na_6[\{Co^{II}(H_2O)_3\}_2\{W^{VI}(OH)_2\}_2\{(Bi^{III}W^{VI}_9O_{33})_2\}]\cdot 8H_2O$ (1)

In compound **1**, two identical tri-lacunary bowls, $\{BiW_9O_{33}\}^{9-}$ are sandwiched together by two units of W^{VI}-OH moieties and two -$Co^{II}(H_2O)_3$ groups which constitute the core of the Krebs type compound. Significantly, the tungsten $\{W^{VI}(OH)_2\}$ units located in the sandwiched positions exhibit distinct geometric and environmental characteristics compared to the other tungsten centers in the framework. Within each $\{W^{VI}(OH)_2\}$ moiety, the W(VI) center is coordinated by two hydroxyl groups, and these groups are symmetrically related, *cis*-$\{W^{VI}(OH)_2\}$. This whole structure has been resulting in Co^{II}-incorporated heteropoly cluster anion $[\{Co^{II}(H_2O)_3\}_2\{W^{VI}(OH)_2\}_2\{(Bi^{III}W^{VI}_9O_{33})_2\}]^{6-}$ (Figure 5.1). Thus, the $W^{VI}(OH)_2$ moieties grafted onto the surface of the tungsten centres in POM surface along with -$Co^{II}(H_2O)_3$ are found to be functionalizing the heteropoly tungstate anion.[12]

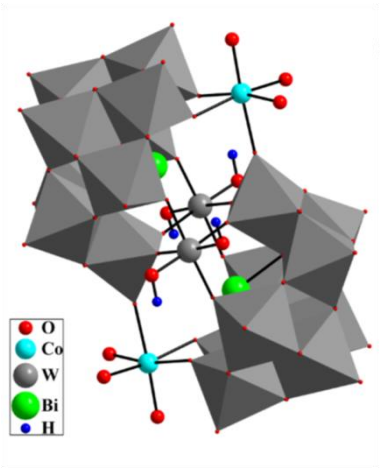

Figure 5.1. Polyhedral representation of crystal structure of compound **1**.

5.3.1.2. $Na_8H_3[\{W^{VI}_{0.75}(OH)(O)\}_2\{Mn^{II}(H_2O)_2\}_2\{BiW^{VI}_9O_{33}\}_2]\cdot 18H_2O$ (2)

Compound 2 also exhibit similar skeleton of formation of the compound to that of compound **1**, but with two distinct differences; (i) compound **2** has been incorporated with –$Mn^{II}(H_2O)_2$ complexes instead of cobalt-aqua complexes , (ii) there are one and a half units of tungsten with mono-hydroxyl groups, represented as *cis*-$\{W^{VI}_{0.75}(OH)(ONa)\}$, occupying distinct environments compared to the remaining framework tungsten centers, instead of *cis*-$\{W^{VI}(OH)_2\}$in compound **1**. A elaborative discussion of the crystal structure of compound **2** is given in the Chapter 4, Section 4.2.1.

5.3.2. Spectroscopic Analyses

5.3.2.1. FTIR Analysis

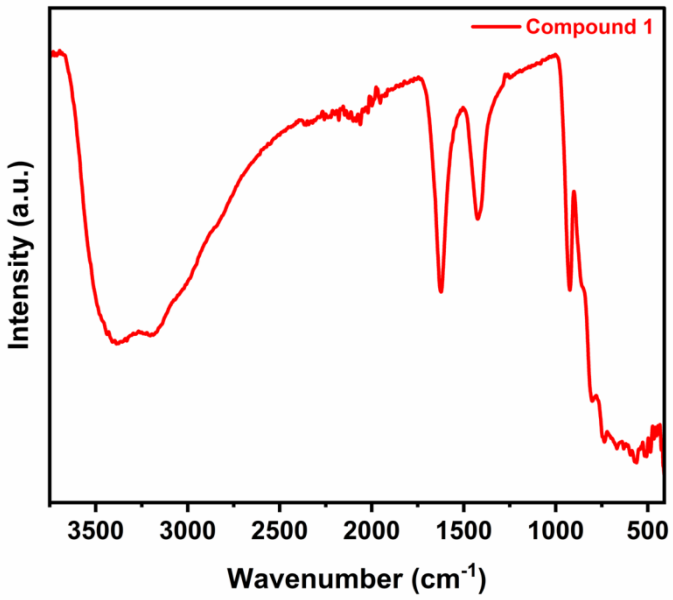

Figure 5.2. FTIR spectrum of compound **1**.

The FTIR spectrum (Figure 5.2) of compound **1** has displayed the major peaks belonging to the POM cluster in the range of 950–500 cm^{-1} showing the W=O, W–O–W, and Co–O stretching and bending vibrations. The broad bands at 1614 and 3378 cm^{-1} are ascribed to the O–H bending and stretching modes of the water molecules respectively.[17]

5.3.2.2. PXRD Analysis

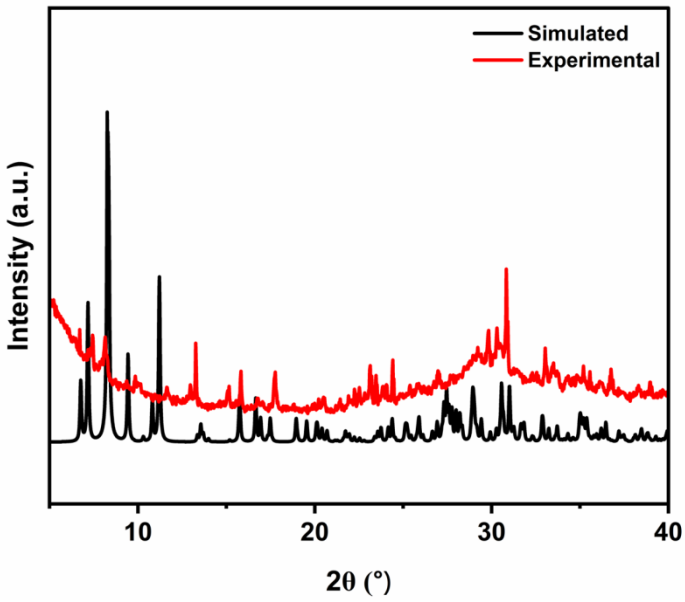

Figure 5.3. PXRD profile of experimentally obtained compound **1** compared with that of simulated one from SCXRD data.

The observed powder X-ray diffraction (PXRD) pattern of compound **1** is consistent to the simulated pattern, obtained from single crystal data of compound **1**, suggesting the bulk purity of the synthesis of the title compound (Figure 5.3).

5.3.2.3. Electronic Absorbance Spectral Analysis

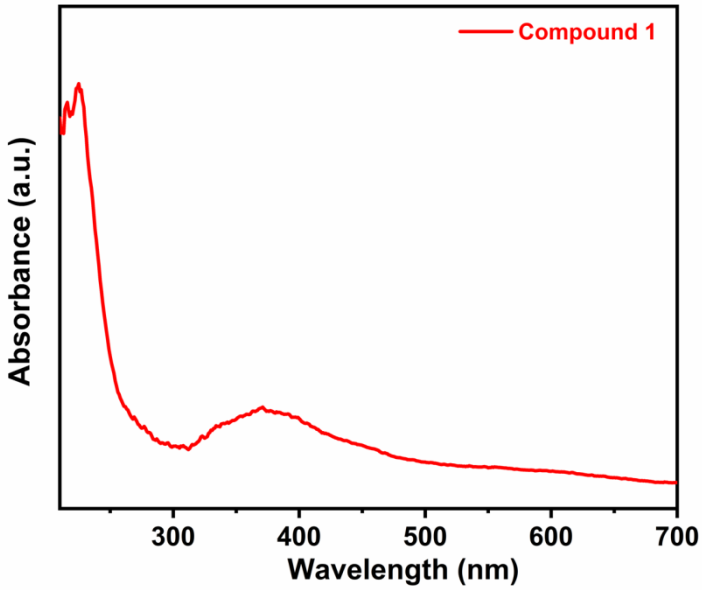

Figure 5.4. UV-DRS electronic spectrum of compound **1**.

The absorbance peak at around 350-420 nm in the solid state electronic spectrum of compound **1** can be attributed to the *d-d* electronic transitions of cobalt ions, and the peaks present below the region of 300 nm in the electronic spectrum may be due to ligand to metal charge transfer (LMCT) transition (Figure 5.4).

All major physical characterization spectra and the analyses of compounds **2** (FTIR, PXRD, Raman, UV-DRS, XPS, ICP-OES, FESEM-EDX analyses and so on) are described in detail in the previous chapter, under Section 4.2.1.

5.3.3. Proton Conductivity Studies

Extensive exploration of the functional characteristics of W^{VI}-OH groups in electrochemical HER has sparked additional interest in investigating their applicability in the energy sector, specifically in the context of conducting proton studies on hydroxylated POM compounds.[18,19] Utilizing the mobile protons within the functionalized hydroxyl groups and the lattice- and coordinated water molecules found in compound **1** and **2**, we conducted a thorough investigation into the solid-state proton conductivity of these compounds. Alternative current electrochemical impedance spectroscopy (AC-EIS) was performed on the pelletized samples of compounds **1** and **2**. Detailed experimental procedure has been supplied

in Appendix, A5.1. Initially, the well ground POM micro-crystals were pelletized between two carbon wafers and impedance spectra were recorded in a temperature range of 40−80 °C at 98% relative humidity (RH). High frequency region in Nyquist plots [Z' (real impedance) *vs.* Z'' (imaginary impedance)] was considered to determine the respective resistance values. Finally, pellet dimensions and the resistance values obtained after fitting the Nyquist plots to equivalent circuits (see details in Appendix, Section A5.2) were taken to calculate the proton conductivity values of the compounds at the respective operational conditions

A preliminary experiment of protonolysis was performed on compounds **1** and **2**. It has been observed that an initial pH of 7.2 and 6.85 for compounds **1** and **2** were observed when they were dispersed in de-ionised water, which later dropped to a pH of 5.8 and 5.6 respectively over a period of 30 minutes. This suggests that the compounds **1** and **2** (insoluble in water) itself acts as an inorganic acid, releasing protons in aqueous environment. Therefore, it was further taken ahead for extensive proton conductivity studies.

5.3.3.1. Impedance measurements varying the relative humidity (RH)

Proton conductivity of any material is highly dependent on the relative humidity (RH) as well as the temperature applied. Initially, we evaluated the variations of the relative humidity (RH=75% to 90% at constant temperature = 50 °C) and their resulting performance shown by the pelletized compounds of **1** and **2**. It has been observed that with increase in the humidification from 75%, there has been an increment in the proton conductivity on them. The results suggested that both compounds **1** and **2** follow the water-mediated proton conduction. Figure 5.5.a,b shows the similar trend of increase in the proton conductivity with increase in relative humidity in both the cases.

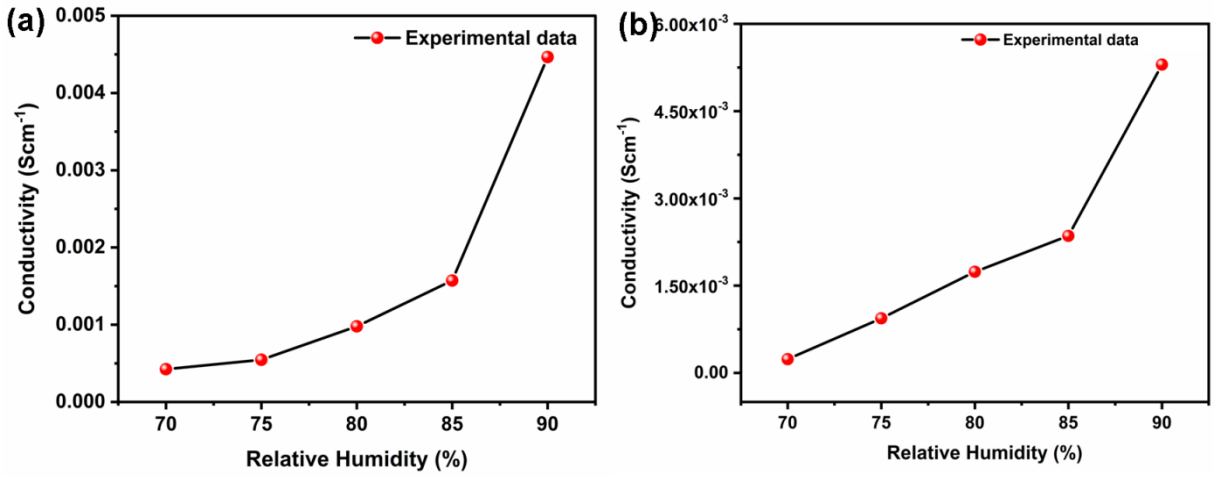

Figure 5.5. Plot showing the linear increment in proton conductivity values with increase in the relative humidity (RH %) for compounds **1** and **2**. The data were recorded at a constant temperature of 50 ℃.

5.3.3.2. Impedance measurement under different temperature

To gain a mechanistic insight on the proton transfer in the compound, temperature-dependent proton conductivity measurements were carried out from 40 °C at 98% relative humidity (RH). Impedance spectra were recorded for the pelletized compound in the temperature range of 40 to 80 °C. The compiled Nyquist plots obtained for compound **1** in the whole range of temperature (40 to 80 °C) have been shown in Figure 5.6.a. At an initial temperature of 40 °C, the conductivity value of 4.58 $\times 10^{-3}$ Scm^{-1} was attained, which increased to 0.978 $\times 10^{-1}$ Scm^{-1} at 80 °C. Similarly, temperature dependent proton conductivity studies have been initially carried out on compound **2**. Figure 5.6.b has displayed a wide range of proton conductivity values from 1.58 $\times 10^{-3}$ Scm^{-1} at 40.1 °C and 98% R.H. to a higher value of 1.07 $\times 10^{-1}$ Scm^{-1} at an elevated temperature of 80 °C at 98% R.H. The proton conductivity value at 80 °C demonstrates a hike by hundred times to that of obtained at 40 °C proving the material to exhibit an excellent performance as a solid-oxide proton conductor. Thus, compounds **1** and **2** can be entitled as super proton conductive materials with a conductivity values in the range of 10^{-1} Scm^{-1} at a temperature of 80 °C and 98% RH.

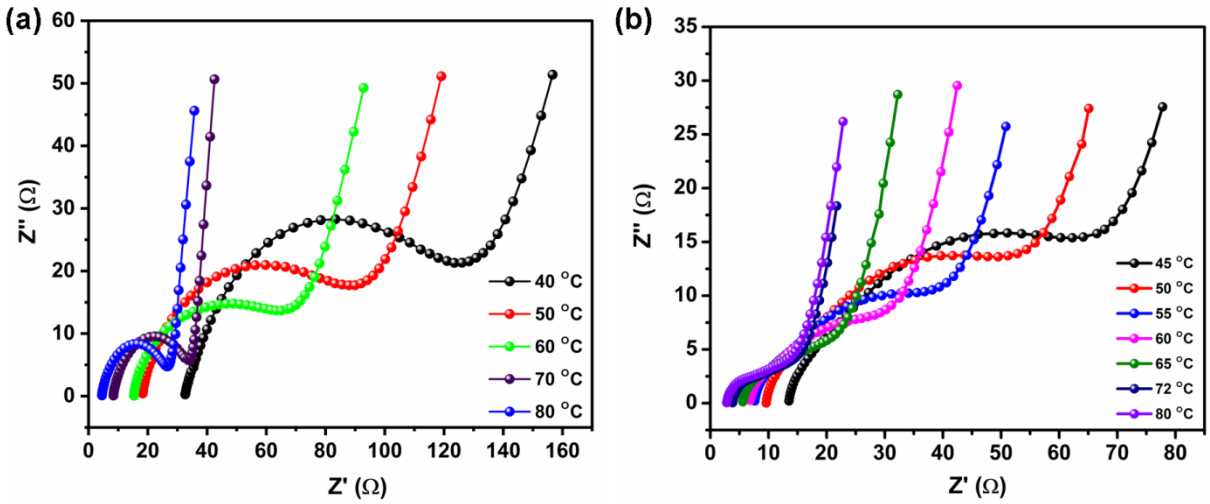

Figure 5.6. (a) Nyquist plots of impedance measurements performed at a constant relative humidity of 98% and variable temperature for (a) compound **1** and (b) compound **2**. Spheres denote experimental data points; solid line denotes fitted curve.

5.3.3.3. Determination of proton conductivity and activation energy

The Arrhenius activation energy (Ea) serves as a valuable indicator of the underlying mechanism governing proton conduction within a material. To discern this mechanism for compounds **1** and **2**, Arrhenius plots were constructed using temperature-dependent conductivity data. The experimentally obtained impedance spectral data were analyzed and fitted with the most relevant equivalent circuit ((R1/Q1) + (R2/Q2) + Q3), where R1 and R2

are resistance and Q1, Q2, and Q3 are constant phase elements)[20] to calculate the proton conductivity values. Notably, a linear relationship was observed over a temperature range spanning from 40 to 80°C, with a high coefficient of determination (R^2 = 0.95−0.97) for the Arrhenius plot. Through this analysis, the activation energy for compound **1** was determined to be 0.64 eV, strongly indicating that a vehicular mechanism predominantly facilitates proton transport within the compound (Figure 5.7.a). The detailed calculation of activation energy has been given in section A5.3 of the Appendix.

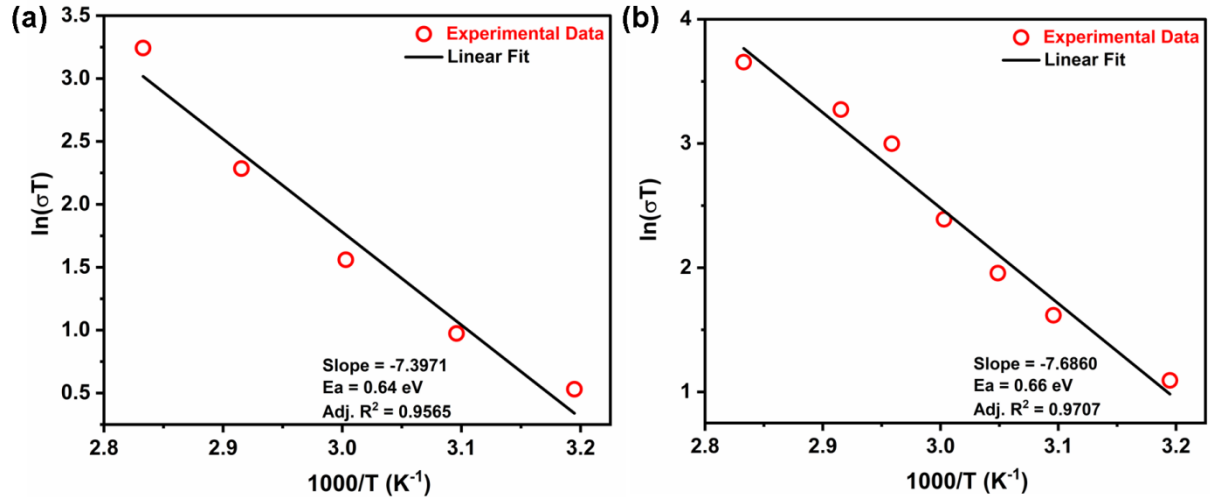

Figure 5.7. Arrhenius plot of constructed for (a) compound **1**, and (b) compound **2**.

On the same note, activation energy (Ea) for proton conduction was calculated for compound **2** as well, based on the proton conductivity values obtained from the temperature-dependent plots (Figure 5.7.b). The activation energy (Ea) for compound 2 is found to be 0.66 eV. The value of activation energy lies predominantly in the range of vehicular mechanism. There are basically two principal mechanisms to explain the proton transportation in any material, the Grotthuss mechanism; which shows activation energies lower than 0.4 eV, and the vehicle mechanism; showing higher activation energies larger than 0.4 eV.[21,22] In our study, the proton transport in both the compounds has been majorly governed by vehicular mechanism; with the involvement of vehicles like, protonated water molecules.

The temperature-dependence and humidity-variation conductivity studies have helped in uncovering the mechanistic pathway of the conduction of protons in the title compound. A major contribution towards the proton conductivity could definitely be attributed due to the tungsten-hydroxyl (−OH) groups present on the surface of POMs, which offer labile and dynamic hydrogen bonding networks by acting as both proton donor as well as acceptor and

by imparting admirable proton conduction with minimal energy barriers.[23,24] In the hydrogen bonded network, the adsorbed water molecules aid in the migration of protons by utilizing the adjacent cation chain {–W(ONa)} (in case of **1**), in enhancing the proton conductivity. Thus, existence of two-dimensional hydrogen bonded network and lattice water molecules in the skeleton of compound **1** and **2**, prominently constitute a major factor for efficient proton conductivity of compound.[25,26]

5.3.3.4. Long-term stability check

Finally, we conducted a comprehensive assessment of the stability of conductivity values for pelletized compound **1** and **2** (see Appendix, Section A5.4). The long-term proton conductivity stability on the pelletized compound studies were carried out for **1** at 80 °C and it was found to be stable for 24 hours (Figure 5.8.a). Each data point was recorded at a time interval of 5 hours. The plot shows no fluctuation in the proton conductivity data obtained from the long-term stability experiment. Long-term proton conductivity experiment for a time period of 24 h validate the stability and reusability of compound **1** as solid proton conductors.

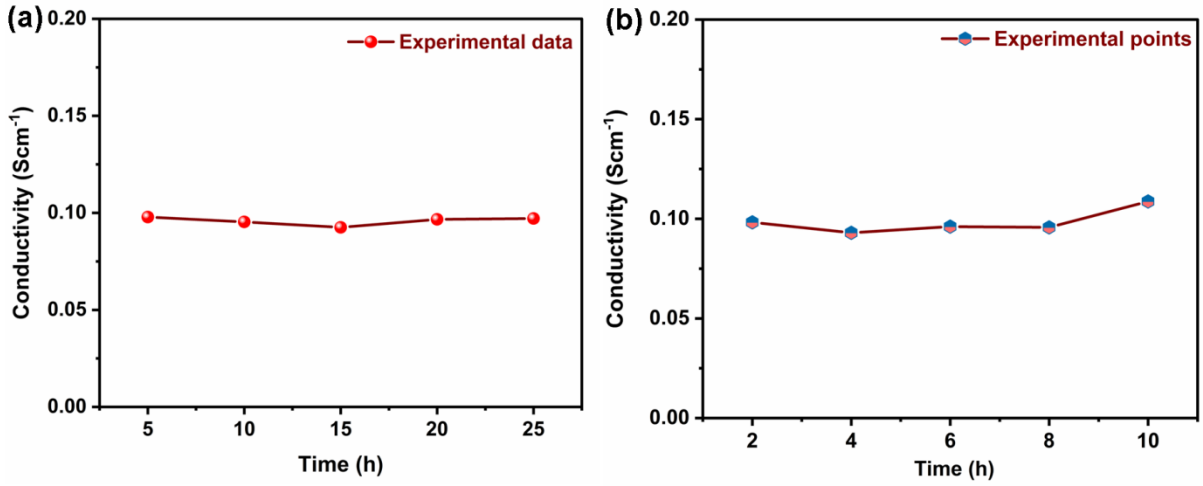

Figure 5.8. Long-term proton conductivity measurements on the pelletized sample of (a) compound **1** for 24 hours, (b) compound **2** for 10 hours.

Correspondingly, our investigation demonstrated that compound **1** maintained its robustness, with conductivity values remaining nearly constant over a 10-hour period at 80°C (Figure 5.8.b). Notably, achieving and sustaining stable conductivity values over an extended duration can be a formidable challenge for POM clusters.

It important to validate the structural integrity of the compound after the extensive proton conductivity experiments. Thus, FTIR and PXRD analyses have been performed on the pelletized samples after their long-term stability measurements. The FTIR spectra (Figure

A4.a, Appendix) have revealed that, the FTIR peaks exhibited by the compounds **1** and **2** before the proton conductivity analyses have remained intact even after long-term studies. Similarly, PXRD profile of the post proton conductive sample material has been compared to the post-pelletized samples of **1** and **2** (Figure A4.b, Appendix). The peaks of the post-analysis sample match well with the PXRD pattern of the post-pelletized ones.

Overall, compounds **1** and **2** have displayed remarkable stability for a long period of time. Thus, they exhibit exceptional proton conductivity values compared to other compounds documented in the literature. Based on this compelling evidence, we propose that hydroxylated POM-based materials have demonstrated their potential as outstanding solid proton conductors.

5.4. CONCLUSIONS

The application of compound **1** and **2** in solid-state proton conduction in the range of 10^{-1} offers a promising approach to harnessing the power of protons as charge carriers in fuel cells, emphasizing its potential in the development of advanced energy storage solutions. This research not only enriches our understanding of catalytic materials but also provides an important contribution to the ongoing efforts to mitigate the environmental impacts of energy generation and consumption. As we move forward, the findings presented in this article serve as a stepping stone for further research and innovation in the field of energy conversion and storage.

5.5. REFERENCES

1. Horn, M.R.; Singh, A.; Alomari, S.; Goberna-Ferrón, S.; Benages-Vilau, R.; Chodankar, N.; Motta, N.; Ostrikov, K.; Macleod, J.; Sonar, P.; et al. Polyoxometalates (POMs): From electroactive clusters to energy materials. *Energy Environ. Sci.* **2021**, *14*, 1652–1700.
2. Fuel Cell Technologies Office Multi-Year Research, Development, and Demonstration Plan Section 1.0 (US DOE, 2016).
3. Steele, B. C. H.; Heinzel, A. Materials for Fuel-Cell Technologies. *Nature*, **2001**, *414*, 345−352.
4. Jacobson, M. Z.; Colella, W. G.; Golden, D. M. Cleaning the Air and Improving Health with Hydrogen Fuel-Cell Vehicles. *Science*, **2005**, *308*, 1901−1905.
5. Zuo, Z.; Fu, Y.; Manthiram, A. Novel Blend Membranes Based on Acid-Base Interactions for Fuel Cells. *Polymers* **2012**, *4*, 1627–1644.

6. Zhai L, Li H. Polyoxometalate-Polymer Hybrid Materials as Proton Exchange Membranes for Fuel Cell Applications. *Molecules*. **2019**, *24*, 3425.
7. Laberty-Robert, C.; Vallé, K.; Pereira, F.; Sanchez, C. Design and Properties of Functional Hybrid Organic−inorganic Membranes for Fuel Cells. *Chem. Soc. Rev*. **2011**, *40*, 961−1005.
8. K. Schmidt-Rohr and Q. Chen, Parallel cylindrical water nanochannels in Nafion fuel-cell membranes. *Nat. Mater*., **2008**, *7*, 75–83.
9. H. N. Miras, L. Vilà-Nadal and L. Cronin, Polyoxometalate based open-frameworks (POM-OFs). *Chem. Soc. Rev.*, **2014**, *43*, 5679–5699.
10. Dolbecq, A.; Dumas, E.; Mayer, C.R.; Mialane, P. Hybrid Organic-Inorganic Polyoxometalate Compounds: From Structural Diversity to Applications. *Chem. Rev*. **2010**, *110*, 6009–6048.
11. S. Miyazawa, R. Hosono, R. Osuga, J. N. Kondo and S. Uchida, Effect of the ammonium ion on proton conduction in porous ionic crystals based on Keggin-type silicododecatungstate. *Acta Crystallogr., Sect. C: Struct. Chem.,* **2018**, *74*, 1289–1294.
12. Mulkapuri, S.; Ravi, A.; Mukhopadhyay, S.; Kurapati, S. K.; Siby V.; Das, S. K. W^{VI}–OH functionality on polyoxometalates for water reduction to molecular hydrogen. *Inorg. Chem. Front.* **2022**, *9*, 3566-3577.
13. Mukhopadhyay, S.; Das, A.; Jana, T.; Das, S. K. Fabricating a MOF Material with Polybenzimidazole into an Efficient Proton Exchange Membrane. *ACS Appl. Energy Mater*. **2020**, *3*, 7964−7977.
14. Mukhopadhyay, S.; Debgupta, J.; Singh, C.; Sarkar, R.; Basu, O.; Das, S. K. *ACS Appl. Mater. Interfaces*. **2019**, *11*, 13423−13432.
15. Basu, O.; Mukhopadhyay, S.; Laha, S.; Das, S. K. Defect Engineering in a Metal-Organic Framework System to Achieve Super-Protonic Conductivity. *Chem. Mater*. **2022**, *34*, 6734−6743.
16. Mulkapuri, S.; Kurapati, S. K.; Mukhopadhyay, S.; Das, S. K**.** A fully reduced $\{V^{IV}_{18}O_{42}\}$ host and VO_4^{3-}, Cl^- as guest anions: synthesis, characterization and proton conductivity. *New J. Chem***.**, **2019**, *43*, 17670-17679.
17. Ravi, A.; Mulkapuri, S.; Das, S. K. Hydroxylated Polyoxometalate with Cu(II)- and Cu(I)-Aqua Complexes: A Bifunctional Catalyst for Electrocatalytic Water Splitting at Neutral pH. *Inorg Chem.* **2023**, *62* 12650.

18. Ogiwara, N.; Iwano, T.; Ito, T.; Uchida, S. Proton Conduction in Ionic Crystals Based on Polyoxometalates. *Coordination Chemistry Reviews* **2022**, *462*, 214524.
19. Meng, X.; Wang, H.-N.; Song, S.-Y.; Zhang, H.-J. Proton-Conducting Crystalline Porous Materials. *Chem. Soc. Rev.* **2017**, *46* (2), 464–480.
20. Jash, P.; Parashar, R. K.; Fontanesi, C.; Mondal, P. C. The Importance of Electrical Impedance Spectroscopy and Equivalent Circuit Analysis on Nanoscale Molecular Electronic Devices. *Adv. Funct. Mater.* **2022**, *32*, 2109956.
21. Kreuer K.-D. Proton Conductivity: Materials and Applications *Chem. Mater.* **1996**, *8* 610.
22. Meng, X.; Wang, H.-N.; Song, S.-Y.; Zhang, H.-J. Proton-Conducting Crystalline Porous Materials. *Chem. Soc. Rev*. **2017**, *46*, 464.
23. Mehra, P.; Paul, A. Covalently Functionalized Hydroxyl-Rich Few-Layer Graphene for Solid-State Proton Conduction and Supercapacitor Applications. *J. Phys. Chem. C* **2022**, *126*, 6135–6146.
24. McKeen, J. C.; Yan, Y. S.; Davis, M. E. Proton Conductivity in Sulfonic Acid-Functionalized Zeolite Beta: Effect of Hydroxyl Group. *Chem. Mater*. **2008**, *20*, 3791–3793.
25. Yoshizawa-Fujita, M.; Kousa, Y.; Kidena, K.; Ohira, A.; Takeoka, Y.; Rikukawa, M. Proton Transport Properties in an Ionic Liquid Having a Hydroxyl Group. *Phys. Chem. Chem. Phys.* **2011**, *13*, 13427.
26. Bagusetty, A.; Choudhury, P.; Saidi, W. A.; Derksen, B.; Gatto, E.; Johnson, J. K. Facile Anhydrous Proton Transport on Hydroxyl Functionalized Graphane. *Phys. Rev. Lett.* **2017**, *118*, 186101.

Chapter 6

Concluding Remarks and Future Scope

6.1. Concluding remarks

The doctoral thesis entitled as "**Functional Inorganic Materials for Heterogeneous Electrocatalytic Water Splitting and Proton Conduction**" describes mainly about the utilization of an inorganic class of compounds, called polyoxometalates (POMs) for two imperative applications towards clean energy harnessing, viz. electrochemical water splitting and proton conduction. Varieties of POMs have been synthesized and extensively characterized and were thoroughly analysed and investigated for electrochemical studies. Thus, the works of this thesis mainly revolves around understanding or studying the behavior of functionalized POMs towards electrochemical water splitting and proton conduction.

Chapter 1 aims to outline the current plight of ever-increasing energy demands in the world, the population's high dependency on depleting fossil fuels, and the severe urge to move towards feasible alternatives to quench energy needs. Progress towards these goals requires, in part, the development of advanced materials and their appropriate utilization for energy storage, conversion, and harnessing. In this respect, hydrogen (H_2) is rising as an excellent fuel that can either be burnt or recombined with oxygen to release the stored energy in a fuel cell. One of the carbon-free methods to produce hydrogen includes electrochemical water splitting, where the development of electrocatalysts plays a vital role. Here, the basics of electrochemical water splitting, the reaction mechanisms involved, and the electrocatalysts utilized, particularly polyoxometalates (POMs) and metal-organic frameworks (MOFs) are briefed. Finally, advancement in fuel-cell technology with sufficient emphasis on the design of proton-conducting materials has also been discussed in this chapter.

Chapter 2 revolves around synthesizing and structurally characterizing a $\{Bi(OH_2)_2\}^{3+}$–functionalized Keggin polyoxometalate (POM) compound, $K_5[Bi(H_2O)_2SiW_{11}O_{39}]\cdot 13H_2O$ (**$K_5$1·13H_2O**) to employ them as electrocatalyst for water oxidation. However, **$K_5$1·13H_2O** *per se* is water soluble and unstable in the oxidation window of water oxidation, thus we encapsulated the functionalized Keggin POM anion $[Bi(OH_2)_2SiW_{11}O_{39}]^{5-}$ inside the cavities of a well-known zeolite type framework material ZIF-8 keeping in mind that $\{Bi(OH_2)_2\}^{3+}$ species on the surface of the POM has the potential to act as an active site for electrocatalytic water oxidation. The resulting host-guest type composite material $H_5[Bi(H_2O)_2SiW_{11}O_{39}]$@ZIF8 (**$H_5$1@ZIF8**) functions as an efficient electrocatalyst for water oxidation.

Chapter 3 describes the synthesis of a sole inorganic framework material $[Li(H_2O)_4][\{Cu^{I}(H_2O)_{1.5}\}\ \{Cu^{II}(H_2O)_3\}_2\ \{W^{VI}_{12}O_{36}(OH)_6\}]\cdot N_2\cdot H_2S\cdot 3H_2O$ (**$LiCu_3$*para-D***), consisting of a hydroxylated polyoxometalate (POM) anion, $\{W^{VI}_{12}O_{36}(OH)_6\}^{6-}$, a mixed-valent Cu(II)– and Cu(I)–aqua cationic complex species, $[\{Cu^{I}(H_2O)_{1.5}\}\{Cu^{II}(H_2O)_3\}_2]^{5+}$, a Li(I)-aqua complex cation and three solvent molecules and its characterization. **$LiCu_3$*para-D*** is found to be a bifunctional electrocatalyst showing oxygen evolution reaction (OER) by water oxidation and hydrogen evolution reaction (HER) by water reduction at the neutral pH. Various electrochemical experiments were performed to conclude that the title POM based material functions as a true bifunctional catalyst for electrocatalytic HER as well as OER at the neutral pH without catalyst reconstruction.

Chapter 4 basically studies a tungsten-hydroxyl, W^{VI}–OH, tethered polyoxotungstate complex, $Na_6[\{W^{VI}_{0.75}(OH)(ONa)\}_2\{Mn^{II}(H_2O)_2\}_2\{BiW^{VI}_9O_{33}\}_2]\cdot 18H_2O$ (**POM-MnW(OH)**), which has been structurally obtained as a 2-D framework. The presence of tungsten-hydroxyls on the surface of POM drove us to investigate electrocatalytic hydrogen evolution which showed excellent hydrogen evolution reaction (HER) activity with a TOF value of 1.81 s^{-1} and stability in terms of 1000 cyclic voltammetric cycles besides 10 hours of chronoamperometry in acidic buffer environment pH 4. POMs in acidic conditions shows its best stability and activity, thus, here the title compound has also exhibited an exemplary stability and promising catalytic activity.

Chapter 5 has dealt two Krebs-type polyoxometalate clusters incorporated with cobalt- and manganese- aqua complexes. These POM compounds possess unique structural distinctness with the presence of hydroxyl groups grafted onto the surface of tungsten centers which are present as the core of sandwitched complex of $\{Bi^{III}W^{VI}_9O_{33}\}^{9-}$ units. The compounds formulated as $Na_6[\{Co^{II}(H_2O)_3\}_2\{W^{VI}(OH)_2\}_2\{(Bi^{III}W^{VI}_9O_{33})_2\}]\cdot 8H_2O$ (**1**) and $Na_8H_3[\{W^{VI}_{0.75}(OH)(O)\}_2\{Mn^{II}(H_2O)_2\}_2\{BiW^{VI}_9O_{33}\}_2]\cdot 18H_2O$ (**2**)**,** possessing labile protons and lattice- and coordinated water molecules encouraged us to perform proton conductivity studies. These compounds have been thoroughly studied for proton conductivity in its solid-state and were found to be revealing conductivity values in the range of 10^{-1} Scm^{-1}, which are extremely high as far as polyoxometalate compounds are concerned.

6.2. Future Scope

The ranges of applications for polyoxometalates (POMs) based materials for energy harnessing are enormous and increasing on a daily basis, as the demand for the same are exponentially increasing. POMs, with their unique molecular structures and tunable properties, have emerged as versatile catalysts in the realm of photochemical reactions. As the world continues to grapple with the challenges of climate change and the need for cleaner energy sources, the application of POMs in these key processes offers a pathway toward more efficient and environmentally friendly solutions. Moreover, POMs can play a crucial role in the reduction of carbon dioxide, offering a sustainable approach to mitigating greenhouse gas emissions. By leveraging POMs' catalytic capabilities, researchers envision a future where these compounds contribute significantly to the development of efficient and selective processes for converting CO2 into valuable chemical feedstocks.

Additionally, POMs show promise in oxygen reduction reactions, essential in fuel cells and other energy conversion technologies. The controlled catalytic activity of POMs in these reactions can enhance the efficiency and longevity of oxygen reduction catalysts, paving the way for more robust and economically viable energy storage solutions. Beyond their applications in specific reactions, the utilization of POMs in photochemical processes aligns with the broader global objectives of achieving sustainable development goals. The future integration of POMs in water splitting, CO_2 reduction, and oxygen reduction reactions not only addresses the pressing need for cleaner energy sources but also contributes to a greener and more sustainable future by reducing the environmental impact of traditional industrial processes.

In future, polyoxometalate compounds can be taken forward for making composite materials for the applications mentioned above. Finally, POM or their composite materials can also be employed as nano-fillers in the proton exchange membranes (PEM) which further can enhance the conductivity of PEM and could be used in the fuel cells.

Appendix 1

Supporting Data for Chapter 2

Contents

Section A2.1 Single crystal X-ray diffraction analysis of K_5**1**·$13H_2O$

Bond distances (Å) and angles (°) for **$K_5$1·$13H_2O$**

Bi(1)-O(8)	2.300(12)	W(8)-O(8)	1.768(11)
Bi(1)-O(6)	2.301(10)	W(8)-O(35)	1.899(10)
Bi(1)-O(7)	2.334(11)	W(8)-O(38)	1.950(11)
Bi(1)-O(5)	2.382(11)	W(8)-O(26)	2.026(11)
Bi(1)-O(41)	2.507(11)	W(8)-O(4)	2.365(11)
Bi(1)-O(34)#1	2.549(11)	W(4)-O(17)	1.711(11)
Bi(1)-O(14)#2	2.586(10)	W(4)-O(16)	1.807(11)
Bi(1)-O(40)	2.688(11)	W(4)-O(18)	1.923(10)
W(9)-O(34)	1.716(10)	W(4)-O(19)	1.928(11)
W(9)-O(7)	1.764(11)	W(4)-O(20)	2.003(11)
W(9)-O(33)	1.924(11)	W(4)-O(2)	2.361(11)
W(9)-O(35)	1.937(11)	W(10)-O(29)	1.705(11)
W(9)-O(30)	2.055(11)	W(10)-O(30)	1.852(11)
W(9)-O(3)	2.335(10)	W(10)-O(28)	1.900(11)
W(11)-O(32)	1.700(11)	W(10)-O(23)	1.938(11)
W(11)-O(15)	1.873(11)	W(10)-O(31)	1.949(11)
W(11)-O(19)	1.880(11)	W(10)-O(3)	2.419(11)
W(11)-O(31)	1.927(11)	W(3)-O(39)	1.718(11)
W(11)-O(33)	1.939(11)	W(3)-O(12)	1.841(11)
W(11)-O(3)	2.341(11)	W(3)-O(13)	1.904(12)
W(1)-O(14)	1.742(11)	W(3)-O(18)	1.933(11)
W(1)-O(5)	1.767(11)	W(3)-O(21)	1.971(12)
W(1)-O(15)	1.938(10)	W(3)-O(2)	2.336(10)
W(1)-O(11)	1.943(11)	W(7)-O(37)	1.708(11)
W(1)-O(16)	2.080(11)	W(7)-O(10)	1.900(11)
W(1)-O(1)	2.253(11)	W(7)-O(13)	1.903(12)
W(2)-O(9)	1.726(10)	W(7)-O(27)	1.911(11)
W(2)-O(6)	1.807(10)	W(7)-O(38)	1.940(11)
W(2)-O(11)	1.929(11)	W(7)-O(4)	2.319(10)
W(2)-O(10)	1.933(11)	W(5)-O(22)	1.751(11)
W(2)-O(12)	2.036(11)	W(5)-O(20)	1.875(11)
W(2)-O(1)	2.257(10)	W(5)-O(23)	1.896(10)
W(8)-O(36)	1.712(11)	W(5)-O(24)	1.899(12)

W(5)-O(21)	1.909(11)	O(34)-W(9)-O(7)	103.6(5)
W(5)-O(2)	2.323(11)	O(34)-W(9)-O(33)	99.1(5)
W(6)-O(25)	1.715(11)	O(7)-W(9)-O(33)	93.7(5)
W(6)-O(26)	1.867(11)	O(34)-W(9)-O(35)	101.2(5)
W(6)-O(28)	1.916(11)	O(7)-W(9)-O(35)	91.8(5)
W(6)-O(24)	1.926(11)	O(33)-W(9)-O(35)	157.0(4)
W(6)-O(27)	1.930(11)	O(34)-W(9)-O(30)	94.4(5)
W(6)-O(4)	2.400(11)	O(7)-W(9)-O(30)	162.0(5)
		O(33)-W(9)-O(30)	84.3(5)
O(8)-Bi(1)-O(6)	77.3(4)	O(35)-W(9)-O(30)	83.6(5)
O(8)-Bi(1)-O(7)	76.1(4)	O(34)-W(9)-O(3)	165.5(4)
O(6)-Bi(1)-O(7)	121.4(4)	O(7)-W(9)-O(3)	89.9(4)
O(8)-Bi(1)-O(5)	122.3(4)	O(33)-W(9)-O(3)	74.2(4)
O(6)-Bi(1)-O(5)	79.6(4)	O(35)-W(9)-O(3)	83.5(4)
O(7)-Bi(1)-O(5)	72.5(4)	O(30)-W(9)-O(3)	72.4(4)
O(8)-Bi(1)-O(41)	81.0(4)	O(32)-W(11)-O(15)	102.5(5)
O(6)-Bi(1)-O(41)	77.0(4)	O(32)-W(11)-O(19)	100.8(5)
O(7)-Bi(1)-O(41)	145.6(4)	O(15)-W(11)-O(19)	87.8(5)
O(5)-Bi(1)-O(41)	141.9(4)	O(32)-W(11)-O(31)	98.8(5)
O(8)-Bi(1)-O(34)#1	78.6(4)	O(15)-W(11)-O(31)	158.7(5)
O(6)-Bi(1)-O(34)#1	143.1(4)	O(19)-W(11)-O(31)	88.5(5)
O(7)-Bi(1)-O(34)#1	78.4(4)	O(32)-W(11)-O(33)	100.2(5)
O(5)-Bi(1)-O(34)#1	137.2(3)	O(15)-W(11)-O(33)	89.7(4)
O(41)-Bi(1)-O(34)#1	72.0(3)	O(19)-W(11)-O(33)	158.9(5)
O(8)-Bi(1)-O(14)#2	145.5(4)	O(31)-W(11)-O(33)	86.3(5)
O(6)-Bi(1)-O(14)#2	75.9(4)	O(32)-W(11)-O(3)	171.9(4)
O(7)-Bi(1)-O(14)#2	137.2(4)	O(15)-W(11)-O(3)	83.2(4)
O(5)-Bi(1)-O(14)#2	73.3(3)	O(19)-W(11)-O(3)	85.1(4)
O(41)-Bi(1)-O(14)#2	72.1(3)	O(31)-W(11)-O(3)	75.5(4)
O(34)#1-Bi(1)-O(14)#2	111.9(3)	O(33)-W(11)-O(3)	73.8(4)
O(8)-Bi(1)-O(40)	139.9(4)	O(14)-W(1)-O(5)	102.0(5)
O(6)-Bi(1)-O(40)	142.4(4)	O(14)-W(1)-O(15)	102.2(5)
O(7)-Bi(1)-O(40)	75.6(4)	O(5)-W(1)-O(15)	93.6(5)
O(5)-Bi(1)-O(40)	74.3(4)	O(14)-W(1)-O(11)	95.5(5)
O(41)-Bi(1)-O(40)	108.4(3)	O(5)-W(1)-O(11)	97.0(5)
O(34)#1-Bi(1)-O(40)	68.5(3)	O(15)-W(1)-O(11)	156.9(5)
O(14)#2-Bi(1)-O(40)	71.0(3)	O(14)-W(1)-O(16)	91.9(5)

O(5)-W(1)-O(16)	165.7(5)	O(26)-W(8)-O(4)	70.7(4)
O(15)-W(1)-O(16)	79.9(4)	O(17)-W(4)-O(16)	104.4(5)
O(11)-W(1)-O(16)	84.9(4)	O(17)-W(4)-O(18)	99.6(5)
O(14)-W(1)-O(1)	168.2(4)	O(16)-W(4)-O(18)	92.6(5)
O(5)-W(1)-O(1)	84.9(5)	O(17)-W(4)-O(19)	103.9(5)
O(15)-W(1)-O(1)	86.8(4)	O(16)-W(4)-O(19)	89.5(5)
O(11)-W(1)-O(1)	73.9(4)	O(18)-W(4)-O(19)	155.1(5)
O(16)-W(1)-O(1)	82.0(4)	O(17)-W(4)-O(20)	98.4(5)
O(9)-W(2)-O(6)	100.0(5)	O(16)-W(4)-O(20)	157.1(5)
O(9)-W(2)-O(11)	96.1(5)	O(18)-W(4)-O(20)	84.9(5)
O(6)-W(2)-O(11)	95.7(5)	O(19)-W(4)-O(20)	83.7(5)
O(9)-W(2)-O(10)	102.5(5)	O(17)-W(4)-O(2)	168.4(4)
O(6)-W(2)-O(10)	92.2(5)	O(16)-W(4)-O(2)	85.4(4)
O(11)-W(2)-O(10)	158.3(4)	O(18)-W(4)-O(2)	73.4(4)
O(9)-W(2)-O(12)	95.0(5)	O(19)-W(4)-O(2)	82.1(4)
O(6)-W(2)-O(12)	164.7(4)	O(20)-W(4)-O(2)	72.1(4)
O(11)-W(2)-O(12)	85.4(4)	O(29)-W(10)-O(30)	100.4(5)
O(10)-W(2)-O(12)	81.8(4)	O(29)-W(10)-O(28)	103.1(5)
O(9)-W(2)-O(1)	169.6(5)	O(30)-W(10)-O(28)	91.8(5)
O(6)-W(2)-O(1)	84.1(4)	O(29)-W(10)-O(23)	104.1(5)
O(11)-W(2)-O(1)	74.0(4)	O(30)-W(10)-O(23)	155.4(5)
O(10)-W(2)-O(1)	86.8(4)	O(28)-W(10)-O(23)	84.7(5)
O(12)-W(2)-O(1)	81.5(4)	O(29)-W(10)-O(31)	98.4(5)
O(36)-W(8)-O(8)	104.5(5)	O(30)-W(10)-O(31)	89.0(5)
O(36)-W(8)-O(35)	101.9(5)	O(28)-W(10)-O(31)	158.0(5)
O(8)-W(8)-O(35)	93.3(5)	O(23)-W(10)-O(31)	85.5(5)
O(36)-W(8)-O(38)	100.3(5)	O(29)-W(10)-O(3)	169.6(5)
O(8)-W(8)-O(38)	90.4(5)	O(30)-W(10)-O(3)	73.7(4)
O(35)-W(8)-O(38)	155.7(5)	O(28)-W(10)-O(3)	85.9(4)
O(36)-W(8)-O(26)	95.2(5)	O(23)-W(10)-O(3)	81.7(4)
O(8)-W(8)-O(26)	159.9(5)	O(31)-W(10)-O(3)	73.3(4)
O(35)-W(8)-O(26)	86.0(4)	O(39)-W(3)-O(12)	102.4(5)
O(38)-W(8)-O(26)	82.4(4)	O(39)-W(3)-O(13)	101.7(5)
O(36)-W(8)-O(4)	164.4(5)	O(12)-W(3)-O(13)	87.6(5)
O(8)-W(8)-O(4)	89.3(5)	O(39)-W(3)-O(18)	98.7(5)
O(35)-W(8)-O(4)	84.3(4)	O(12)-W(3)-O(18)	91.9(5)
O(38)-W(8)-O(4)	71.8(4)	O(13)-W(3)-O(18)	159.2(5)

O(39)-W(3)-O(21)	99.3(5)	O(24)-W(5)-O(2)	84.4(4)
O(12)-W(3)-O(21)	158.2(5)	O(21)-W(5)-O(2)	73.8(4)
O(13)-W(3)-O(21)	87.6(5)	O(25)-W(6)-O(26)	103.5(5)
O(18)-W(3)-O(21)	85.1(5)	O(25)-W(6)-O(28)	101.7(5)
O(39)-W(3)-O(2)	169.1(5)	O(26)-W(6)-O(28)	88.7(5)
O(12)-W(3)-O(2)	86.0(4)	O(25)-W(6)-O(24)	100.6(5)
O(13)-W(3)-O(2)	85.4(4)	O(26)-W(6)-O(24)	155.8(5)
O(18)-W(3)-O(2)	73.8(4)	O(28)-W(6)-O(24)	84.3(5)
O(21)-W(3)-O(2)	72.5(4)	O(25)-W(6)-O(27)	98.3(5)
O(37)-W(7)-O(10)	99.3(5)	O(26)-W(6)-O(27)	88.8(5)
O(37)-W(7)-O(13)	102.2(5)	O(28)-W(6)-O(27)	159.9(5)
O(10)-W(7)-O(13)	86.0(5)	O(24)-W(6)-O(27)	89.8(5)
O(37)-W(7)-O(27)	101.1(5)	O(25)-W(6)-O(4)	170.8(5)
O(10)-W(7)-O(27)	159.6(5)	O(26)-W(6)-O(4)	72.4(4)
O(13)-W(7)-O(27)	88.6(5)	O(28)-W(6)-O(4)	86.7(4)
O(37)-W(7)-O(38)	99.6(5)	O(24)-W(6)-O(4)	84.0(4)
O(10)-W(7)-O(38)	91.1(5)	O(27)-W(6)-O(4)	73.6(4)
O(13)-W(7)-O(38)	158.2(5)	O(1)-Si(1)-O(3)	112.5(6)
O(27)-W(7)-O(38)	86.7(5)	O(1)-Si(1)-O(4)	110.6(6)
O(37)-W(7)-O(4)	172.0(5)	O(3)-Si(1)-O(4)	108.6(6)
O(10)-W(7)-O(4)	84.1(4)	O(1)-Si(1)-O(2)	107.9(6)
O(13)-W(7)-O(4)	85.2(4)	O(3)-Si(1)-O(2)	108.1(6)
O(27)-W(7)-O(4)	75.9(4)	O(4)-Si(1)-O(2)	109.1(6)
O(38)-W(7)-O(4)	73.0(4)	W(10)-O(30)-W(9)	121.9(5)
O(22)-W(5)-O(20)	99.9(5)	W(9)-O(33)-W(11)	120.3(5)
O(22)-W(5)-O(23)	101.4(5)	W(11)-O(15)-W(1)	155.3(6)
O(20)-W(5)-O(23)	91.5(5)	W(8)-O(35)-W(9)	145.8(6)
O(22)-W(5)-O(24)	100.7(5)	W(4)-O(18)-W(3)	121.2(5)
O(20)-W(5)-O(24)	159.5(5)	W(11)-O(32)-K(5)	140.8(6)
O(23)-W(5)-O(24)	84.7(5)	W(11)-O(31)-W(10)	120.9(5)
O(22)-W(5)-O(21)	100.0(5)	W(9)-O(34)-Bi(1)#1	156.8(6)
O(20)-W(5)-O(21)	88.4(5)	W(7)-O(38)-W(8)	122.0(6)
O(23)-W(5)-O(21)	158.3(5)	W(2)-O(6)-Bi(1)	133.8(5)
O(24)-W(5)-O(21)	87.8(5)	W(1)-O(5)-Bi(1)	132.5(6)
O(22)-W(5)-O(2)	172.0(4)	W(11)-O(19)-W(4)	147.4(7)
O(20)-W(5)-O(2)	75.2(4)	W(10)-O(28)-W(6)	151.8(6)
O(23)-W(5)-O(2)	85.2(4)	W(2)-O(11)-W(1)	116.5(5)

W(4)-O(16)-W(1)	151.2(6)	W(9)-O(3)-W(10)	91.9(4)
W(7)-O(10)-W(2)	153.2(6)	W(11)-O(3)-W(10)	90.2(3)
W(6)-O(26)-W(8)	124.4(6)	Si(1)-O(1)-W(1)	127.2(6)
W(9)-O(7)-Bi(1)	154.9(6)	Si(1)-O(1)-W(2)	128.4(6)
W(5)-O(21)-W(3)	120.9(6)	W(1)-O(1)-W(2)	93.8(4)
W(5)-O(20)-W(4)	120.7(6)	Si(1)-O(4)-W(7)	124.9(6)
W(7)-O(13)-W(3)	149.7(7)	Si(1)-O(4)-W(8)	123.0(6)
W(5)-O(23)-W(10)	152.7(7)	W(7)-O(4)-W(8)	93.1(4)
W(5)-O(24)-W(6)	153.0(6)	Si(1)-O(4)-W(6)	123.9(6)
W(7)-O(27)-W(6)	120.6(6)	W(7)-O(4)-W(6)	89.9(4)
W(8)-O(8)-Bi(1)	154.4(6)	W(8)-O(4)-W(6)	92.6(4)
W(3)-O(12)-W(2)	150.9(6)	Si(1)-O(2)-W(5)	125.9(6)
W(1)-O(14)-Bi(1)#2	138.3(5)	Si(1)-O(2)-W(3)	122.1(6)
Si(1)-O(3)-W(9)	123.6(6)	W(5)-O(2)-W(3)	92.8(4)
Si(1)-O(3)-W(11)	123.6(6)	Si(1)-O(2)-W(4)	123.4(6)
W(9)-O(3)-W(11)	91.6(4)	W(5)-O(2)-W(4)	92.0(4)
Si(1)-O(3)-W(10)	125.9(6)	W(3)-O(2)-W(4)	91.3(4)

Symmetry transformations used to generate equivalent atoms: #1 -x,-y+1,-z+1 #2 -x+1,-y+1,-z+1 #3 -x,-y,-z+1 #4 -x+1,-y+2,-z+1 #5 x-1,y-1,z #6 x+1,y+1,z #7 -x+1,-y+1,-z+2 #8 x-1,y,z #9 x,y-1,z #10 x+1,y,z #11 -x+2,-y+1,-z+2 #12 -x+3,-y+2,-z+2 #13 -x+2,-y+2,-z+2 #14 x,y+1,z

---

Bond Valence Sum (BVS) Calculations

```
Bond valence calculation. Numbers in brackets after atom symbols are
at.no., r and c - see O"Keeffe and Brese, J.A.C.S. 1991, 113, 3226
......Bi1

  Bi (83, 1.54, 1.67)                          Rij   Dij   Vij
                      -O  ( 8,  .63, 3.15) 2.12  2.30   .62
                      -O  ( 8,  .63, 3.15) 2.12  2.30   .61
                      -O  ( 8,  .63, 3.15) 2.12  2.33   .56
                      -O  ( 8,  .63, 3.15) 2.12  2.38   .49
                      -O  ( 8,  .63, 3.15) 2.12  2.59   .28
                      -O  ( 8,  .63, 3.15) 2.12  2.55   .31

  Bond valence sum for Bi  2.88

......W1

  W  (74, 1.38, 1.40)                          Rij   Dij   Vij
                      -O  ( 8,  .63, 3.15) 1.93  1.74  1.67
```

```
                      -O  ( 8,  .63, 3.15) 1.93  1.77  1.56
                      -O  ( 8,  .63, 3.15) 1.93  1.94   .98
                      -O  ( 8,  .63, 3.15) 1.93  1.94   .97
                      -O  ( 8,  .63, 3.15) 1.93  2.08   .67
                      -O  ( 8,  .63, 3.15) 1.93  2.25   .42

  Bond valence sum for W   6.28

......W2

  W  (74, 1.38, 1.40)                        Rij   Dij   Vij
                      -O  ( 8,  .63, 3.15) 1.93  1.73  1.75
                      -O  ( 8,  .63, 3.15) 1.93  1.81  1.40
                      -O  ( 8,  .63, 3.15) 1.93  1.93  1.01
                      -O  ( 8,  .63, 3.15) 1.93  1.93  1.00
                      -O  ( 8,  .63, 3.15) 1.93  2.04   .76
                      -O  ( 8,  .63, 3.15) 1.93  2.26   .42

  Bond valence sum for W   6.33

......W3
   W  (74, 1.38, 1.40)                        Rij   Dij   Vij
                      -O  ( 8,  .63, 3.15) 1.93  1.72  1.78
                      -O  ( 8,  .63, 3.15) 1.93  1.84  1.28
                      -O  ( 8,  .63, 3.15) 1.93  1.90  1.08
                      -O  ( 8,  .63, 3.15) 1.93  1.93  1.00
                      -O  ( 8,  .63, 3.15) 1.93  1.97   .90
                      -O  ( 8,  .63, 3.15) 1.93  2.34   .34

  Bond valence sum for W   6.38

......W4

  W  (74, 1.38, 1.40)                        Rij   Dij   Vij
                      -O  ( 8,  .63, 3.15) 1.93  1.71  1.82
                      -O  ( 8,  .63, 3.15) 1.93  1.81  1.40
                      -O  ( 8,  .63, 3.15) 1.93  1.92  1.03
                      -O  ( 8,  .63, 3.15) 1.93  1.93  1.01
                      -O  ( 8,  .63, 3.15) 1.93  2.00   .83
                      -O  ( 8,  .63, 3.15) 1.93  2.36   .31

  Bond valence sum for W   6.40

......W5

  W  (74, 1.38, 1.40)                        Rij   Dij   Vij
                      -O  ( 8,  .63, 3.15) 1.93  1.75  1.63
                      -O  ( 8,  .63, 3.15) 1.93  1.88  1.17
                      -O  ( 8,  .63, 3.15) 1.93  1.90  1.10
                      -O  ( 8,  .63, 3.15) 1.93  1.90  1.09
                      -O  ( 8,  .63, 3.15) 1.93  1.91  1.07
                      -O  ( 8,  .63, 3.15) 1.93  2.32   .35

  Bond valence sum for W   6.41
```

```
......W6

  W  (74, 1.38, 1.40)                          Rij   Dij   Vij
                      -O  ( 8,  .63, 3.15) 1.93  1.72  1.80
                      -O  ( 8,  .63, 3.15) 1.93  1.87  1.19
                      -O  ( 8,  .63, 3.15) 1.93  1.92  1.05
                      -O  ( 8,  .63, 3.15) 1.93  1.93  1.02
                      -O  ( 8,  .63, 3.15) 1.93  1.93  1.01
                      -O  ( 8,  .63, 3.15) 1.93  2.40   .28

  Bond valence sum for W   6.34

......W7

  W  (74, 1.38, 1.40)                          Rij   Dij   Vij
                      -O  ( 8,  .63, 3.15) 1.93  1.71  1.83
                      -O  ( 8,  .63, 3.15) 1.93  1.90  1.09
                      -O  ( 8,  .63, 3.15) 1.93  1.90  1.08
                      -O  ( 8,  .63, 3.15) 1.93  1.91  1.06
                      -O  ( 8,  .63, 3.15) 1.93  1.94   .98
                      -O  ( 8,  .63, 3.15) 1.93  2.32   .35

  Bond valence sum for W   6.40

......W8

  W  (74, 1.38, 1.40)                          Rij   Dij   Vij
                      -O  ( 8,  .63, 3.15) 1.93  1.71  1.81
                      -O  ( 8,  .63, 3.15) 1.93  1.77  1.56
                      -O  ( 8,  .63, 3.15) 1.93  1.90  1.09
                      -O  ( 8,  .63, 3.15) 1.93  1.95   .95
                      -O  ( 8,  .63, 3.15) 1.93  2.03   .78
                      -O  ( 8,  .63, 3.15) 1.93  2.37   .31

  Bond valence sum for W   6.51

......W9

  W  (74, 1.38, 1.40)                          Rij   Dij   Vij
                      -O  ( 8,  .63, 3.15) 1.93  1.72  1.79
                      -O  ( 8,  .63, 3.15) 1.93  1.76  1.58
                      -O  ( 8,  .63, 3.15) 1.93  1.92  1.02
                      -O  ( 8,  .63, 3.15) 1.93  1.94   .99
                      -O  ( 8,  .63, 3.15) 1.93  2.06   .72
                      -O  ( 8,  .63, 3.15) 1.93  2.34   .34

  Bond valence sum for W   6.43

......W10

  W  (74, 1.38, 1.40)                          Rij   Dij   Vij
                      -O  ( 8,  .63, 3.15) 1.93  1.71  1.85
                      -O  ( 8,  .63, 3.15) 1.93  1.81  1.40
                      -O  ( 8,  .63, 3.15) 1.93  1.92  1.03
                      -O  ( 8,  .63, 3.15) 1.93  1.93  1.01
```

```
                        -O   ( 8,   .63, 3.15) 1.93   2.00    .83
                        -O   ( 8,   .63, 3.15) 1.93   2.36    .31

  Bond valence sum for W    6.43

......W11

  W   (74, 1.38, 1.40)                              Rij    Dij    Vij
                        -O   ( 8,   .63, 3.15) 1.93   1.70   1.87
                        -O   ( 8,   .63, 3.15) 1.93   1.87   1.17
                        -O   ( 8,   .63, 3.15) 1.93   1.88   1.15
                        -O   ( 8,   .63, 3.15) 1.93   1.93   1.01
                        -O   ( 8,   .63, 3.15) 1.93   1.94    .98
                        -O   ( 8,   .63, 3.15) 1.93   2.34    .33

  Bond valence sum for W    6.53

......Si1

  Si  (14, 1.12, 1.58)                              Rij    Dij    Vij
                        -O   ( 8,   .63, 3.15) 1.70   1.61   1.27
                        -O   ( 8,   .63, 3.15) 1.70   1.59   1.33
                        -O   ( 8,   .63, 3.15) 1.70   1.64   1.17
                        -O   ( 8,   .63, 3.15) 1.70   1.65   1.16

  Bond valence sum for Si   4.93
```

Section A2.2. Raman spectral study

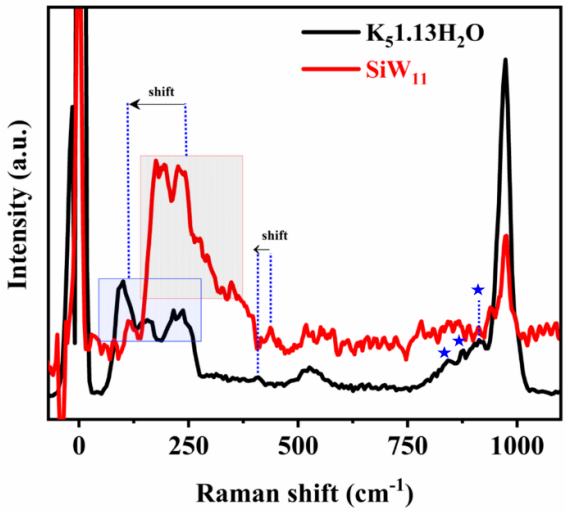

Figure A2.1. Raman spectrum of $K_8[SiW_{11}O_{39}]\cdot 13H_2O$ (SiW_{11}) and **$K_5$1·13H_2O**. The newly arose Raman bands in **$K_5$1·13H_2O** are marked with a star ( ) symbol and Raman shifts are given with shaded boxes.

Section A2.3. ICP-OES analysis of $K_5$1·13H_2O

Issued to:
Prof Samar K.Das
School Of Chemistry
University of Hyderabad, Gachibowli,
Hyderabad-500046
Kind Attn.:Mr.M.Sateesh, 9908652965

Report No. : LL/19-20/006110
Issue Date : 25/09/2019
Customer Ref.: TRF
Ref.Date : 08/08/2019

Sample Particulars : Bi@ L-POM

Sample description : Bi@ L-POM

Qty. Received : 1no Vial

Test Parameters : Silicon as Si,Tungsten as W,Bismuth as Bi,Potassium as K

Date of Receipt of Sample : 21/09/2019
Date of completion of analysis : 25/09/2019
Date of Starting of Analysis : 23/09/2019

SAMPLE TESTED AS RECEIVED

TEST RESULTS

S.No.	Parameters	Units	Results
1	Silicon as Si	% by mass	0.90
2	Tungsten as W	% by mass	66.52
3	Bismuth as Bi	% by mass	7.05
4	Potassium as K	% by mass	6.53

Instrument used:ICP-OES VARIAN 720-ES.
NOTE : This report and results relate only to the sample / items tested.

Figure A2.2. ICP-OES analysis of **$K_5$1·13H_2O**.

Section A2.4. Thermogravimetric study of $K_5$1·13H_2O

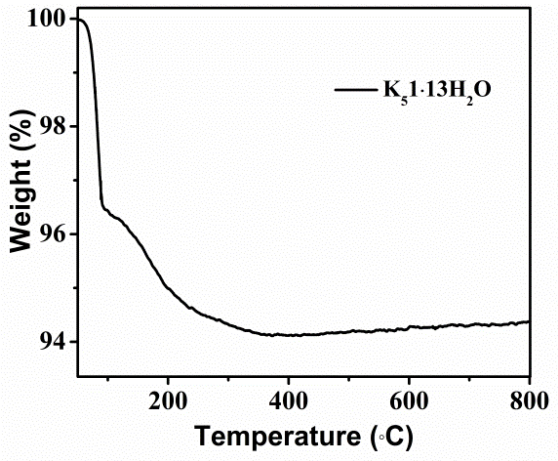

Figure A2.3. TGA profile of **$K_5$1·13H_2O**.

$H_5$1@ZIF8 analyses:

Section A2.5. ICP-OES analysis of $H_5$1@ZIF8

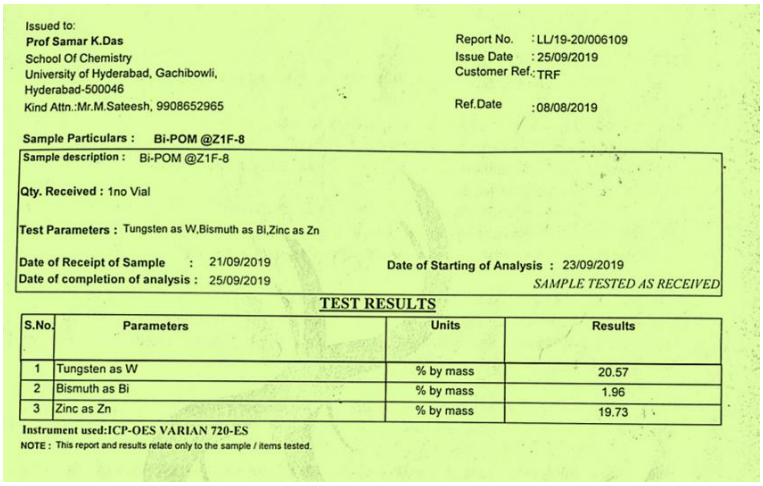

Issued to:
Prof Samar K.Das
School Of Chemistry
University of Hyderabad, Gachibowli,
Hyderabad-500046
Kind Attn.:Mr.M.Sateesh, 9908652965

Report No. : LL/19-20/006109
Issue Date : 25/09/2019
Customer Ref. : TRF
Ref.Date : 08/08/2019

Sample Particulars : Bi-POM @Z1F-8

Sample description : Bi-POM @Z1F-8

Qty. Received : 1no Vial

Test Parameters : Tungsten as W,Bismuth as Bi,Zinc as Zn

Date of Receipt of Sample : 21/09/2019
Date of completion of analysis : 25/09/2019
Date of Starting of Analysis : 23/09/2019
SAMPLE TESTED AS RECEIVED

TEST RESULTS

S.No.	Parameters	Units	Results
1	Tungsten as W	% by mass	20.57
2	Bismuth as Bi	% by mass	1.96
3	Zinc as Zn	% by mass	19.73

Instrument used:ICP-OES VARIAN 720-ES
NOTE : This report and results relate only to the sample / items tested.

Figure A2.4. ICP-OES analysis of $H_5$1@ZIF8.

The elemental composition of **$H_5$1@ZIF8** composite is obtained from ICP-OES. The ICP-OES data supplies a strong evidence for the elements present and their composition.

Calculation of unit cell occupancy by POM units

From the ICP-OES analysis data, Bi has the lowest molar mass percentage. Considering Bi composition to be unity, the composition of W and Zn are calculated.

Bi	**W**	**Zn**
1	**11.8057**	**31.8585**

Now, each unit cell of ZIF-8 consists of 24 ($C_8H_{10}N_4Zn$) units (from SCXRD). 4 Zn ions are situated on each face of the unit cell. Thus, each of the Zn is shared between two adjacent unit cells.

Therefore, contribution per Zn = ½.

Effective number of Zn in each unit cell = 24 × ½ =12

Thus, each unit cell has 12($C_8H_{10}N_4Zn$) units.

From the calculated composition of elements from the ICP-OES data, we can derive at the unit cell occupancy of **$K_5$1·13H_2O** in ZIF-8 cavities, to be 2.65 (~3) cages of ZIF-8 for each **$K_5$1·13H_2O**.

So, the unit cell occupancy of **$K_5$1·13H_2O** should be approximately one **$K_5$1·13H_2O** unit per 3 unit cells of ZIF-8.

Empirical formula of $H_5$1@ZIF8 from ICP-OES analysis

The empirical formula can be derived from the molar ratio between Bi and Zn. Thus, it is given as **$(C_8H_{10}N_4Zn)(H_5Bi(H_2O)SiW_{11}O_{39})_{0.0322}$**. This indicates that the loading level of **$K_5$1·13H_2O** in the cavities of ZIF-8 is found to be comparatively low.

Section A2.6. Average crystallite size calculation of ZIF-8 and $H_5$1@ZIF8 using Scherrer's equation

The average crystallite size of any material can be calculated from its PXRD profile using Scherrer's equation, which is formulated as:

$$D = K\lambda/\beta\cos\theta \qquad \ldots. (1)$$

D – crystallite size (nm)

K – Scherrer's constant (0.90)

λ – wavelength of the X-ray source (0.15406 nm)

β – Full width half maximum of intense PXRD peaks (rad), see Table below.

θ – Bragg angle (rad), see Table below.

Equation (1) gives the crystallite size value corresponding to each diffraction peak. Crystallite size for the intense diffraction peaks from the PXRD profile are separately calculated and thereby deriving the average value of crystallite size for the material under consideration.[6]

Table for crystallite size calculation of ZIF-8:

2θ	θ	**FWHM β (°)**	**Crystallite size D (nm)**
7.17428	3.58714	0.24923	31.9379
10.21851	5.109255	0.24339	32.77037
12.56834	6.28417	0.24966	32.01279
16.29116	8.14558	0.2708	29.63535
17.8766	8.9383	0.28147	28.57125
21.98018	10.99009	0.25544	31.68144
24.35625	12.17813	0.28774	28.24487
26.52911	13.26456	0.31481	25.92689
29.51706	14.75853	0.32275	25.45416
30.45236	15.22618	0.31763	25.92106
31.36397	15.68199	0.32802	25.15528
32.22946	16.11473	0.33301	24.8317
34.80237	17.40119	0.30237	27.5335

Average crystallite size for ZIF-8 = $\frac{D1+D2+D3+\cdots+D13}{13}$

= 28.436 nm

Table for crystallite size calculation of $H_5$1@ZIF8:

2θ	θ	**FWHM β (°)**	**Crystallite size D (nm)**
6.92868	3.46434	1.27895	6.222943
10.07994	5.03997	0.19953	39.96955
12.42383	6.211915	0.19452	41.08169
16.14285	8.071425	0.22247	36.06677
17.72557	8.862785	0.22866	35.16264
21.82379	10.9119	0.28178	28.71237
24.19875	12.09938	0.27168	29.90569
26.37339	13.1867	0.31783	25.67233
29.35388	14.67694	0.42378	19.37858
30.28003	15.14002	0.44056	18.68065
31.2022	15.6011	0.49956	16.51088
32.08802	16.04401	0.33771	24.4774
34.6271	17.31355	0.28598	29.09758

Similarly, Average crystallite size for **$H_5$1@ZIF8** = $\frac{D1+D2+D3+\cdots+D13}{13}$

= 26.995 nm

Thus, we have calculated the average crystallite size for ZIF-8 and the composite **$H_5$1@ZIF8** by following the above method and found to be 28.436 nm and 26.995 nm respectively.

Section A2.7. HRTEM-EDS and FESEM-EDX elemental mapping on $H_5$1@ZIF8 composite material

(a) HRTEM-EDS mapping

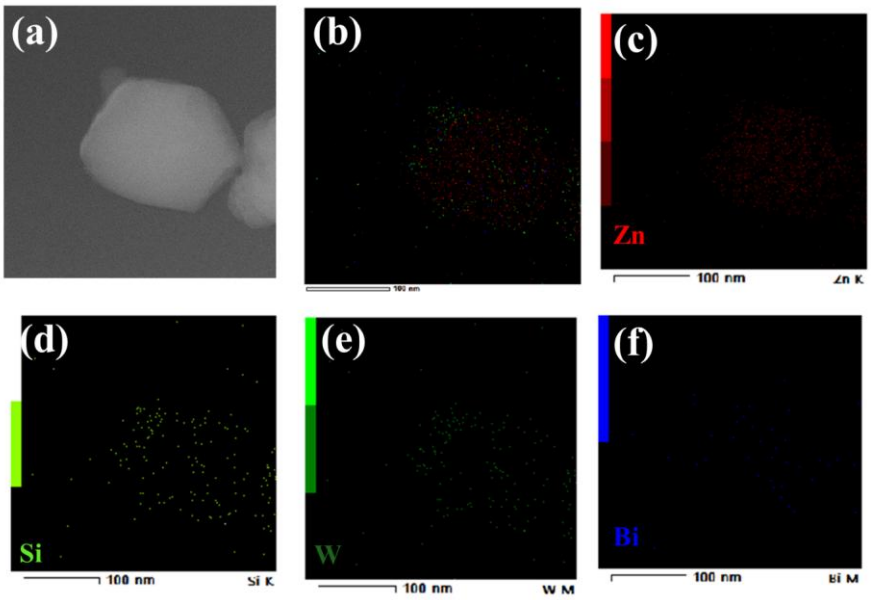

Figure A2.5. HRTEM-EDS elemental mapping on **$H_5$1@ZIF8** composite: (a) hexagonal particle, (b) mixed elemental mapping, (c) zinc, (d) silicon, (e) tungsten and (f) bismuth.

(b) FESEM-EDX mapping

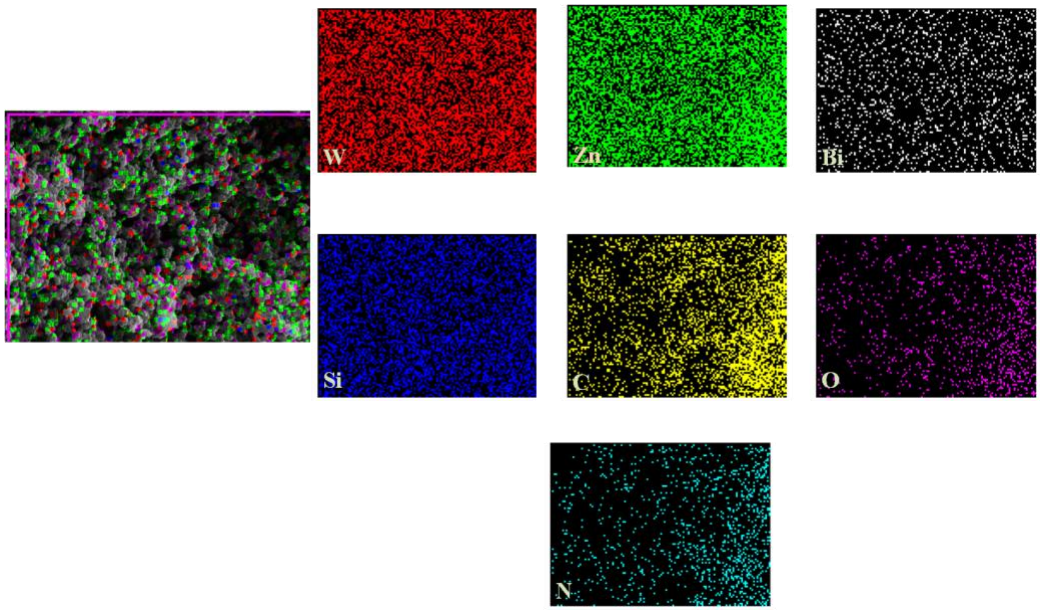

Figure A2.6. FESEM-EDX elemental mapping on **$H_5$1@ZIF8** composite.

Section A2.8. Thermogravimetric study

The thermogravimetric analyses for the compounds ZIF-8 and **$H_5$1@ZIF8** are carried out under N_2 atmosphere upto a temperature of 800 °C. There is an initial loss of weight upto 400 °C observed in **$H_5$1@ZIF8** composite as well as in ZIF-8. This can be attributed to the loss of bismuth coordinated water molecules and slow degradation of the host MOF in the composite **$H_5$1@ZIF8**, whereas in the case of ZIF-8, the concerned weight loss could be assigned to the collapse of MOF framework.

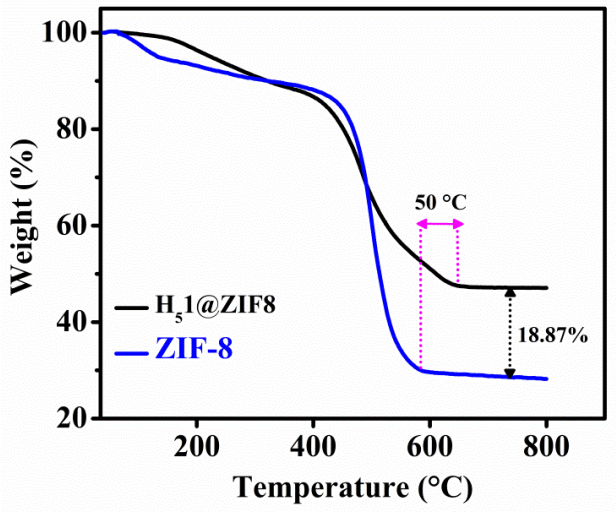

Figure A2.6. Thermogravimetric analysis of ZIF-8 and **$H_5$1@ZIF8**.

Section A2.9. Si2p XPS spectral analysis of $K_5$1·13H_2O and $H_5$1@ZIF8

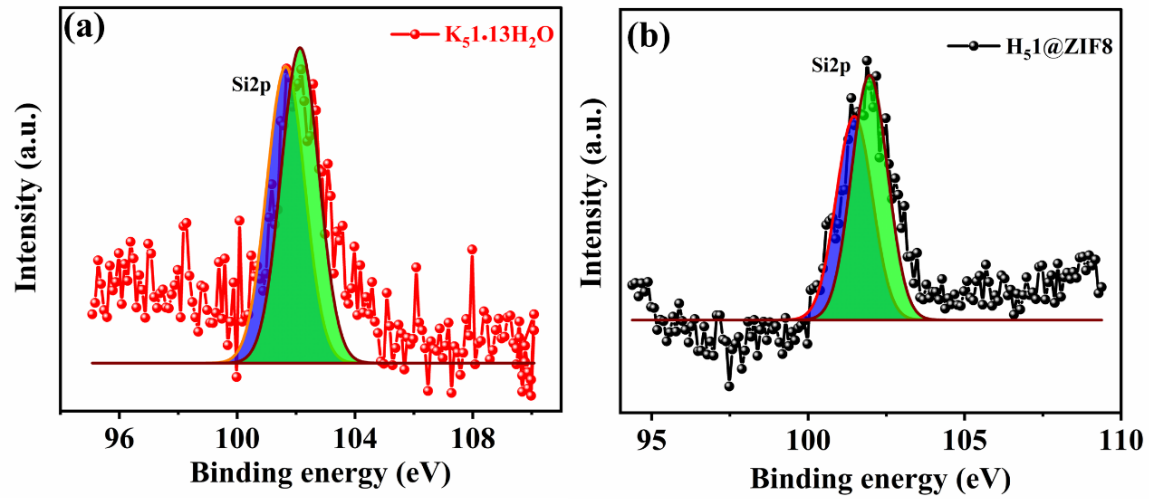

Figure A2.7. Si2p core level XPS spectrum of (a) **$K_5$1·13H_2O** and (b) **$H_5$1@ZIF8**.

Electrochemical studies:

Section A2.10. PXRD profiles of $H_5$1@ZIF8 immersed in different electrolytes

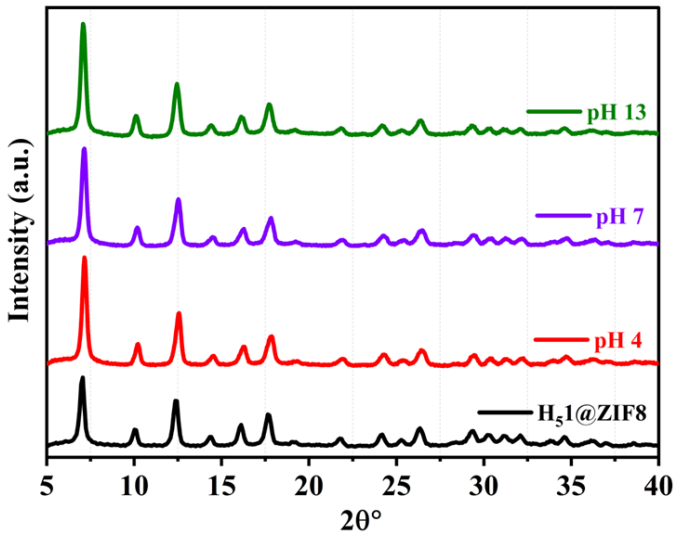

Figure A2.8. PXRD profiles of composite **$H_5$1@ZIF8** after its dipping for more than half an hour in different electrolytes of three different pH values (4.0, 7.0 and 13.0). The aqueous suspensions were filtered and the solids were dried at room temperature.

Section A2.11. Differential pulse voltammogram (DPV) profile of $H_5$1@ZIF8

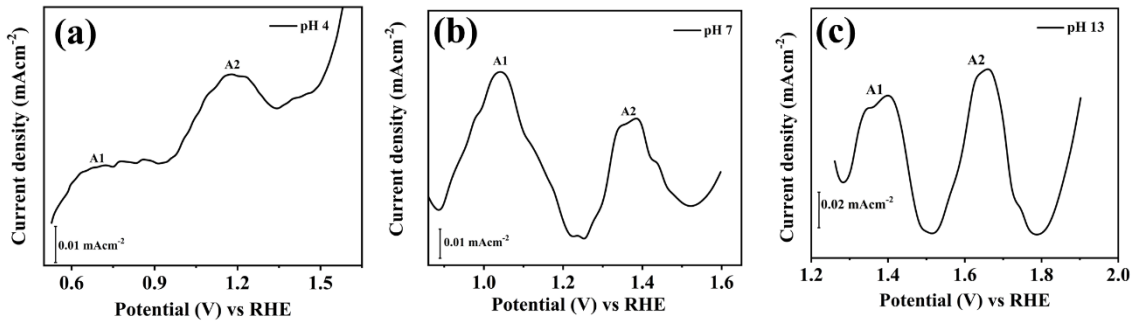

Figure A2.9. Differential pulse voltammogram (DPV) of **$H_5$1@ZIF8** was recorded in 0.1 M phosphate solution of (a) acidic pH 4 (b) neutral pH; and (c) in 0.1 M KOH solution of pH 13. The DPV was performed using the 50 mV pulse for 100 ms time and 5 mV step height for 80 ms step width and the integration time was 5 ms.

Section A2.12. Electrochemical stability of $H_5$1@ZIF8

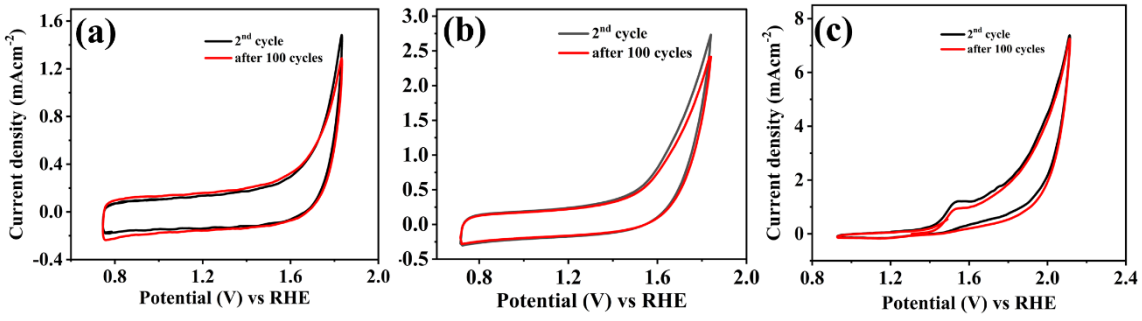

Figure A2.10. Cycling stability analysis of **$H_5$1@ZIF8** for oxygen evolution reaction was done for 100 CV cycles with a scan rate of 100 mVs^{-1}; in 0.1 M phosphate electrolyte (a) at pH 4, (b) at pH 7 and (c) in an alkaline pH 13 electrolyte of 0.1M KOH.

Section A2.13. Post-electrolysis electrode material characterization

(a) ICP-OES analysis of post electrolysis electrolyte

Issued to:
University of Hyderabad
C/O Prof Samar.K.Das
School of Chemistry
Hyderabad-500046
Kind Attn.:Mr.A Ravi, 889153430

Report No. : LL/21-22/010156
Issue Date : 13/01/2022
Customer Ref.: TRF
Ref.Date : 13/01/2022

Sample Particulars : Electrolyte Solution

Qty. Received : 1 No Vial

Test Parameters : Bismuth as Bi

Date of Receipt of Sample : 13/01/2022 **Date of Starting of Analysis** : 13/01/2022
Date of completion of analysis : 13/01/2022 *SAMPLE TESTED AS RECEIVED*

TEST RESULTS

S.No.	Parameters	Units	Results
1	Bismuth as Bi	ppm	Not Detected

Instrument Used: ICP-OES Varian 720-ES

NOTE : This report and results relate only to the sample / Items tested.

Figure A2.11. ICP-OES analysis report of the electrolyte after OER at pH 13.

(b) Electronic spectra of post electrolysis electrolyte

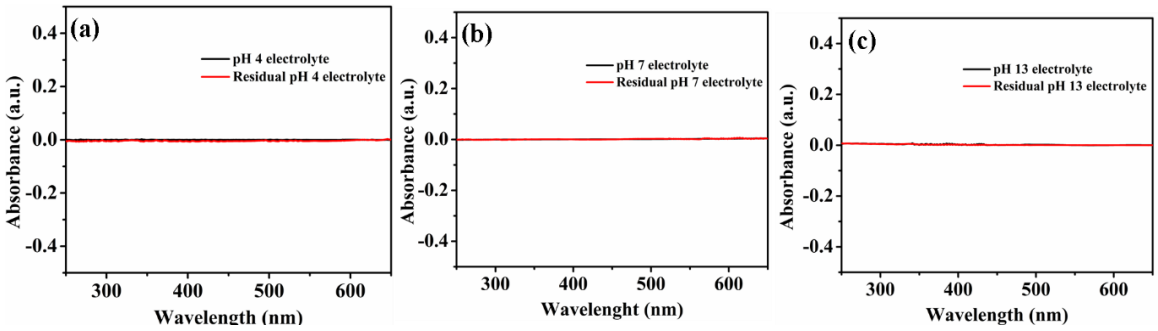

Figure A2.12. UV-visible spectra of **$H_5$1@ZIF8** recorded before (black line) and after (red line) electrolysis at (a) acidic pH 4 (0.1M) phosphate electrolyte (b) neutral pH 7 (0.1 M) phosphate buffer electrolyte and (c) alkaline pH 13 (0.1 M KOH) electrolyte.

(c) XPS analyses

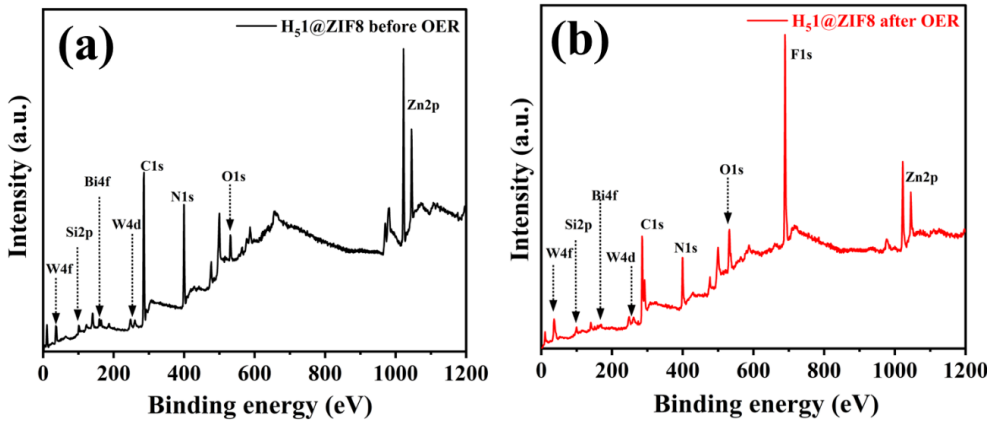

Figure A2.13. XPS survey scans of composite **$H_5$1@ZIF8**: (a) before electrolysis (b) after electrolysis at pH 13. F1s peak is from FTO plate.

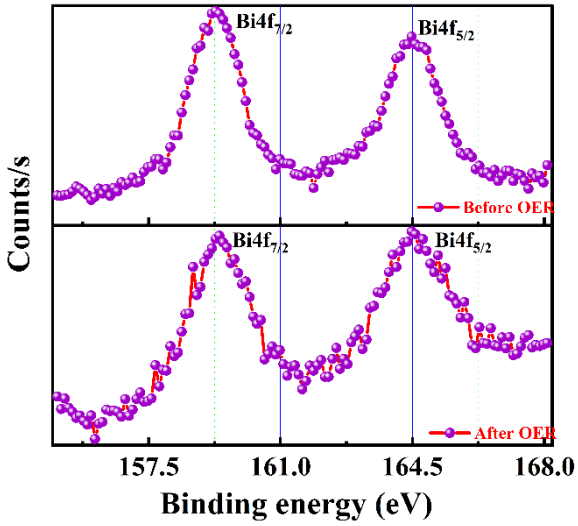

Figure A2.14. Core level XPS scans of Bi4f of composite **$H_5$1@ZIF8**: before electrolysis and after OER electrolysis at pH 13.

(d) FTIR spectra

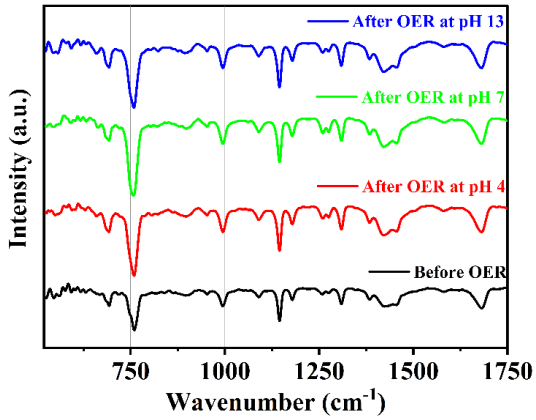

Figure A2.15. FTIR profiles showing the before and after OER analysis on **$H_5$1@ZIF8** films at different pH electrolytes.

(e) Raman spectra

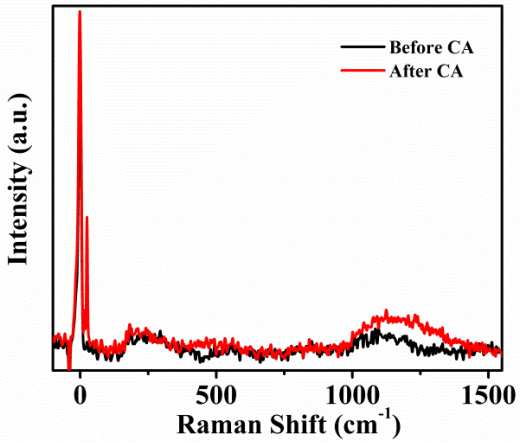

Figure A2.16. Raman spectral analysis of **$H_5$1@ZIF8** electrode material after CPE at pH 4.

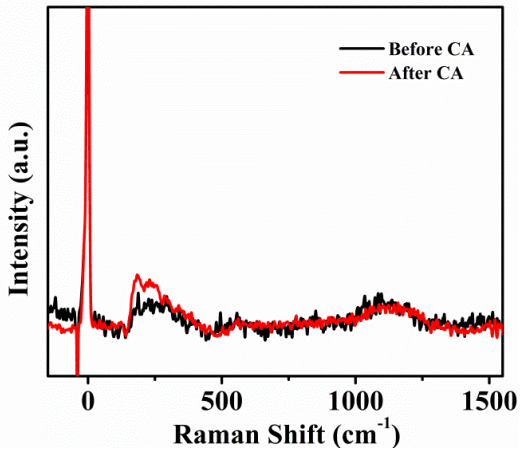

Figure A2.17. Raman spectral analysis of **$H_5$1@ZIF8** electrode material after CPE at pH 7.

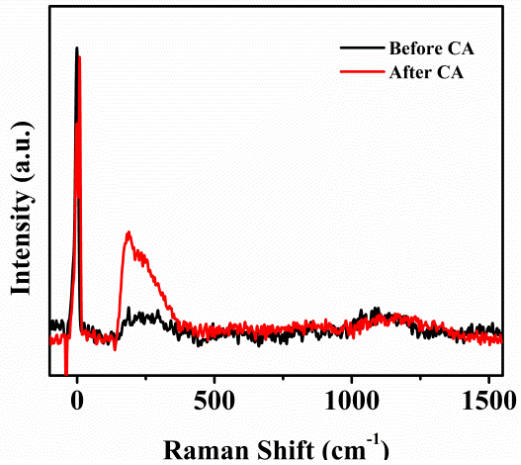

Figure A2.18. Raman spectral analysis of **$H_5$1@ZIF8** electrode material after CPE at pH 13.

(f) FESEM-EDX analysis:

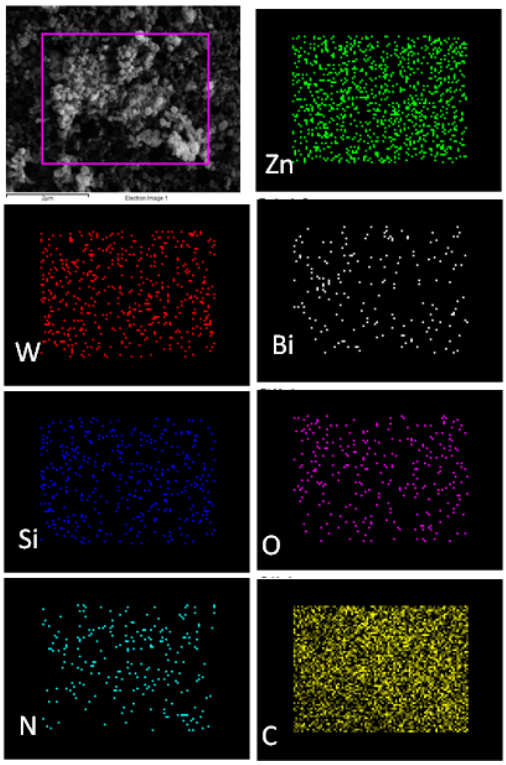

Figure A2.19. FESEM-EDX analysis of **$H_5$1@ZIF8-CPE** electrode material performed before electrolysis.

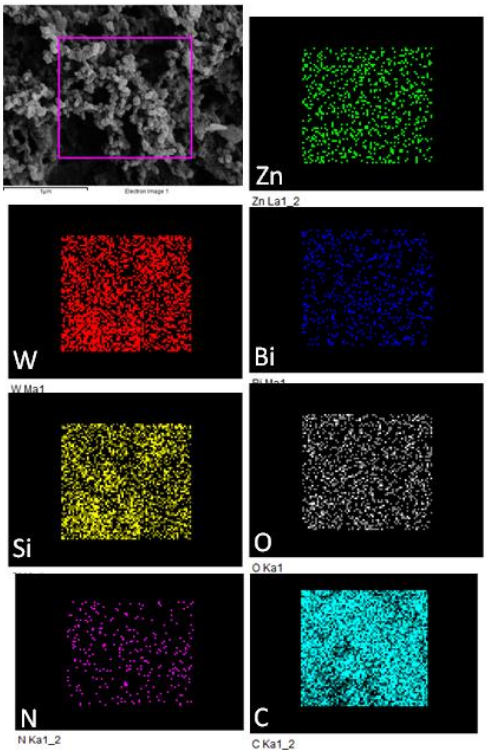

Figure A2.20. FESEM-EDX analysis of **$H_5$1@ZIF8-CPE** electrode material performed after OER at acidic pH 4.

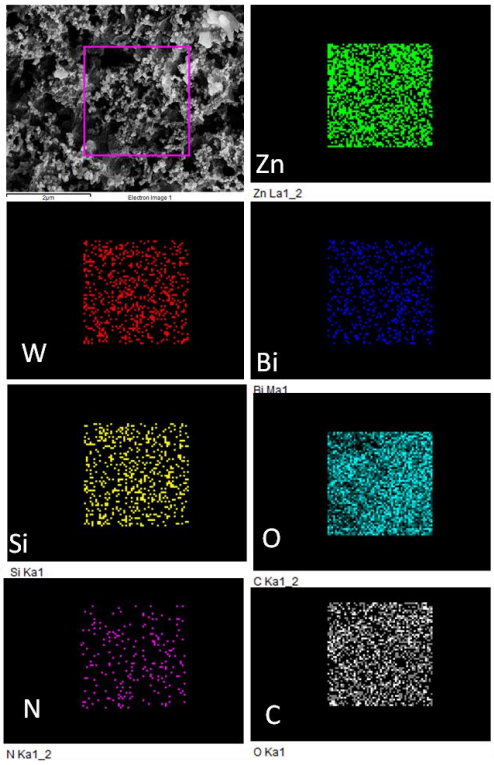

Figure A2.21. FESEM-EDX analysis of **$H_5$1@ZIF8-CPE** electrode material performed after OER at neutral pH.

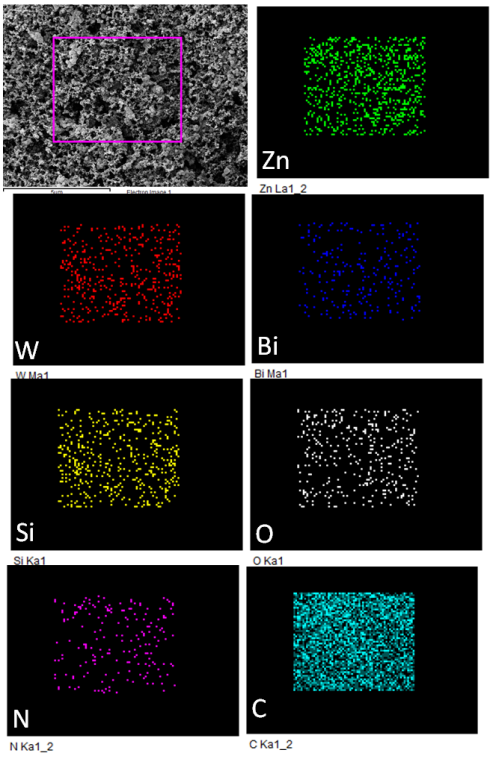

Figure A2.22. FESEM-EDX analysis of **$H_5$1@ZIF8-CPE** electrode material performed after OER at pH 13.

Section A2.14. Scan rate variation

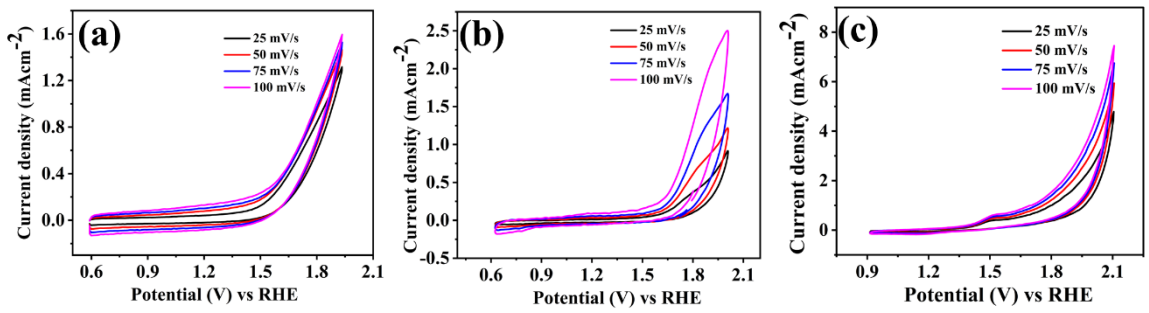

Figure A2.23. Scan rate variation cyclic voltammogram of **$H_5$1@ZIF8** performed at (a) acidic pH 4 (0.1 M) phosphate solution, (b) neutal pH 7 (0.1 M) phosphate buffer and (c) alkaline pH 13 (0.1M) KOH.

Section A2.15. Tafel data analysis

Tafel data collection was conducted in a galvanostatic mode by applying a constant current for 10 minutes and recording the corresponding steady state potential obtained. In a similar way, different currents values were applied in the range of 10^{-5} to 10^{-3} amperes and steady state potential were recorded. The electrolyte solution was continuously stirred at 480 rpm throughout the experiment. Prior to the Tafel data collection, solution resistance was obtained from the instrument iR function. The resistance value was used to correct the uncompensated cell resistance manually for each current value.

Table A2.1. Several ZIF-8 caged OER electrocatalysts working in acidic, neutral and alkaline conditions.

Catalysts	**Electrolyte (pH)**	**j ($mAcm^{-2}$)**	**Overpotential (mV)**	**Tafel slope ($mVdec^{-1}$)**	**Ref**
POM@ZIF-8	0.1 M Na_2SO_4 (7)	1	784.19	783.62	40 (main text)
CTMZ-8	0.1 M KCl (7)	1	387	210	7
	0.1 M KCl (2)	1	562	253.68	
FSWZ-8	0.1 M KCl (7)	1	516	344.4	8
SiW_9Co_3@ZIF-8	0.1 M KOH (13)	10	273	69.4	9
ZIF-8@ZIF-67@POM	1 M KOH (13)	10	490	88	10
$H_5$1@ZIF8	**0.1 M KOH (13)**	**1**	**375**	**188**	**Present work**
	0.1 M phosphate buffer (7)	**1**	**585.21**	**233**	
	0.1 M phosphate solution (4)	**1**	**830.1**	**448**	

Section A2.16. Faradaic efficiency calculation

Figure A2.24. The above figure shows the complete bulk electrolysis setup on which the quantitative measurement of O_2 evolution for **$H_5$1@ZIF8** was carried out. The working electrode is the stainless steel mesh and Pt wire is the counter electrode. The experiment is performed with a two-electrode set up which is visible from the image. The inverted graduated glass tube shows the amount of O_2 that evolved during the OER. The real-time O_2 bubbles are captured during the experiment.

The Faradaic efficiency can be calculated by bulk electrolysis where a constant current was applied for a period of time using a two-electrode cell.[1] The sample coated on stainless steel mesh with a surface area of 1 cm^2 (1.5 cm^2 for pH 13) was the working electrode (anode here) and a long platinum wire was used as the counter electrode. A loading of 1 mg/cm^2 was utilized on stainless steel mesh. A homemade setup was used for the quantitative oxygen evolution studies (which has two different chambers to separate the gases, oxygen, which will be collected in an inverted graduated tube with a precision of 0.05 mL, and hydrogen, collected in a separate chamber). The electrolysis was performed by applying a current density of 1 $mAcm^{-2}$. The oxygen bubbles initially were formed on the surface of the electrode and later were collected at the top of the inverted tube displacing the electrolyte. The H_2 gas bubbles were formed as a ring on the outer counter electrodic chamber and were not mixed with the O_2 bubbles due to the inverted tube setup. This way the amount of oxygen gas evolved was quantified.

The Faradaic efficiency can be calculated by bulk electrolysis where a constant current was applied for a period of time using a two-electrode cell.

Calculation of Faradaic Efficiency

Faradaic efficiency is defined as the efficiency with which charge is transferred in a system facilitating an electrochemical reaction.

Faradaic efficiency can be formulated as $\frac{number\ of\ moles\ of\ oxygen\ experimentally\ evolved}{number\ of\ moles\ of\ oxygen\ ideally\ should\ be\ evolved} * 100$

The quantitative oxygen evolution by bulk electrolysis was carried out in different pH solutions of acidic pH 4.0 and neutral pH 7.0 (in 0.1 M potassium phosphate electrolyte) and 0.1 M KOH of pH 13.0 electrolytic solution. The Faradaic efficiency was calculated for all the cases.

Case I: in acidic pH 4 potassium phosphate electrolyte

From the bulk electrolysis, O_2 evolved with the current density of 1 $mAcm^{-2}$ was found to be 0.2 mL/hour, at 1 atm pressure.

Thus, No. of moles of O_2 evolved = $\frac{0.2}{22400}$ = 8.9285 x 10^{-6} mol

O_2 ideally evolved = $\frac{Q\ (charge\ employed)}{n\ (no.of\ electrons\ involved\ in\ chemical\ reaction) * 1\ Farad}$

Here a current density of 1 $mAcm^{-2}$ was employed and 'n' = 4 for OER (as it is a 4 electron reaction)

Hence, O_2 ideally evolved = (0.001 A x 3600 s)/(4 x 96500 C) = 9.3264 x 10^{-6} mol.

Therefore, Faradaic efficieny was found out to be **95.7%**.

Case. II: in neutral pH 7 potassium phosphate buffer

From the bulk electrolysis, O_2 evolved with the current density of 1 $mAcm^{-2}$ was found to be 0.183 mL/hour, at 1 atm pressure.

No. of moles evolved = 0.183/22400 = 8.1696 x 10^{-6} mol

Thus, Faradaic efficiency obtained was **87.6%**.

Case III : in pH 13 potassium hydroxide electrolyte

For 0.1 M KOH, the amount of oxygen evolved on applying a current of 1.5 mA for 1.5 cm^{-2} was found to be 0.25 mL/1 hour at 1 atm pressure.

No. of moles evolved = 0.25/22400 = 1.11607 x 10^{-5} mol

Hence, O_2 ideally evolved = (0.0015 A x 3600 s)/(4 x 96500 C) = 1.3989 x 10^{-5} mol.

Therefore, Faradaic efficieny was found out to be **79.8%**.

Section A2.17. Turnover Frequency (TOF) calculation

Calculation of surface coverage and number of catalytically active atoms

The calculation of active surface coverage area on the surface of electrode is done using a method reported previously by our group. A graph of i_p *vs* scan rate has been constructed for all the pH values of which the slope value is used in the formula (1) for the measuring surface coverage (Γ_0).

$$\text{Slope} = n^2F^2A\,\Gamma_0/4RT \text{ ..... (1)}$$

where,

n = no. of electrons involved, here it is 2. For Bi(III)→Bi(V) conversion

F = 96500 C/mol; R= 8.314 J/mol K (ideal gas constant); T=298 K;

A= 0.071 cm^2 = geometrical surface area of GC electrode.

T = temperature during experiment = 298 K

Γ_0 – surface density of active bismuth atoms

Calculation of Turn over Frequency (TOF) from Tafel plot

TOF at any given over potential = $\frac{(Current\ density\ at\ given\ overpotential)}{4\ X\ F\ X\ surface\ density\ of\ bismuth\ atoms}$ …… (1)

Here, 4 is the number of electrons involved in OER. The TOF was calculated at current density of 1 mA/cm^2 or 0.001 A/cm^2.

Case I: at alkaline pH 13.0

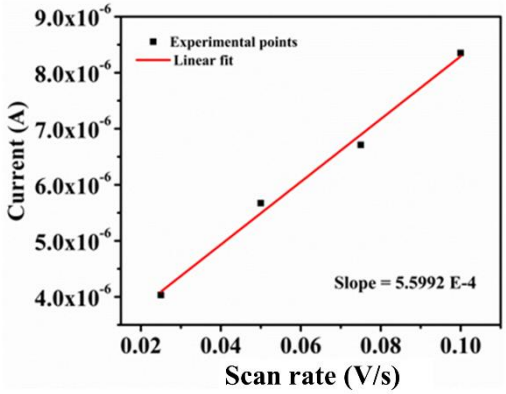

Figure A2.25. A graph of i *vs* scan rate was constructed for pH 13.

Slope = 5.5592 × 10^{-4}; $\Gamma 0 = (\text{Slope})(4RT)/ n^2F^2A$

or, $\Gamma 0 = (5.5592 \times 10^{-4} \times 4 \times 8.314 \times 298) / \{(2)^2 \times (96500)^2 \times 0.071\} = 2.083 \times 10^{-9}$

Thus, at pH 13.0, we obtained surface density of active bismuth atoms as 2.083 × 10^{-9} mol/cm^2.

Thus the TOF at the given overpotential,

$$TOF = \frac{0.001}{4 \times 96500 \times 2.083 \times 10^{-9}}$$

Thus $(TOF)_{j=1\ mA/cm^2} = 1.24\ s^{-1}$ at pH 13.0

Case II: at neutral pH 7.0

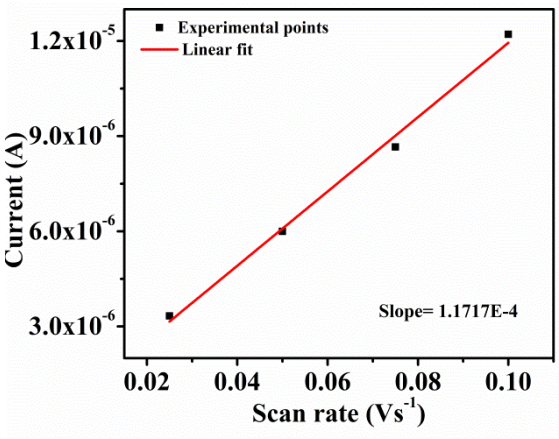

Figure A2.26. A graph of i *vs* scan rate was constructed for pH 7.

Slope = 1.1717×10^{-4}; $\Gamma 0 = (Slope)(4RT)/ n^2F^2A$

or, $\Gamma 0 = (1.1717 \times 10^{-4} \times 4 \times 8.314 \times 298) / \{(2)^2 \times (96500)^2 \times 0.071\} = 4.3906 \times 10^{-10}$

Thus, at pH 7.0, we obtained surface density of active bismuth atoms as 4.3906×10^{-10} mol/cm^2.

Accordingly,

$$TOF = \frac{0.001}{4 \times 96500 \times 4.3906 \times 10^{-10}}$$

Thus $(TOF)_{j=1\ mA/cm^2} = 5.90\ s^{-1}$ at pH 7.0

Case III: at acidic pH 4.0

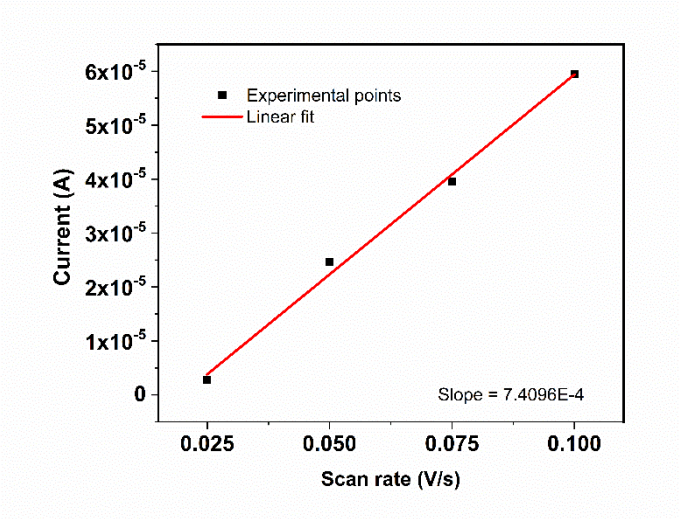

Figure A2.27. A graph of i *vs* scan rate was constructed for pH 4.

Slope = 7.4096×10^{-4}; $\Gamma 0 = (\text{Slope})(4RT)/ n^2F^2A$

or, $\Gamma 0 = (7.4096 \times 10^{-4} \times 4 \times 8.314 \times 298) / \{(2)^2 \times (96500)^2 \times 0.071\} = 2.7766 \times 10^{-9}$

Thus, at pH 4.0, we obtained surface density of active bismuth atoms as 2.7766×10^{-9} mol/cm^2.

Therefore,

$$\text{TOF} = \frac{0.001}{4 \times 96500 \times 2.7766 \times 10^{-9}}$$

Thus $(\text{TOF})_{j=1\ \text{mA/cm}^2} = 0.93\ \text{s}^{-1}$ at pH 4.0

Table A2.2. Comparison table for TOF values of a series of OER catalysts.

Catalysts	TOF (s^{-1})	References
Co-WOC-1	0.05	*Angew. Chem. Int. Ed.* **2016**, *55*, 2425 –2430
Y-$Co^{II}(H_2O)_2$	0.35	*Chem. Eur. J.* **2017**, *23*, 8051 – 8057
CoO_x@G-Ph-SN	1.2	*Chem. Sci.*, **2017**, *8*, 6111-6116
Nickel(II) porphyrin complex 1	0.67	*Inorg. Chem.* **2015**, *54*, 5604−5613
$Co(PO_3)_2$	0.21	*Adv. Funct. Mater.* **2013**, *23*, 227–233
$H_5$1@ZIF8	**0.93 (pH 4.0)**	**Present work**
	5.90 (pH 7.0)	
	1.24 (pH 13.0)	

Section A2.18. Oxygen Analysis by Gas Chromatography

For identifying the gas evolved during electrolysis, bulk electrolysis (constant current) has been carried out using a two-electrode system, where the stainless-steel mesh was used as working electrode (anode) and a large area platinum flag was used as a counter electrode (or cathode in the present case) in phosphate buffer of pH 7.0. The electrolysis was carried out by applying a constant current density of 2 $mAcm^{-2}$ for a period of 6 h. The head space of the electrolysis cell was purged with high purity N_2 gas for 1 h prior to electrolysis. Portion of gas mixtures in the head space of the electrolysis cell was directly injected into injection port of GC instrument (equipped with TCD detector) in order to know the composition of the evolved gas mixture over time. Below is the gas chromatographic trace of the gas mixture before and after electrolysis. The retention peak at around 2.5 corresponds to O_2 and around 3.5 corresponds to nitrogen. Increase in peak area of the oxygen in the plot clearly indicates evolution of oxygen gas over the experiment.

Before electrolysis:

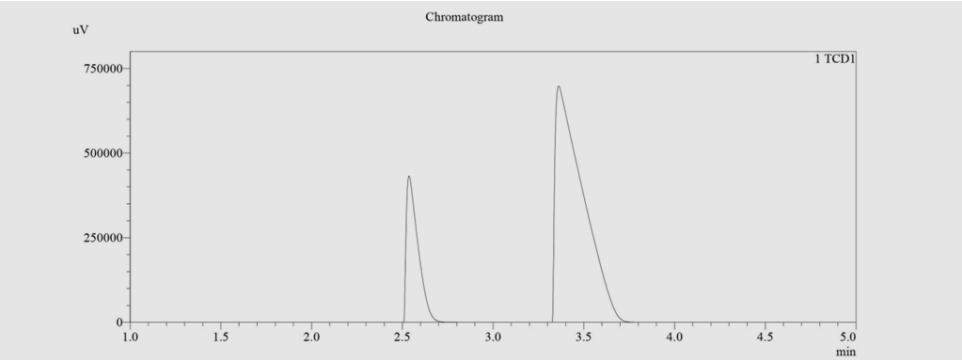

Figure A2.28. Gas chromatogram of the aerial gas.

After electrolysis:

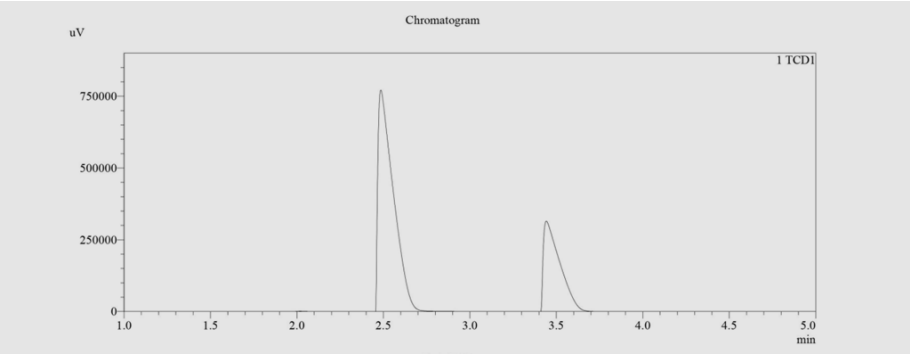

Figure A2.29. Gas chromatogram of the gas produced in OER bulk electrolysis.

Section A2.19. References:

1. Bose, S.; Debgupta, J.; Ramsundar, R. M.; Das, S. K. Electrochemical Water Oxidation Catalyzed by an In Situ Generated α-$Co(OH)_2$ Film on Zeolite-Y Surface, *Chem. Eur.J.* **2017**, *23*, 8051 −8057.

2. Sheldrick, G. M., *SADABS, Program for Absorption Correction*, **1997**, University of Gottingen, Gottingen, Germany.
3. Dolomanov, O.V.; Bourhis, L.J.; Gildea, R.J.; Howard, J.A.K.; Puschmann, H., OLEX2: A complete structure solution, refinement and analysis program. *J. Appl. Cryst.* **2009**, *42*, 339-341.
4. Sheldrick, G.M. *Acta Cryst.* **2015**, *C71*, 3-8. The SHELX-97 Manual. http://linux.uni-ac.gwdg.de/SHELX/
5. Bourhis, L.J.; Dolomanov, O.V., Gildea, R.J., Howard, J.A.K., Puschmann, H. *Acta Cryst.* **2015**, *A71*, 59-75.
6. Langford, J. I.; Wilson, A. J. C. Scherrer after sixty years: A survey and some new results in the determination of crystallite size. *J. Appl. Cryst.* **1978**, *11*,102-113.
7. Mukhopadhyay, S.; Basu, O.; Das, S. K. ZIF-8 MOF Encapsulated Co-porphyrin, an Efficient Electrocatalyst for Water Oxidation in a Wide pH Range: Works Better at Neutral pH, *ChemCatChem*, **2020**, *12*, 5430.
8. Mukhopadhyay, S.; Basu, O.; Kar, A.; Das, S. K. Efficient Electrocatalytic Water Oxidation by Fe(salen)−MOF Composite: Effect of Modified Microenvironment, *Inorg. Chem.*, **2020**, *59*, 472−483.
9. Abdelkader-Fernández, V. K.; Fernandes, D. M.; Balula, S. S.; Cunha-Silva, L.; Freire, C. Advanced framework-modified POM@ZIF-67 nanocomposites as enhanced oxygen evolution reaction electrocatalysts. *J. Mater. Chem. A*, 2020, *8*, 13509– 13521.
10. Wang, Y.; Wang, Y.; Zhang, L.; Liu, C. S.; Pang, H. Core–shell-type ZIF-8@ZIF-67@POM hybrids as efficient electrocatalysts for the oxygen evolution reaction, *Inorg. Chem. Front.*, **2019, *6*,** 2514−2520.

**********END**********

Appendix 2

Supporting Data for Chapter 3

Contents

Physical Characterizations

Section A3.1. Single Crystal X-ray Diffraction (SCXRD) analysis

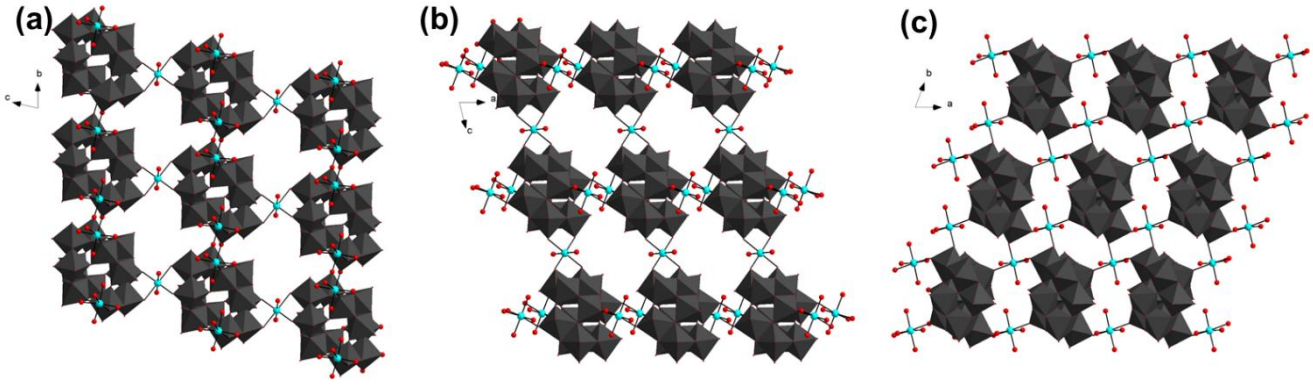

Figure A3.1. Compound $[Li(H_2O)_4][\{Cu^{I}(H_2O)_{1.5}\}\{Cu^{II}(H_2O)_3\}_2\{W^{VI}_{12}O_{36}(OH)_6\}]\cdot N_2\cdot H_2S\cdot 3H_2O$ (**$LiCu_3$*para-D***), shown in polyherdal-ball-stick representation viewed down to the: (a) *a*-axis, (b) *b*-axis, and (c) *c*-axis.

Alert level A

PLAT430_ALERT_2_A Short Inter D...A Contact S1 ..O16 . 2.78 Ang.
1-x,1-y,1-z = 2_666 Check
PLAT430_ALERT_2_A Short Inter D...A Contact S1 ..O16 . 2.78 Ang.
x,y,z = 1_555 Check

Author Response: The sulfur atom (S1), which is present in the form of H_2S as a lattice component in the concerned crystal and located in a special position, has been held by the POM framework oxygens with hydrogen bond distance of 2.78 Å; we, therefore, have been unsuccessful to assign hydrogen atoms to it. However, the distance of S1···O16 is reasonable and this is on par with H-bond distances, in general.[1]

Table A3.1. Bond lengths [Å] and angles [°] in the crystal structure of **$LiCu_3$*para-D***.

W(3)-O(10)	1.729(8)	W(2)-O(2)	2.070(8)
W(3)-O(11)	1.821(8)	W(2)-O(5)	2.245(8)
W(3)-O(12)	1.914(8)	W(1)-O(1)	1.719(9)
W(3)-O(9)	1.943(8)	W(1)-O(3)	1.837(9)
W(3)-O(3)	2.069(8)	W(1)-O(2)	1.871(8)
W(3)-O(5)	2.255(8)	W(1)-O(4)	1.960(8)
W(2)-O(7)	1.741(9)	W(1)-O(19)#1	1.992(9)
W(2)-O(8)	1.802(8)	W(1)-O(5)	2.277(8)
W(2)-O(6)	1.900(8)	W(6)-O(13)	1.726(9)
W(2)-O(9)	1.944(8)	W(6)-O(14)	1.784(8)

W(6)-O(4)	1.864(8)	O(10)-W(3)-O(3)	95.0(4)
W(6)-O(15)	1.960(8)	O(11)-W(3)-O(3)	161.0(4)
W(6)-O(8)#1	2.168(8)	O(12)-W(3)-O(3)	82.9(3)
W(6)-O(12)	2.231(8)	O(9)-W(3)-O(3)	82.4(3)
W(4)-O(21)	1.742(8)	O(10)-W(3)-O(5)	165.4(3)
W(4)-O(20)	1.780(8)	O(11)-W(3)-O(5)	88.1(3)
W(4)-O(19)	1.865(8)	O(12)-W(3)-O(5)	86.3(3)
W(4)-O(18)	1.950(8)	O(9)-W(3)-O(5)	71.1(3)
W(4)-O(11)	2.112(8)	O(3)-W(3)-O(5)	73.0(3)
W(4)-O(6)#1	2.237(8)	O(7)-W(2)-O(8)	104.0(4)
W(5)-O(17)	1.749(8)	O(7)-W(2)-O(6)	103.0(4)
W(5)-O(16)	1.754(9)	O(8)-W(2)-O(6)	95.4(4)
W(5)-O(18)	1.909(8)	O(7)-W(2)-O(9)	98.6(4)
W(5)-O(15)	1.911(8)	O(8)-W(2)-O(9)	92.5(3)
W(5)-O(6)#1	2.273(8)	O(6)-W(2)-O(9)	154.5(3)
W(5)-O(12)	2.280(8)	O(7)-W(2)-O(2)	93.1(4)
Cu(2)-O(14)	1.991(8)	O(8)-W(2)-O(2)	162.6(3)
Cu(2)-O(23)	1.997(11)	O(6)-W(2)-O(2)	83.7(3)
Cu(2)-O(24)	2.006(11)	O(9)-W(2)-O(2)	81.6(3)
Cu(2)-O(25)	2.018(10)	O(7)-W(2)-O(5)	163.8(4)
Cu(1)-O(20)	1.967(9)	O(8)-W(2)-O(5)	89.4(3)
Cu(1)-O(20)#2	1.967(9)	O(6)-W(2)-O(5)	84.6(3)
Cu(1)-O(22)	2.000(11)	O(9)-W(2)-O(5)	71.3(3)
Cu(1)-O(22)#2	2.000(11)	O(2)-W(2)-O(5)	73.3(3)
Cu(1)-O(17)#2	2.437(8)	O(1)-W(1)-O(3)	103.6(4)
Cu(1)-O(17)	2.437(8)	O(1)-W(1)-O(2)	103.9(4)
O(1)-Li(1)#3	2.70(9)	O(3)-W(1)-O(2)	93.4(4)
O(27)-Li(1)	2.12(10)	O(1)-W(1)-O(4)	100.5(4)
N(1)-N(2)	1.21(5)	O(3)-W(1)-O(4)	88.6(3)
O(26)-Li(1)	1.91(10)	O(2)-W(1)-O(4)	154.3(3)
O(28)-Li(1)#4	1.87(10)	O(1)-W(1)-O(19)#1	99.5(4)
		O(3)-W(1)-O(19)#1	156.1(4)
O(10)-W(3)-O(11)	104.0(4)	O(2)-W(1)-O(19)#1	86.7(3)
O(10)-W(3)-O(12)	100.7(4)	O(4)-W(1)-O(19)#1	81.4(3)
O(11)-W(3)-O(12)	94.0(3)	O(1)-W(1)-O(5)	179.6(4)
O(10)-W(3)-O(9)	99.6(4)	O(3)-W(1)-O(5)	76.7(3)
O(11)-W(3)-O(9)	93.7(3)	O(2)-W(1)-O(5)	76.2(3)
O(12)-W(3)-O(9)	155.8(3)	O(4)-W(1)-O(5)	79.4(3)

O(19)#1-W(1)-O(5)	80.1(3)	O(16)-W(5)-O(6)#1	165.3(3)
O(13)-W(6)-O(14)	102.2(4)	O(18)-W(5)-O(6)#1	73.2(3)
O(13)-W(6)-O(4)	99.8(4)	O(15)-W(5)-O(6)#1	87.4(3)
O(14)-W(6)-O(4)	96.7(4)	O(17)-W(5)-O(12)	163.3(3)
O(13)-W(6)-O(15)	95.4(4)	O(16)-W(5)-O(12)	92.9(3)
O(14)-W(6)-O(15)	95.3(4)	O(18)-W(5)-O(12)	82.8(3)
O(4)-W(6)-O(15)	158.1(3)	O(15)-W(5)-O(12)	73.5(3)
O(13)-W(6)-O(8)#1	91.9(4)	O(6)#1-W(5)-O(12)	76.6(3)
O(14)-W(6)-O(8)#1	165.3(3)	O(14)-Cu(2)-O(23)	85.0(4)
O(4)-W(6)-O(8)#1	84.8(3)	O(14)-Cu(2)-O(24)	89.9(4)
O(15)-W(6)-O(8)#1	79.0(3)	O(23)-Cu(2)-O(24)	173.1(5)
O(13)-W(6)-O(12)	166.3(4)	O(14)-Cu(2)-O(25)	173.9(4)
O(14)-W(6)-O(12)	87.5(3)	O(23)-Cu(2)-O(25)	91.8(5)
O(4)-W(6)-O(12)	88.5(3)	O(24)-Cu(2)-O(25)	93.8(5)
O(15)-W(6)-O(12)	73.8(3)	O(20)-Cu(1)-O(20)#2	180.0
O(8)#1-W(6)-O(12)	77.8(3)	O(20)-Cu(1)-O(22)	89.5(4)
O(21)-W(4)-O(20)	102.1(4)	O(20)#2-Cu(1)-O(22)	90.5(4)
O(21)-W(4)-O(19)	99.8(4)	O(20)-Cu(1)-O(22)#2	90.5(4)
O(20)-W(4)-O(19)	96.3(4)	O(20)#2-Cu(1)-O(22)#2	89.5(4)
O(21)-W(4)-O(18)	98.3(4)	O(22)-Cu(1)-O(22)#2	180.0
O(20)-W(4)-O(18)	92.6(4)	O(20)-Cu(1)-O(17)#2	85.3(3)
O(19)-W(4)-O(18)	157.7(3)	O(20)#2-Cu(1)-O(17)#2	94.7(3)
O(21)-W(4)-O(11)	90.0(3)	O(22)-Cu(1)-O(17)#2	90.8(4)
O(20)-W(4)-O(11)	166.9(4)	O(22)#2-Cu(1)-O(17)#2	89.2(4)
O(19)-W(4)-O(11)	86.3(3)	O(20)-Cu(1)-O(17)	94.7(3)
O(18)-W(4)-O(11)	80.7(3)	O(20)#2-Cu(1)-O(17)	85.3(3)
O(21)-W(4)-O(6)#1	165.9(3)	O(22)-Cu(1)-O(17)	89.2(4)
O(20)-W(4)-O(6)#1	89.7(3)	O(22)#2-Cu(1)-O(17)	90.8(4)
O(19)-W(4)-O(6)#1	86.2(3)	O(17)#2-Cu(1)-O(17)	180.0
O(18)-W(4)-O(6)#1	73.3(3)	W(5)-O(15)-W(6)	117.5(4)
O(11)-W(4)-O(6)#1	77.6(3)	W(2)-O(8)-W(6)#1	140.2(4)
O(17)-W(5)-O(16)	103.0(4)	W(2)-O(6)-W(4)#1	139.7(4)
O(17)-W(5)-O(18)	100.6(4)	W(2)-O(6)-W(5)#1	124.5(4)
O(16)-W(5)-O(18)	95.6(4)	W(4)#1-O(6)-W(5)#1	94.3(3)
O(17)-W(5)-O(15)	98.4(4)	W(1)-O(3)-W(3)	116.2(4)
O(16)-W(5)-O(15)	99.5(4)	W(3)-O(9)-W(2)	119.6(4)
O(18)-W(5)-O(15)	152.4(3)	W(3)-O(11)-W(4)	137.3(4)
O(17)-W(5)-O(6)#1	88.7(3)	W(1)-O(2)-W(2)	115.5(4)

W(5)-O(18)-W(4)	117.9(4)	W(2)-O(5)-W(3)	96.6(3)
W(6)-O(14)-Cu(2)	138.8(5)	W(2)-O(5)-W(1)	95.0(3)
W(3)-O(12)-W(6)	137.5(4)	W(3)-O(5)-W(1)	94.2(3)
W(3)-O(12)-W(5)	126.9(4)	O(28)#4-Li(1)-O(26)	171(5)
W(6)-O(12)-W(5)	94.4(3)	O(28)#4-Li(1)-O(27)	86(5)
W(6)-O(4)-W(1)	145.7(5)	O(26)-Li(1)-O(27)	101(3)
W(5)-O(17)-Cu(1)	125.5(4)	O(28)#4-Li(1)-O(1)#3	89(3)
W(4)-O(19)-W(1)#1	148.4(5)	O(26)-Li(1)-O(1)#3	85(4)
W(4)-O(20)-Cu(1)	141.0(5)	O(27)-Li(1)-O(1)#3	95(3)
W(1)-O(1)-Li(1)#3	137(2)		

Symmetry transformations used to generate equivalent atoms: #1 -x+1,-y+2,-z+1 #2 -x+1,-y+2,-z #3 -x+1,-y+1,-z+2 #4 -x+1,-y+1,-z+1

Section A3.2. Bond Valence Sum (BVS) Calculations

```
Bond valence calculation. Numbers in brackets after atom symbols are at.no.,
r and c - see O"Keeffe and Brese, J.A.C.S. 1991, 113, 3226

......W3

  W  (74, 1.38, 1.40)                          Rij   Dij   Vij
                      -O  ( 8,  .63, 3.15) 1.93  2.07   .69
                      -O  ( 8,  .63, 3.15) 1.93  1.94   .97
                      -O  ( 8,  .63, 3.15) 1.93  1.82  1.35
                      -O  ( 8,  .63, 3.15) 1.93  1.91  1.05
                      -O  ( 8,  .63, 3.15) 1.93  1.73  1.73
                      -O  ( 8,  .63, 3.15) 1.93  2.25   .42

  Bond valence sum for W   6.22

......W2

  W  (74, 1.38, 1.40)                          Rij   Dij   Vij
                      -O  ( 8,  .63, 3.15) 1.93  1.80  1.42
                      -O  ( 8,  .63, 3.15) 1.93  1.90  1.09
                      -O  ( 8,  .63, 3.15) 1.93  1.94   .97
                      -O  ( 8,  .63, 3.15) 1.93  2.07   .69
                      -O  ( 8,  .63, 3.15) 1.93  1.74  1.68
                      -O  ( 8,  .63, 3.15) 1.93  2.24   .43

  Bond valence sum for W   6.28

......W1

  W  (74, 1.38, 1.40)                          Rij   Dij   Vij
                      -O  ( 8,  .63, 3.15) 1.93  1.84  1.29
                      -O  ( 8,  .63, 3.15) 1.93  1.87  1.18
                      -O  ( 8,  .63, 3.15) 1.93  1.96   .93
                      -O  ( 8,  .63, 3.15) 1.93  1.72  1.78
                      -O  ( 8,  .63, 3.15) 1.93  2.28   .39
```

```
  Bond valence sum for W   5.58

......W6

  W  (74, 1.38, 1.40)                          Rij   Dij   Vij
                      -O  ( 8,  .63, 3.15) 1.93  1.96   .93
                      -O  ( 8,  .63, 3.15) 1.93  1.78  1.49
                      -O  ( 8,  .63, 3.15) 1.93  2.23   .45
                      -O  ( 8,  .63, 3.15) 1.93  1.86  1.20
                      -O  ( 8,  .63, 3.15) 1.93  1.73  1.75

  Bond valence sum for W   5.82

......W4

  W  (74, 1.38, 1.40)                          Rij   Dij   Vij
                      -O  ( 8,  .63, 3.15) 1.93  2.11   .62
                      -O  ( 8,  .63, 3.15) 1.93  1.95   .95
                      -O  ( 8,  .63, 3.15) 1.93  1.86  1.20
                      -O  ( 8,  .63, 3.15) 1.93  1.78  1.51
                      -O  ( 8,  .63, 3.15) 1.93  1.74  1.67

  Bond valence sum for W   5.95

......W5

  W  (74, 1.38, 1.40)                          Rij   Dij   Vij
                      -O  ( 8,  .63, 3.15) 1.93  1.91  1.06
                      -O  ( 8,  .63, 3.15) 1.93  1.91  1.07
                      -O  ( 8,  .63, 3.15) 1.93  1.75  1.62
                      -O  ( 8,  .63, 3.15) 1.93  2.28   .39
                      -O  ( 8,  .63, 3.15) 1.93  1.75  1.64

  Bond valence sum for W   5.78

......Cu2

  Cu (29,  .87, 1.75)                          Rij   Dij   Vij
                      -O  ( 8,  .63, 3.15) 1.47  2.02   .23
                      -O  ( 8,  .63, 3.15) 1.47  1.99   .24
                      -O  ( 8,  .63, 3.15) 1.47  2.00   .24
                      -O  ( 8,  .63, 3.15) 1.47  2.01   .23

  Bond valence sum for Cu   .94

......Cu1

  Cu (29,  .87, 1.75)                          Rij   Dij   Vij
                      -O  ( 8,  .63, 3.15) 1.47  2.44   .07
                      -O  ( 8,  .63, 3.15) 1.47  1.97   .26
                      -O  ( 8,  .63, 3.15) 1.47  2.00   .24

  Bond valence sum for Cu   .57

......O8

  O  ( 8,  .63, 3.15)                          Rij   Dij   Vij
                      -W  (74, 1.38, 1.40) 1.93  1.80  1.42

  Bond valence sum for O   1.42
```

```
......O6

  O  ( 8,  .63, 3.15)                          Rij   Dij   Vij
                      -W  (74, 1.38, 1.40) 1.93  1.90  1.09

  Bond valence sum for O   1.09

......O19

  O  ( 8,  .63, 3.15)                          Rij   Dij   Vij
                      -W  (74, 1.38, 1.40) 1.93  1.86  1.20

  Bond valence sum for O   1.20

......O13

  O  ( 8,  .63, 3.15)                          Rij   Dij   Vij
                      -W  (74, 1.38, 1.40) 1.93  1.73  1.75

  Bond valence sum for O   1.75

......O3

  O  ( 8,  .63, 3.15)                          Rij   Dij   Vij
                      -W  (74, 1.38, 1.40) 1.93  2.07   .69
                      -W  (74, 1.38, 1.40) 1.93  1.84  1.29

  Bond valence sum for O   1.98

......O9

  O  ( 8,  .63, 3.15)                          Rij   Dij   Vij
                      -W  (74, 1.38, 1.40) 1.93  1.94   .97
                      -W  (74, 1.38, 1.40) 1.93  1.94   .97

  Bond valence sum for O   1.94

......O11

  O  ( 8,  .63, 3.15)                          Rij   Dij   Vij
                      -W  (74, 1.38, 1.40) 1.93  1.82  1.35
                      -W  (74, 1.38, 1.40) 1.93  2.11   .62

  Bond valence sum for O   1.97

......O12

  O  ( 8,  .63, 3.15)                          Rij   Dij   Vij
                      -W  (74, 1.38, 1.40) 1.93  1.91  1.05
                      -W  (74, 1.38, 1.40) 1.93  2.23   .45
                      -W  (74, 1.38, 1.40) 1.93  2.28   .39

  Bond valence sum for O   1.89

......O10

  O  ( 8,  .63, 3.15)                          Rij   Dij   Vij
                      -W  (74, 1.38, 1.40) 1.93  1.73  1.73

  Bond valence sum for O   1.73
```

```
......O5

  O  ( 8,  .63, 3.15)                          Rij   Dij   Vij
                      -W  (74, 1.38, 1.40) 1.93  2.25   .42
                      -W  (74, 1.38, 1.40) 1.93  2.24   .43
                      -W  (74, 1.38, 1.40) 1.93  2.28   .39

  Bond valence sum for O   1.24

......O8

  O  ( 8,  .63, 3.15)                          Rij   Dij   Vij
                      -W  (74, 1.38, 1.40) 1.93  1.80  1.42

  Bond valence sum for O   1.42

......O2

  O  ( 8,  .63, 3.15)                          Rij   Dij   Vij
                      -W  (74, 1.38, 1.40) 1.93  2.07   .69
                      -W  (74, 1.38, 1.40) 1.93  1.87  1.18

  Bond valence sum for O   1.87

......O7

  O  ( 8,  .63, 3.15)                          Rij   Dij   Vij
                      -W  (74, 1.38, 1.40) 1.93  1.74  1.68

  Bond valence sum for O   1.68

......O4

  O  ( 8,  .63, 3.15)                          Rij   Dij   Vij
                      -W  (74, 1.38, 1.40) 1.93  1.96   .93
                      -W  (74, 1.38, 1.40) 1.93  1.86  1.20

  Bond valence sum for O   2.13

......O1

  O  ( 8,  .63, 3.15)                          Rij   Dij   Vij
                      -W  (74, 1.38, 1.40) 1.93  1.72  1.78

  Bond valence sum for O   1.78

......O15

  O  ( 8,  .63, 3.15)                          Rij   Dij   Vij
                      -W  (74, 1.38, 1.40) 1.93  1.96   .93
                      -W  (74, 1.38, 1.40) 1.93  1.91  1.06

  Bond valence sum for O   1.99

......O14

  O  ( 8,  .63, 3.15)                          Rij   Dij   Vij
                      -W  (74, 1.38, 1.40) 1.93  1.78  1.49
                      -Cu (29,  .87, 1.75) 1.47  1.99   .24
  Bond valence sum for O   1.23
```

```
......O18

  O  ( 8,  .63, 3.15)                          Rij   Dij   Vij
                     -W  (74, 1.38, 1.40) 1.93  1.95   .95
                     -W  (74, 1.38, 1.40) 1.93  1.91  1.07

  Bond valence sum for O   2.02

......O20

  O  ( 8,  .63, 3.15)                          Rij   Dij   Vij
                     -W  (74, 1.38, 1.40) 1.93  1.78  1.51
                     -Cu (29,  .87, 1.75) 1.47  1.97   .26

  Bond valence sum for O   1.77

......O21

  O  ( 8,  .63, 3.15)                          Rij   Dij   Vij
                     -W  (74, 1.38, 1.40) 1.93  1.74  1.67

  Bond valence sum for O   1.67

......O16

  O  ( 8,  .63, 3.15)                          Rij   Dij   Vij
                     -W  (74, 1.38, 1.40) 1.93  1.75  1.62

  Bond valence sum for O   1.62

......O17

  O  ( 8,  .63, 3.15)                          Rij   Dij   Vij
                     -W  (74, 1.38, 1.40) 1.93  1.75  1.64
                     -Cu (29,  .87, 1.75) 1.47  2.44   .07

  Bond valence sum for O   1.71

......O22

  O  ( 8,  .63, 3.15)                          Rij   Dij   Vij
                     -Cu (29,  .87, 1.75) 1.47  2.00   .24

  Bond valence sum for O    .24

......O23

  O  ( 8,  .63, 3.15)                          Rij   Dij   Vij
                     -Cu (29,  .87, 1.75) 1.47  2.00   .24

  Bond valence sum for O    .24

......O24

  O  ( 8,  .63, 3.15)                          Rij   Dij   Vij
                     -Cu (29,  .87, 1.75) 1.47  2.01   .23

  Bond valence sum for O    .23

......O25
```

```
  O   ( 8,   .63, 3.15)                          Rij    Dij    Vij
                      -Cu (29,   .87, 1.75) 1.47   2.02    .23

  Bond valence sum for O    .23

......O26

  O   ( 8,   .63, 3.15)                          Rij    Dij    Vij
                      -Li ( 3, 1.00,   .97) 1.50   1.91    .33

  Bond valence sum for O    .33

......O27

  O   ( 8,   .63, 3.15)                          Rij    Dij    Vij
                      -Li ( 3, 1.00,   .97) 1.50   2.12    .18

  Bond valence sum for O    .18

......O28

  O   ( 8,   .63, 3.15)                          Rij    Dij    Vij
                      -Li ( 3, 1.00,   .97) 1.50   1.87    .36

  Bond valence sum for O    .36
```

Section A3.3. ICP-OES Analysis

Issued to:
Athira Ravi
C/o. Prof. S K Das
University of Hyderabad
Gachibowli, Hyderabad - 500 046
Kind Attn.:Mr. Athira Ravi,

Report No. : LL/22-23/005912
Issue Date : 12/09/2022
Customer Ref.: Mail
Ref.Date : 17/08/2022

Sample Particulars : CuW12

Qty. Received : 1No Vial

Test Parameters : Copper as Cu,Lithium as Li,Sulphur as S,Tungsten as W.

Date of Receipt of Sample : 26/08/2022
Date of completion of analysis : 12/09/2022
Date of Starting of Analysis : 09/09/2022
SAMPLE TESTED AS RECEIVED

TEST RESULTS

S.No.	Parameters	UOM	Results
1	Copper as Cu	% by mass	5.51
2	Lithium as Li	% by mass	0.11
3	Sulphur as S	% by mass	0.62
4	Tungsten as W	% by mass	64.05

Instrument Used: ICP-OES Varian 720-ES
NOTE : This report and results relate only to the sample / items tested.

Figure A3.2. ICP-OES analysis report of **$LiCu_3$*para-D*.**

Section A3.4. X-ray Photoelectron Spectroscopy (XPS) Analysis

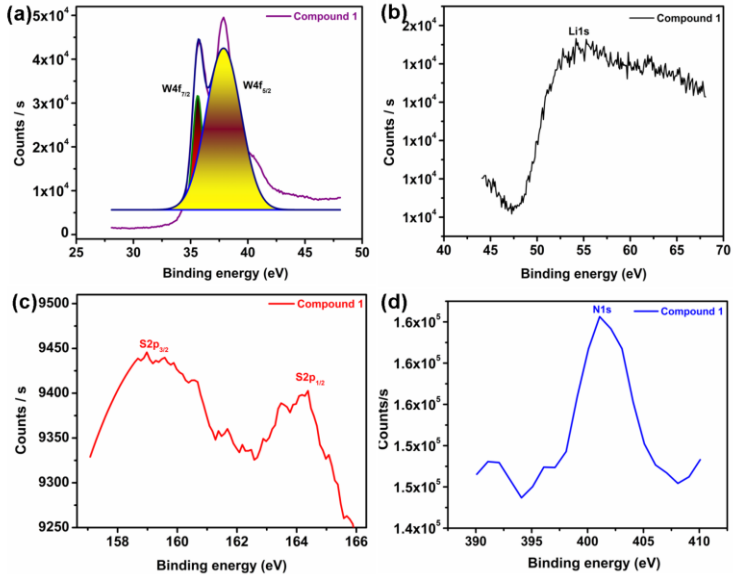

Figure A3.3. High-resolution XPS plots of (a) W 4f, (b) Li 1s, (c) S 2p and (d) N1s of **LiCu$_3$*para-D***.

Electrochemical Analysis

Water Reduction (WR)

Section A3.5. Differential pulse voltammogram (DPV) of LiCu$_3$*para-D*

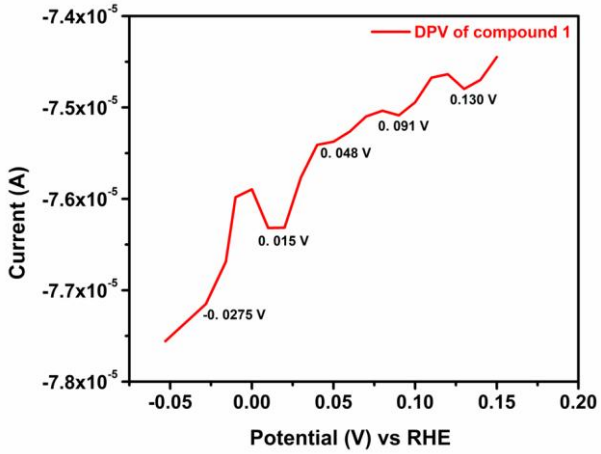

Figure A3.4. Differential pulse voltammogram (DPV) of **LiCu$_3$*para-D***, shown in the above Figure, was recorded prior to the onset potential. DPV was performed using the 50 mV pulse for 100 ms time and 5 mV step height for 80 ms step width and the integration time was 5 ms. This shows that **LiCu$_3$*para-D*** undergoes 5-electron transfer reaction towards electrocatalytic water reduction in the present work.

Section A3.6. Spectroscopic and Microscopic Analyses of Post-HER Material of LiCu$_3$*para-D*

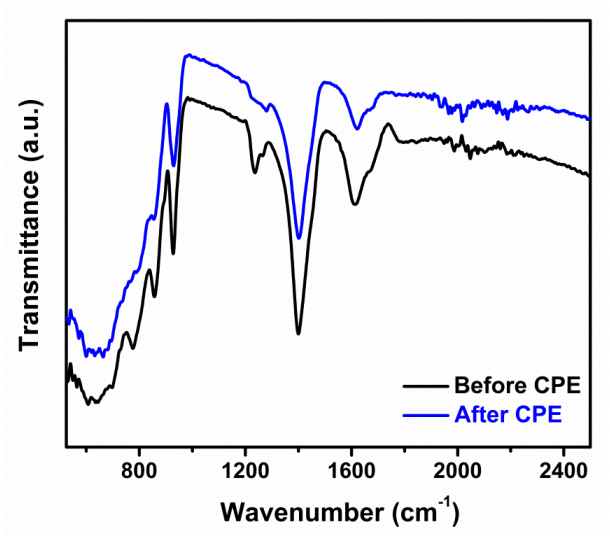

Figure A3.5. FTIR spectrum of post-WR-CPE electrolysis electrode material, compared with that of pre-electrolysis sample.

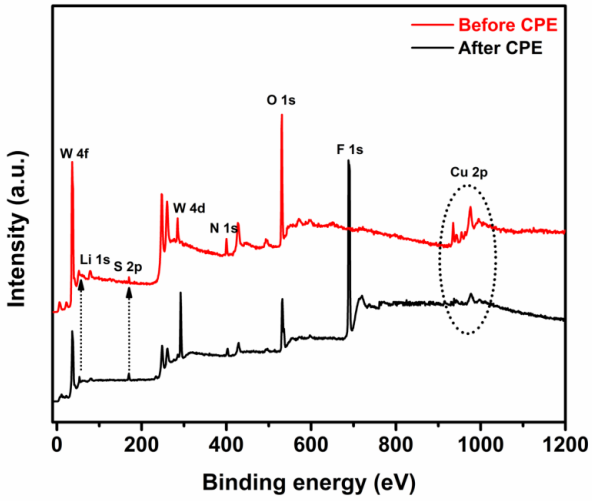

Figure A3.6. Survey scan XPS plot of the post-WR-CPE electrolysis electrode material of **$LiCu_3$*para-D***.

The extra peak of fluorine obtained in the XPS survey scan of 'after CPE' has come from the Nafion binder used during the preparation of sample ink for the electrochemical studies.

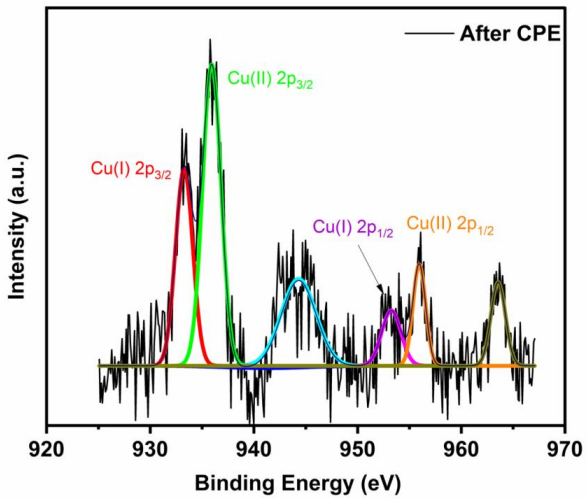

Figure A3.7. Core level XPS plot of copper ions from the post-WR-CPE electrolysis electrode material of **$LiCu_3$*para-D***.

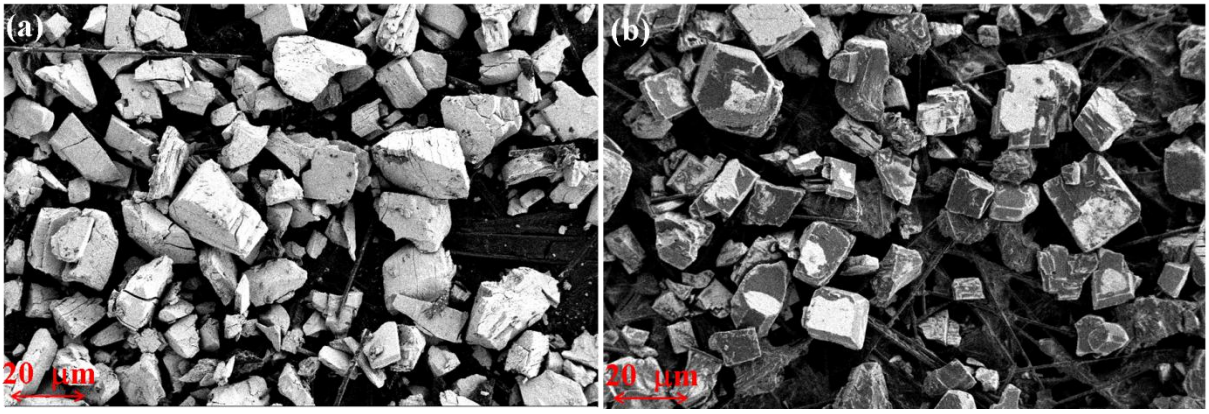

Figure A3.8. FESEM images of the post-electrolysis electrode material of **$LiCu_3$*para-D*** analysed (a) before and (b) after CPE analysis.

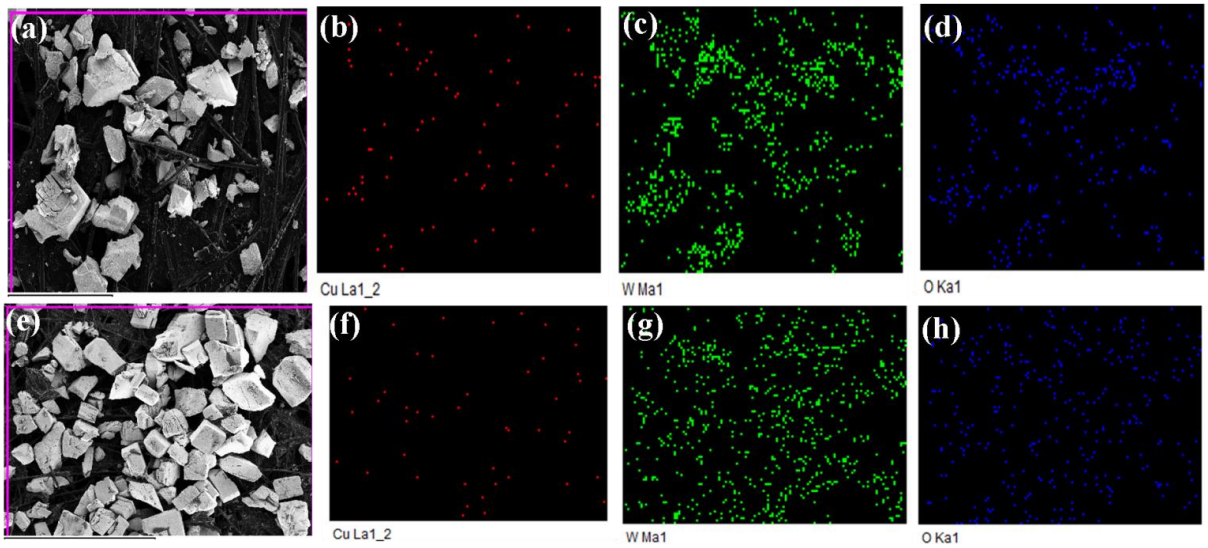

Figure A3.9. EDX mapping of the post electrolysis electrode materials of **$LiCu_3$*para-D*** analysed (a-d) before and (e-h) after CPE analysis.

Section A3.7. Cyclic Voltammograms at Different Scan Rates in the non-Faradaic Region

To understand the origins of the catalytic activities of **$LiCu_3$*para-D***, we measured the double-layer capacitance by cyclic voltammetry (CV) measurements. Double-layer capacitance measurements are performed by running a cyclic voltammogram in a non-Faradaic region at the following scan rates: from 25 to 100 mVs^{-1} in pH 7 (0.1 M) KCl electrolyte. All current is assumed to be due to capacitive charging. The cathodic and anodic charging currents measured at -0.35 V vs. RHE were plotted as a function of scan rate. The double-layer capacitance of the system is the difference between anodic and cathodic current densities at a potential of -0.35 V vs RHE.[2]

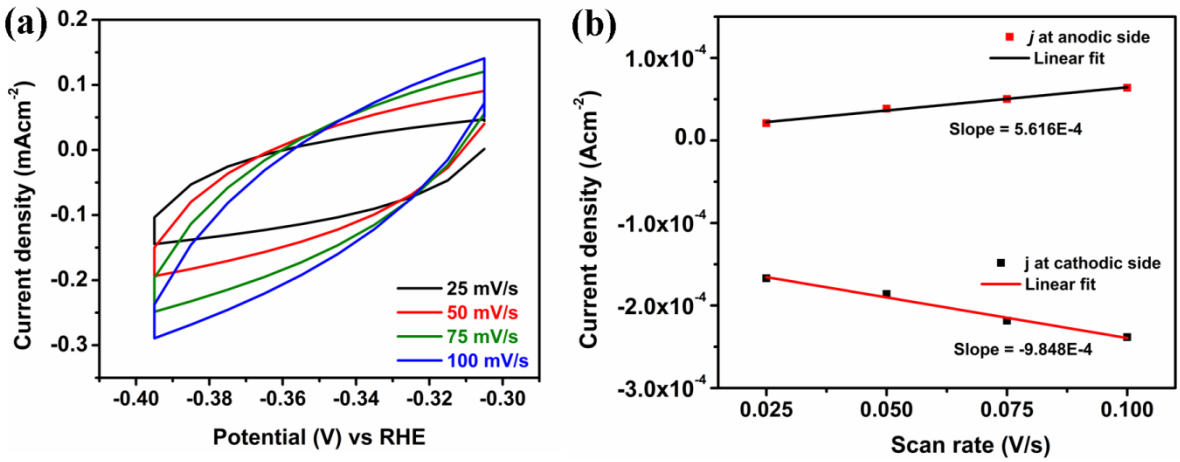

Figure A3.10. (a) Cyclic voltammogram of **LiCu$_3$*para-D*** at different scan rates in the non-faradaic region (-0.03 to -0.04 V vs RHE) with different scan rates from 25 to 100 mVs^{-1} in pH 7 (0.1 M) KCl electrolyte (b) Plot of slopes of current density against scan rates at a potential of -0.35 V vs RHE for **LiCu$_3$*para-D*** illustrating the double layer capacitance of **LiCu$_3$*para-D***.

Double layer capacitance of LiCu3para-D (**C$_1$**) = {5.616 - (-9.848)} × 10^{-4} Fcm^{-2} /2

= 7.732 × 10^{-4} Fcm^{-2}

Section A3.8. Turn over frequency calculations

We have calculated turnover frequency (TOF) to get further insights into the catalysts' activity. The TOF value of respective system has been calculated following the reported procedures as described below. The TOF is defined as the number of reactants getting converted into the product molecules in a unit of time per active site. Thus, the TOF of **LiCu$_3$*para-D*** for HER is calculated as,

$$\text{TOF} = \frac{I}{2mF} \qquad \text{.....(S3)}$$

I = current (A) value obtained from chronoamperometry electrolysis,

F = Faraday constant (C mol^{-1}),

m = number of active sites (mol); here W–OH centers of the POM clusters are the catalytically active sites for water reduction reaction,

2 = number of electrons required to form one mole of hydrogen

Here, the number of active sites being 'm' calculated by the equation

$$m = \frac{Q}{nF} \qquad \text{..... (S5)}$$

Q = charge (-3.28525×10^{-5} for **LiCu$_3$*para-D***) calculated by integrating the current (i_p) *vs.* time plot generated from the trace of cyclic voltammogram recorded under non-catalytic conditions using non-aqueous medium (CH_3CN medium),

From equations (S3) and (S5),

$$\text{TOF} = \frac{I}{2\times F\times Q/nF} \quad \text{.....(S6)}$$

Here, the factor n = 5, because 5 electrons are involved in the HER reaction (refering the K-L plot)

$$\text{TOF} = \frac{I}{2Q/5} \quad \text{..... (S7)}$$

$$\text{TOF} = \frac{5\times I}{2\times Q} \quad \text{..... (S8)}$$

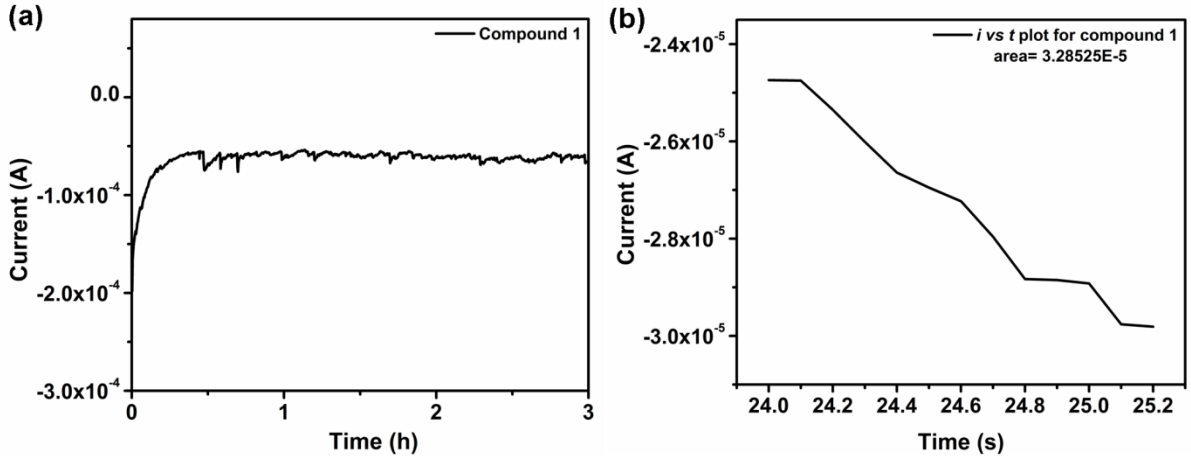

Figure A3.11. (a) Plot of chronoamperometric electrolysis of **LiCu$_3$*para-D*** performed at a potential of -0.4 V vs RHE for 3 hours at the neutral pH; (b) *i-t* plot, constructed from the trace of cyclic voltammogram of **LiCu$_3$*para-D*** [the concerned CV was recorded in a non-aqueous (acetonitrile) medium having 0.1 M TBAClO$_4$ as supporting electrolyte under nitrogen atmosphere].

Calculation of TOF values for LiCu3para-D using equation S8

The current (*I*) value, obtained from CA electrolysis (Figure A11a) = -6.125×10^{-5} A and the charge (*Q*) (from Figure A11b) = -3.28525×10^{-5} C.

$$\text{TOF} = \frac{5\times 6.125E-5}{2\times 3.2852E-5}$$

TOF = **4.66** mol (H_2) s^{-1}

Section A3.9. Faradaic efficiency

Following the recent procedure,[3] the Faradaic efficiency was determined from the evolved hydrogen (H_2) gas over a period of time. The chronopotentiometry electrolysis was carried out using a two-electrode system at 1 atm pressure. A known amount of sample coated on carbon paper (1 cm^2 area surface) was used as a working electrode (in the present case, it works as a cathodic electrode), and a large surface area graphite rod was taken as a counter electrode (works as an anode). The catalyst loading on the carbon paper working electrode

was maintained as 1 mg/cm^2, and neutral pH 7.0 (0.1 M) KCl elecrolyte was used as the electrolyte. A homemade setup was utilized to conduct the electrolysis process by employing a constant cathodic current -0.001 A or -1 mA for 3 hours. The details of the home-made setup has been discussed in Appendix 2.11.

Calculation of Faradaic efficiency.

The Faradaic efficiency can be expressed as the efficiency, with which charge is utilized in the electrochemical reaction. The Faradaic efficiencies of the catalyst were determined by the following equation:

In a chronopotentiometric electrolysis at pH 7.0 condition, the evolved hydrogen gas was collected by a homemade setup. We found 1.15 mL/3 hours (0.383 mL/hour) of hydrogen gas under 1 atm pressure at 25 °C.

Thus, the number of moles of hydrogen evolved in one hour for = (0.383/24500)

= 1.563×10^{-5} mol

$$H_{2\ ideal} = \frac{\text{Q (total charge employed)}}{\text{n(number of electrons required for the chemical change)}\times 1\text{Farad}} \quad \text{.....(S9)}$$

Here, we employed a constant cathodic current -0.001 A and n = 2 for HER (a two-electron process).

Thus, the H_2 ideally should evolve = $\frac{(0.001\times3600)}{(2\times96500)}$ mol = 1.865×10^{-5} mol .....(S10)

Faradaic efficiency = $\frac{\text{Experimentally evolved hydrogen}}{\text{Ideally evolved hydrogen}} \times 100$ .....(S11)

Therefore, the Faradaic efficiency of **$LiCu_3$*para-D*** = [(1.563×10^{-5}) / (1.865×10^{-5})] $\times100$

= 83.8 % ≈ **84%**

Water Oxidation (WO)

Section A3.10. Spectroscopic and Microscopic Analyses of Post-OER Material of $LiCu_3$*para-D*

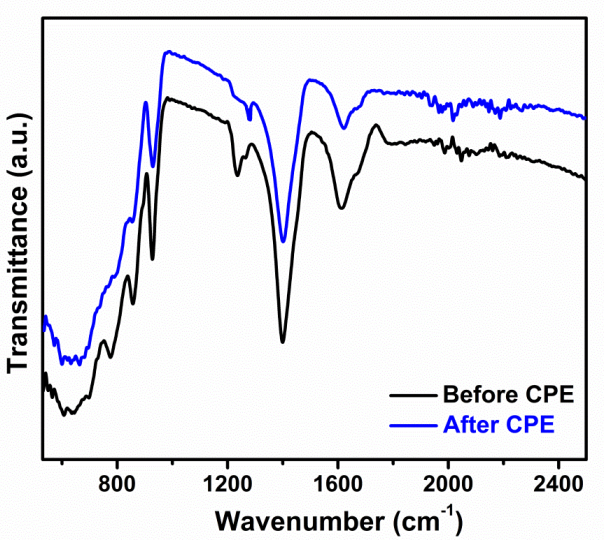

Figure A3.12. FTIR spectrum of post OER-CPE electrolysis electrode material of **$LiCu_3$*para-D***, compared with that of pre-electrolysis sample.

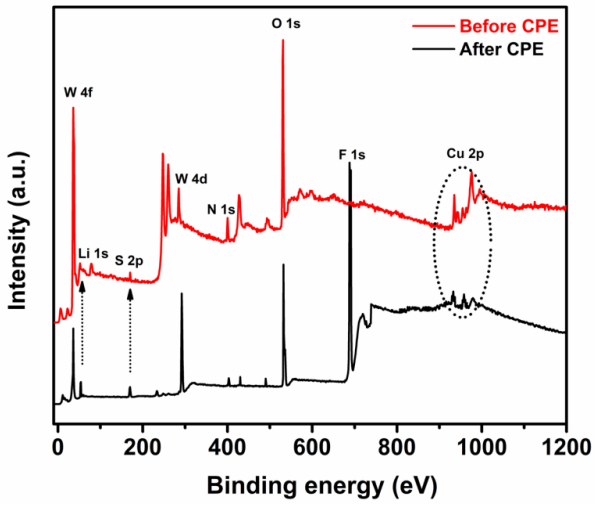

Figure A3.13. XPS Survey scan plot of the post OER-CPE electrolysis electrode material of **$LiCu_3$*para-D***.

The extra peak of fluorine obtained in the XPS survey scan of 'after CPE' has come from the Nafion binder used during the preparation of sample ink for the electrochemical studies.

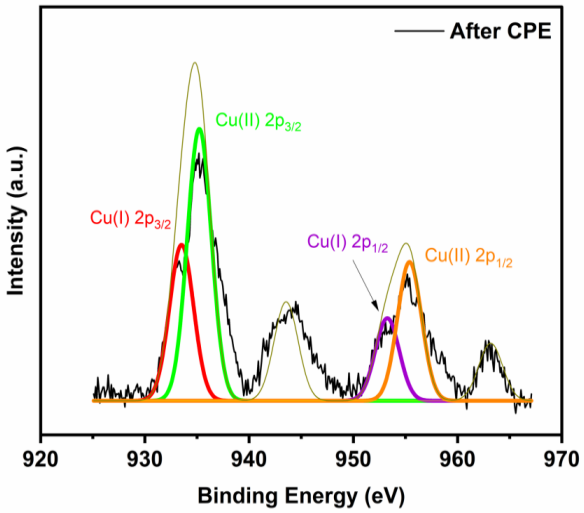

Figure A3.14. XPS core level plot of copper ions from the post-WO-CPE electrolysis electrode material of **LiCu$_3$*para-D***.

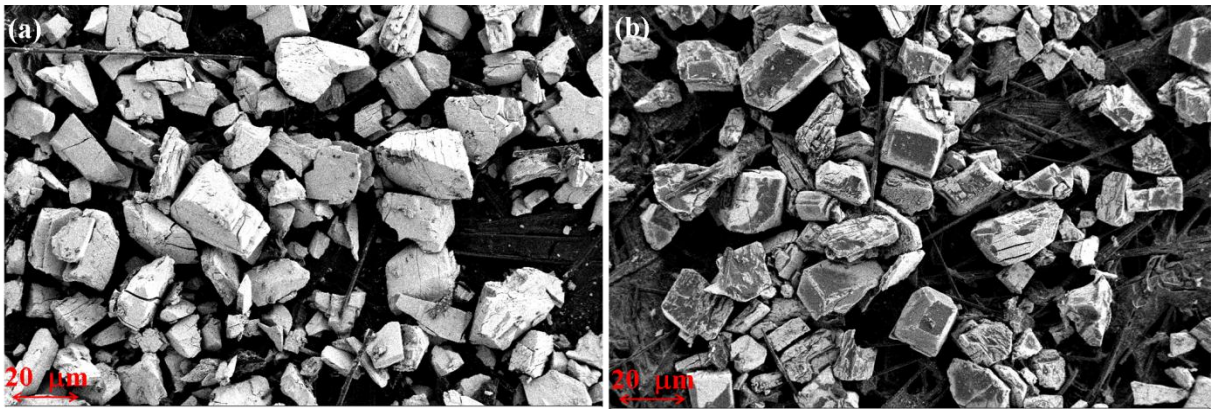

Figure A3.15. FESEM images of the post electrolysis electrode material of **LiCu$_3$*para-D***: (a) before and (b) after CPE analysis.

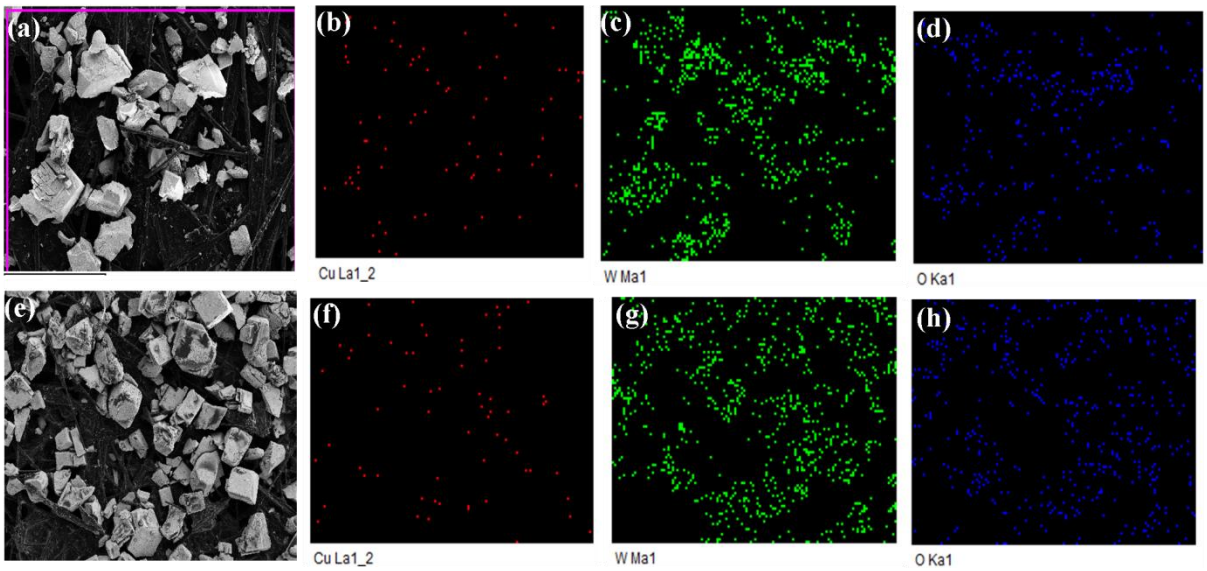

Figure A3.16. EDX mapping of the post electrolysis electrode material of **LiCu$_3$*para-D***: (a-d) before and (e-h) after CPE analysis.

Section A3.11. Cyclic Voltammograms at Different Scan Rates in the non-Faradaic Region

CV profiles of **LiCu$_3$*para-D*** have been recorded in the non-Faradaic region at the following scan rates: from 25 to 100 mVs^{-1} in pH 7 (0.1 M) KCl electrolyte in the potential window of 0.3 V to 0.4 V vs RHE. Current produced is assumed to be due to capacitive charging. The cathodic and anodic charging currents measured at 0.35 V vs. RHE have been plotted as a function of scan rate. The double-layer capacitance of the system is taken as the difference between anodic and cathodic current densities at a potential of 0.35 V vs RHE separately for **LiCu$_3$*para-D*** (C_1).

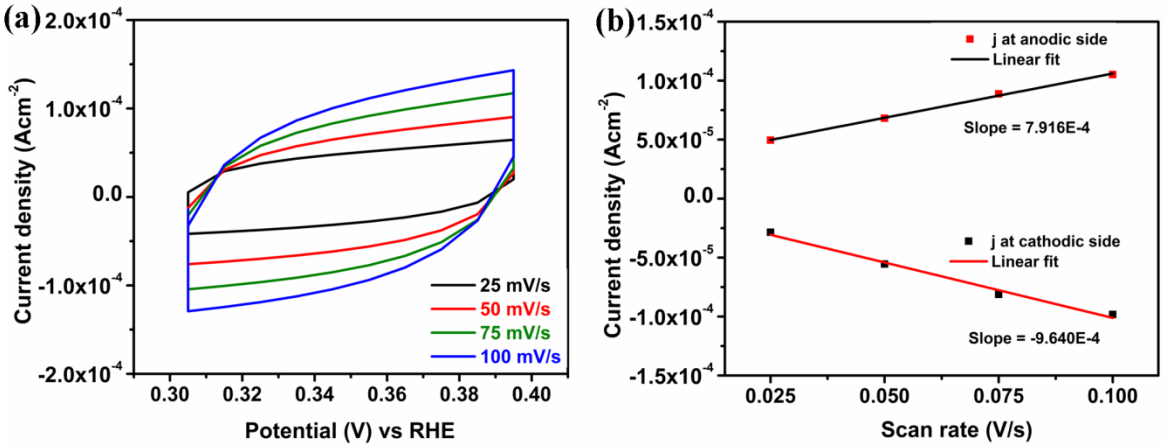

Figure A3.17. (a) Cyclic voltammograms of **LiCu$_3$*para-D*** at different scan rates in the non-faradaic region (0.03 to 0.04 V vs RHE) with different scan rates from 25 to 100 mVs^{-1} in pH 7 (0.1 M) KCl electrolyte, (b) Plot of slopes of current density against scan rates at a potential of 0.35 V vs RHE for **LiCu$_3$*para-D*** illustrating the double layer capacitance of **LiCu$_3$*para-D*.**

Double layer capacitance of **LiCu$_3$*para-D*** (**C_1**) = $\{7.916-(-9.640)\}\times10^{-4}$ Fcm^{-2} / 2

$= 8.778\times10^{-4}$ Fcm^{-2}

Section A3.12. Turn over frequency calculations

Calculation of surface coverage and number of catalytically active atoms: The calculation of active surface coverage area on the surface of electrode is done using a method reported previously by our group. A graph of i_p *vs* scan rate has been constructed for which the slope value is used in the formula (S12) for the measuring surface coverage (Γ_0).

$$\text{Slope} = n^2F^2A\,\Gamma_0/4RT \qquad \text{(S12)}$$

where,

n = no. of electrons involved, here 2 (from DPV)

F = 1 Farad = 96,500 C

A = geometrical surface area of GC electrode (0.0706 cm^2)

R = ideal gas constant

T = temperature during experiment

Γ_0 = surface density of active copper atoms/ions

Calculation of Turn over Frequency (TOF) from Tafel plot

TOF at any given over potential = $\frac{(Current\ density\ at\ given\ overpotential)}{4\ X\ F\ X\ surface\ density\ of\ active\ atoms/ions}$ …… (S13)

Here, 4 is the number of electrons involved in OER. The TOF was calculated at current density of 1 mA/cm^2 or 0.001 A/cm^2.

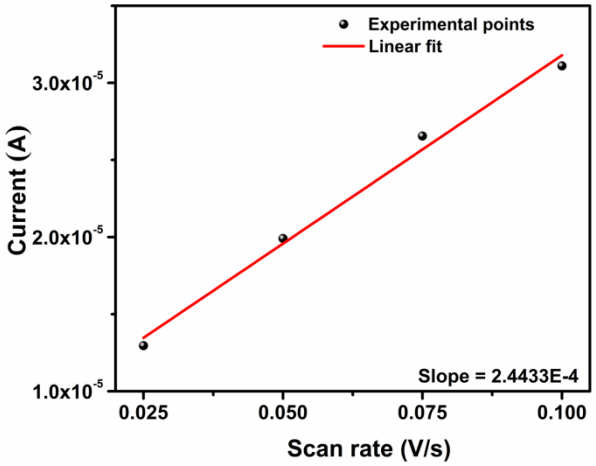

Figure A3.18. A graph of i *vs* scan rate.

Slope = 2.4433×10^{-4}

$\Gamma_0 = (Slope)(4RT)/n^2F^2A$

$\Gamma_0 = (2.4433\times10^{-4}\times4\times8.314\times298) / \{(2)^2\times(96500)^2\times0.0706\} = 9.2075\times10^{-10}$ mol/cm^2.

Therefore, the surface density of copper atoms is 9.2075×10^{-10} mol/cm^2.

$$TOF = \frac{0.001}{4 \times 96500 \times 9.2075 \times 10^{-10}}$$

Thus $(TOF)_{j=1\ mA/cm^2}$ = **2.81** s^{-1}

Table A3.2. Several POM based HER and OER electrocatalysts (from literature)

HER Electrocatalysts				
Catalysts	**Substrate**	**Electrolyte**	**η_j (mV)**	**References**
$\{Mo_{72}Fe_{30}\}_{NM}$	glassy carbon	pH 2.5, 0.1 M Na_2SO_4	767 (η_1)	36 (main article)
$\{W_{72}Fe_{30}\}_{NM}$	glassy carbon	pH 2.5, 0.1 M Na_2SO_4	527 (η_1)	36 (main article)
LiCu-POM	glassy carbon	pH 7, 0.1 M KPi buffer	612 (η_1)	38 (main article)
$[\{Cu^{II}(2,2´bpy)(H_2O)_2\}]$ $[\{Co^{II}W^{VI}_{12}O_{40}\}$ $\{(Cu^{II}(2,2´\text{-}bpy)(H_2O)\}$ $\{(Cu^{II}(2,2´\text{-}bpy)\}]\cdot 2H_2O$	glassy carbon	pH 4.8, 0.1 M sodium acetate buffer	520 (η_1)	69 (main article)
$[(UO_2)_2(\mu\text{-}L)_2]$	glassy carbon	pH 7, 0.1 M phosphate buffer	730 (η_1)	4
LiCu3para-D	glassy carbon	pH 7.0, 0.1 M KCl	418.5 (η_1)	Present work

OER Electrocatalysts				
H_2O_2-CuO_x	glassy carbon	0.1 M KOH	440 (η_1)	5
CuO–FTO	1 cm^2 FTO	pH 12, 0.2 M PBS	500 (η_1)	6
CuO nanowire	1 cm^2 FTO	pH 9.2, 0.2 M KPi	430 ($\eta_{0.1}$)	7
$Cu(OH)_2$-NWs/CF	1 cm^2 CF	pH 13.0, 0.1 M NaOH	530 (η_{10})	8
LiCu3para-D	glassy carbon	pH 7.0, 0.1 M KCl	418.5 (η_1)	Present work

Section A3.13. Faradaic efficiency

Calculation of Faradaic efficiency

In a chronopotentiometric electrolysis at pH 7.0 condition, the evolved oxygen gas was collected by a homemade setup. We found 0.55 mL/3 hours (0.183 mL/hour) of oxygen gas under 1 atm pressure at 25 °C.

The number of moles of oxygen evolved in one hour for **$LiCu_3$*para-D*** = (0.183/24500) = 7.469×10^{-6} mol

$$O_{2\ ideal} = \frac{Q\ (\text{total charge employed})}{n(\text{number of electrons required for the chemical change}) \times 1\text{Farad}} \quad \ldots\ldots\ldots\ldots\ (S14)$$

Here, we employed a constant anodic current 0.001 A and n = 4 for OER (a four-electron process).

Thus, the O_2 ideally should evolve = $\frac{(0.001\times3600)}{(4\times96500)}$ mol = 9.326×10^{-6} mol …… (S15)

Faradaic efficiency = $\frac{\text{Experimentally evolved oxygen}}{\text{Ideally evolved oxygen}} \times 100$ …… (S16)

Therefore, the Faradaic efficiency of **$LiCu_3$*para-D*** = $[(7.469\times10^{-6}) / (9.326\times10^{-6})] \times100$

= 80.08 % ≈ **80 %**

Section A3.14. Gas chromatograms for electrochemically generated hydrogen and oxygen gases

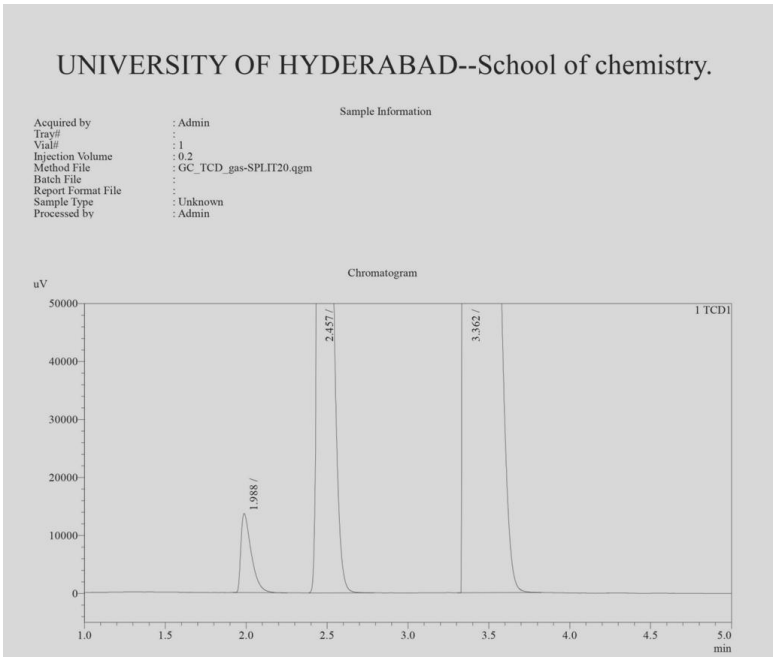

Figure A3.19. Gas chromatogram obtained during bulk electrolysis for **$LiCu_3$*para-D*** detecting hydrogen gas.

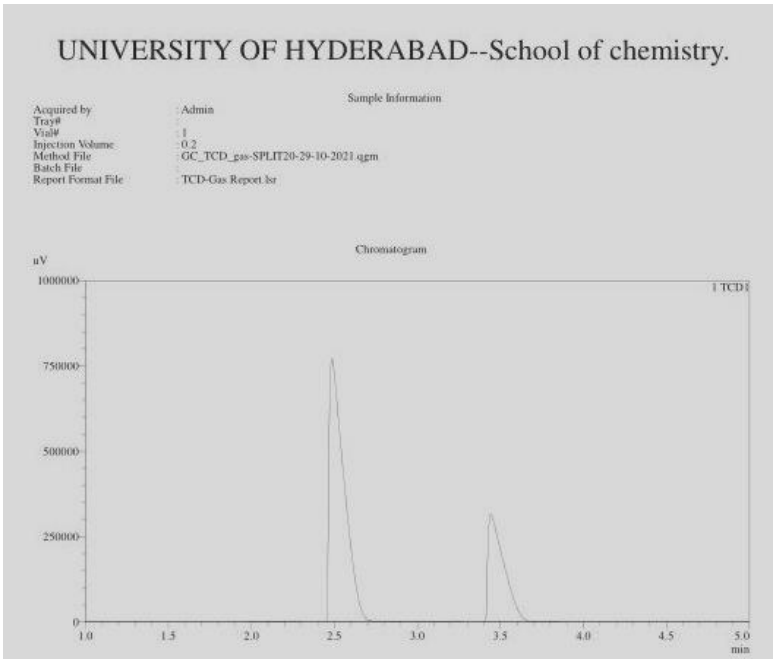

Figure A3.20. Gas chromatogram obtained during bulk electrolysis for **$LiCu_3$*para-D*** detecting oxygen gas.

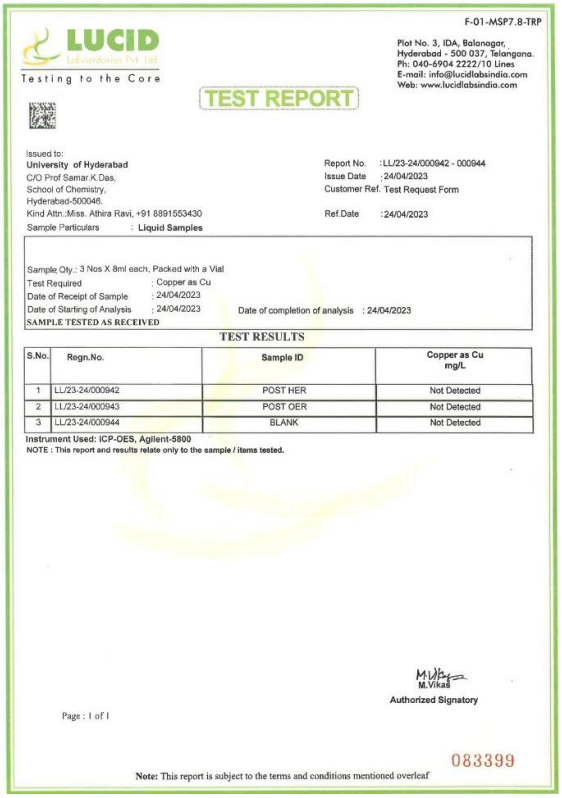

F-01-MSP7.8-TRP

LUCID Laboratories Pvt. Ltd.
Testing to the Core

Plot No. 3, IDA, Balanagar, Hyderabad - 500 037, Telangana.
Ph: 040-6904 2222/10 Lines
E-mail: info@lucidlabsindia.com
Web: www.lucidlabsindia.com

TEST REPORT

Issued to:
University of Hyderabad
C/O Prof Samar K.Das,
School of Chemistry,
Hyderabad-500046.
Kind Attn.:Miss. Athira Ravi, +91 8891553430
Sample Particulars : Liquid Samples

Report No. : LL/23-24/000942 - 000944
Issue Date : 24/04/2023
Customer Ref. Test Request Form
Ref.Date : 24/04/2023

Sample Qty.: 3 Nos X 8ml each, Packed with a Vial
Test Required : Copper as Cu
Date of Receipt of Sample : 24/04/2023
Date of Starting of Analysis : 24/04/2023
Date of completion of analysis : 24/04/2023
SAMPLE TESTED AS RECEIVED

TEST RESULTS

S.No.	Regn.No.	Sample ID	Copper as Cu mg/L
1	LL/23-24/000942	POST HER	Not Detected
2	LL/23-24/000943	POST OER	Not Detected
3	LL/23-24/000944	BLANK	Not Detected

Instrument Used: ICP-OES, Agilent-5800
NOTE : This report and results relate only to the sample / items tested.

M.Vikas
Authorized Signatory

Page : 1 of 1

083399

Note: This report is subject to the terms and conditions mentioned overleaf

Figure A3.21. ICP-OES analyses of the electrolyte solutions before and after the CPE (controlled potential electrolysis) for HER (hydrogen evolution reaction) as well as for OER (oxygen evolution reaction), for the probable detection of copper.

A3.15. References

1. Zou, Y.; Chen, J.; Li,Y.-Y.; Li, L.; Liua, J.-L.; Ren, X.-M. Three Zn(II)/Cd(II)/Mn(II) coordination polymers based on a 2-hydroxy-*N*-(1*H*-tetrazol-5-yl) benzamide ligand: structures, and magnetic and photoluminescence properties. *RSC Adv.*, **2015**, *5*, 78642-78647.
2. Zhao, Y.; Wang, Y.; Dong, Y.; Carlos, C.; Li, J.; Zhang, Z.; Li, T.; Shao, Y.; Yan, S.; Gu, L.; Wang, J.; Wang, X. Quasi-two-dimensional earth-abundant bimetallic electrocatalysts for oxygen evolution reactions. *ACS Energy Lett.* **2021**, *6*, 3367-3375.
3. Mulkapuri, S.; Ravi, A.; Nasani, R.; Kurapati, S. K.; Das, S. K. Barrel-shaped-polyoxometalates exhibiting electrocatalytic water reduction at neutral pH: A synergy effect. *Inorg. Chem.* **2022**, *35*, 13868–13882.
4. Ghosh, S.; Srivastava, A.K.; Pal, R. G. U.; Pal, S. A diuranyl(VI) complex and its application in electrocatalytic and photocatalytic hydrogen evolution from neutral aqueous medium. *Inorg. Chem.* **2019**, *58*, 14410–14419.
5. Handoko, A. D.; Deng, S.; Deng, Y.; Cheng, A. W. F.; Chan, K. W.; Tan, H. R.; Pan, Y.; Tok, E. S.; Sow, C. H.; Yeo, B. S. Enhanced activity of H_2O_2-treated copper(II) oxide nanostructures for the electrochemical evolution of oxygen**.** *Catal. Sci. Technol.* **2016**, *6*, 269–274.
6. Wang, J.; Zhu, L.; Ji, L.; Chen, Z. Preparation of nanostructured $Cu(OH)_2$ and CuO electrocatalysts for water oxidation by electrophoresis deposition. *J. Mater. Res.* **2018**, *33*, 581–589.
7. Liu, X.; Cui, S.; Sun, Z.; Du, P. Copper oxide nanomaterials synthesized from simple copper salts as active catalysts for electrocatalytic water oxidation**.** *Electrochim. Acta* **2015**, *160*, 202–208.
8. Hou, C.-C.; Fu, W.-F.; Chen, Y. Self-supported Cu-based nanowire arrays as noble-metal-free electrocatalysts for oxygen evolution**.** *ChemSusChem*, **2016**, *9*, 2069–2073.

==========

Appendix 3

Supporting Data for Chapter 4

Contents

Section A4.1. ICP-OES Analysis

Sample Particulars : **Sample**

Qty. Received : 1No Vial
Date of Receipt of Sample : 10/05/2022
Date of Starting of Analysis : 15/05/2022
Date of completion of analysis : 16/05/2022
SAMPLE TESTED AS RECEIVED

TEST RESULTS

S.No.	Parameters	UOM	Results
1	Manganese as Mn	% by mass	1.91
2	Sodium as Na	% by mass	2.95
3	Tungsten as W	% by mass	62.71
4	Bismuth as Bi	% by mass	7.52

Instrument Used: ICP-OES Varian 720-ES
NOTE : This report and results relate only to the sample / items tested.

Figure A4.1. ICP-OES analysis report of **POM-MnW(OH)**.

Section A4.2. Bond valence sum calculations

BV-sum of Bi01: 2.5787v.u.
Bonds for atom:

1	Bi01	Bi	0.5491	0.4346	0.6250	x, y, z + (0,0,0)	

N.	Atom	Type	xyz			Sym. Op.	d(A)	BV(v.u.)
16	O17	O	0.5196	0.3335	0.5665	x, y, z + (0,0,0)	2.182	0.670
18	O25	O	0.7439	0.4645	0.5827	x, y, z + (0,0,0)	2.853	0.166
22	O23	O	0.6799	0.3844	0.6811	x, y, z + (0,0,0)	2.135	0.739
32	O8	O	0.3355	0.4679	0.6116	x, y, z + (0,0,0)	2.862	0.162
37	O18	O	0.6914	0.5314	0.7170	x, y, z + (0,0,0)	3.012	0.119
39	O10	O	0.4660	0.3898	0.7020	x, y, z + (0,0,0)	2.146	0.722

BV-sum of W7: 6.2839v.u.
Bonds for atom:

2	W7	W	0.4825	0.3649	0.4630	x, y, z + (0,0,0)	

N.	Atom	Type	xyz			Sym. Op.	d(A)	BV(v.u.)
13	O15	O	0.3905	0.2802	0.4836	x, y, z + (0,0,0)	2.034	0.730
16	O17	O	0.5196	0.3335	0.5665	x, y, z + (0,0,0)	2.122	0.574
19	O29	O	0.5879	0.2795	0.4669	x, y, z + (0,0,0)	2.080	0.644
21	O33	O	0.3834	0.4248	0.4838	x, y, z + (0,0,0)	1.789	1.413
31	O39	O	0.4589	0.3558	0.3735	x, y, z + (0,0,0)	1.766	1.503
33	O32	O	0.5876	0.4274	0.4764	x, y, z + (0,0,0)	1.787	1.421

BV-sum of W4: 6.1664v.u.
Bonds for atom:

3	W4	W	0.7233	0.2781	0.7355	x, y, z + (0,0,0)	

N.	Atom	Type	xyz			Sym. Op.	d(A)	BV(v.u.)
15	O13	O	0.5982	0.2794	0.7719	x, y, z + (0,0,0)	1.882	1.101
17	O22	O	0.8419	0.3033	0.6857	x, y, z + (0,0,0)	2.004	0.790

22	O23	O	0.6799	0.3844	0.6811	x, y, z + (0,0,0)	2.251	0.406
23	O27	O	0.6725	0.2364	0.6562	x, y, z + (0,0,0)	1.795	1.392
25	O20	O	0.7735	0.3552	0.7988	x, y, z + (0,0,0)	1.940	0.940
27	O34	O	0.7829	0.2013	0.7772	x, y, z + (0,0,0)	1.758	1.539

BV-sum of W5: 6.2498v.u.
Bonds for atom:

4	W5	W	0.8187	0.3878	0.6277	x, y, z + (0,0,0)		

N.	Atom	Type	xyz			Sym. Op.	d(A)	BV(v.u.)
14	O21	O	0.8528	0.4465	0.7077	x, y, z + (0,0,0)	1.914	1.007
17	O22	O	0.8419	0.3033	0.6857	x, y, z + (0,0,0)	1.919	0.994
18	O25	O	0.7439	0.4645	0.5827	x, y, z + (0,0,0)	1.868	1.140
22	O23	O	0.6799	0.3844	0.6811	x, y, z + (0,0,0)	2.226	0.434
24	O24	O	0.9361	0.3934	0.5982	x, y, z + (0,0,0)	1.726	1.676
26	O26	O	0.7430	0.3205	0.5661	x, y, z + (0,0,0)	1.917	0.999

BV-sum of W3: 6.0477v.u.
Bonds for atom:

5	W3	W	0.7413	0.4585	0.7662	x, y, z + (0,0,0)		

N.	Atom	Type	xyz			Sym. Op.	d(A)	BV(v.u.)
14	O21	O	0.8528	0.4465	0.7077	x, y, z + (0,0,0)	1.994	0.812
22	O23	O	0.6799	0.3844	0.6811	x, y, z + (0,0,0)	2.228	0.431
25	O20	O	0.7735	0.3552	0.7988	x, y, z + (0,0,0)	2.014	0.769
30	O5	O	0.6135	0.4456	0.8044	x, y, z + (0,0,0)	1.947	0.922
37	O18	O	0.6914	0.5314	0.7170	x, y, z + (0,0,0)	1.726	1.676
51	O19	O	0.8150	0.5009	0.8374	x, y, z + (0,0,0)	1.783	1.438

BV-sum of W8: 5.8573v.u.
Bonds for atom:

6	W8	W	0.3977	0.2486	0.5756	x, y, z + (0,0,0)		

N.	Atom	Type	xyz			Sym. Op.	d(A)	BV(v.u.)
13	O15	O	0.3905	0.2802	0.4836	x, y, z + (0,0,0)	1.900	1.048
16	O17	O	0.5196	0.3335	0.5665	x, y, z + (0,0,0)	2.253	0.403
20	O16	O	0.5235	0.1929	0.5646	x, y, z + (0,0,0)	1.979	0.845
29	O12	O	0.4490	0.2389	0.6748	x, y, z + (0,0,0)	2.001	0.796
36	O7	O	0.3154	0.3258	0.5994	x, y, z + (0,0,0)	1.871	1.131
50	O14	O	0.3119	0.1759	0.5656	x, y, z + (0,0,0)	1.735	1.634

BV-sum of W2: 6.0955v.u.
Bonds for atom:

7	W2	W	0.2966	0.3991	0.6711	x, y, z + (0,0,0)		

N.	Atom	Type	xyz			Sym. Op.	d(A)	BV(v.u.)
32	O8	O	0.3355	0.4679	0.6116	x, y, z + (0,0,0)	1.834	1.250
36	O7	O	0.3154	0.3258	0.5994	x, y, z + (0,0,0)	1.984	0.834
38	O6	O	0.1664	0.4060	0.6561	x, y, z + (0,0,0)	1.710	1.751
39	O10	O	0.4660	0.3898	0.7020	x, y, z + (0,0,0)	2.249	0.408
40	O9	O	0.3109	0.3103	0.7282	x, y, z + (0,0,0)	1.967	0.874
43	O3	O	0.3237	0.4541	0.7545	x, y, z + (0,0,0)	1.925	0.979

BV-sum of W6: 6.3491v.u.
Bonds for atom:

8	W6	W	0.6424	0.2452	0.5519	x, y, z + (0,0,0)		

N.	Atom	Type	xyz	Sym. Op.	d(A)	BV(v.u.)
16	O17	O	0.5196 0.3335 0.5665	x, y, z + (0,0,0)	2.324	0.333
19	O29	O	0.5879 0.2795 0.4669	x, y, z + (0,0,0)	1.851	1.195
20	O16	O	0.5235 0.1929 0.5646	x, y, z + (0,0,0)	1.878	1.111
23	O27	O	0.6725 0.2364 0.6562	x, y, z + (0,0,0)	2.058	0.683
26	O26	O	0.7430 0.3205 0.5661	x, y, z + (0,0,0)	1.903	1.038
52	O28	O	0.7140 0.1766 0.5290	x, y, z + (0,0,0)	1.662	1.990

BV-sum of W10: 6.2819v.u.
Bonds for atom:

9	W10	W	0.4490 0.2823 0.7601	x, y, z + (0,0,0)		

N.	Atom	Type	xyz	Sym. Op.	d(A)	BV(v.u.)
15	O13	O	0.5982 0.2794 0.7719	x, y, z + (0,0,0)	1.954	0.906
29	O12	O	0.4490 0.2389 0.6748	x, y, z + (0,0,0)	1.864	1.155
39	O10	O	0.4660 0.3898 0.7020	x, y, z + (0,0,0)	2.293	0.362
40	O9	O	0.3109 0.3103 0.7282	x, y, z + (0,0,0)	1.920	0.992
42	O4	O	0.4604 0.3583 0.8247	x, y, z + (0,0,0)	1.875	1.121
49	O11	O	0.4214 0.2090 0.8088	x, y, z + (0,0,0)	1.710	1.748

BV-sum of W1: 5.9881v.u.
Bonds for atom:

10	W1	W	0.4699 0.4643 0.7896	x, y, z + (0,0,0)		

N.	Atom	Type	xyz	Sym. Op.	d(A)	BV(v.u.)
30	O5	O	0.6135 0.4456 0.8044	x, y, z + (0,0,0)	1.911	1.016
39	O10	O	0.4660 0.3898 0.7020	x, y, z + (0,0,0)	2.195	0.471
41	O2	O	0.4860 0.5381 0.7333	x, y, z + (0,0,0)	1.773	1.475
42	O4	O	0.4604 0.3583 0.8247	x, y, z + (0,0,0)	2.059	0.681
43	O3	O	0.3237 0.4541 0.7545	x, y, z + (0,0,0)	1.974	0.856
46	O1	O	0.4516 0.5011 0.8700	x, y, z + (0,0,0)	1.770	1.488

BV-sum of W9: 4.7642v.u.
Bonds for atom:

11	W9	W	0.7208 0.4981 0.4841	x, y, z + (0,0,0)		

N.	Atom	Type	xyz	Sym. Op.	d(A)	BV(v.u.)
18	O25	O	0.7439 0.4645 0.5827	x, y, z + (0,0,0)	2.029	0.738
21	O33	O	0.6166 0.5752 0.5162	-x, -y, -z + (1,1,1)	2.117	0.582
28	O31	O	0.8274 0.5634 0.4938	x, y, z + (0,0,0)	1.833	1.256
32	O8	O	0.6645 0.5321 0.3884	-x, -y, -z + (1,0,1)	2.041	0.715
33	O32	O	0.5876 0.4274 0.4764	x, y, z + (0,0,0)	2.167	0.509
34	O30	O	0.7947 0.4208 0.4446	x, y, z + (0,0,0)	1.930	0.964

BV-sum of Mn1: 2.0087v.u.
Bonds for atom:

12	Mn1	Mn	0.4048 0.3753 0.2699	x, y, z + (0,0,0)		

N.	Atom	Type	xyz	Sym. Op.	d(A)	BV(v.u.)
27	O34	O	0.2829 0.2987 0.2772	x+1/2, -y+1/2, z+1/2 + (-1,0,-1)	2.146	0.345

31	O39	O	0.4589	0.3558	0.3735	x, y, z + (0,0,0)	2.114	0.377
35	O40	O	0.4958	0.2807	0.2430	x, y, z + (0,0,0)	2.201	0.298
37	O18	O	0.3086	0.4686	0.2830	-x, -y, -z + (1,1,1)	2.154	0.338
41	O2	O	0.5140	0.4619	0.2667	-x, -y, -z + (0,0,0)	2.141	0.351
45	O41	O	0.3516	0.3775	0.1600	x, y, z + (0,0,0)	2.199	0.299

BV-sum of O31: 0.9208v.u.

Bonds for atom:

28	O31	O	0.8274	0.5634	0.4938	x, y, z + (0,0,0)		

N.	Atom	Type	xyz			Sym. Op.	d(A)	BV(v.u.)
11	W9	W	0.7208	0.4981	0.4841	x, y, z + (0,0,0)	1.833	0.921

BV-sum of O30: 0.7369v.u.

Bonds for atom:

34	O30	O	0.7947	0.4208	0.4446	x, y, z + (0,0,0)		

N.	Atom	Type	xyz			Sym. Op.	d(A)	BV(v.u.)
11	W9	W	0.7208	0.4981	0.4841	x, y, z + (0,0,0)	1.930	0.707
57	Na4	Na	0.8960	0.2826	0.4539	x, y, z + (0,0,0)	2.842	0.030

Section A4.3. X-ray Photoelectron Spectroscopy (XPS) Analysis

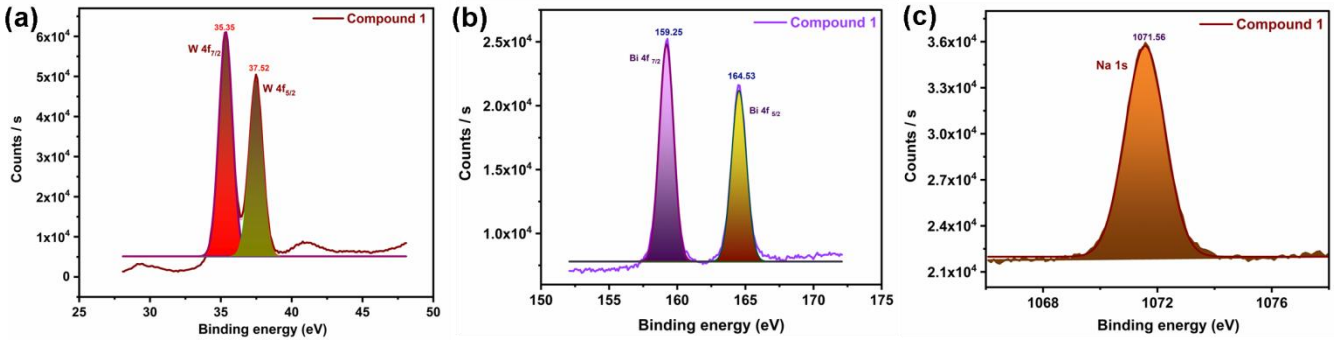

Figure A4.2. High-resolution XPS plots of (a) W 4f, (b) Bi 4f, and (c) Na 1s of **POM-MnW(OH)**.

Section S4.4. Differential pulse voltammogram (DPV) of POM-MnW(OH)

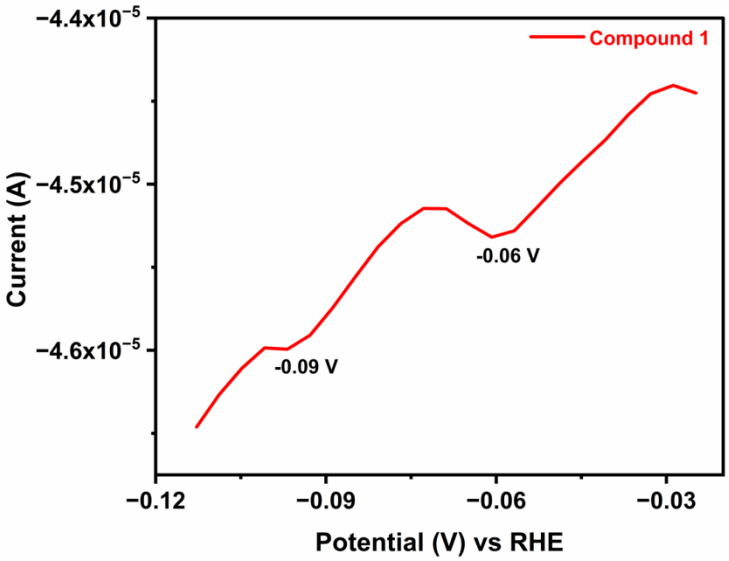

Figure A4.3. Differential pulse voltammogram (DPV) of **POM-MnW(OH)** recorded prior to the onset potential. DPV was performed using the 60 mV pulse for 100 ms time and 3 mV step height for 80 ms step width and the integration time was 3 ms.

Section S4.5. Spectroscopic and Microscopic Analyses of Post-HER Material of POM-MnW(OH)

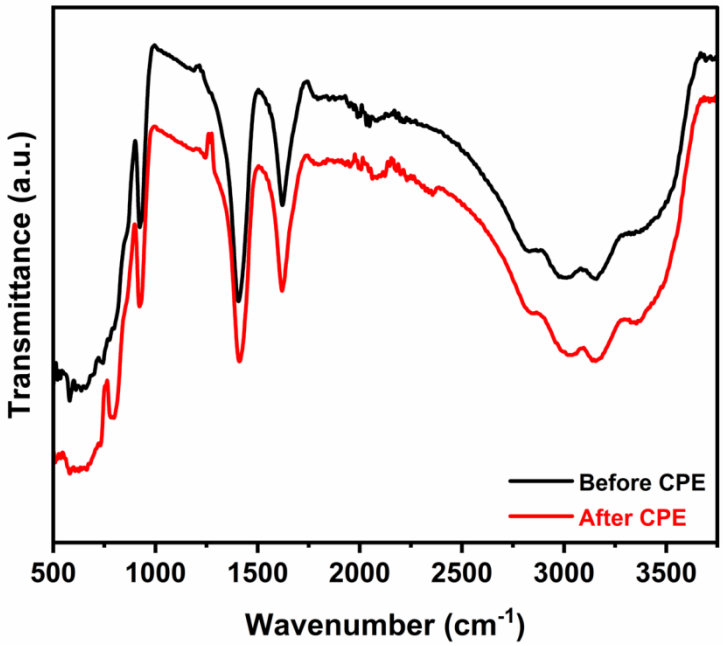

Figure A4.4. FTIR spectrum of post-WR-CPE electrolysis electrode material, compared with that of pre-electrolysis sample.

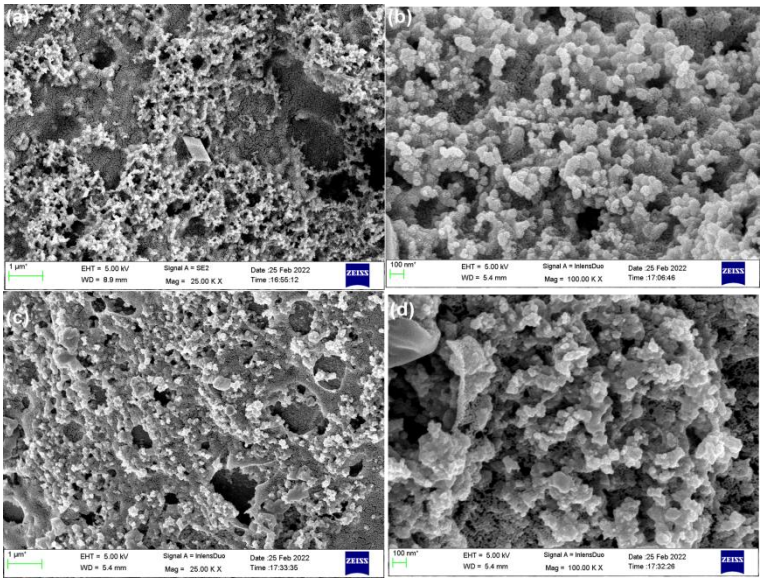

Figure A4.5. FESEM images of the post-electrolysis electrode material of **POM-MnW(OH)** analysed (a,b) before and (c,d) after CPE analysis.

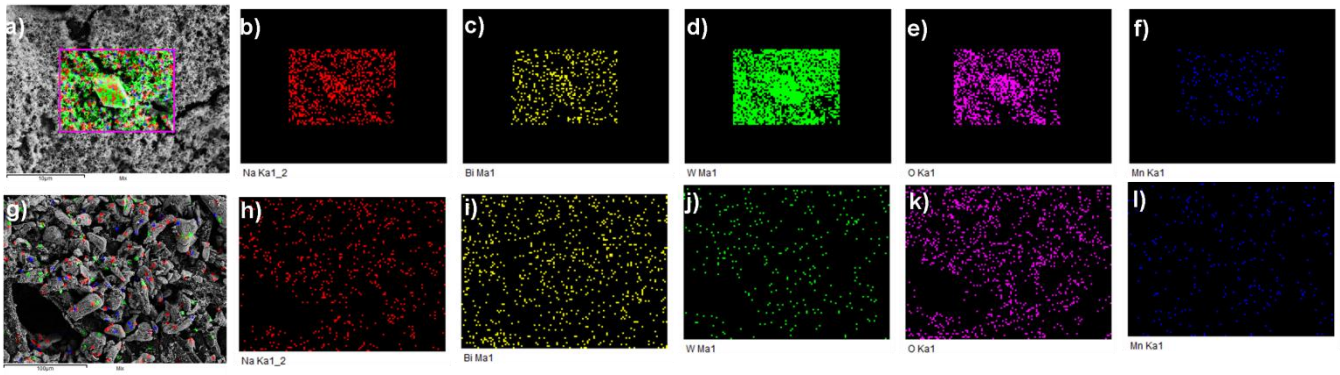

Figure A4.6. EDX mapping of the post electrolysis electrode materials of **POM-MnW(OH)** analysed (a-f) before and (g-l) after CPE analysis.

Section S4.6. Scan Rate Variation

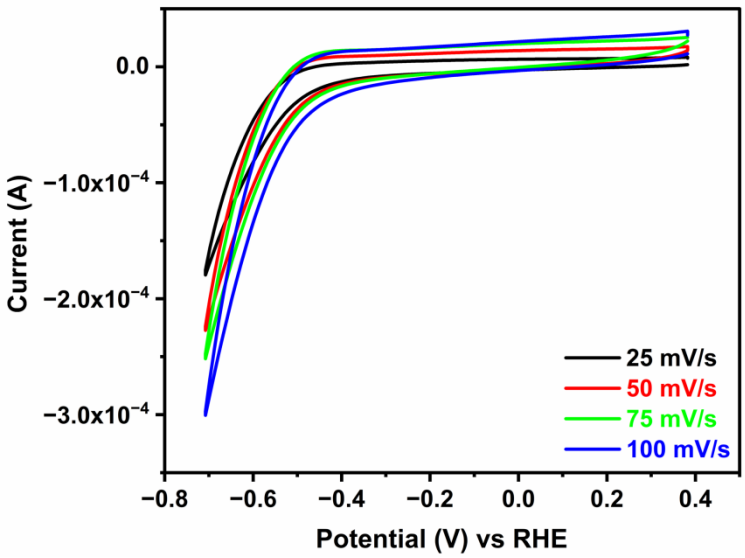

Figure A4.7. Cyclic voltammogram of **POM-MnW(OH)** at different scan rates from 25 mVs^{-1} to 100 mVs^{-1} in the cathodic operational window.

Section S4.7. Cyclic Voltammograms at Different Scan Rates in the non-Faradaic Region

To understand the origins of the catalytic activities of **POM-MnW(OH)**, we measured the double-layer capacitance by cyclic voltammetry (CV) measurements.[5] Double-layer capacitance measurements are performed by running a cyclic voltammogram in a non-Faradaic region at the following scan rates: from 25 to 100 mVs^{-1} in 0.1 M sodium acetate buffer of pH 4.8. All current is assumed to be due to capacitive charging. The cathodic and anodic charging currents measured at -0.14 V vs. RHE were plotted as a function of scan rate. The double-layer capacitance of the system is the difference between anodic and cathodic current densities at a potential of 0.09 to 0.19 V vs RHE**.**

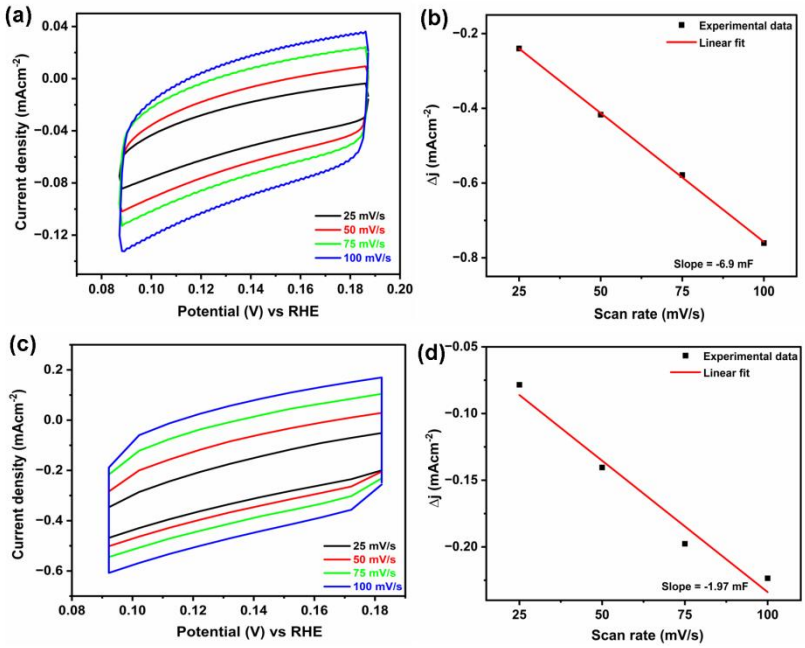

Figure A4.8. (a) Cyclic voltammogram of **POM-MnW(OH)** at different scan rates in the non-faradaic region (0.09 to 0.19 vs RHE) with different scan rates from 25 to 100 mVs^{-1} in 0.1 M sodium acetate buffer of pH 4.8 (b) Plots displaying the slope of current density against scan rates at a potential of 0.14 V vs RHE for **POM-MnW(OH)**.

Section S4.8. Turn over frequency calculations

Calculation of surface coverage and number of catalytically active atoms.

The calculation of active surface coverage area on the surface of electrode is done using a method reported previously by our group.[6] A graph of i_p vs scan rate has been constructed of which the slope value is used in the formula (1) for the measuring surface coverage (Γ_0).

$$\text{Slope} = n^2F^2A\Gamma_0/2RT \qquad ...(1)$$

where,

n = no. of electrons involved, here it is 2, from DPV plot (Figure A4.3)

F = 96500 C/mol; R= 8.314 J/mol K (ideal gas constant); T = temperature during experiment = 298 K

A= 0.0706 cm^2 = geometrical surface area of GC electrode.

Γ_0 – surface density of active W-OH groups.

Calculation of Turn over Frequency (TOF) from Tafel plot

TOF at any given over potential = $\frac{(Current\ density\ at\ given\ overpotential)}{2\ X\ F\ X\ surface\ density\ of\ bismuth\ atoms}$ …(2)

Here, 2 is the number of electrons involved in HER. The TOF was calculated at current density of -1 mA/cm^2 or -0.001 A/cm^2.

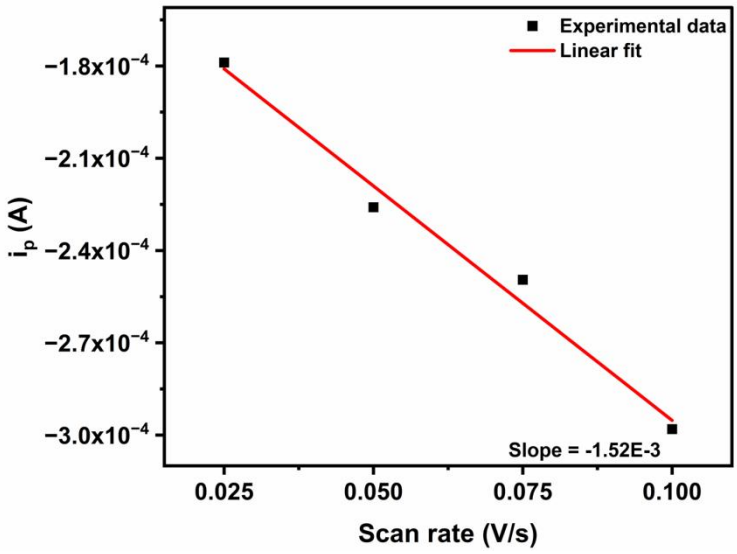

Figure A4.9. A graph of i_p *vs* scan rate.

$$\text{Slope} = 1.52 \times 10^{-3};$$

$$\Gamma_0 = (\text{Slope})(4RT)/\ n^2F^2A$$

or, $$\Gamma_0 = [(1.52 \times 10^{-3}) \times 2 \times 8.314 \times 298)] / [(2)^2 \times (96500)^2 \times 0.0706]$$

$$= 2.864 \times 10^{-9}\ \text{mol/cm}^2$$

Thus, we obtained surface density as **2.864×10^{-9} mol/cm^2**

Thus, the TOF at the given overpotential,

$$\text{TOF} = \frac{0.001}{2 \times 96500 \times 2.864 \times 10^{-9}}$$

Thus,

$$(\text{TOF})_{j=1\ \text{mA/cm}^2} = \mathbf{1.81\ \ s^{-1}}$$

Section A4.9. Faradaic efficiency

Following the recent procedure,[6,7] the Faradaic efficiency was determined from the evolved hydrogen (H_2) gas over a period of time. The chronopotentiometry electrolysis was carried out using a two-electrode system at 1 atm pressure and 25 °C. A known amount of sample coated on carbon paper (1 cm^2 area surface) was used as a working electrode (in the present case, it works as a cathodic electrode), and a platinum coil was taken as a counter electrode (works as an anode). The catalyst loading on the carbon paper working electrode was maintained as 1 mg/cm^2, and 0.1 M sodium acetate pH 4.8, was used as the buffer. A homemade setup was utilized to conduct the electrolysis process by employing a constant cathodic current -0.001 A or -1 mA for 3 hours. The detailed description of this homemade setup along with its schematic- as well as its real-time photographs are provided below.

Calculation of Faradaic efficiency

The Faradaic efficiency can be expressed as the efficiency, with which charge is utilized in the electrochemical reaction. The Faradaic efficiency of the catalyst was determined by the following equation:

In a chronopotentiometric electrolysis, the evolved hydrogen gas was collected by a homemade setup. We found 1.15 mL/3 hours (0.383 mL/hour) of hydrogen gas under 1 atm pressure at 25 °C.

Thus, the number of moles of hydrogen evolved in one hour for **POM-MnW(OH)** = (0.366 / 24500) = 1.5632×10^{-5} mol

$$H_{2\ ideal} = \frac{\text{Q (total charge employed)}}{\text{n(number of electrons required for the chemical change)}\times 1\text{Farad}} \quad \ldots\ldots\ldots\ldots(3)$$

Here, we employed a constant cathodic current -0.001 A and n = 2 for HER (a two-electron process).

Thus, the H_2 ideally should evolve = $\frac{(0.001\times3600)}{(2\times96500)}$ mol = 1.8652×10^{-5} mol …… (4)

Faradaic efficiency = $\frac{\text{Experimentally evolved hydrogen}}{\text{Ideally evolved hydrogen}} \times 100$ …… (5)

Therefore, the Faradaic efficiency of compound **1** = $[(1.5632\times10^{-5}) / (1.8652\times10^{-5})] \times 100$

= 83.8% ≈ **84%**

Appendix 4

Supporting Data for Chapter 5

Contents

Section A5.1. Details of the proton conductivity measurements by the home-made setup

All the impedance spectra were recorded at open circuit potential of each of the sample pellet. A sinusoidal signal of 5 mV was applied over a frequency range from 1 Hz to 10^6 Hz. The electrochemical workstation was attached with a stainless steel-made two-electrode set up. The real-time images of the two electrode home-made cell are provided in Figure A22. The complete details of the two electrode cell are provided below.

The home-made cell consists of (1) a conical flask of 5 L, (2) a heating source to heat water (3) 1-2 L of distilled water inside the conical flask (4) the two electrode set up fitted with a digital thermometer to check the temperature. The whole set up was heated to maintain the temperature and also to generate sufficient humidity. The water vapors maintain the near saturated relative humidity (98%) as well as the temperature inside the system.

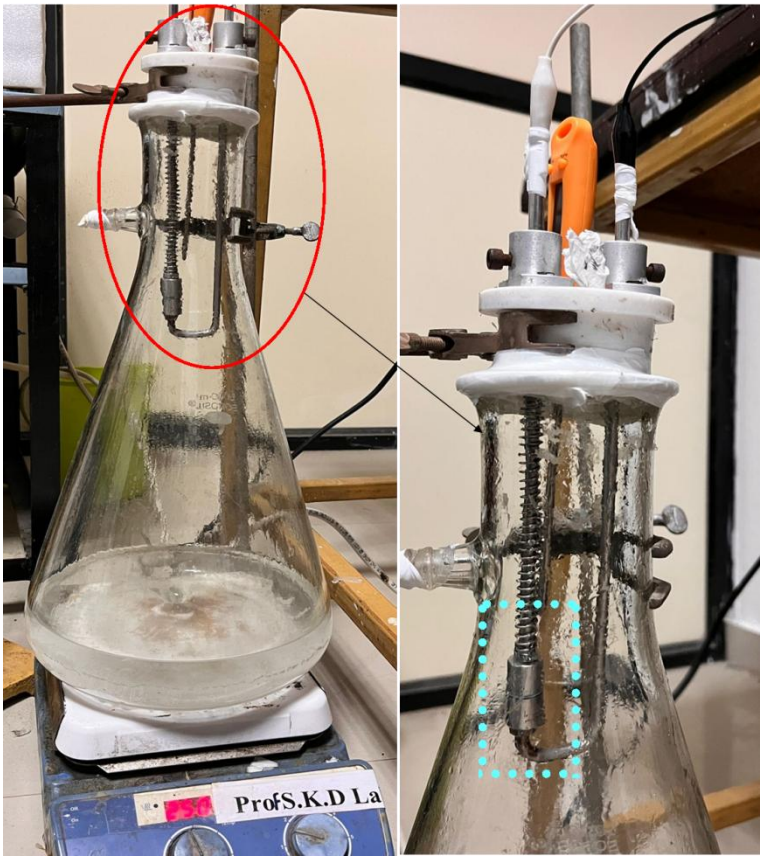

Figure A1. Real-time photographs of the home-made set up for proton conductivity measurement at a relative humidity of 98%. The photograph shows the whole setup (left side) and a close-up view of the two-electrode set-up where the pelletized sample is the working electrode (dotted square box).

Section A5.2. Calculation of proton conductivity from impedance spectra by fitting to relevant equivalent circuit

Nyquist plot displays the general features obtained, and the simplest equivalent circuit which fitted these experimentally obtained data plots well, is given below**.**

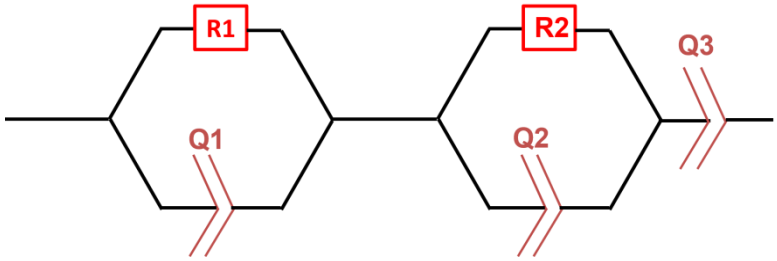

Figure A2. Schematic representation of the equivalent circuit utilized for fitting the impedance spectra obtained.

Impedance data were fitted to the most suitable equivalent circuit mentioned above with the help of EC-Lab software. The equivalent circuit is composed of three major components connected to each other in series. The pellet impedance (R1/Q1), impedance at the electrode electrolyte junction/interface (R2/Q2) and a constant phase element (Q3) are connected in series. The constant phase element (Q3) accounts for the linear low frequency region of the Nyquist plot of impedance spectrum. R1/Q1 is composed of a resistance (R1) and constant phase element (Q1) connected to each other in parallel mode. Similarly, R2/Q2 consists of a resistance (R2) and a constant phase element (Q2) connected in parallel mode. Here R1 accounts for the bulk resistance of the pellet while R2 represents the charge transfer resistance existing between the electrodes and the pellet electrolyte. Here, it should be noted that, charge transfer resistance R2 is not associated with the conductivity of the electrolyte. Instead R1 is the crucial factor which quantifies the resistance of the bulk electrolyte. R2 depends mainly on the particle size, is a combination of (a) resistance created between the carbon paper and sample particles (b) inter-grain resistance (c) resistance existing between electrode surface and carbon paper of pellet. Use of (a) different coating method (e.g., use of silver paint instead of carbon paper) (b) different methods to prepare pellet with more intimate contact between the particles (c) use of thin film instead of pellet can be useful to reduce the value of R2 in actual application. On the other hand, the bulk resistance of electrolyte i.e., R1 is of our primary interest as it represents conductivity of the bulk pellet, which in this case is the proton conductivity of the pellet. R1 depends on (a) intrinsic conductivity of the pelletized sample (b) thickness of the pellet and (c) area of cross section of the pellet.

Here, Table S1 shows the values of R1 at different temperature, by fitting the experimentally obtained data points along the curve generated by the equivalent circuit mentioned above and its respective proton conductivity values.

Table S1. Proton conductivity of compound 1 at different temperature

Temperature (°C)	Conductivity (Scm^{-1})
40	0.00543
50	0.00819
60	0.01216
70	0.02344
80	0.09786

Calculation of proton conductivity from R value

Resistivity (**ρ**) of a material = (**R** × **A)/l** ……. (1)

Thus, conductivity (**σ**) = 1/ **ρ** = **l**/(**R** × **A**) ……. (2)

R = resistance of sample; **σ** = conductivity of the sample.

l = thickness of pellet

A = area of cross section of pellet

The conductivity values were calculated using similar data fitting and calculations.

Section A5.3. Activation energy calculation

Activation energy of compound **1** for their proton conductivity was calculated from their variable temperature conductivity values. The derived plot was constructed as ln(σT) *vs* 1000/T. The slope value of the plot was used to calculate the activation energies for compound **1**.

From Arrhenius equation,

$$\sigma T = A\, e^{-Ea/RT} \qquad \text{……. (3)}$$

Here, σ = conductivity of electrolyte, *i.e.,* proton conductivity;

Ea = activation energy for proton conduction;

R = Ideal gas constant; *T* = temperature in Kelvin (K) scale.

$$\ln(\sigma T) = \ln A - \frac{Ea}{RT} \qquad \text{……. (4)}$$

$$\ln(\sigma T) = (\ln A) - \frac{Ea}{R\times 1000} \times \frac{1000}{T} \qquad \text{……. (5)}$$

Eqn (6) represent the straight line between ln(σT) and 1000/T.

Thus, value of slope **(m)** = ($\frac{Ea}{R\times1000}$)

For compound **1 s**lope (**m**) = -7.3971 K

Therefore, the activation energy for compound **1**, ***Ea* = 0.64 eV.**

Table S2. Proton conductivity of compound 2 at different temperature

Temperature (°C)	**Conductivity (Scm^{-1})**
40	0.0095
50	0.0139
55	0.0195
60	0.0327
65	0.0593
70	0.0850
80	0.1095

Activation energy calculation

From Arrhenius equation,

$$\ln(\sigma T) = (\ln A) - \frac{Ea}{R\times1000} \times \frac{1000}{T}$$

Eqn (6) represent the straight line between ln(σT) and 1000/T.

Thus, value of slope **(m)** = ($\frac{Ea}{R\times1000}$)

For compound **2, s**lope (**m**) = -7.6860 K

Therefore, the activation energy for compound **2**, ***Ea* = 0.66 eV.**

Section A5.4. Long-term stability check for proton conductivity

Apart from measuring proton conductivity of the sample, FTIR and PXRD analyses were also performed to check the durability of the material as proton conducting material. After 40 hours of stability check at 65 °C, compound **1** and **2** was examined by FTIR and PXRD analyses.

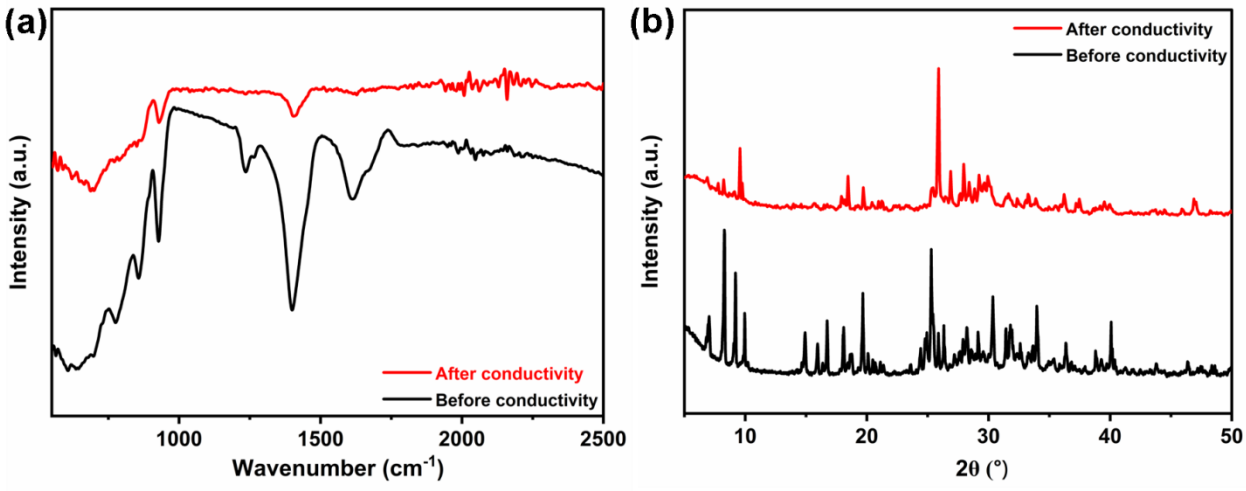

Figure A3. (a) FTIR spectrum of compound **1** after long-term stability studies, compared with the spectrum of original compound, (b) PXRD pattern of compound **1** after long-term stability measurements compared to the experimentally obtained PXRD pattern.

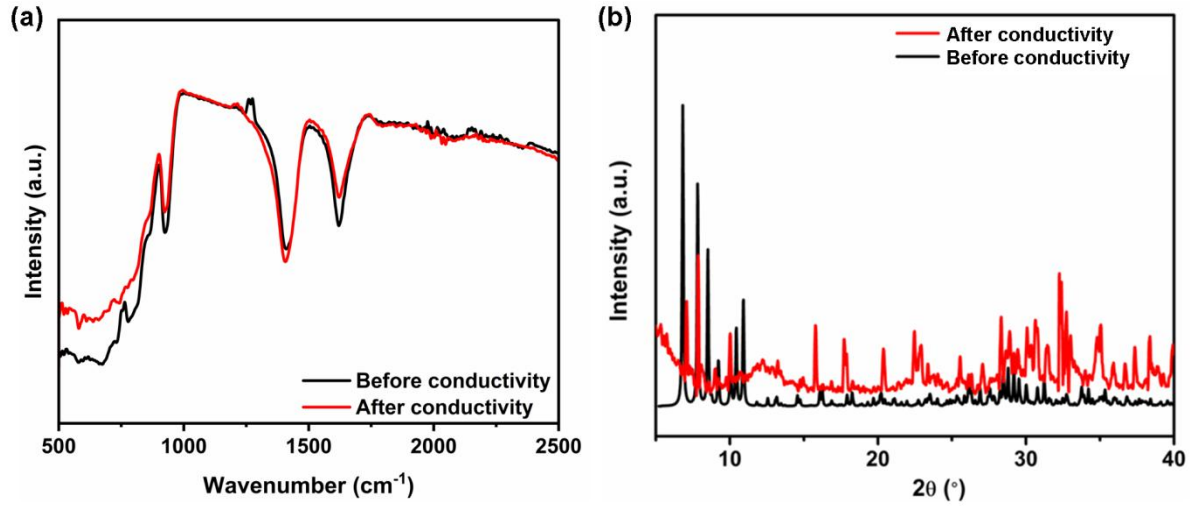

Figure A4. (a) FTIR spectrum of compound **2** after long-term stability studies, compared with the spectrum of original compound, (b) PXRD pattern of compound **2** after long-term stability measurements compared to the experimentally obtained PXRD pattern.

The FTIR spectra and PXRD profiles of the post-conductivity sample material do not show any prominent changes in their spectral features as seen from the above figure.

A5.5. References

1. Mukhopadhyay, S.; Debgupta, J.; Singh, C.; Sarkar, R.; Basu, O.; Das, S. K. *ACS Appl. Mater. Interfaces* **2019**, *11*, 13423–13432.

2. Basu, O.; Mukhopadhyay, S.; Laha, S.; Das, S. K. *Chem. Mater.* **2022**, *34*, 6734–6743.

3. Tandekar, K.; Singh, C.; Supriya, S. *Eur J Inorg Chem* **2021**, *2021*, 734–739.

Functional Inorganic Materials for Heterogeneous Electrocatalytic Water Splitting and Proton Conduction

by Athira Ravi

Submission date: 19-Nov-2023 01:07PM (UTC+0530)
Submission ID: 2232668340
File name: Athira_Ravi.pdf (4.71M)
Word count: 28897
Character count: 152461

LIST OF PUBLICATIONS

Thesis Chapter Publications

1. **Fabricating a Functionalized Polyoxometalate with ZIF-8: A Composite Material for Water Oxidation in a Wide pH Range**
   Mulkapuri, S.;† **Ravi, A.;**† Das, S. K. *Chem. Mater.* **2022**, *34*, 3624–3636. (DOI:10.1021/acs.chemmater.1c03917) †(contributed equally)

2. **Hydroxylated Polyoxometalate with Cu(II)- and Cu(I)-Aqua Complexes: A Bifunctional Catalyst for Electrocatalytic Water Splitting at Neutral pH**
   Ravi, A.; Mulkapuri, S.; Das, S. K. *Inorg. Chem.* **2023,** *62*, 32, 12650–12663. (DOI:10.1021/acs.inorgchem.3c00423)

Other Publications

3. **Exploring Proton Conductivity Studies of a Copper based Hydroxylated Polyoxometalate**
   Ravi, A.; Biswas, R.; Das, S.; Das, S. K., *J. Chem. Sci.* **2023**, just accepted.

4. **Electrocatalytic Hydrogen Evolution by a Uranium(VI) Polyoxometalate: an Environmental Toxin for Sustainable Energy Generation**
   Mulkapuri, S.; † Siddikha, A.;† **Ravi, A.**;† Saha P.; Kumar, A. V.; Boodida, S.; Vithal, M.; Das. S. K. *Inorg. Chem.* **2023**, (DOI:10.1021/acs.inorgchem.3c03018) †(contributed equally)

5. **Cobalt Formate, a Functional MOF: Electrocatalytic Water Oxidation**
   Ravi, A.; Nasani, R.; Das, S. K., *Journal of Molecular and Engineering Materials*, **2022**, (DOI: 10.1142/S2251237322400020)

6. **WVI–OH Functionality on Polyoxometalates for Water Reduction to Molecular Hydrogen**
   Mulkapuri, S.; **Ravi, A**.; Mukhopadhyay, S.; Kurapati, S. K.; Siby, V.; Das, S. K. ***Inorg. Chem. Front.*** **2022**, *9*, 3566–3577. (DOI: 10.1039/D2QI00421F)

7. **Barrel-Shaped-Polyoxometalates Exhibiting Electrocatalytic Water Reduction at Neutral pH: A Synergy Effect**
   Mulkapuri, S.; **Ravi, A.**; Nasani R.; Kurapati, S. K.; Das, S. K. *Inorg. Chem.* **2022**, *61*, 13868 13882. (DOI: 10.1021/acs.inorgchem.2c01811)

LIST OF PRESENTATIONS

1. **Athira Ravi** and Samar K. Das

   Fabricating a Functionalized Polyoxometalate with ZIF-8: A Composite Material for Water Oxidation in a Wide pH Range

   Poster Presentation at *ChemFest 2022*, held at University of Hyderabad, during April 22-23, 2022

   Received Best Poster Award.

2. **Athira Ravi** and Samar K. Das,

   Fabricating a Functionalized Polyoxometalate with ZIF-8: A Composite Material for Water Oxidation in a Wide pH Range

   Poster Presentation at International Conference on *Modern Trends in Inorganic Chemistry* (MTIC-XIX) at Institute of Science, Banaras Hindu University (BHU), Varanasi, during December 15-17, 2022.

3. **Athira Ravi** and Samar K. Das,

   Fabricating a Functionalized Polyoxometalate with ZIF-8: A Composite Material for Water Oxidation in a Wide pH Range

   Oral Presentation Dr. K. V. Rao Scientific Society Research Award, 2022-23

4. **Athira Ravi** and Samar K. Das,

   Hydroxylated Polyoxometalate with Cu(II)- and Cu(I)-Aqua Complexes: A Bifunctional Catalyst for Electrocatalytic Water Splitting at Neutral pH

   Oral Presentation at ChemFest 2023, held at University of Hyderabad, during March 7-8th, 2023

   Received Best Oral Presentation Award.

Functional Inorganic Materials for Heterogeneous Electrocatalytic Water Splitting and Proton Conduction

by Athira Ravi

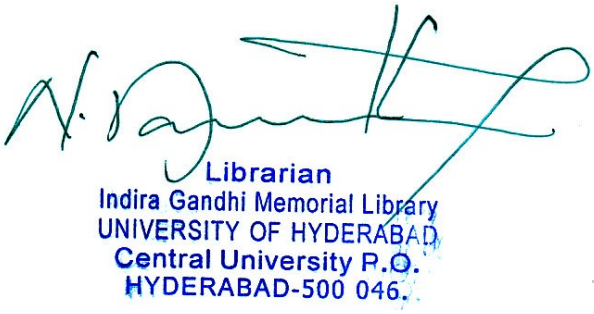

Submission date: 19-Nov-2023 01:07PM (UTC+0530)
Submission ID: 2232668340
File name: Athira_Ravi.pdf (4.71M)
Word count: 28897
Character count: 152461

Functional Inorganic Materials for Heterogeneous Electrocatalytic Water Splitting and Proton Conduction

ORIGINALITY REPORT

53%	12%	53%	6%
SIMILARITY INDEX	INTERNET SOURCES	PUBLICATIONS	STUDENT PAPERS

PRIMARY SOURCES

1	Athira Ravi, Sateesh Mulkapuri, Samar K. Das. "Hydroxylated Polyoxometalate with Cu(II)- and Cu(I)-Aqua Complexes: A Bifunctional Catalyst for Electrocatalytic Water Splitting at Neutral pH", Inorganic Chemistry, 2023 Publication	25%
2	Sateesh Mulkapuri, Athira Ravi, Samar K. Das. "Fabricating a Functionalized Polyoxometalate with ZIF-8: A Composite Material for Water Oxidation in a Wide pH Range", Chemistry of Materials, 2022 Publication	19%
3	Submitted to University of Hyderabad, Hyderabad Student Paper	2%
4	www.unboundmedicine.com Internet Source	1%
5	Sateesh Mulkapuri, Asha Siddikha, Athira Ravi, Pinki Saha, Avulu Vinod Kumar, Sathyanarayana Boodida, Muga Vithal, Samar	1%

S.K.Das 20.11.2023

Prof. Samar K. Das
School of Chemistry
University of Hyderabad
Hyderabad-500 046., INDIA.
skdas@uohyd.ac.in

S.K.Das 20.11.2023

Prof. Samar K. Das
School of Chemistry
University of Hyderabad
Hyderabad-500 046., INDIA.
skdas@uohyd.ac.in

K. Das. "Electrocatalytic Hydrogen Evolution by a Uranium(VI) Polyoxometalate: an Environmental Toxin for Sustainable Energy Generation", Inorganic Chemistry, 2023
Publication

6	Subhabrata Mukhopadhyay, Joyashish Debgupta, Chandani Singh, Rudraditya Sarkar, Olivia Basu, Samar K. Das. "Designing UiO-66-Based Superprotonic Conductor with the Highest Metal–Organic Framework Based Proton Conductivity", ACS Applied Materials & Interfaces, 2019 Publication	<1 %
7	www.researchgate.net Internet Source	<1 %
8	www.rsc.org Internet Source	<1 %
9	pubs.rsc.org Internet Source	<1 %
10	Sateesh Mulkapuri, Athira Ravi, Subhabrata Mukhopadhyay, Sathish Kumar Kurapati, Vinaya Siby, Samar K Das. "WVI–OH Functionality on polyoxometalates for water reduction to molecular hydrogen", Inorganic Chemistry Frontiers, 2022 Publication	<1 %

11	Ken-ichi Otake, Hiroshi Kitagawa. "Control of Proton-Conductive Behavior with Nanoenvironment within Metal–Organic Materials", Small, 2021 Publication	<1 %
12	Sateesh Mulkapuri, Athira Ravi, Rajendar Nasani, Sathish Kumar Kurapati, Samar K. Das. "Barrel-Shaped-Polyoxometalates Exhibiting Electrocatalytic Water Reduction at Neutral pH: A Synergy Effect", Inorganic Chemistry, 2022 Publication	<1 %
13	Wen-Jing Liu, Long-Zhang Dong, Run-Han Li, Yong-Jun Chen, Sheng-Nan Sun, Shun-Li Li, Ya-Qian Lan. "Different Protonic Species Affecting Proton Conductivity in Hollow Spherelike Polyoxometalates", ACS Applied Materials & Interfaces, 2019 Publication	<1 %
14	Xiumin Li, Xiaogang Hao, Abuliti Abudula, Guoqing Guan. "Nanostructured catalysts for electrochemical water splitting: current state and prospects", Journal of Materials Chemistry A, 2016 Publication	<1 %
15	www.ncbi.nlm.nih.gov Internet Source	<1 %

16	d-nb.info Internet Source	<1 %
17	Michael Horn, Amandeep Singh, Suaad Alomari, Sara Goberna-Ferrón et al. "Polyoxometalates (POMs): from Electroactive Clusters to Energy Materials", Energy & Environmental Science, 2021 Publication	<1 %
18	Naoki Ogiwara, Tsukasa Iwano, Takeru Ito, Sayaka Uchida. "Proton conduction in ionic crystals based on polyoxometalates", Coordination Chemistry Reviews, 2022 Publication	<1 %
19	unsworks.unsw.edu.au Internet Source	<1 %
20	ebin.pub Internet Source	<1 %
21	Athira Ravi, Rajendar Nasani, Samar K. Das. "Cobalt Formate, a Functional MOF: Electrocatalytic Water Oxidation", Journal of Molecular and Engineering Materials, 2022 Publication	<1 %
22	Dae-Woon Lim, Hiroshi Kitagawa. "Rational strategies for proton-conductive metal–organic frameworks", Chemical Society Reviews, 2021 Publication	<1 %

23	Shasha Li, Xiaogang Hao, Abuliti Abudula, Guoqing Guan. "Nanostructured Co-based bifunctional electrocatalysts for energy conversion and storage: current status and perspectives", Journal of Materials Chemistry A, 2019 Publication	<1 %
24	Debu Jana, Hema Kumari Kolli, Samar K. Das. " Co(OH) Intercalated in MoO by Molecular Electrodeposition Resulting in a Conductive Material: A Molybdenum Bronze for Efficient Electrocatalytic Hydrogen Evolution ", Chemistry of Materials, 2023 Publication	<1 %
25	Hai-Ning Wang, Xing Meng, Long-Zhang Dong, Yifa Chen, Shun-Li Li, Ya-Qian Lan. " Coordination polymer-based conductive materials: ionic conductivity electronic conductivity ", Journal of Materials Chemistry A, 2019 Publication	<1 %
26	Sateesh Mulkapuri, Sathish Kumar Kurapati, Subhabrata Mukhopadhyay, Samar K. Das. " A fully reduced {VIV18O } host and VO , Cl as guest anions: synthesis, characterization and proton conductivity ", New Journal of Chemistry, 2019 Publication	<1 %

27	www.science.gov Internet Source	<1%
28	repositorio.ufscar.br Internet Source	<1%
29	Maryam Samaniyan, Masoud Mirzaei, Ruhollah Khajavian, Hossein Eshtiagh-Hosseini, Carsten Streb. "Heterogeneous Catalysis by Polyoxometalates in Metal–Organic Frameworks", ACS Catalysis, 2019 Publication	<1%
30	Michael G. Walter, Emily L. Warren, James R. McKone, Shannon W. Boettcher, Qixi Mi, Elizabeth A. Santori, Nathan S. Lewis. "Solar Water Splitting Cells", Chemical Reviews, 2010 Publication	<1%
31	hdl.handle.net Internet Source	<1%
32	Submitted to Imperial College of Science, Technology and Medicine Student Paper	<1%
33	books.rsc.org Internet Source	<1%
34	"Advances in Materials Science for Environmental and Energy Technologies", Wiley, 2012 Publication	<1%

35	J LEGER. "Contribution of In-situ Infrared Reflectance Spectroscopy in the Study of Nanostructured Fuel Cell Electrodes", In-situ Spectroscopic Studies of Adsorption at the Electrode and Electrocatalysis, 2007 Publication	<1 %
36	Yuzhuang Song, Chengcheng Yu, Dingxuan Ma, Kang Liu. "Recent progress on ZIF-8 based MOF derivatives for electrocatalysis", Coordination Chemistry Reviews, 2024 Publication	<1 %
37	eprints.qut.edu.au Internet Source	<1 %
38	conference.cusat.ac.in Internet Source	<1 %
39	discovery.ucl.ac.uk Internet Source	<1 %
40	smartech.gatech.edu Internet Source	<1 %
41	Paulami Manna, Samar K. Das. "Perceptive Approach in Assessing Rigidity versus Flexibility in the Construction of Diverse Metal–Organic Coordination Networks: Synthesis, Structure, and Magnetism", Crystal Growth & Design, 2015 Publication	<1 %

42	Submitted to University of Nottingham Student Paper	<1 %
43	www.nature.com Internet Source	<1 %
44	dspace.stir.ac.uk Internet Source	<1 %
45	ir.niist.res.in:8080 Internet Source	<1 %
46	tel.archives-ouvertes.fr Internet Source	<1 %

Exclude quotes	On	Exclude matches	< 14 words
Exclude bibliography	On		